EPIGENETIC REPRESSION IN THE CONTEXT OF ADULT NEUROGENESIS

by

CHRISTOPHER RHODES, M.S.

DISSERTATION
Presented to the Graduate Faculty of
The University of Texas at San Antonio
in Partial Fulfillment
of the Requirements
for the Degree of

DOCTOR OF PHILOSOPHY IN CELL AND MOLECULAR BIOLOGY

COMMITTEE MEMBERS:
Chin-Hsing Annie Lin, Ph.D., Chair
Astrid Cardona, Ph.D.
Brian Derrick, Ph.D.
Vance Lemmon, Ph.D.
Isabel Muzzio, Ph.D.
Yufeng Wang, Ph.D.

THE UNIVERSITY OF TEXAS AT SAN ANTONIO
College of Sciences
Department of Biology
December 2017

DEDICATION

Dedicated to my wife Karla, my parents Tom and Ellen, my aunt Elizabeth and my brother Justin for their unwavering support in everything I do, for providing me with inspiration and for instilling in me boundless wonder of the world around us.

ACKNOWLEDGEMENTS

First and foremost, I would like to acknowledge my mentor Dr. Chin-Hsing Annie Lin for her boundless enthusiasm for biology, her support of me throughout my graduate studies, and for her guidance and technical expertise which has prepared me well to start the journey to becoming a successful research scientist. I would also like to thank all the members of my Dissertation Committee, Drs. Astrid Cardona, Brian Derrick, Vance Lemmon, Isabel Muzzio, and Yufeng Wang for their advice, guidance, mentoring and critical input throughout this project. The current and past members of the University of Texas at San Antonio Lin Lab were instrumental allowing me to focus on learning highly technical methodologies and therefore greatly increased my overall productivity. Among the Lin lab members, Angela Huang and Bethany Zablotsky deserve special mention and praise for help in every facet of research we completed. I would like to acknowledge my cohort of graduate students in the University of Texas at San Antonio Biology Department, Natalia Castro, Megan Malke, Daniel Montenegro and Jesus Romo. I had the pleasure and good fortune to know them as we all developed into independent researchers and with whom I could seek help, input and motivation during the inevitable challenges all graduate students face. I would also like to thank Dr. Richard Sandstrom for his tutelage in the arena of sequence analysis. I would like to thank Guilia Zunino for ongoing input and collaboration in the Lin Lab's use of light sheet microscopy. I would like to acknowledge Drs. Alexander Tarakhovsky and Gunnar Schotta for generously providing the Lin lab with *Ezh2* and *Suv4-20h1* conditional knockout mice, respectively. I would also like to acknowledge Dr. Mitchel Berger, the University of Texas at San Antonio Laboratory Animal Research Committee, and the Texas Biomedical Institute/Southwest National Primate Research Center.

"This Master's Thesis/Recital Document or Doctoral Dissertation was produced in accordance with guidelines which permit the inclusion as part of the Master's Thesis/Recital Document or Doctoral Dissertation the text of an original paper, or papers, submitted for publication. The Master's Thesis/Recital Document or Doctoral Dissertation must still conform to all other requirements explained in the "Guide for the Preparation of a Master's Thesis/Recital Document 6 or Doctoral Dissertation at The University of Texas at San Antonio." It must include a comprehensive abstract, a full introduction and literature review, and a final overall conclusion. Additional material (procedural and design data as well as descriptions of equipment) must be provided in sufficient detail to allow a clear and precise judgment to be made of the importance and originality of the research reported.

It is acceptable for this Master's Thesis/Recital Document or Doctoral Dissertation to include as chapters authentic copies of papers already published, provided these meet type size, margin, and legibility requirements. In such cases, connecting texts, which provide logical bridges between different manuscripts, are mandatory. Where the student is not the sole author of a manuscript, the student is required to make an explicit statement in the introductory material to that manuscript describing the student's contribution to the work and acknowledging the contribution of the other author(s). The approvals of the Supervising Committee which precede all other material in the Master's Thesis/Recital Document or Doctoral Dissertation attest to the accuracy of this statement."

December 2017

EPIGENETIC REPRESSION IN THE CONTEXT OF ADULT NEUROGENESIS

Christopher Rhodes Ph.D.
The University of Texas at San Antonio, 2017

Supervising Professor: Chin-Hsing Annie Lin, Ph.D.

Neural stem progenitor cells (NSPCs) in the mammalian brain contribute to life-long neurogenesis and brain health. Adult mammalian neurogenesis primarily occurs in the subventricular zone (SVZ) and the subgranular zone (SGZ) of the dentate gyrus. Epigenetic repression is a crucial regulator of cell fate specification during adult neurogenesis. How epigenetic repression impacts adult neurogenesis and how epigenetic dysregulation may impact neoplasia or tumorigenesis remains poorly understood. Examination of epigenetic regulation in the adult mammalian brain is complicated by the heterogeneous nature of neurogenic niches and by the highly orchestrated fate specification processes within neural stem progenitor cells involving myriad intrinsic and extrinsic factors. To overcome these challenges, we utilized a cross-species approach. To model histone modifications as they exist *in vivo* for epigenetic profiling, we isolated neural stem progenitor cells from the adult SVZ and SGZ of non-human primate baboon brains. To determine cellular and molecular changes within the adult SVZ and SGZ following loss of epigenetic repression, we utilized multiple mouse models, including conditional *Ezh2* and *Suv4-20h1* knockouts. To model the non-cell type specific effects common to small molecule screening and brain chemotherapeutic agents, induction of conditional knockout utilized a recombinant Cre protein. Finally, to model epigenetic mechanisms during SVZ-associated glioblastoma (GBM) tumorigenesis, we conducted comparative analysis between healthy NSPCs and GBM specimens from humans. The convergence of baboon, mouse and human models of adult neurogenesis

revealed that epigenetic repression is a critical mechanism regulating proper neural cell fate and that epigenetic dysregulation may be a driver of GBM.

TABLE OF CONTENTS

LIST OF TABLES

LIST OF FIGURES

CHAPTER ONE: INTRODUCTION

Cell Fate and Neurogenesis

Cell Fate Determination

One key requirement for organismal development is generation of correct cell types in appropriate regions of the nervous system. Cell fate is the process of determining which cell type a stem cell will become (Livesey and Cepko, 2001). Several factors influence cell fate, including genetic factors, epigenetic factors, extrinsic signaling cues, and the microenvironment of a cell. Cells may have a distinct genotype that is associated with a given phenotype. Additionally, cell type specific or tissue specific combinations of gene expression play a major role in cell fate determination. Another component that influences cell fate is a cell's epigenetic state. Epigenetics is loosely described as heritable changes in gene expression without involving alterations in DNA sequence. The term "epi" means "over or above" and generally refers to changes associated with DNA, but not directly altering the nucleotide sequence of DNA. As such, epigenetic regulation involves DNA associated proteins, non-coding RNAs, and chemical modifications to DNA nucleotides, but does not directly change the sequence of DNA. Epigenetic mechanisms will be described extensively in a later section.

One of the earliest attempts to represent the process of development in a simplified, abstract manner was by the British evolutionary developmental biologist C. H. Waddington. The resulting metaphor now called "Waddington's landscape" was first described in 1966 (Waddington, 1966) and has since become an established abstraction of regulatory processes during organismal development. While Waddington's landscape was developed to describe organismal development, it is commonly used in contemporary biology to represent cell fate (Fig. 2) (Moris et al., 2016). In the context of development, a pebble at the top of Waddington's landscape represents a pluripotent

or multipotent stem cell. As the pebble rolls down Waddington's landscape, the fate potential become increasingly restricted. Importantly, cell fate does not imply commitment or differentiation; it only states that a stem cell will eventually become a specific cell type (Livesey and Cepko, 2001). During cell fate determination, cells start as an "early-born" cell meaning they display properties that arise early in a lineage. Eventually, one of many "late-born" cell types occur in the lineage (Kohwi and Doe, 2013). Exactly how intrinsic and extrinsic factors integrate to specify cell fate remains a central question in biology (Artavanis-Tsakonas et al., 1999; Guillemot, 2007; Schuurmans and Guillemot, 2002).

Cell Fate Models

There are at least three competing models of neural cell fate determination. The first is the progressive restriction model, in which progenitors start off with broad fate potential before gradually losing their ability to produce earlier-generated cell types (Desai and McConnell, 2000; Kriegstein and Alvarez-Buylla, 2009; Livesey and Cepko, 2001; Mathis and Nicolas, 2003). As such, adult NSCs and other early-born cells only lose the ability to make earlier cell properties (Fig. 3A). However, adult NSCs can make all cell types produced during later developmental stages. Thus, NSPCs progress through an ever-narrowing funnel of possible fates. Conversely, in the competence model of cell fate early-born cells experience periods of competence during which a cell is only able to generate a subset of cell types (Kohwi and Doe, 2013; Livesey and Cepko, 2001). As such, NSPCs will first acquire and then lose the ability to make a single subtype at each developmental stage (Fig. 3B). The third possibility is the stochastic model where NSPCs randomly commit to a cell fate due to chaotic events at the epigenetic level. Such randomness of individual cell fate events is masked at the population level (Moris et al., 2016; Nimmo et al.,

2015; Wagers et al., 2002). The stochastic view of cell fate has gained popularity for several stem cell niches as single cell transcriptomics is applied to the problem (Fig. 3C). Evidence for the stochastic model is only beginning to be described in neurogenic cells. Even so, this model will likely clarify early cell fate mechanisms of neural lineages including epigenetic landscapes, transcription factors, and gene regulatory networks (Bonaguidi et al., 2012; Moris et al., 2016; Nimmo et al., 2015; Signolet and Hendrich, 2015). Importantly, cell fate clearly involves intrinsic and extrinsic factors (Guillemot, 2007; Schuurmans and Guillemot, 2002), yet the stochastic model centers around intrinsic processes. Consequently, the stochastic model may not be mutually exclusive to the progressive model nor competence model. The competency model of neural fate determination is currently well established only within the retina. The stochastic model is currently established in hematopoietic and embryonic stem cells. While likely not the only model influencing adult neurogenesis, a number of recent reports support the notion of neural fate determination by progressive restriction in the adult mammalian brain (Desai and McConnell, 2000; Gonzales-Roybal and Lim, 2013; Heinrich et al., 2010; Mathis and Nicolas, 2003; Noctor et al., 2008; Xu et al., 2016).

Waddington's Landscape and Embryogenesis

Examples of cell fate and loss of lineage potential can be seen at the different developmental stages of embryogenesis (Wennekamp et al., 2013). During embryogenesis, a fertilized zygote develops into a multicellular structure called the blastocyst (Fig. 4A) (Tam and Loebel, 2007). The blastocyst contains an external layer called the trophoblast, a collection of cells called the inner cell mass (ICM), and a fluid-filled cavity called the blastocoel (Li and Belmonte, 2017). The ICM is capable of developing all the different cell types in an adult organism except

for germline cells. It is the ICM from which all three primary germ layers originate: the endoderm, mesoderm and ectoderm. During the next major developmental step, gastrulation, the single layer blastocyst is reorganized into a multilayer gastrula (Tam and Behringer, 1997). Initiation of gastrulation is marked by the formation of the primitive streak. Throughout gastrulation, the ICM of the blastocyst splits into 2 layers: the epiblast and the hypoblast (Tam and Behringer, 1997). The epiblast is destined to develop into the ectoderm and the mesoderm, while the hypoblast and trophoblast develop into the endoderm. Each of the fundamental germ layer further gives rise to specific subsets of tissues and cell types. For example, the ectoderm and primitive streak ultimately become the neural tube after induction by Sox transcription factors (Rex et al., 1997). From a cell fate perspective, the ICM of the blastocyst has high fate potential and can generate virtually any cell type in the adult body (Fig. 4B). Indeed, prior to the wide-spread adoption of induced pluripotent stem cells, the ICM was used to derive embryonic stem cells (ESCs). Alterations in cell fate potential are often associated with changes to the gene regulatory networks anchoring cells in a particular cell state (Li and Belmonte, 2017). Thus, cells within the various fundamental germ layers are more developed and restricted to multipotency. This means they can generate cells of several, but not all, cell lineages in an organism. Ultimately, cells are fated to convert into a single, terminally differentiated cell type such as a skin cell, or a hepatocyte, or a specific neuronal subtype in the retina. Importantly, it is the ectoderm that gives rise to the central nervous system, the brain, and all the neural lineages of an organism (Tam and Behringer, 1997).

Neurogenesis

Neurogenesis is the transition from proliferative, undifferentiated cells to differentiated, functional neurons (Urban and Guillemot, 2014). Mature neurons interact with one another

through connections called synapses. Synaptic connections between a series of neurons form functional networks that provide the foundation for cognition. A related process of gliogenesis produces glia, including astrocytes and oligodendrocytes, from a type of stem cell called neural stem cells. Glial cells provide support and insulation for neurons. There are 2 main types of neurogenesis characterized by when the process occurs during the life of an organism: embryonic and adult. Embryonic neurogenesis occurs during fetal formation and is responsible for producing the central and peripheral nervous system (Kriegstein and Alvarez-Buylla, 2009). In mammals, adult neurogenesis occurs in the mature organism and involves maintenance of existing neuronal populations within the brain throughout the life of an organism.

Stem Cells

Both embryonic and adult neurogenesis in mammals are primarily driven by stem cells residing in specialized neurogenic niches devoted to neurogenesis (Bond et al., 2015; Ming and Song, 2011). A niche is a microenvironment that anatomically restricts stem cells and influences their development (Schofield, 1978). In general, stem cells are cells that can reproduce themselves (i.e. self-renew) and provide long-term reconstitution of multiple cell types or lineages (Bonthagarala et al., 2013; Morrison and Spradling, 2008). There are multiple types of mammalian stem cells including embryonic stem cells (ESCs) which are derived from embryos, and various adult stem cells (also referred to somatic stem cells) that are restricted to a particular tissue in a mature organism (Evans and Kaufman, 1981; Morrison and Spradling, 2008). Stem cells generating germ-cell lineages separate from somatic lineages early in development (Ohinata et al., 2009; Surani, 2015; Wu and Izpisua Belmonte, 2016). Additionally, somatic cells can be reprogrammed into induced pluripotent stem cells (iPSCs) which are cells with similar properties

to ESCs (Yamanaka, 2012). In the mammalian embryo, ESCs are pluripotent and can therefore produce all the cell types in a body (Evans and Kaufman, 1981). Adult stem cells are generally thought of as tissue specific and able to only give rise to progeny cells corresponding to their tissue of origin (Wagers and Weissman, 2004). Importantly, most cells in adult bodies are not stem cells. Adult stem cells have an essential role in tissue homeostasis, repair and regeneration of tissue or an organ (Singh, 2012). Consequently, adult stem cells have to respond to tissue damage and proliferate based on tissue requirements, while avoiding over-proliferation (Biteau et al., 2011). The stem cells residing in the mammalian brain are called neural stem cells (NSCs) (Fuentealba et al., 2015; Kriegstein and Alvarez-Buylla, 2009).

Adult Neural Stem Cells

NSCs exist in an undifferentiated state and can perform 2 related tasks: 1) self-renewing to maintain a reservoir of NSCs; and 2) giving rise to differentiated progeny within the brain (Fig. 5A) (Gage, 2000; Ming and Song, 2011). Such NSCs are responsible for central nervous system (CNS) formation during embryogenesis (Kriegstein and Alvarez-Buylla, 2009; Martynoga et al., 2012). NSCs also establish neurogenic homeostasis during adulthood and may re-establish such homeostasis in response to neuropathology or traumatic brain injuries (Imitola et al., 2004). Neural stem cells have long been suspected of being tri-potent with the capacity to generate neurons, astrocytes and oligodendrocytes (Ma et al., 2009; Ming and Song, 2011). Cultured NSCs and neurospheres derived from adult rodent and human brains demonstrate long-term self-renewal and differentiation into all neural lineages (Kukekov et al., 1999; Palmer et al., 1999; Palmer et al., 1995; Palmer et al., 1997; Reynolds and Weiss, 1992; Richards et al., 1992; Roy et al., 2000) Intriguingly, in a living brain (i.e. *in vivo*), NSCs typically only generate a subset of cell types. For

example, NSCs within the hippocampus generate neurons and astrocytes, but not oligodendrocytes (Bonaguidi et al., 2011) Within the SVZ, fate-mapping studies have shown NSCs generating both neurons and oligodendrocytes, while clonal analysis found only neuronal lineages from NSCs (Calzolari et al., 2015). One explanation for this apparent difference between *in vitro* and *in vivo* fate capacity could be due to NSCs being gradually lineage restricted during the transition from embryonic to adult neurogenesis (Kriegstein and Alvarez-Buylla, 2009). A second possible explanation is researchers have not yet developed methods to manipulate cells *in vitro* which effectively recapitulate cell fate *in vivo*. Alternatively, adult NSCs could be inherently tri-potent but various latent lineage potentials are suppressed through interactions with the local niche environment (Livesey and Cepko, 2001; Ming and Song, 2011). Recent evidence supports the importance of routine interactions between NSCs and their local surroundings. These recurring interactions are very likely to influence lineage potential *in vivo*. Niche input from astrocytes, oligodendrocytes and ependymal cells influence the behavior of NSCs. Neuro-immunological interactions influence NSC homeostasis as microglia phagocytose the progeny of NSCs (Sierra et al., 2010) while activated microglia reduce neurogenesis (Ekdahl et al., 2003). Further, metabolic influx likely has a large impact on neurogenesis as the blood-brain barrier is leaky near regions of proliferating NSCs. Such leakiness increases NSC access to blood borne growth factors and metabolites (Tavazoie et al., 2008). Another source of niche nutrients and growth factors is the lateral ventricle choroid plexus. This network of cells is alongside the SVZ and produces the bulk of the brains cerebrospinal fluid (Redzic et al., 2005). Indeed, even NSCs and their progeny are critical constituents of neurogenic niches and often participate in autocrine and paracrine signaling (Alfonso et al., 2012).

Embryonic Neurogenesis

Neurodevelopmental events are conserved across diverse vertebrates (Workman et al., 2013). The primordium of the CNS, the neural plate, originates from the ectoderm during early embryogenesis (Martynoga et al., 2012). The neural plate is a single sheet of neuroepithelial (NE) cells, which undergo rapid, planar symmetric divisions. Cells in adjacent developmental layers do not grow as quickly, resulting in uneven cell movement along the neural plate. The resulting asymmetry in the primate streak forms the neural crest, which further develops into the neural groove followed by the neural tube. The interior of the neural tube becomes the fluid-filled cerebral ventricles of the brain, the central canal of the spinal cord and the passages that connect them.

At mid-gestation, the first neurons of the CNS are born in the NE layer by the earliest proliferative population of NSCs called neuroepithelial cells (Fig 4B) (Martynoga et al., 2012). In mice, this occurs at embryonic day 9 (E9) and E10. At this point, neurogenesis is considered to initiate and two corresponding developmental transitions occur. Firstly, neuroepithelial cells convert into a distinct population of NSCs termed radial glial (RG) cells (Kriegstein and Alvarez-Buylla, 2009). Secondly, as the RG cells elongate away from the ventricle, the NE layer morphs into the ventricular zone (VZ). The VZ forms the innermost, or apical, surface of the cerebral cortex for the remainder of neurodevelopment. Adjacent to the VZ is the subventricular zone (SVZ) which is contiguous with the intermediate zone (IZ). The outermost zone, or basal surface, of the brain is the cortical plate (CP) or neocortex. During embryogenesis, each layer is built on top of the previous. As such, the apical VZ is formed first, followed by SVZ, then IZ, and finally the CP (Dehay and Kennedy, 2007). As neurodevelopment progresses, RG cells expand into the VZ/SVZ layers. Along with the early NE cells, it is these RGs which are responsible for populating the mammalian cortex with excitatory neurons during embryonic neurodevelopment (Fig. 5B-C)

(Kriegstein and Alvarez-Buylla, 2009). There are 2 types of radial glial cells: ventricular radial glial cells (vRG) and outer radial glial cells (oRG). The vRGs are conserved between mice and humans. In both species, vRGs undergo asymmetric division and give rise to intermediate progenitor cells (IPs). The IPs in turn, are restricted to the SVZ and undergo symmetric cell division. Ultimately, IPs undergo further differentiation into immature neurons which migrate radially along the body of an adjacent RG cell and integrate into the cortex. Similar to vRGs, oRGs exist within the outer SVZ (oSVZ) of humans but are largely, yet not entirely, absent within the mouse brain (Fig. 5C) (Bershteyn et al., 2017; Wang et al., 2011). Such oRGs are highly dependent the activity of *ARHGAP11B* to initiate amplification of IP cells (Florio et al., 2015). Upon *ARHGAP11B* expression, oRGs become responsible for increasing the neurogenic rate during human embryogenesis to quickly expand the cerebral cortex. As a result, differences in brain volume and cortical folding between mice and humans are almost solely due to the relative quantity of oRGs within the oSVZ/IZ (Bershteyn et al., 2017).

From a developmental perspective, the generation of the dentate gyrus (DG) of the hippocampus is distinct from the telencephalon. The DG originates from the dentate neuroepithelium (DNE), a part of the VZ of the medial pallium that is in direct contact with the cortical hem (Urban and Guillemot, 2015). The embryonic SVZ is seen as a continuation of the ventricular zone (VZ) of the telencephalon. In contrast, the formation of the DG involves the generation of a dedicated progenitor cell source in close proximity to the pial surface and away from the VZ (Fig. 5D). This additional proliferative zone remains active postnatally and eventually becomes the subgranular zone (SGZ) of the DG. Following development, the SGZ/DG will become the site of adult hippocampal neurogenesis.

Adult Neurogenesis

It is now well accepted that all mammals generate neurons throughout their lives and such ability is due to NSCs residing in brain (Kempermann and Gage, 1999). The primary role of adult neurogenesis is to maintain an existing populations of neurons originally developed during embryogenesis. During the life of an adult mammal, there is a continual loss of neurons for a number of reasons including normal cell turnover, stroke, traumatic brain injury, neuro-inflammatory diseases, autoimmune diseases, and neurodegenerative diseases. Adult neurogenesis involves replacement of such lost neurons from a reservoir, or pool, of undifferentiated stem and progenitor cells. Thus one of the primary functions of adult neurogenesis is to maintain a steady level of neurons within the brain, a process known as neurogenic homeostasis. If neurons are lost, adult neurogenesis will increase production of neurons to replace the lost neurons. Conversely, production of cells destined to become neurons will decrease if neuronal turnover or death is low. Among the processes underlying neurogenic homeostasis is establishment and maintenance of a balance between NSC self-renewal and differentiation (Fig. 6). Maintaining such a delicate balance is exquisitely complex and dysregulation of such a balance can have monumentally deleterious effects on brain health.

In contrast to developing brains, adult neurogenesis is spatially restrained into specialized regions called neurogenic niches. The reason for this spatial restriction may be to prevent over-proliferation and unbounded expansion of brain volume in fully developed organisms, or it may prevent disruption of existing functional neural networks. One of the largest, most conserved and best studied adult neurogenic niches retaining NSCs within the adult mammalian brain is the SVZ adjacent to the walls of the lateral ventricles (Fig. 7A-B). The SVZ contains quiescent, slowly dividing neural stem cells (NSCs) with astrocyte-like morphology and active stem cells expressing

Nestin. The SVZ also contains mitotic, undifferentiated neural progenitors called neuroblasts (NBs). In rodent models, NSCs give rise to transiently-amplifying cells, which subsequently give rise to NBs. NBs ultimately migrate along the rostral migratory stream to integrate into the olfactory bulb and differentiate into interneurons to function in olfaction. This process also occurs in humans, but the rate of SVZ-OB migration is far lower than that of rodents. Additionally, in human and mouse, NBs of SVZ origin migrate into the striatum a region which coordinates limb movement. In humans the striatum is the primary target of SVZ derived neural progenitors; striatal invasion in the rodent occurs primarily in response to stroke and disease (Ernst et al., 2014; Ernst and Frisen, 2015; Inta et al., 2015; Kandasamy et al., 2015; Luzzati et al., 2011).

The other large adult neurogenic niche is the SGZ within the DG of the hippocampus (Fig. 7C-D). Although adult neurogenesis exists in fish, amphibians and reptiles, the appearance of the DG as a structural and functional unit is more recent and is exclusive to mammals (Grandel and Brand, 2013; Treves et al., 2008). The SGZ is a thin layer between the hilus and granular cellular layer of the DG (Goncalves et al., 2016). Like in the SVZ, quiescent and active NSCs reside in the SGZ. These NSCs give rise to intermediate progenitor cells (IPs) which migrate toward the molecular layer and transition to post-mitotic immature neurons. During the maturation phase, immature neurons extend dendrites into the molecular layer and their axon to CA3. This allows the immature neurons to begin integration into the trisynaptic circuit of the hippocampus (Kempermann et al., 2015).

Neurons originating in the SGZ primarily contribute to the hippocampus proper and the trisynaptic circuit. Briefly, the trisynaptic circuit connects inputs from the entorhinal cortex to the three areas of the hippocampus proper (Rolls and Kesner, 2006). The trisynaptic circuit consists of three interconnected regions: the dentate gyrus (DG), cornu ammonis 3 (CA3) and cornu

ammonis 1 (CA1). Inputs from the entorhinal cortex travel along the medial Perforant Pathway towards the DG, which helps in spatial pattern separation tasks (Rolls and Kesner, 2006). Consistent with this, rats with DG lesions have impaired spatial pattern separation abilities (Gilbert et al., 2001; Goodrich-Hunsaker et al., 2008). The signal is relayed from the DG along the Mossy Fiber Pathway to CA3 which has been suggested to act as an autoassociation memory which enables episodic memories to be formed and stored in the CA3 network and also to perform pattern completion (Rolls and Kesner, 2006). The signal is subsequently relayed from CA3 along the Shaffer Collateral Pathway to CA1 which recodes information from CA3 and sets up associatively learned backprojections to neocortex to allow subsequent retrieval of information to neocortex. The CA1 participates in sequence memory and associations across time, and behaviorally, is implicated in processing temporal information (Rolls and Kesner, 2006).

Lineage specification and commitment

Cell fate determination is a broad and complex process. Fate determination broadly consists of three sequential steps: fate specification, linage commitment and differentiation. In multipotent NSCs, fate specification establishes the potential to differentiate into multiple lineages (Alvarez-Buylla et al., 2008; Guillemot, 2007; Livesey and Cepko, 2001; Nimmo et al., 2015; Schuurmans and Guillemot, 2002). Yet, a cell having the ability to proceed down different lineages and a cell truly pursuing a single fate are quite different conditions (Livesey and Cepko, 2001). Lineage commitment is when a cell becomes irreversibly restricted to one particular cell fate (Nimmo et al., 2015). Consequently, commitment is the cell fate event where a cell loses the potential to differentiate into other cell types. As cultured cells can be forced into discrete states not observed *in vivo*, lineage commitment solely refers to events under physiological conditions. The processes

of fate specification and lineage commitment are conceptually distinct. However, recent evidence suggests these are interlinked processes with related and overlapping mechanisms (Nimmo et al., 2015). Lastly, neurogenesis requires producing an appropriate proportion of neurons and initiating gliogenesis at the correct time. The expression of proneural genes in an NSPC should be restrained until when neurons have reached a suitable number at specific CNS positions. A mechanism called "lateral inhibition" regulates the rate of cells committing to a particular lineage. Thus, commitment to a particular fate by one NSPC has the consequence of inhibiting its neighbors to follow the same fate (Bertrand et al., 2002).

NSC stepwise differentiation

Following cell fate specification and lineage commitment, NSPCs undergo stepwise differentiation. During stepwise differentiation NSPCs are directed to execute a terminal differentiation program in a stepwise fashion (Ezhkova et al., 2009; Ohlemacher et al., 2016). Each differentiation phase is highly correlated with a unique cell properties and transcriptional profile (Ezhkova et al., 2009). Consequently, early-born NSCs transform into one of many late-born neuronal subtypes (Fig. 8A).

Early-born neural cells can be grouped into quiescent NSCs (qNSC) and active NSCs (aNSC) by established cell-type specific histological markers (Fig. 8B-C). Both NSC populations are mitotically active, undifferentiated, neurogenic populations. The majority of NSCs are quiescent and express GFAP and CD133, while active NSC express Nestin and EGFR but not GFAP (Codega et al., 2014; Fischer et al., 2011). Based on recent single cell transcriptome experiments, each group of NSC can be further divided into NSC subtypes. Currently, two distinct populations of qNSC can be detected: dormant qNSC and primed qNSC. There are at least three

putative aNSCs populations: aNSC-early, aNSC-mid and aNSC-late (Dulken et al., 2017; Llorens-Bobadilla et al., 2015). Consistent with histological markers, dormant and primed qNSCs enter the cell cycle at a relatively low rate. NSCs reportedly pass from dormancy to primed NSCs based on physiological cues in the CNS. Both dormant and primed qNSC exhibit extensive transcriptional heterogeneity. Dormant qNSCs exhibit lower rates of global protein synthesis than primed qNSCs. Additionally, dormant qNSCs are more receptive than primed qNSCs to Notch signaling, which inhibits proneuronal gene activation in adult NSCs. The transition to primed qNSCs is marked by global transcriptional activation and upregulation of lineage specific transcription factors. Indeed, transcription factor expression alone is often sufficient to identify many populations in the neuronal lineage (Dulken et al., 2017; Johnson et al., 2015; Llorens-Bobadilla et al., 2015; Pollen et al., 2015; Pollen et al., 2014). Transition from quiescent to active NSCs is primarily mediated by ASCL1 transcription factor and potentially BRN2 and MYT1L (Dulken et al., 2017). Collectively, these proteins comprise a group called the "BAM" factors which rapidly induce neuronal differentiation of human induced pluripotent cells (Mall et al., 2017; Pang et al., 2011). Once activated, aNSCs transition through three distinct states. Each aNSC state has a transcriptional profile that correlates with early-, mid-, and late-differentiation. The aNSC profiles include aNSC-early ($EGFR^{+}CDK1^{-}$), aNSC-mid ($EGFR^{+}CDK1^{+}DLX2^{low}$), aNSC-late ($EGFR^{+}CDK1^{+}DLX2^{high}$) markers.

Following intrinsic and extrinsic signals, aNSC-late cells transition to neural progenitor cells (NPCs). Nomenclature and classification schemes for NPCs varies extensively. We will simply denote an NPC as an intermediate developmental state arising after aNSCs but prior to neurons. As such, NPCs share characteristics of both NSCs and neurons, but are a distinct population. NPCs are similar to NSCs in that they are undifferentiated and mitotically active. The

ability to undergo proliferative growth allows NPCs to quickly amplify progeny populations. In contrast to NSC-like features, NPCs and neurons are post-lineage committed cell types and possess limited cell fate potential. At a minimum, NPCs are bipotent and can give rise to additional NPCs or contribute to a neuronal subtype. The transition from NSCs to NPCs likely involves a collapse of the multipotent gene regulatory network and establishment of a neuronal gene expression program (Bertrand et al., 2002; Li and Belmonte, 2017). In such a transition, stemness genes including Sox1, Sox2, and Sox3 become inhibited (Guillemot, 2007; Schuurmans and Guillemot, 2002). Meanwhile, activation of proneuronal genes, including NeuroD and Tbr1, ultimately prompt terminal neuronal differentiation (Schuurmans and Guillemot, 2002). Following the switch away from a stem cell program, neuronal differentiation cascades activate in NPCs, including the Mash1-Dlx2-GAD67 cascade (Schuurmans and Guillemot, 2002). However, many of the genetic components determining specific neuronal subtypes have yet to be elucidated.

Progression from NPC to neuron involves two related processes: 1) highly motile NPCs migrate away from a niche and 2) an NPC differentiates into an immature neuron (Fig. 8B-C). Both immature and mature neurons commonly exit cell cycle and only re-enter cell cycle to initiate apoptosis in response to stress cues (Herrup and Yang, 2007). Immature neurons morphologically transform by extending axons and dendrites. These cells also establish appropriate input/output connectivity within a preexisting network (Piatti et al., 2011). Interestingly, immature neurons may participate in information processing before reaching a fully mature stage. Within the hippocampus, immature neurons exhibit reduced GABAergic inhibition, high excitability and a lower threshold for the induction of long-term potentiation (Piatti et al., 2011). The final stages of stepwise differentiation involve maturation of neuronal cells and integration into preexisting networks.

NSPC Cell Fate in the Context of Cell Division

Adult neurogenesis seems to be largely influenced by the physiological state of the organism (Guillemot, 2007; Hagg, 2005). As such, various intrinsic and extrinsic factors have been shown to control the rate of neuronal production. Cell fate determination is influenced, at least in part, by cell division. An NSPC undertakes mitotic cell division in one of three main ways: symmetric-proliferative division, symmetric-differentiative division and asymmetric-differentiative division (Fig. 9A) (Florio et al., 2015; Florio and Huttner, 2014). For simplicity, symmetric-proliferative division will be denoted symmetric division and symmetric-differentiative division denoted as differentiative division. Likewise, asymmetric-differentiative division will be denoted asymmetric division. Completion of symmetric division of an NSPC yields two duplicate daughter NSPCs of identical cell type to the parent cell. This form of cell division is a self-amplifying or proliferative process as it expands an existing NSPC population. Without such amplifying growth, a persistent NSPC pool would be unsustainable during periods of high demand for neuron production. In contrast, completion of differentiative divisions by an NSPC yields two duplicate daughter cells with a cell type dissimilar to the parent cell. Symmetric-differentiation is a self-consuming process as cell divisions will eventually deplete the parent population. This process allows for rapid differentiation towards late-born cells, at the expense of early-born populations. A special instance of differentiative division is neurogenic division, where both daughter cells are neuronal cell types. Alternatively, asymmetric division yields two divergent cell types; one daughter identical in cell state to the parent and one daughter with a distinct cell type. The ability to complete this form of mitotic cell division is a defining characteristic of NSCs. Commonly, a NSC will produce one daughter NSC that retains stem cell identity and fate capacity. The remaining daughter cell is often lineage restricted and fated to become a neuron.

Importantly, during symmetric division and asymmetric division a daughter cell retains parental cell type but also inherits all state-specific elements. This includes mitotic inheritance of the parental epigenetic landscape, transcriptome, proteome and post-translational modifications (Moazed, 2011; Schweisguth, 2015; Xie et al., 2015; Xie et al., 2017). Depending on the cell division performed, this process is called symmetric epigenetic inheritance or asymmetric epigenetic inheritance. Conversely, differentiative cell divisions yield a cell type disparate from the parent cell and do not inherit the parental epigenetic state. Epigenetic inheritance in neurogenesis is fascinating and will be discussed extensively in a later section.

Neurogenesis adheres to a weakly ordered sequence of cell divisions and generally starts with symmetric divisions by NSPCs (Fig. 9B). Next NSPCs enter sustained asymmetric divisions before concluding with differentiative and neurogenic divisions. The different types of mitotic cell divisions are often described in scientific literature as discrete and mutually exclusive. However, neurogenesis involves a spectrum of asymmetric and symmetric cell divisions occurring concurrently in a stem cell niche. Additionally, individual NSPCs dynamically alter cell division from one type to another. Incredibly, NSPCs which can switch between any mitotic cell division type by altering expression of a single gene. Herein, NSPCs transition from symmetric to asymmetric to differentiative divisions based on increasing expression of *ARHGAP11B* (Florio et al., 2015).

In embryonic neurogenesis, neuroepithelial cells utilize symmetric division to expand neurogenic niche volume. Following sustained self-amplification of neuroepithelial cells, radial glia arise and begin neurogenesis via asymmetric division. Ultimately, stepwise differentiation utilizes both asymmetric and differentiative divisions for rapid cortical expansion. Unlike embryonic neurogenesis, adult NSCs prefer asymmetric divisions, and reserve symmetric division

for response to trauma or physiological stressors. When symmetric divisions occur in neural progenitors, the rate is highly dependent on the rate of upstream NSC asymmetric division. Consequently, asymmetric division during adult neurogenesis inherently promotes a steady balance between NSPC self-renewal and differentiation. Thus, adult neurogenesis ostensibly contains a built-in mechanism to ensure homeostasis and properly regulated fate determination.

Epigenetic Regulation of Cells

Chromatin Structure

The development of the nervous system requires fidelity in the expression of specific genes determining different neural cell types. The development of the nervous system is regulated by a multitude of intracellular signals interacting with the extracellular microenvironment in a temporal and spatial manner. These signals induce expression of genes involved in lineage commitment, differentiation, maturation, migration and cell survival. Silencing of genes responsible for the maintenance of stem cells in a pluripotent state and for cell fate decisions are important hallmarks of neurodevelopment. Intracellular effectors of adult neurogenesis include cell-cycle inhibitors (p16/INK4A and p21) and transcription factors. Additionally, epigenetic status is highly correlated with NSC fate decisions during neurogenesis (Mikkelsen et al., 2007; Ming and Song, 2011; Podobinska et al., 2017; Yao et al., 2016). The term “epigenetics” describes interactions between genotype and the environment, which together shape the expressed characteristic traits of an organism. Different definitions of the term epigenetics exist and a clear consensus is still lacking. The prefix “epi” means to “over, above or outer”. Thus, epigenetics refers to exogenous dynamic mechanisms which change gene expression without changing the DNA sequence. These changes are often mitotically inherited through subsequent cell divisions and can be passed to offspring by

epigenetic inheritance. An important concept is each cell type has a distinctive epigenetic signature giving rise to a unique gene expression profile (transcriptome) (Sha and Boyer, 2008).

Within the nucleus of each cell, genomic DNA interacts with structural proteins to form chromatin. The fundamental unit of chromatin is the nucleosome (Fig. 10). A nucleosome is comprised of 146 base pairs (bp) of DNA wrapped approximately 1.7 times in left-handed super-helical turns around a "core" of 8 histone proteins. The core is comprised of 4 related core histone proteins denoted H2A, H2B, H3, and H4. Each core contains 2 copies of each core histone protein to form a histone octamer containing 2 H2A, 2 H2B, 2 H3 and 2 H4 proteins. The core histone proteins are arranged into a $(H3\text{-}H4)_2$ tetramer flanked by two H2A-H2B dimers to form the cylinder-like "core" around which DNA wraps. Core histones contain a globular C-terminal domain and a N-terminal tail that extends away from a histone core (Podobinska et al., 2017). Histones are highly conserved in eukaryotes but absent in prokaryotes. Connecting adjacent nucleosome is a 10-50 bp long stretched of linker DNA (i.e. DNA not associated with structural proteins). Many linear repeats of nucleosomes and linker DNA form a nucleosome polymer colloquially termed the "beads on a string" conformation. Lastly, "linker histone" H1 contains a DNA-binding domain similar to catabolic gene activator protein (CAP), allowing it to simultaneously bind linker DNA and nucleosomes (Finn et al., 2017). Unlike the highly conserved core histones, linker histone is a divergent group of histones. As such, multiple cell-type and stage-specific variants of H1 have been described (Finn et al., 2017). Chromatin is often conceptualized into a hierarchical model of increasingly higher order structures. The 11 nm diameter nucleosome polymer can be folded subsequently into 30-, 120- and 300 nm fibers. Chromatin fibers of any diameter can be knotted into large loops called topological domains (Dixon et al., 2012). The highest order chromatin structure is the 700 nm mitotic chromosome. Chromatin structure is

commonly visualized using cell free samples and electron microscopy, yet recent advances in DNA labeling and electron microscopy have enabled the visualization of chromatin within intact human cells. A recent report describes a typical chromatin structure which is a disordered curvilinear chain that is dynamically packed together at different 3D densities (Ou et al., 2017).

Intrinsic Regulation by Epigenetic Mechanisms

Epigenetic regulation is one of the most influential players in broad aspects of biology including cell fate determination during neurogenesis. Epigenetic regulation includes 4 main mechanisms to regulate gene expression levels within a cell: 1) DNA methylation; 2) histone post-translational modifications and histone variants; 3) non-coding RNAs and 4) higher order chromatin architecture (Fig. 10-11) (Podobinska et al., 2017). Non-Coding RNAs (ncRNAs) such as long non-coding RNA (lncRNA) and small non-coding RNAs (sncRNAs), including microRNAs (miRNAs); and small interfering RNAs (siRNAs) have been discussed extensively and will not be covered here. Neither will higher order chromatin architecture nor dynamic chromatin topology be discussed here. Cataloging large scale chromatin features is a nascent research area with few studies evaluating potential roles in neurogenesis.

Both DNA methylation and histone modifications either affect the recruitment of nonhistone proteins to chromatin or disrupt chromatin contacts and thereby altering chromatin structure (Kouzarides, 2007). Three broad classes of enzymes coordinate epigenetic mechanisms for chromatin modification based on their function. Epigenetic writers catalyze addition of chemical groups to chromatin; epigenetic erasers catalyze removal of a chemical group. Epigenetic readers contain a domain that recognizes a particular chromatin modification. Each chromatin modification may have several writers, readers and/or erasers. This is especially relevant for

histone Post-Translational Modifications (PTMs) but is also true regarding DNA methylation. In humans, over 100 histone PTMs are written, read, and erased by approximately 150 enzymes (Khare et al., 2012). Across species, over 580 histone modifying proteins from eight model organisms are currently recognized (Khare et al., 2012; Xu et al., 2017). Despite the broad variation in histone PTMs, a majority of histone modifications involve adding, recognizing, and removing methyl or acetyl groups on core histone tails (Wen et al., 2009). We will focus on methylation of DNA and histones which are known to influence cell fate events and the balance of stem cell self-renewal versus differentiation. Furthermore, such methylated marks are commonly dysregulated in aggressive SVZ-associated CNS tumors, underlying a critical role in neurogenesis and tumorigenesis.

DNA Methylation

One of the best investigated epigenetic mechanisms is genomic DNA methylation (DNAme). Multiple enzymes termed DNA methyltransferases (DNMTs) perform the epigenetic writing of DNAme marks. The DNMTs catalyze the transfer of single methyl group (-CH3) from a methyl donor onto the C5 position of cytosine, resulting in 5-methylcytosine (5mC) (Fig. 11A). DNMTs are classified largely by the role of the resulting DNAme modifications within the cell. DNMT3A and DNMT3B catalyze DNA methylation at unmethylated regions of DNA in a process called *de novo* DNA methylation. Alternatively, DNMT1 is responsible for maintenance of existing DNA methylation patterns. DNMT1 acts on hemi-methylated DNA following DNA replication. DNMT1 can also maintain DNAme in regions where active DNA demethylation is occurring by epigenetic erasers.

Recent advances in biotechnology have revealed several intermediate modifications resulting from progressive demethylation of mC to unmethylated cytosine (Song et al., 2012). Such

intermediate states of methylated cytosine include 5-hydroxymethylcytosine (5hmC), 5-formylcytosine (5fC), and 5-carboxylcytosine (5caC) (Lunnon et al., 2016; Song et al., 2012). Among all these DNA methylation variants, only 5mC, 5hmC and unmodified cytosine are thought to change gene expression levels. DNAme by 5mC inhibits gene expression through 2 main mechanisms. Firstly, catalysis of 5mC occurs within proximal promoters and distal regulatory elements of genes (Bogdanovic et al., 2016; Podobinska et al., 2017). 5mC within promoters blocks DNA binding by transcription factors thereby repressing transcription. Alternatively, DNMTs can modify cytosine contained in a cytosine-guanine dinucleotide called a CpG site. The vast majority of proximal promoters contain groups of CpG dinucleotides termed CpG islands (Deaton and Bird, 2011; Saxonov et al., 2006). 5mC modified CpG sites are recognized by methyl-CpG-binding domain (MBD) proteins including MBD1 and MeCP2. MeCP2 recruitment to CpG islands makes promoters inaccessible to transcriptional machinery resulting in gene repression (Podobinska et al., 2017; Sun et al., 2014). Alternatively, DNAme within gene bodies has recently been reported to increase gene expression and be required for post-natal neurogenesis (Lister et al., 2009; Wu et al., 2010).

The 5hmC form of DNAme occurs in fetal and adult cerebellum of mice and humans and is highly correlated with neurodevelopmental genes (Lunnon et al., 2016; Podobinska et al., 2017). Additionally, dysregulation of 5hmC could be involved in multiple diseases including cancer and neurological disorders (Sun et al., 2014). Intriguingly, 5hmC increases gene expression. As such, 5mC is converted to 5hmC in proximal promoters, distal enhancers, and gene bodies (Sun et al., 2014). This process is actively mediated by the TET family of proteins (TET1, TET2, TET3) that recognize and oxidize 5mC into 5hmC (Bogdanovic et al., 2016). The 5hmC form subsequently

recruits epigenetic writers that catalyze H3K4me3, H3K4me1, and H3K26me3 marks in gene promoters, enhancers, and gene bodies, respectively (Sun et al., 2014).

Histone Post-Translational Modifications

The N-terminal tail of each core histone protein is the site of addition of numerous post-translational modifications (PTMs), often at lysine or arginine residues (Fig. 10, 11B). Many histone PTMs have been reported including methylation, acetylation, phosphorylation, ubiquitination, SUMOylation, ADP-ribosylation, deamination, proline isomerization, crotonylation, and citrullination (Podobinska et al., 2017). Each histone PTM is highly associated with a specific effect on chromatin structure and consequently influences expression of nearby genes. Additionally, multiple modifications are often added concurrently and interact with one another in agnostic or antagonistic ways. The shear breadth of histone PTMs and the outcomes of different PTM combinations has led to the "histone code" hypothesis. This model states that different combinations of histone PTMs confer different chromatin states. A histone code suggests that each type of PTM can be recognized by one or more effector molecules. Such a hypothesis conceptually echo's the view of the "genetic code" which provides rules to interpret linear sequences of DNA into genotypic information. Thus epigenetic modifications convey information of a chromatin state to transcriptional machinery (Baker, 2011). Indeed, recent evidence indicates that transcription factors not only recognize DNA sequence motifs, but also read the epigenetic state of chromatin when initiating gene expression (Hughes and Lambert, 2017).

Histone methylation is the reversible process of transferring methyl groups onto the N-terminal tail of core histones (Fig. 12A). Up to three methyl groups are transferred successively onto specific amino acids, frequently a lysine or an arginine. Consequently, the two main classes

of histone methyltransferases (HMTs) transfer a methyl group to lysine or arginine positions. Lysine-specific HMTs are further subdivided into SET domain HMTs and non-SET domain containing HMTs. The vast majority of HMTs are lysine-specific and part of the SET domain superfamily proteins. The SET domain is named after the first three HMTs identified in *D. melanogaster*: Suppressor of variegation 3-9 (Su(var)3-9), enhancer of zeste (E(z)), and trithorax (Trx) (Dillon et al., 2005). The catalytic mechanism of SET domain enzymes involves transferring a methyl group from S-adenosyl-L-methionine (SAM) to a lysine residue of a histone tail (Trievel et al., 2002). Ultimately, histone methylations are actively removed by one of two groups of lysine-specific demethylases (LSD). Members of the first group, LSD1, are flavin adenine dinucleotide (FAD) dependent amine oxidases. Members of the second group, the Jumonji domain containing enzymes (JmJC) act as Fe(II)/ α-ketoglutarate dependent dioxygenases and are further divided into seven subgroups: JHDM1, JHDM2, JHDM3/JMJD2, JARID, JMJC domain only, PHF2/PHF8 and UTX/UTY (Khare et al., 2012).

Multiple amino acid positions along histone tails provide a substrate for PTMs. As such, a strict nomenclature defines the nature of a histone PTM. Histone PTM shorthand first identifies the histone being modified, followed by the amino acid and its position (counted from the N-terminus) and ending with the nature of the PTM. For example, monomethylation of the fourth position (a lysine) on histone H3 is denoted H3K4me1. Consistent with the histone code hypothesis, methylation PTMs have different effects depending on methylation site and magnitude of methylation. For example, methylation at lysine 4, 36, or 79 of histone 3 (H3K4, H3K36 and H3K79) are associated with transcriptional activity. Such histone modifications are commonly termed chromatin activation marks. Methylation of lysine 9 or 27 on histone 3 and lysine 20 on histone 4 (H3K9, H3K27 and H4K20) are highly associated with gene repression. These

modifications are often denoted chromatin repressive marks. Similarly, the magnitude of methylation at any given site may have different outcomes. For example, monomethylation can be associated with active or poised transcription while di- and trimethylation are associated with repression of gene expression. It is also possible to have subtle outcomes between subsequent methylation states. For instance, dimethylation and trimethyation of H3K27 are both repressive marks. However, H3K27me2 is suspected to confer minute differences in a cell's chromatin state compared to H3K27me3 (Juan et al., 2016). The subtle differences in outcome are suspected to be important in stem cell fate decisions.

Similar to DNAme, the goal of histone PTMs are to regulate accessibility of DNA by transcription factors and RNA polymerase. Yet, the mechanism underlying histone PTMs is quite unique. Histone cores and genomic DNA are not covalently bound together; the spatial relationship of histones and DNA is not static. Consequently, the cumulative electrochemical effects of multiple PTMs often displaces histones along DNA. Depending on the PTMs present, nucleosomes reversibly alternate between a form of chromatin with a high packing density (heterochromatin) and a form with low packing density (euchromatin) (Fig. 11B). By altering combinations of histone PTMs within a genomic region, histone modifying enzymes alter the structure of chromatin. Because the highly dense form of chromatin is inaccessible to DNA binding proteins, all genes contained within the region are often repressed. In contrast, the low nucleosome density associated with chromatin activation marks promotes opened chromatin and transcriptional activity. In sum, histone PTMs regulate gene expression by altering accessibility of transcription proteins to DNA via reversibly switching between heterochromatin and euchromatin states. While this may seem an overly complicated way to regulate genes, the mechanism has at least two advantages. Adult NSPCs can change their chromatin state in response from environmental cues

(i.e. exercise or trauma) and revise their cell fate capability. This mechanism also allows for resetting DNA and histone modifications to an epigenetic "ground state" within germline cells and multipotent lineage progenitors.

The Role of Histone Methylation in Adult Neurogenesis

Preservation of Endogenous Chromatin Profiles in NSPCs

Epigenetic changes are highly dependent on environmental factors (Zhu et al., 2013), very likely because the main methyl donor of chromatin methylation, SAM, is also utilized in many housekeeping metabolic processes (Fig. 12B). This includes SAM producing pathways (i.e. glutamate and/or folate synthesis) and SAM consuming pathways (i.e. phosphatidylcholine, creatine and/or homocysteine synthesis) (Blom and Smulders, 2011; Locasale, 2013; Miller et al., 2013; Tchantchou and Shea, 2008; Yang and Vousden, 2016). Accounting for potentially confounding effects of environment when investigating neural cell fates is a recent methodological development (Foret et al., 2014; Lin et al., 2017; Rhodes et al., 2016; Sandstrom et al., 2014). Genome-wide sequencing experiments require a homogeneous cell population with high cell numbers as input. To perform genome-wide experiments, cells are routinely harvested from a tissue of interest and sorted into homogeneous populations. The sorted, homogenous population of interest is expanded in culture prior to preparing sequencing libraries. However, such culturing leads to metabolite accumulation and altered methylation patterns resulting in sequencing artifacts. An ideal alternative is to prepare sequencing libraries directly after NSPC extraction from the brain. Our lab developed a method to purify subpopulations of undifferentiated cells from SVZ and SGZ/DG tissue while preserving the endogenous genomic signatures. This approach maintains *in vivo* chromatin state and is ideal for genome-wide studies (i.e. ChIP-Seq and RNA-Seq). Such

a method has allowed the identification of putative targets of trimethylation of lysine 4 on histone 3 (H3K4me3), lysine 9 on histone 3 (H3K9me3), lysine 27 on histone 3 (H3K27me3) and lysine 20 on histone 4 (H4K20me3) within adult primate neurogenic niches (Foret et al., 2014; Rhodes et al., 2016; Sandstrom et al., 2014). These findings will enhance our understanding of histone methylations marks in adult neurogenic niches in parallel with *in vivo* models.

H3K4me3

The chromatin activation mark H3K4me3 is present in undifferentiated progenitor cells residing within the SVZ of adult rodent and primate brains (Sandstrom et al., 2014). An epigenetic mechanism through MLL1 (mixed-lineage leukaemia 1, a histone methyltransferase responsible for histone 3 lysine 4 trimethylation-H3K4me3) has been shown to induce postnatal neurogenesis in SVZ (Lim et al., 2009). The MLL family of methyltransferases (MLL1, MLL2, MLL3, MLL4, MLL5) reside within the Trithorax (Trx) group protein complex, which also contains WDR5/RbBP5/ASH2 subunits to convert the demethylated forms of H3K4 to the trimethylated form that render open chromatin (Ruthenburg et al., 2007; Wysocka et al., 2005). To date, the emerging consensus from genome-wide scale analysis reveals that tri-methylation at H3K4 (H3K4me3) is characteristic of transcriptionally active or poised status (Bernstein et al., 2006; Voigt et al., 2013). Importantly, the H3K4me3/MLL family is also known to be associated with distinct types of hematologic disorders (Shen and Laird, 2013; Yokoyama et al., 2005). Thus, oncogenesis under MLL deregulation could result in changes of gene expression through the alteration of H3K4me3 epigenetic landscape.

Using ChIP-Seq, H3K4me3 is significantly enriched for genes involved in cell cycle, cell signaling, nervous system development, metabolism, and ribosomal biogenesis (Sandstrom et al.,

2014). Among these genes, RNA-Seq identified that genes associated with cellular signaling/maintenance, DNA replication, metabolism, and protein synthesis are expressed. As subset of such H4K3me3 enriched genes were not only detectable in endogenous NSPCs, but upregulated in SVZ-associated GBM (Sandstrom et al., 2014).

H3K9me3

Underlying the specialized chromatin structure around centromere and telomere, H3K9me3 was originally identified to be a heterochromatin-enriched mark, with roles in silencing gene expression and preventing chromosomal instability (Black et al., 2012; Czvitkovich et al., 2001; Lachner et al., 2001; Peters et al., 2002; Peters et al., 2001). For instance, a previous study has shown that loss of H3K9 methylation in Drosophila causes DNA damage in heterochromatin and mitotic defect (Peng and Karpen, 2009). In mice, loss of H3K9me2/me3 causes disruption of heterochromatin and increases telomere length (Benetti et al., 2007; Garcia-Cao et al., 2004; Peters et al., 2001). Trimethylation of H3K9 is also involved in pluripotency of ESCs and multipotency of NPCs, in which the pluripotent genes (e.g., Nanog, Oct4) and non-neural genes (e.g., GATA4, NODAL) gain H3K9me3 leading to long-term repression during differentiation (Golebiewska et al., 2009; Hirabayashi and Gotoh, 2010). Thus, H3K9me3 plays a repressive role in numerous neuronal and non-neuronal genes in addition to its known function in genome stability (Roopra et al., 2004; Schaefer et al., 2009). Among all lysine methyltransferases, the KMT1 family composed of G9a/GLP and Suv39h1/h2 are essential for H3K9me1/2 and H3K9me3 modifications, respectively (Black et al., 2012; Czvitkovich et al., 2001; Lachner et al., 2001; Peters et al., 2001). Studies from KMT1 knock-out mice demonstrated that loss of H3K9 methylation contributes to

behavioral abnormalities and cognitive impairment in addition to its protective role in genome stability (Schaefer et al., 2009).

While robust adult neurogenesis occurs outside the CNS, H3K9me3 is present in the adult rodent and primate SVZ, the largest neurogenic niche in the adult mammalian brain (Foret et al., 2014; Kulkarni et al., 2017). As detected by ChIP-Seq and RNA-Seq, H3K9me3-enriched genes associated with cellular maintenance, post-transcriptional and translational modifications, signaling pathways, and DNA replication are detectable by RNA-Seq analysis, while genes involved in axon/neuron, hepatic stellate cell, or immune-response activation are not expressed (Foret et al., 2014) . As neurogenesis progresses in the adult SVZ, cell fate restriction is essential to direct proper lineage commitment. These findings highlight that H3K9me3 repression in undifferentiated SVZ cells is engaged in the maintenance of cell type integrity. This implicates a role for H3K9me3 as a repressive epigenetic mechanism to protect against improper lineage differentiation within the SVZ.

H3K27me3

Methylation of lysine 27 on histone H3 (H3K27me3) is associated with chromatin compaction and transcriptional repression, which has been implicated in tumorigenesis upon dysregulation (Bracken et al., 2003; Kleer et al., 2003; Shen and Laird, 2013; Ting et al., 2006; Varambally et al., 2002). The balance between NSC self-renewal and differentiation are maintained, at least in part, by epigenetic repression to prevent transcriptional noise of lineage-specific genes (Hirabayashi et al., 2009; Pereira et al., 2010; Rhodes et al., 2016; Sher et al., 2012; Xie et al., 2013; Yao and Jin, 2014). One such mechanism to inhibit transcription is post-translational modifications on histone tails, including trimethylation at histone 3 lysine 27

(H3K27me3). H3K27me3 is catalyzed by enhancer of zeste homolog 2 (EZH2) which is ubiquitously expressed in a wide range of mammalian tissues (Fig. 12C-D). EZH2 is present in undifferentiated cells of the murine and primate subventricular zone (SVZ) and subgranular zone (SGZ). *Ezh2* deletion by crossing to glial fibrillary acidic protein (GFAP)-Cre mouse line results in deficit of postnatal neurogenesis in the mouse SVZ (Hwang et al., 2014). Using Nestin-CreERT2 and tamoxifen inducible system to knockout *Ezh2* in the SGZ/DG showed that Ezh2 is important for learning and memory capabilities in 6-week old mice (Zhang et al., 2014). Using ChIP-Seq, H3K27me3 was found to function primarily in regulation of cell cycle and developmentally critical regulators involved in differentiation (Fig. 13) (Rhodes et al., 2016).

H4K20me3

Methylation of lysine 20 on histone H4 (H4K20me3) is associated with chromatin compaction and transcriptional repression, which has been implicated in tumorigenesis upon dysregulation (Evertts et al., 2013). H4K20me3 is catalyzed by suppressor of variegation 4-20 homologs (KMT5B (human)/Suv4-20h1 (mouse) and KMT5C (human)/Suv4-20h2 (mouse)) (Fig. 12E). Suv4-20h1 is ubiquitously present in adult tissues including brain, whereas Suv4-20h2 displays restricted abundance in some adult tissues. Double knockout of Suv4-20h1 and Suv4-20h2 results in compromised genomic integrity via impaired double strand break repair and perinatal lethality. Germline deletion of Suv4-20h1/Suv4-20h2 by Mox2-Cre showed that Suv4-20 homologs (denoted Suv4-20h) impaired the maintenance of lymphoid progenitors (Schotta et al., 2008). In addition to the known role of H4K20me3 in DNA replication licensing, our ChIP-Seq using endogenous NSPCs isolated from baboon brain identified putative targets of H4K20me3 to function in cell cycle, metabolism, cellular organization, and immune response (Rhodes et al.,

2016). The role of H4K20me3 in NSPC cell cycle regulation is somewhat unique with respect to adult neurogenesis.

Epigenetic Regulation of Cell Cycle

Methylation of histone tails often regulate proneuronal genes or represses non-neurogenic genes. Consequently, many histone PTMs directly regulate lineage commitment and differentiation genes. As we saw, H3K27me3/H3K9me3 prevent untimely expression of late neuronal genes and repress non-neural genes, while H3K4me3 activates neuronal genes. In contrast, H4K20me3 is highly associated with regulating cell cycle. This is intriguing as many of the early NSC fate determination steps are dependent on cell cycle events (Fig. 14). For example, does an NSC undergo symmetric cell division or asymmetric-differentiative cell division? How frequently should NSPCs initiate cell cycle and should proliferation be sustained? Regarding cell cycle exit and re-entry, H4K20me3 has potentially profound implications on neural cell fate events important for adult neurogenesis.

NSPC Dysregulation and SVZ–Associated Tumorigenesis

Glioblastoma Overview

Glioblastoma (GBM) is a devastating brain cancer with poor prognosis, uncontrolled proliferation, resistance to cell death, robust angiogenesis, and vascular edema, and rapid, aggressive tumor relapse. Virtually all GBM cases are diagnosed with MRI, often utilizing gadolinium contrast media to aid visualization of tumor boundaries. The standard of care for GBM is non-biopsy surgical resection followed by Temozolomide-based chemo- and radiation therapy. Unfortunately, no contemporary treatment is curative (Carlsson et al., 2014). Surgical intervention

and radiotherapy are often hindered by finger-like projections which extend from the tumor to infiltrate vital brain regions. Further, a major factor limiting the development of pharmaceutical treatments is the incredible heterogeneity exhibited by GBM tumors. Heterogeneity manifests at multiple levels including intratumoral heterogeneity and multifocal intertumoral heterogeneity in a patient, and interpatient intertumoral heterogeneity (Patel et al., 2014; Soeda et al., 2015). Such heterogeneity has been described at the level of the genome, transcriptome, signaling networks and correlates with aggressive clonal behavior and drug resistance (Meyer et al., 2015; Patel et al., 2014; Soeda et al., 2015; Spyros Darmanis, July 19, 2017; Wei et al., 2016). A recent approach by The Cancer Genome Atlas Consortium (TCGA) aimed to account for observed heterogeneity. As such, genome-wide biomarkers defined molecular signatures and core pathways of GBM to allow tailoring patient specific therapeutics. Using genotypic features, TCGA classified GBM into 4 clinically relevant subtypes: Classical, Mesenchymal, Neural, Proneural. The subtypes were so named because each type exhibits neural lineage specific transcriptional profiles. Thus, each TCGA GBM subtype corresponded to the transcriptome pattern of at least one neural lineage.

GBM Tumorigenesis Models

At least 3 models have been proposed to explain the origin of cancer: the Clonal Evolution Model, the Cancer Stem Cell (CSC) model, and the reprogramming model (Bradshaw et al., 2016). Clonal evolution hypothesizes somatic cells undergoes a series of mutations to form an immortalized cancerous cell (Fig. 15B). The cancerous cell then expands to form the bulk of a tumor. Alternatively, the CSC model proposes that resident adult stem cells undergo dysregulation to form a cancer stem cell (Fig. 15C). The designation of ‘CSC’ was devised to echo two fundamental properties of normal stem cells: self-renewal capacity and multipotency (Ahmed et

al., 2013). Consequently, CSCs can self-renew while also contributing to the bulk of a tumor. Evidence supports the CSC model in numerous cancers impacting adult tissues. The CSC model might also explain the formation of multifocal CNS tumors and GBM recurrence. In the reprogramming model, a "late" born neuronal cell is reprogrammed into a tumorigenic CSC, which then conforms to the CSC model of tumorigenesis (Fig. 15D). This concept is best demonstrated when Yamanaka factors reprogram cells into a new cell type. Yamanaka factors are a group of 4 transcription factors (OCT4, NANOG, SOX2 and c-MYC). When expressed in unison, these factors cause a late-born, differentiated cell to transform into an induced pluripotent stem cells (iPSC). The ability to reprogram cells with crucial changes to a cell's transcriptional program demonstrates that cell state and cell fate is inherently plastic and dynamic phenomena. The reprogramming model hypothesizes late-born neuronal cells exploit this plasticity by turning on stem cell transcriptional programs and turning off proneuronal programs. Importantly, two of the Yamanaka factors (SOX2 and c-MYC) are pro-stem cell transcription factors but also oncogenic (Berezovsky et al., 2014). Such a dichotomy of function draws parallels between cellular reprograming and oncogenic transformation. Importantly, the cellular reprogramming model is not exclusive from either the CSC model or clonal evolution model of cancer. Indeed, the reprogramming and CSC models of GBM may act cooperatively, although this has yet to be thoroughly tested. Additionally, parts of the clonal evolution, CSC and reprogramming models explain aspects of GBM pathobiology. Therefore, it is not implausible that multiple models influence distinct stages of CNS tumorigenesis.

GBM – NSPC Intersection

Intriguingly, the SVZ harbors undifferentiated NSPCs with great proliferative potential. The proliferative NSCs are effectively immortalized via self-renewal capacity. Such a mass of undifferentiated cells with a potentially endless proliferative capacity underlies the suspicion that the SVZ is a vulnerable site of cancer initiation. Some of the earliest and most formative clues implicating SVZ NSPCs in the CSC model of GBM utilized magnetic resonance imaging (MRI) data (Fig. 16A) (Lim et al., 2007). Specifically, MRIs classified GBM into 4 groups based on tumor location: Group I GBM contacts both the SVZ and the cortex (SVZ^+/CTX^+), Group II GBM contacts only the SVZ but does not infiltrate to the cortex (SVZ^+/CTX^-), Group III GBM contacts only the cortex (SVZ^-/CTX^+), Group IV GBM contacts neither the SVZ nor cortex (SVZ^-/CTX^-). Utilizing such spatial characterization of GBM, there is a strong inverse correlation between SVZ proximity to GBM and patient survival time (Jafri et al., 2013). Thus, patients diagnosed with GBM in close proximity to the SVZ denoted as SVZ^+ GBM (i.e. Groups I/II GBM) have severely diminished survival times versus SVZ^- GBM (i.e. Groups III/IV GBM). Attempts have even been made to correlate GBM-SVZ proximity with the TCGA GBM molecular subtypes, with mixed and contradicting results (Jungk et al., 2016; Steed et al., 2016). Such correlations between GBM-SVZ proximity and patient survival, as well as NSPC/GBM molecular signatures suggest the importance of NSPC fate regulation and cell type of origin in subtypes of GBM.

Stem Cell Signature in SVZ^+ GBM

In support of the CSC model of GBM, a compendium of literature published over the past decade has compared GBM and adult NSCs. Particularly, subtypes of aggressive GBM harbor NSPC signatures at the transcriptional and proteomic levels (Fig. 16B-C) (Gollapalli et al., 2017;

Haskins et al., 2013; Lin et al., 2017). Recently, gene expression signatures of GBM and GBM derived CSCs resemble those of NSCs, suggesting CSCs share features with non-neoplastic stem cells (Fig. 16B). Additionally, GBM-derived CSCs express NANOG, SALL4, SOX2, pSTAT3, and OCT4 at transcriptional and protein levels (Bradshaw et al., 2016). These markers are normally expressed in embryonic and/or neural stem cells further implicating CSCs and non-neoplastic stem cells. Molecular signatures of SVZ^+ GBM and SVZ^- GBM are currently being established. Still, an emerging consensus discriminates the signatures of SVZ^+ GBM versus SVZ^- GBM. Thus, current evidence supports NSPC dysregulation, at least partially, in driving SVZ-associated neoplasia.

Evidence for Reprogramming NSPCs or differentiated cells into CSCs

In many TCGA GBM specimens and primary GBM I/II specimens, Sox2 and Myc are upregulated. Sox family transcription factors are necessary to induce a neural stem cell transcriptional program (Berezovsky et al., 2014), while Myc is a transcriptional amplifier of gene networks in endogenous and cancerous cells (Lin et al., 2012; Nie et al., 2012). Thus, co-upregulation of Sox2 and Myc may induce reprogramming of neural cells into CSCs by regulating cell plasticity (Berezovsky et al., 2014). Additionally, differentiated cancer cells have been reprogrammed into tumor propagating stem cells with only four neurodevelopmental transcription factors: SOX2, OLIG2, SALL2 and POU3F2 (Suva et al., 2014). This implicates an epigenetic component in the developmental hierarchy of GBM. As such, reprogramming would reset the epigenetic landscape in a cell to be distinct from brain tissue and also attenuate tumorigenesis (Friedmann-Morvinski et al., 2012; Stricker et al., 2013; Suva et al., 2013). For instance, ESC-derived NPCs can be transformed with overexpression of H3.3-K27M and PDGFRA and short

hairpin RNA knockdown of TP53 (Funato et al., 2014). The H3.3-K27M mutation is a primary driver in pediatric high grade gliomas. Importantly, such evidence suggests NPCs are a susceptible neural population for epigenetic reprogramming, even during GBM tumorigenesis. Both NSCs and differentiated neurons seem resistant, but not immune, to cellular reprogramming. Thus, the impact of the K27M mutation is likely restricted to a subpopulation of NPCs arising during embryogenesis (Funato et al., 2014; Mack et al., 2016). Cumulatively, such evidence raises the possibility that "late-born" neural cells are undergoing a reprogramming back to a stem cell state to form the bulk of a tumor.

Origin of Diffuse Aggressive Brain Cancer

When examining the cell type of origin of SVZ-associated GBM, there is an unanswered question regarding the spatial origin of most GBMs. The established view describes SVZ^{+} GBM arising in the SVZ as a result of NSPC dysregulation. After originating in the SVZ, the GBM may infiltrate the cortex. Alternatively, a new finding hypothesizes that tumors originate far away from the SVZ, such as the cortex or brain stem (Qin et al., 2017). In such a scenario, neural precursors in the SVZ secrete PTN, SPARC, SPARCL, and various heat shock proteins. Such signaling molecules are then detected by differentiated neural cells which have undergone cellular reprogramming into glioma stem cells (GSC). The distant GSCs then invade the SVZ in response to PRN/SPARC/SPARCL signaling originating within the SVZ. Such findings may explain aspects of diffuse intrinsic pontine gliomas (DIPG) and GBM tumorigenesis. However, current brain tumor diagnosis is performed symptomatically and classification is done retrospectively. Thus, contemporary diagnostic methods cannot test such a model of CNS tumorigenesis. As

intriguing as these findings are, more study is required to determine the location and mechanisms driving SVZ^+ GBM tumorigenesis.

Epigenetic Gateway to CNS Tumors

One elegant proposal to connect intrinsic and extrinsic regulators of cell fate events to CNS tumorigenesis is the so-called Epigenetic Gateway to CNS tumors. Epigenetic modifications are reversible and sensitive to many intra- and extracellular factors. The epigenetic landscape is intimately connected to regulatory gene networks and influences cell fate events. Thus, epigenetic mechanisms form a fundamental link between intrinsic and extrinsic factors in an organism, balancing cell fate decisions, and transforming cell type identities (Fig. 17A). Extrinsic cues are metabolism or injury while intrinsic genotypic factors are shuttled through a "gateway" or "gatekeeper" to influence cell fate and potential lineages. Interestingly, among both TCGA evidence and GBM I/II specimens, few histone modifiers are differentially expressed (Fig. 17B) (Lin et al., 2017). This implies that mutations to histone modifiers are not commonly correlated with GBM. Likely, input from metabolism, physiological stress, and other extrinsic factors help drive alterations to the epigenome landscape. This in turn shifts the downstream cell identity toward an oncogenic potential.

Such a gateway model is supported by studies of group I and II GBM specimens. Comparative gene expression profiles between these 2 groups of primary GBM and endogenous neural stem progenitor cells revealed dysregulation of cell cycle, chromatin status, cellular morphogenesis, and signaling pathways (Lin et al., 2017). In the absence of *IDH* mutation, several genes associated with metabolism are differentially expressed in these subtypes of primary GBM, implicating metabolic reprogramming occurring in a tumor microenvironment. Further support for

an epigenetic gateway of tumors derives from comparisons of childhood versus adult GBM (Mack et al., 2016). Childhood GBM typically results from H3.3-K27M mutation occurring in *H3F3A* with encodes histone H3.3 variant and decreases a cell's ability to methylate H3K27. Alternatively, H3-G34R or H3.3-G34V mutations may affect methylation capacity at nearby H3K36 (Bjerke et al., 2013). Such commonly occurring alterations in amino acid sequence may be related to mechanisms underlying adult GBM. While pediatric GBM is often driven by mutations to histone H3, there are relatively few other mutations in the genomes of pediatric GBM patients. In contrast, adult GBM often present higher number of total mutations and greater variety of mutation types (i.e. insertions/deletions, copy number aberrations, single nucleotide polymorphisms) compared to pediatric cases. Adult GBM typically does not involve *H3F3A* mutation (i.e. H3.3 K27M) and instead results from mutation or dysregulation of histone modification enzymes. Frequent mutations include to *MLL3, SMARCA4*, and *SETD2,* and *KDM6A.* Additionally, atypical activity of histone modifiers is well supported adult GBM and often includes overexpression of non-mutated *EZH2* and increased H3K27me3 deposition (Mack et al., 2016). Critically, global loss of H3K27me3 in pediatric GBM contrasts global gains of H3K27me3 in adult GBM. These glaring differences may reflect cell type specific or chromatin state dependencies in neoplasia transformation, and consequently, the cellular reprogramming model of GBM.

Growing evidence from genome-wide *in vivo* GBM experiments and large cohorts of TCGA GBM cases demonstrate that chromatin modifiers and genes participating in metabolism are differentially regulated. In the case of histone methyltransferases, at least one gene appears universally upregulated across every known GBM specimen: *EZH2*. What's more, epigenetic regulation of NSCs has been described for some time. Histone modifying enzymes, including EZH2, are known to regulate the state of healthy, endogenous NSCs *in vivo* while overexpression

of EZH2 in astrocytes induces dedifferentiation towards neural stem cells (Sher et al., 2011). Such a prominent role in endogenous NSPCs and SVZ associated tumorigenesis is a primary factor motivating our assessment of epigenetic regulation of adult NSCs.

As such, we found elevated levels of H3K4me3 in group I/II GBM, which has a transcriptional profile that reflects the H3K4me3 modifications in the undifferentiated progenitor cells of the baboon SVZ. Furthermore, *EZH2* was upregulated while histone lysine demethylases *KDM2* and *KDM4* were downregulated in both group I and II primary GBM. Perhaps, the EZH2 mediated balance between self-renewal and differentiation during adult neurogenesis is in part co-regulated by these KDMs. Disruption of this balance may be responsible for tumorigenesis. Our analysis across large TCGA and Rembrandt datasets identified 9 genes (*PBK*, *CENPA*, *KIF15*, *DEPDC1*, *CDC6*, *DLG7*, *KIF18A*, *EZH2*, *HMMR*) crucial for cell cycle, centromere assembly, and chromosome segregation were commonly upregulated, highlighting a unique mechanism to distinguish GBM from non-neoplastic tissues (Fig. 17C). Our genome-wide findings underscore the complex interplay between epigenetic factors, genetic factors and metabolic factors in SVZ-associated GBM. Upon dysregulation, such factors could transform a normal neural stem cell toward a cancer-initiating cell. The potential mechanisms underlying such a transformation should be explored using *in vivo* models.

In Vivo **Models of Adult Neurogenesis**

Motivation for in vivo studies

While many features of adult neurogenesis are conserved between species, there are several crucial differences between primate (i.e. human and non-human) and mouse brains. Mouse studies facilitate understanding the genetic and biochemical components of adult neurogenesis. Yet much

biomedical-based neuroscience is clearly targeted for human therapeutic applications. It is therefore prudent to examine the similarities and significant differences between rodent and primate models when designing neurogenesis studies.

Firstly, the microarchitecture of the niche dramatically differs between rodents and humans in some respects. For example, developing human brains have oRGS in the oSVZ, while developing rodent brains lack an oSVZ and have limited oRGs in the IZ (Bershteyn et al., 2017). Adult primate brains have a greatly expanded SVZ with a thick astrocyte ribbon, while the adult rodent SVZ is compressed to only several cells and lacks a thick astrocyte ribbon. Secondly, the gross anatomy differs dramatically between rodents and primates. For example, mice have smaller brain volumes and lissencephaly (i.e. little or no cortical folding), while healthy primates have extensive cortical folding and large brain volumes. Unlike rodents, lissencephaly in humans is a pathological condition. Both the expansion of brain volume and amount of cortical folding is primarily due to genetic factors impacting oRGs populations that are present in humans and largely absent in rodents. Any of these differences in brain structure can directly or indirectly affect neurogenesis via autophagy or neuro-immunological interactions.

In Vivo Epigenetic Landscape of Endogenous Adult NSPCs

Cross-species similarities and differences present unique challenges and opportunities for choosing an appropriate model to study adult neurogenesis. Previous studies have shown that there is significant correlation between baboon and human regarding genomic similarity and brain structure (Fig. 18). Given such extensive correlation, findings regarding regulation of neurogenesis in baboon models may hold significant relevance in humans. Emerging technologies such as patient derived organoids will undoubtedly be useful for investigating neurogenesis. However,

among current options, one of the best models of healthy human NSPCs as they exist *in vivo* for genomic profiling (i.e. ChIP-Seq, RNA-Seq, CNA, SNP, etc) are NSPCs isolated from the adult SVZ of the baboon brain.

In Vivo Genotypic Components of Primary Tumors

Humans, non-human primates and even rodents have genotypic components that are largely conserved, including genomes, proteomes and signaling pathways. Yet many diseases exhibit etiologies and mechanisms that cannot be readily recapitulated in non-human models. The high degree of heterogeneity in CNS tumors is representative of many disease-specific features that are simply not well suited for study in non-humans. In such deleterious conditions, the diseased system may be so complex that surrogate models are strained to produce relevant findings. Alternatively, ethical considerations may inhibit allocating resources for surrogate animal models even if specimens/biopsies from afflicted humans are rare and in high demand. Burgeoning methods including disease in a dish and precision medicine will unquestionably prove beneficial for investigating human disease. Alternatively, we explore a technology to model *in vivo* profiling of primary tumors, including diffuse high grade gliomas. Such an innovative approach preserves many of cellular characteristics of interest to cancer biologists, including genotypic (i.e. genomic, transcriptomic, proteomic), epigenetic, intracellular signaling, metabolome and cell cycle components.

In Vivo Conditional Knockout Models

Many of the genomic findings using non-human primates and primary GBM specimens are correlative in nature. As such, they are fundamentally incapable of describing regulatory

mechanisms in a deterministic, causative manner. On the other hand, mice and other rodents have a long history of use in transgenic models. Existing mouse models for knockouts, knock-ins and other genetic manipulations are unsurpassed versus other species. One application of murine models is probing the role of epigenetic writers in the brain, including during healthy neurogenesis or CNS tumorigenesis. Murine models are also attractive to probe potential connections between extrinsic microenvironment, epigenetic mechanisms, non-neoplastic stem cell biology and neoplastic stem cell pathobiology.

The methylation of lysine residues in histone proteins is a critical post-translational modification that regulates diverse biological processes including cell cycle, development, metabolism, and multipotency of stem cells. Conventional promoter-driven knock-out mouse models have demonstrated the importance of histone modifications in specific cell types in the adult brain. However, histone modifying enzymes and resulting methylations are ubiquitous in multiple cell types and are vulnerable to regional changes due to environmental influx of methyl donors or inhibitors. For instance, Ezh2/H3K27me3 and Suv4-20h/H4K20me3 are present in heterogeneous populations within adult neurogenic niches (Rhodes et al., 2016). Herein, we developed an innovative method to gain broad insight into the role of Ezh2/H3K27me3 or Suv4-20h/H4K20me3 in a wide range of adult NSPCs. Using conditional *Ezh2* and *Suv4-20h1* mouse models, we utilized a recombinant Cre protein based approach to examine the long-term *in vivo* effect of loss of Ezh2 or Suv4-20h in the SVZ or SGZ/DG. Such an approach will accelerate and deepen our understanding of the functional consequences of ubiquitously regional loss of histone methylations in adult neurogenic niches. The following result section will describe our findings of region-specific knock-out of *Ezh2* or *Suv4-20h1* in the adult SVZ or SGZ/DG. In summary, our approach will be of considerable interest to those applying cutting-edge techniques to phenomena

with tight temporal and spatial regulation for cell fate transition and disease associated with NSPCs.

CHAPTER TWO: METHODS

Mouse Models

Mice contained a floxed SET domain of Ezh2 (*Ezh2*$^{flox/flox}$) or Suv4-20h (*Suv4-20h1* $^{flox/flox}$;*Suv4-20h2*$^{-/-}$). *Ezh2*$^{flox/flox}$ mice or *Suv4-20h1*$^{flox/flox}$;*Suv4-20h2*$^{-/-}$ mice were crossed to R26R-lacZ (denoted by *ROSA26*) or R26R-EYFP (denoted by *ROSA26*$^{Y/Y}$) reporter mice (Jackson laboratory) with loxP sites flanking a stop cassette upstream of β-galactosidase (β-gal) or yellow fluorescent protein (YFP). The crosses resulted in *Ezh2*$^{flox/flox}$;*ROSA26*, *Ezh2*$^{flox/flox}$;*ROSA26*$^{Y/Y}$, *Suv4-20h1*$^{flox/flox}$;*Suv4-20h2*$^{-/-}$;*ROSA26* and *Suv4-20h1*$^{flox/flox}$;*Suv4-20h2*$^{-/-}$;*ROSA26*$^{Y/Y}$ mouse colonies for experiments. For simplicity, these mouse colonies will be denoted *Ezh2*$^{flox/flox}$;*ROSA26*, *Ezh2*$^{flox/flox}$;*ROSA26*$^{Y/Y}$, *Suv4-20h*$^{flox/flox}$;*ROSA26* and *Suv4-20h*$^{flox/flox}$;*ROSA26*$^{Y/Y}$. Mouse genotypes were confirmed by PCR genotyping of tissues obtained from ear punch. Ear punch samples were lysed in 90 uL of fresh-made 50 mM NaOH shaking at 95.0 °C for 10 min. After 10 min, samples were cooled on ice and NaOH was neutralized immediately with 10 uL 1M Tris HCL, briefly vortexing. Samples can be used immediately for genotyping or stored at -20 °C. PCR cocktail includes: 25 uL Apex Taq RED Master Mix (Genesee Scientific, Cat #: 42-137), 1 uL per primer, 1 uL template DNA, bring to 50 uL with nuclease free water. Thermocyler program was as follows: 1 cycle: 95.0 °C @ 3 min; 25-35 cycles: 95.0 °C @ 20 sec, 58 °C @ 40 sec, 72.0 °C @ 1 min; 1 cycle: 72 °C @ 7 min, hold at 4 °C. Visualize amplicons using 1 - 1.5 % agarose gel in 1X TAE with 0.5 ug/mL final concentration of EtBr in gel (100 V for 45 - 90 min for separation of bands). All mouse strains were congenic prior to experiments. Mice (males and females) between 12 and 24 weeks old were used. All animal experiments were approved by the Institutional Animal Care and Use Committee of the University of Texas at San Antonio (UTSA).

Baboon Models

Brain tissue used for all non-human primate experiments, including immunohistochemistry, flow cytometry and genome-wide sequencing, were obtained from healthy baboons housed at the Texas Biomedical Institute/Southwest National Primate Research Center. All baboons were between 13 – 17 years old; equivalent to a human age of 40 – 50 years old. Brain tissue from both male and female baboons were utilized. All baboons were kept as part of an active breeding colony; they were not used in any experiments prior to euthanasia. All baboons used for the current study were euthanized when the breeding colony was culled to reduce colony size; they were not euthanized due to illness, injury or old age.

Immunohistochemistry of Baboon Tissue

Fresh baboon forebrain was fixed in 4% paraformaldehyde overnight and cryoprotected in 30% sucrose before embedding in OCT. Sixty-micrometer floating coronal sections were blocked with 10% goat serum in 0.5% TritonX-100/1X PBS for 30 minutes at room temperature. Each section was kept in a separate well of a 24 well, flat-bottom, non-treated polystyrene tissue culture plate. Following blocking, sections were incubated 4 °C overnight in 0.5% TritonX-100/1X PBS with antibodies against H3K27me3 (Active Motif #39155; 1:1000) or H4K20me3 (Upstate #07-463; 1:1000) plus cell type markers GFAP– clone GA5 (Millipore #MAB3402; 1:500), Nestin (Abcam #ab134017; 1:500), or DCX–clone C-18 (Santa Cruz #sc-8066; 1:200). Following incubation of primary antibody cocktail, sections were washed 3 times, 10 min. per wash, in 0.5% TritonX-100/1X PBS at room termperature. Fluorescent labeling used secondary antibodies AlexaFlour 488 (Life Technologies #A21200 1:1000) and AlexaFlour 594 (Life Technologies #A21207; 1:2000) in 0.5% TritonX-100/1X PBS were added and samples were incubated 2 hours

at room temperature. Sections were mounted on Superfrost Plus microscope slides (Fisher; 12-550-15) and counterstained by DAPI in Vectashield (Vector Labratories; #H-1200). SVZ and SGZ sections were imaged on a Zeiss 710 confocal microscope (40X and 100X oil immersion objective). Images were processed using Zeiss Zen Black 2011, Zen v2 (Carl Zeiss Microscopy) and ImageJ (NIH) software.

Immunohistochemistry of Mouse Tissue

Mice were anesthetized with 450 mg/Kg Avertin, transcardially perfused with 1x PBS, and fixed with 4% paraformaldehyde. Following fixation, mouse brains were cryopreserved with 30% sucrose/PBS overnight and frozen in OCT compound. Frozen brains were sectioned at 12 μm, blocked with 10% goat serum in 0.5% TritonX-100/1X PBS for 30 minutes, and incubated 4 °C overnight with combinations of antibodies specific for: H3K27me3 (Active Motif, Cat#39155;Lot#31814017, 1:1000), β-galactosidase (Promega, Cat#z378B;Lot#0000040733, 1:750), GFP (Invitrogen, Cat#A11122, 1:500; Aves Labs, Cat#GFP-1020;Lot#1229FP08, 1:500), and cell type specific markers: GFAP (Millipore, Clone GA5, Cat#mab3402, Lot#2580632, 1:750), Nestin (AbCam, Cat#ab27952, 1:300; AbCam, Cat#ab134017, 1:250), DCX (Santa Cruz, Cat#sc-8066; Lot#10314, 1:200), βIII-Tubulin (Millipore, clone TU-20, Cat#MAB1637, Lot#JC1686015, 1:200), and NeuN (Millipore, clone A60, Cat#MAB377, Lot#NG1876252, 1:200). On the subsequent day, sections were washed 3 times, 10 min. per wash with 0.5% TritonX-100/1X PBS at room termperature. Following wash, antibody combinations needing only secondary antibodies (i.e. H3K27me3, GFAP, GFP, chicken anti-Nestin, and/or DCX) were incubated with AlexaFlour-488 or -594 conjugated secondary antibodies (anti-mouse: Life Technologies, Cat#A21200; Life Technologies, Cat#A21201; anti-rabbit: Invitrogen,

Cat#A21441; Life Technologies, A21207, anti-chicken Life Technologies, Cat#A11039, anti-goat: Life Technologies Cat#A11055; Life Technologies, Cat#A11058) in 0.5% TritonX-100/1X PBS for 2 hours at room temperature, protected from light. Sections probed with all other antibodies (rabbit anti-Nestin; mouse anti-βIII-Tubulin, NeuN, β-gal) were incubated with Biotinylated-rabbit or –mouse secondary antibody for 1 hour at room temperature (Vector Laboratories, Cat#BA-1000, 1:1000; Vector Laboratories, Cat#BA-2000, 1:1000), followed by Avidin-conjugated AlexaFlour-488 or Avidin-conjugated AlexaFlour-594 tertiary antibody for 1 hour (Life technology, Cat#A21370, 1:2000; Life technology, Cat#S32356, 1:2000). Analysis of thymidine analog incorporation involved administration of EdU (5-ethynyl-2'-deoxyuridine) or BrdU (5-bromo-2'-deoxyuridine) into mice by intraperitoneal (IP) injection 2 hours or 12 hours prior to perfusion. EdU was detected by Click-iT EdU 488 or 647 imaging kits (Invitrogen, C10337; Invitrogen, C10640), following manufacturer's instructions. BrdU was detected by anti-BrdU antibody (Life technology, #033900, 1:1000). All sections were mounted with Vectashield mounting medium with DAPI (Vector Laboratories, Cat# H-1200). Images were acquired on a either a Zeiss 510 or 710 confocal microscope with 20X, 40X, or 63X objectives and were processed using the associated analysis software, Zen. Scale bars were added by ImageJ (https://imagej.nih.gov/ij/).

Chromatin Immunoprecipitation and Sequencing

Neural stem progenitor cells were purified using Dynabeads-conjugated antibodies against cell type–specific markers (GFAP, nestin, vimentin, PSA-NCAM, or DCX) as previously described (Sandstrom et al., 2014). Briefly, cells from fresh dissected baboon SVZ were immediately dissociated with Accutase, equilibrated in binding buffer containing phosphate-

buffered saline (PBS) and 0.05% TritonX-100 (or saponin, detergent choice depends upon antibody), and subsequently subjected to Dynabeads-conjugated antibody purification. After elution with high-salt and pH-gradient buffer (citrate buffer base), the purified populations were cross-linked in 1.1% formaldehyde before chromatin shearing by Diagenode Bioruptor. The sheared chromatin obtained from purified NSPCs was incubated with Protein A Dynabeads (Life Technologies #10001D) conjugated with antibodies against either H3K27me3 (Active Motif #39155; 1:1000) or H4K20me3 (Upstate #07-463; 1:1000). For normalization, aliquots of sheared chromatin were incubated with antibodies against either total H3 (Millipore #05-499; 1:1000) or total H4K20me3, and 202,275,106 total H4 pass filtered reads which were assessed for read quality using FastQC v0.11.2 (http://www.bioinformatics.babraham.ac.uk/projects/fastqc/). Pass filtered reads were aligned to Papio anubis (PapAnu2.0) reference genome (ftp://ftp.ensembl.org/pub/release-78/fasta/papio_anubis/dna/) lacking mitochondrial genome with Bowtie v1.1.1 (http://bowtie-bio.sourceforge.net/index.shtml) aligner before sorting with Samtools v1.1 (http://www.htslib.org/). Genomic regions enriched with target histone modifications were detected using MACS2 v2.1.0.20140616 (https://github.com/taoliu/MACS/) callpeak function (with a false discovery rate [FDR] ≤ 0.05 for each peak). Total H3 and total H4 alignments were used as input controls when calling peaks for HK27me3 and H4K20me3, respectively. MACS2 was run with default parameters with the exception of setting fold change range to 2–50 (-m 2 50) for all data sets and broad peak detection (—broad) for H3K27me3 enrichment. ChIP-Seq peaks were associated to a nearest transcription start site using baboon transcript annotation (ftp://ftp.ensembl.org/pub/release-78/gtf/papio_anubis/) and the closest-features function included in BEDOPS v2.4.3 toolkit.

RNA-Seq Analysis

Total RNA was extracted from purified baboon SVZ cells as described previously (Sandstrom et al., 2014), and sequencing libraries were generated with Illumina Tru-Seq stranded total RNA library prep kit (Illumina; RS-122-2301; RS-122-2302). RNA libraries were deep sequenced using paired-end sequencing, (2 x 36 base pairs, >300 million reads) on an Illumina HiSeq2000 sequencer. Reads were quality filtered resulting in 148,304,589 total pass filtered reads which were assessed for read quality using FastQC v0.11.2. Pass filtered reads from individual flow cells were aligned to PapAnu2.0 containing mitochondrial genome (ftp://ftp.ensembl.org/pub/release-78/fasta/papio_anubis/dna/) by Tophat2 v2.0.13 (https://ccb.jhu.edu/software/tophat/index.shtml) plus PapAnu2.0 transcript annotation (ftp://ftp.ensembl.org/pub/release-78/gtf/papio_anubis/) to guide alignment. Transcripts were assembled by Cufflinks v2.2.1 (http://cole-trapnell-lab.github.io/cufflinks/) using PapAnu2.0 transcript annotation to guide assembly and perform bias correction and multiread rescue prior to merging assembled transcripts into a single sorted BAM file using Samtools v1.1. Genes with a read density of >1 fragment per kilobase (kb) of exon per million fragments mapped (FPKM) over the entire gene were considered detectable via RNA-Seq and used in our integrative analysis. The GBM samples were snap-frozen surgical resection tumor (~200 mg tissues for each RNA-Seq), which were not expanded in culture. Expression data for GBM and control were generated as previously described (Sandstrom et al., 2014). Genes with expression values >1 FPKM were considered for subsequent analyses. Cuffdiff was applied to analyze the differential gene expression between GBM and control. Integrated analysis of ChIP-Seq and RNA-Seq data across species was performed with R (https://cran.r-project.org/). Area-proportional Venn diagrams were generated using the R package Vennerable v3.0 (http://r-forge.rproject.org/projects/vennerable),

and heatmaps were rendered using heatmap.3 function (https://github.com/obigriffith/biostar-tutorials/blob/master/Heatmaps/heatmap.3.R).

Sample Sizes for Genome Wide Sequencing

For ChIP-Seq, we had 2 independent sets of ChIP performed with 2 antibodies from different vendors (i.e., Millipore and Active Motif for H3K27me3; Abcam and Active Motif for H4K20me3). The summary of H3K27me3 (or H4K20me3) putative targets in Supplementary Tables is common between 2 independent ChIP-Seqs, and each set has obtained 120–200 million pass-filter reads. For RNA-Seq, we also had at least 2 sample sets for baboon SVZ cells (n = 3), GBM I (n = 2) GBM II (n=2), and control region specimens (n=3) to obtain at least 300 million pass-filtered reads for each sample set. The summary in Supplementary Tables is common across independent samples after standard pipeline of RNA-Seq analysis (Cufflink and Cuffdiff).

Gene Ontology, Network and Pathway Analysis

Duplicate gene references were removed prior to Gene Ontology (GO) or functional pathway and network analyses. DAVID Functional Annotation Tool (DAVID Bioinformatics Resources 6.7, NIAID/NIH) was used to perform (GO) analysis. For GO, a significance cutoff was set at P value < 0.05, including Bonferroni multiple test correction. Functional pathway and network analyses of enriched loci were performed using Ingenuity Pathway Analysis (IPA) (Ingenuity Systems, Redwood City, CA). Data for up to 10 of the top networks and pathways predicted by IPA are presented in supplementary tables, with significance cutoff set at P value < 0.05 (calculated by IPA using right-tailed Fisher exact test).

Cre protein induction and purification

For Cre protein induction and purification, His-Cre-CTP was transformed into BL21(ED3)pLysS (Invitrogen) for protein expression. The overnight bacterial culture was inoculated at dilution of 1:80 in LB with 100 mg/mL ampicillin for 2 hours at 37 ^{0}C and proteins were induced with 0.5 mM IPTG for 2 hr at room temperature. Total protein was extracted with lysis buffer (50 mM NaH_2PO_4, pH 8, 0.5 M NaCl, 10 mM imidazole, 0.2% Triton X-100, 6 mM 2-mercaptoethanol) and purified with Ni-NTA superflow cartridge (Qiagen). After wash with buffer containing 50 mM NaH_2PO_4, pH 8.0, 0.3 M NaCl, 20 mM imidazole, Cre protein was eluted with elution buffer (250 mM imidazole in PBS). The eluted protein fractions went through buffer exchange with PBS using 10 K Amicon centrifugal filter (Millipore) and then stored in 20% glycerol/PBS at -80 ^{0}C. Protein concentration was determined by Bradford Assay (BioRad).

Stereotaxic Injection of Cre-CTP protein and vehicle solutions

Experimental design: For external controls, *ROSA26* "reporter" mice were utilized which only have the lacZ or YFP reporter (R26R-lacZ or R26R-EYFP), but do not have conditional alleles for *Ezh2*$^{flox/flox}$ or *Suv4-20h1*$^{flox/flox}$;*Suv4-20h2*$^{-/-}$. These mice were injected with Cre and the phenotypic effects were compared to animals harboring *Ezh2*$^{flox/flox}$*:ROSA26* or *Suv4-20h1*$^{flox/flox}$;*Suv4-20h2*$^{-/-}$;*ROSA26* that were also injected with Cre. For internal controls, one hemisphere of the brain was injected with vehicle (20% glycerol in PBS) and the contralateral hemisphere was injected with Cre protein. Phenotypes were then compared among conditional knock-out (cKO) of *Ezh2*, cKO of *Suv4-20h1*, and both internal and external controls.

Mice were anesthetized with 1.5-2% isoflurane at a flow rate of 0.5 L/min. Upon reaching a deep plane of anesthesia, mice were centered on a model 1900 stereotaxic frame (KOPF Model

1900 stereotax). Prior to Cre injections, 10 mg/kg Lidocaine and 2 mg/kg Marcaine solutions were administered by subcutaneous injection at the incision site, prior to a 1 cm incision being cut along the dorsomedial scalp to expose the frontal and parietal bones between Bregma and Lambda landmarks. Subsequently, 5 mg/Kg Baytril was administered by IP injection. Bore holes of 0.53 mm diameter were drilled into the mouse skull at the appropriate A/P and M/L coordinates using a #75 drill bit on a model 1911 stereotaxic drill (KOPF). Using a custom-made Hamilton Neuro syringe with a 12° beveled tip (custom-made Hamilton 0.5 uL, Neuro model 7000.5 KH syringe including a 32 gauge needle with Point Style 4, hamiltoncompany.com, Cat #: 65457-02), Cre was injected into the SVZ including 4 injection sites per hemisphere per mouse at the following coordinates: anteroposterior (+0.97; +0.49; +0.25; -0.11), mediolateral (±0.95; ±1.32; ±1.35; ± 1.5), and dorsoventral (-2.6; -2.2 -2.15; -2.0). The coordinates for SGZ/DG stereotaxic injection are anteroposterior (-1.50; -2; -2.53; -2.91), mediolateral (±1.50; ±1.62; ±1.68; ±1.8), and dorsoventral (-1.95; -2.1; -2.1; -2.22). All coordinates are measured from the Bregma landmark on exterior of the balanced skull. After needle placement at proper coordinates, 350 nL Cre or vehicle was infused at each injection site from the Hamilton syringe at a rate of 60-100 nL/min using a UltraMicroPump driven by a SYS-Micro4 controller (World Precision Instruments). During initial validation of stereotaxic coordinates, potential Cre diffusion was quantified by injecting 50-500 nL Cre into *ROSA26* mice, and detecting β-galactosidase expression throughout the brain using immunohistochemistry at time points for conditional knockout experiments. Following a 5 min post-injection recovery period, the mice were returned to normal habitat containing a DietGel gel cup with Caprophen tablets (10 mg/kg PO). A 4 day post-surgical period ensured complete degradation of Ezh2 or Suv4-20h protein that had been translated prior to Cre mediated knockout.

Gene Expression Analysis

For RT-qPCR validation, total RNA was extracted from the SGZ/DG using TRIzol (Invitrogen) reagent followed by aqueous/organic phase separation, isopropyl alcohol RNA precipitation, dissolving RNA with 25-50 uL nuclease free water and subsequently cDNA synthesis by iScript reverse transcriptase supermix (Bio-Rad, #170-8841) according to the manufacturer's instructions. Briefly, 5 uL input RNA (1 pg – 1 ug) was combined with 4 uL iScript supermix and brought to 20 uL total volume with nuclease free water. RT reaction protocol is as follows: priming: 5 min @ 25 °C; RT: 20 min @ 46 °C; inactivation: 1 min @ 95 °C. The transcript expression level was measured by Real-Time PCR with SYBR Select Master Mix (Life Technologies, #4472908) and detection on ABI7900HT system (Applied Biosystems). S16 RNA was used as internal control for normalization (ΔCt). The differential expression was measured by subtraction of ΔCt between wildtype and *Ezh2* knockout animals to obtain ΔΔCt (log2). Primers were designed using ABI Primer Express Software version 3.0, PrimerBank (https://pga.mgh.harvard.edu/primerbank/), and Primer3Plus (http://www.bioinformatics.nl/cgi-bin/primer3plus/primer3plus.cgi). At least one primer pair per gene spanned 2 or more exons.

Flow Cytometry of Baboon Tissue

Rostral and caudal baboon SVZ was microdissected from forebrain tissue, digested with Accutase for 10 minutes, and strained with a 40-μm cell strainer (BD #352340) to yield single cell suspension. Cells were stained with viability dye (BD Biosciences #564406; 1:1000), subsequently fixed in 4% PFA, permeabilized, and blocked using FC Block (BD Pharmigen #553141; 1:200). Following blocking, cells were incubated for 60 minutes at 4°C with primary antibodies anti-GFAP (mouse: Millipore #MAB3402; 1:500; rat: Invitrogen #130300; 1:500), nestin (rabbit:

Abcam #AB27952; 1:500, mouse: DHSB #rat-401, 1:500), DCX (Santa Cruz #sc-8066, 1:500), H3K27me3 (rabbit: Millipore #07-449; 1:500; mouse: Active Motif #61017;1:500), and/or H4K20me3 (Abcam #ab9053; 1:500). Flourochrome labeling used secondary antibodies conjugated with either AlexaFlour 488 (Life Technologies anti-mouse #A21200/anti-goat #A11055; 1:300), AlexaFlour 647 (Life Technologies anti-mouse #A21463/anti-rat #A21247; 1:300), and PE (Cell Signaling #8885S; 1:300) for 30 minutes at 4°C. Staining controls included single color positive controls labeled with each separate antibody, viability control, and unstained cells. Flow cytometry was run on a LSRII (BD Biosciences) configured with violet (405 nm with 450/50 BP), argon (488 nm with 530/30 BP), green (561 nm with 660/20 BP), and red (633 nm with 780/30 BP) lasers. Data analysis was performed using FlowJo software (FlowJo, LLC). Final reported baboon SVZ populations were averaged across rostral and caudal baboon flow cytometry replicates.

Flow Cytometry of Mouse Tissue

Mice were anesthetized with 450 mg/Kg Avertin prior to decapitation. Following euthanasia, the dentate gyrus was dissected under microscope, dissociated into single cells by Accutase, and passed through a 40 um cell strainer. Freshly isolated SGZ/DG cells were fixed with 4% paraformaldehyde, permeabilized, incubated 4 ℃ overnight with primary antibodies (anti-GFAP, Nestin, PSA-NCAM, Doublecortin, NeuN, H3K27me3, S100-β, and ALDH1L1), and subsequently labeled with BV421, PE, PE-Cy7 (BD Biosciences) and Alexa fluor 488, -594, -647 (Life Technologies) conjugated secondary antibodies. Primary antibody sources: Doublecortin (Cell Signaling #4604; Millipore clone2G5 MABN707, 1:500), Polysialic Acid Neural Cell Adhesion Molecule PSA-NCAM, clone 2-2b (Millipore #MAB5324, Lot# 1966892, 1:500), Glial

Fibrillary Acidic Protein GFAP, clone GA5 (Millipore #MAB3402, Lot#1993774, 1:500; Abcam clone 2A5 #ab4648, 1:500), Nestin (Abcam #AB27952; 1:500), NeuN (Millipore MAB377, 1:500). H3K27me3 (Active Motif, 1:1000), S100-β (AbCam, Cat#ab41548 1:500), β-galactosidase (Promega, Cat#z378B, 1:750). Secondary antibody sources: BD Biosciences. Analysis of thymidine analog incorporation involved administration of BrdU (5-bromo-2'-deoxyuridine) and EdU (5-ethynyl-2'-deoxyuridine) into mice by intraperitoneal (IP) injection 5 days post-injection and 2 hours prior to dissection, respectively. For BrdU detection, following paraformaldehyde fixation, cells were treated with 1.5N HCl, incubated with anti-BrdU primary (Life Technologies, #033900, 1:100) and labeled with Alexa fluor-647 (anti-mouse: Life Technologies, Cat#A21463, 1:300) conjugated secondary. EdU was detected by Click-iT EdU 647 imaging kit (Invitrogen, C10340), following manufacturer's instructions. For analysis, controls included single color controls stained with each antibody separately, unstained cells for gate placement, and compensation beads for spectral compensation. Briefly, a drop of OneComp eBeads (eBioscience 01-1111-42) was incubated with 1 ul of fluorochrome-conjugated anti-mouse antibody for 15 – 30 min on ice and protected for light. Beads were washed with 1 mL of cell staining buffer and resuspended in 300 ul of same buffer prior running the samples on an LSR-II cytometer. Flow cytometry data was acquired on a LSR-II (BD Biosciences) configured with an argon 488 laser with a 505 LP dichroic and 525/50 filter to detect Alexa fluor 488 and a green 510 laser with a 735 LP dichroic and a 575/26 filter to detect PE. Compensation and data analysis was performed using FlowJo software (Tree Star, Inc, Ashland, OR).

Imaging Flow Cytometry

Mice were anesthetized with 450 mg/Kg Avertin prior to decapitation. Following euthanasia, the dentate gyrus was dissected under microscope, dissociated into single cells by Accutase, and passed through a 40 um cell strainer. Cells were subsequently fixed by 4% paraformaldehyde, blocked with FC Block (BD Pharmigen #553141; 1:200), incubated 4 °C overnight with antibody against GFP (Invitrogen, Cat#A11122, 1:250; Aves Labs, Cat#GFP-1020;Lot#1229FP08, 1:500), H4K20me3 (AbCam, Cat#ab9053), MCM2 (Santa Cruz, Cat#sc-9839), p-H3(S10) (Millipore, Cat#06-570), p-s780-Rb (Cell Signaling, Cat#9307S), NeuN (Millipore, clone A60, Cat#MAB377, Lot#NG1876252, 1:200), subsequently washed with Perm/Wash buffer (BD Biosciences, Cat#554723) and incubated with anti-mouse AlexaFluor-488, AlexaFluor-647 (Life Technologies, Cat#A21200), and anti-rabbit PE (BD Biosciences). Analysis of thymidine analog incorporation involved administration of EdU (5-ethynyl-2'-deoxyuridine) into mice by intraperitoneal (IP) injection 12 hours prior to dissection. EdU was detected by Click-iT EdU 488 or 647 imaging kits (Invitrogen, C10337; Invitrogen, C10340), following manufacturer's instructions. Processed cells were imaged by Amnis ImageStreamX MKII imaging flow cytometer and quantified with associated IDEAs software.

Tissue Clearing and Light Sheet Microscopy

The new iDISCO+ protocol (May 2016, https://idisco.info/idisco-protocol/update-history/) was followed for all steps and reagents used during tissue fixing, immunohistochemistry and clearing. Briefly, mice were perfusion fixed with PBS and 4% paraformaldehyde (PFA) followed by overnight incubation in 4% PFA in 4° C. Brains were cut into 2 mm sagittal blocks in a brain matrix (Braintree Scientific, BS-A 5000S) prior to clearing. Following overnight fixing with 4%

PFA, brains were pretreated with methanol (Fisher A412-4) and bleached with 30% hydrogen peroxide (Sigma 216763-100ML) on an orbital rocker. For immunohistochemistry, doublecortin was detected using goat anti-doublecortin primary (Santa Cruz, sc-8066, 1:200) and Alexa Fluor 594-conjugated secondary antibodies (Life Technologies, A11058, 1:200). NeuN detection utilized mouse anti-NeuN (Millipore, MAB377, 1:200), biotinylated secondary (Vector Laboratories, BA-2000, 1:200) and Alexa Fluor 488-conjugated avidin (Life Technologies, A21370, 1:200). For all steps prior to tissue clearing, incubation times (listed as "n" in iDISCO+ protocol)/ Solution volume followed table in iDISCO+ protocol and were as follows: 3 day/ 4 mL for 2 mm sagittal mouse sections. Tissue clearing involved methanol dehydration series and overnight 66%:33% methanol: Dichloromethane (DCM) incubation, and clearing with 100% DCM (Sigma 270997-1L) and Dibenzyl Ether (DBE) (Sigma 108014-1KG). Cleared tissues were imaged on an Ultramicroscope, LaVision BioTec light sheet microscope (LaVision, Bielefeld, Germany) and were processed with Imaris software (Imaris x64 8.1.2).

Image Quantification

All steps of light sheet imaging quantification were performed in ImageJ following manufacturer's example in "Area Measurements and Particle Counting" (https://imagej.nih.gov/ij/docs/pdfs/examples.pdf). Mean fluorescence intensity (MFI) was determined by splitting RGB Color images into 8-bit greyscale images using the Split Channels tool before auto-adjusting with the Threshold setting. After thresholds were set, the Analyze Particles tool detected the average pixel intensity per area within the threshold range. The sizes used for particle analysis were 100-Infinity.

Olfaction-based Behavioral Assay

Mice were pre-trained to condition animals for behavior testing. Pre-training involved a single 12 hour fasting period prior to conducting olfaction-based behavior assay. While target fasting period was 12 hours, maximum fasting period did not exceed 16 hours for any reason. Following 12 hour fasting, animals were placed in a new cage and tested for their ability to find standard LARC provided chow or pieces of chocolate chip cookies in their cage. Following behavior test, animals were returned to their cages containing regular chow. Water was not be withheld at any time, and no other alterations to animal's housing, enrichment, or other living conditions.

Statistics

For all experiments utilizing conditional mouse models: sample sizes, statistical test method and p-value (if test is significant) are listed in relevant figures and/or figure legends. For flow cytometry and immunohistochemistry, two-sample t-tests were performed in R (https://cran.r-project.org/). For differential gene expression analysis by RT-qPCR, a moderated t-test was performed using empirical Bayes method by the ebayes function of limma package in R/Bioconductor (https://bioconductor.org/packages/release/bioc/html/limma.html). Such an empirical Bayes method provides improves statistical power, typically resulting in a reduction of false discovery rates false non-discovery rates. Empirical Bayes methods are commonly used for differential expression analysis of gene expression using RT-qPCR or microarrays with samples size of 3 – 5 biological replicates per test condition.

Supplementary Information

Supplementary tables related to genomic analyses can be found online at: http://dx.doi.org/10.1016/j.nepig.2016.04.001

CHAPTER THREE: RESULTS

Genome-wide Targets of H3K27me3 and H4K20me3 in NSPCs

H3K27me3 and H4K20me3 are ubiquitously enriched in the NSPC of adult primate SVZ

In mammals, the lateral ventricle is lined with NSPCs including radial-glia–like neural stem cells (NSCs), amplifying progenitor cells, and immature neuroblasts, as well as postmitotic ependymal cells (Sandstrom et al., 2014; Jessberger et al., 2007; Ihrie and Alvarez-Buylla, 2008; Clelland et al., 2009; Ming and Song, 2011). To quantify mean enrichment ratios of H3K27me3 and H4K20me3 across NSPCs, rostral and caudal parts of baboon SVZ tissue were subjected to flow cytometry to measure the percent colocalization of H3K27me3, H4K20me3, and established cell type–specific markers including GFAP, nestin, and DCX. H3K27me3-positve cells comprised approximately 54% GFAP-positive, 50% nestin-positive, and 59% DCX-positive SVZ subpopulations (Fig. 19). H4K20me3-positive cells constituted approximately 80% GFAP-positive, 68% nestin-positive, and 85% DCX-positive cells within the SVZ (Fig. 19). Co-immunostaining with antibodies for H3K27me3, H4K20me3, and established cell type–specific markers including GFAP, nestin, and DCX revealed that H3K27me3 and H4K20me3 are present in quiescent/active NSCs and migrating neuroblasts (Fig. 20). The presence of H3K27me3 and H4K20me3 is not mutually exclusive to any subpopulation within the adult SVZ.

Chromatin immunoprecipitation from endogenous NSPCs of adult SVZ

To assess the role of H3K27me3 and H4K20me3 within NSPCs *in vivo* without resorting to cultural NSPC expansion required a multispecies approach using baboon for endogenous NSPCs, human GBM specimens for pathobiology, and mice for genetic manipulations (Fig. 1). To interrogate the roles of H3K27me3 and H4K20me3 in endogenous NSPCs, we initially carried out

genomewide analyses including ChIP-Seq and RNA-Seq on purified baboon SVZ cells. Because histone modifications are vulnerable to cultured condition (i.e., methyl donors from metabolism of cultured medium can alter histone methylation) (Black et al., 2012), we used *in vivo* NSPCs purified from nonhuman primate to avoid culture artifacts and the ethical obstacle of obtaining fresh brain tissue from healthy humans (Fig. 21A).

To identify the molecular targets of H3K27me3 and H4K20me3 in cell populations of the adult SVZ, *in vivo* NSPCs were purified from baboon brain as previously described (Sandstrom et al., 2014) and subjected to ChIP-Seq using antibodies against H3K27me3 or H4K20me3 and parallel ChIP-Seq with antibodies against total H3 or H4 for normalization. ChIP-Seq reads were aligned to the newly annotated baboon genome maintained by the Ensembl project (PapAnu2.0) with Bowtie aligner prior to MACS2 peak calling (Fig. 21B). Chromatin enriched with histone modifications identified by MACS2 peak calling (FDR ≤ 0.05) was then associated to the nearest transcription start sites (TSSs) using BEDOPS Closest Features tool and baboon TSS coordinates obtained from PapAnu2.0 annotation. H3K27me3- and H4K20me3-enriched peaks, and genome-wide ChIP "read density" can be visualized on the robust UCSC genome browser (Fig. 22). Our work presented here is the first to align brain-derived baboon ChIP-Seq reads to baboon genome. We identified a total of 709 loci enriched with H3K27me3 (Supplementary Table 1i online: http://dx.doi.org/10.1016/j.nepig.2016.04.001) corresponding to 271 unique genes (Fig. 23A; Supplementary Table 1ii online: http://dx.doi.org/10.1016/j.nepig. 2016.04.001). In addition, 10,000 loci corresponding to H4K20me3 peaks were detected (Supplementary Table 1 iii online: http://dx.doi.org/10.1016/j.nepig.2016.04.001), resulting in 763 unique baboon genes associated with H4K20me3 enrichment (Fig. 23B; Supplementary Table 1iv online: http://dx.doi.org/10.1016/j.nepig.2016.04.001).

Molecular targets of H3K27me3 and H4K20me3 in the endogenous NSPCs of adult SVZ

As H3K27me3 and H4K20me3 are associated with transcriptional repression, we compared our ChIP-Seq data with gene expression data of baboon NSPCs obtained from deep RNA-Seq (Fig. 21, 23A-B). RNA-Seq reads were aligned to baboon genome with splice aware Tophat aligner then assembled into transcripts using Cufflinks (Supplementary Table 2i–ii online: http://dx.doi.org/10.1016/j.nepig. 2016.04.001). Subsequently, integrated analysis was performed for ChIP-Seq loci (ChIP by H3K27me3 or H4K20me3), and RNA transcripts either detectable or undetectable were determined by a cutoff of 1 FPKM (Supplementary Table 2iii–vi online: http://dx.doi.org/10.1016/j.nepig.2016.04.001). Genes enriched with either H3K27me3 or H4K20me3 are largely associated with low or undetectable expression levels (FPKM $\leq$ 1), as 92.25% (250/271) of H3K27me3 (Fig. 23A; Supplementary Table 2iii online: http://dx.doi.org/10.1016/j.nepig.2016.04.001) associated genes had no detectable RNA transcripts (FPKM $\leq$ 1) and 89.65% (684/763) of H4K20me3 (Fig. 23B; Supplementary Table 2v online: http://dx.doi.org/10.1016/j.nepig.2016.04.001) associated genes did not produce a detectable transcript. To predict the role of genes enriched with H3K27me3, we used GO to examine the 250 genes enriched by H3K27me3 with FPKM $\leq$ 1 and found that these genes are correlated with transcriptional activity, particularly via transcription factors, as well as various processes related to differentiation (top 15 GO categories had Bonferroni-adjusted P-values ranging from 1.89×10^{-43} to 2.22×10^{-14}) (Fig. 23C; Supplementary Table 2vii online: http://dx.doi.org/10.1016/j.nepig.2016.04.001). Using GO to assess the cellular functions of the 684 genes enriched by H4K20me3 (FPKM $\leq$ 1) revealed that H4K20me3 enrichment is correlated with transcriptional regulation, mainly via zinc ion binding and DNA binding (top 15 GO categories had Bonferroni-adjusted P values between 1.57×10^{-27} and 3.09×10^{-4}) (Fig. 23D;

Supplementary Table 2viii online: http://dx.doi.org/10.1016/j.nepig.2016.04.001) in addition to olfaction and GPCR signaling pathway. Using IPA, the 250 H3K27me3-enriched genes (FPKM ≤ 1) were predicted to function in transcriptional regulatory networks, lineage differentiation, and development (Fig. 23A [box]; Supplementary Table 2ix and x online: http://dx.doi.org/10.1016/j.nepig.2016.04.001). The roles of these genes are largely relegated to coordination and commitment of differentiation by stem cells. In addition, IPA predicted that the 684 genes enriched with H4K20me3 and lacking detectable transcripts (FPKM ≤ 1) function in cellular assembly/organization/maintenance, innate immune responses, and metabolism (Fig. 23B [box]; Supplementary Table 2xi and xii: http://dx.doi.org/10.1016/j.nepig.2016.04.001).

The SET-domain family proteins have been implicated in cancers and can interact with non-SET proteins to form chromatin modifying complexes (Ciferri et al., 2012; Dou et al., 2005). In addition, we found colocalization of H3K27me3 and H4K20me3 in the baboon SVZ (Fig. 24), suggesting that spatial overlap of modifications has common genomic enrichment of a subclass of genes in the NSPCs. Therefore, we carried out comparison of H3K27me3- and H4K20me3-enriched loci and found 79 genes to be commonly enriched with both H3K27me3 and H4K20me3 (Fig. 24C; Supplementary Table 3i online: http://dx.doi.org/10.1016/j.nepig.2016.04.001), comprising 8.27% (79/955) of all genes enriched by either H3K27me3 or H4K20me3. However, many of the H3K27me3 and H4K20me3 peaks in this co-enriched subset are located at different genomic intervals of a specific gene. Through ChIP-Seq and RNA-Seq overlap comparison, of the 79 H3K27me3/H4K20me3 co-enriched genes identified by ChIP-Seq (from Fig. 24C), 62 have no detectable transcript (FPKM ≤ 1) (Fig. 24D; Supplementary Table 3iv online: http://dx.doi.org/10.1016/j.nepig.2016.04.001), suggesting the co-repression of a set of genes by H3K27me3 and H4K20me3 in the NSPCs. Furthermore, these 62 genes were classified by IPA

with potential functions in cell-to-cell signaling and interaction, various metabolic processes, cancer, cell cycle, cellular growth and proliferation, cellular compromise, and cellular maintenance (Fig. 24D [blue box]; Fig. 25; Supplementary Table 3v and vi online: http://dx.doi.org/10.1016/j.nepig.2016.04.001). Our results suggest a protective role of H3K27me3/H4K20me3 against improper differentiation or aberrant cell cycle progression. Lastly, the 17 H3K27me3/H4K20me3 co-enriched genes with detectable expression levels (FPKM > 1) are associated with xenobiotic metabolism, antigen presentation, and cellular assembly and organization (Fig. 24D [green box]; Supplementary Table 3viii and ix online: http://dx.doi.org/10.1016/j.nepig.2016.04.001). Taken together, our data implicate that H3K27me3 and H4K20me3 play common yet distinct roles in NSPCs of SVZ. We anticipate EZH2 and KMT5B interactions to function as a protective mechanism critical for the identity of adult NSPCs in the SVZ by preventing precocious lineage commitment and untimely cell cycle progression.

Conditional Knock-out of Histone Methyltransferases in Adult Neurogenic Niches

Recombinant Cre protein induces homologous recombination in vitro and in vivo

The development of cell-penetrating peptide (CPP) tagging-Cre fusion proteins has provided an alternative approach to introducing Cre into a cell, in addition to transgenic or viral transduction methods (Lin et al., 2004; Will et al., 2002). One such Cre fusion protein contains a cell transduction peptide (CTP: APWHLSSQYSRT) and a nuclear localization sequence (NLS) and bacteriophage P1 Cre recombinase (Fig. 26A). The Cre recombinase specifically recognizes 34 base-pair loxP sequences flanking a target DNA sequence (Fig. 26B-C). As a proof of principle, this Cre has been successfully delivered to cardiac muscle via ultrasound guided injection (Chien

et al., 2014) and administrated into the adult SVZ by stereotaxic injection in our previous study for short-term analysis (Rhodes et al., 2016). To simplify the description of this NLS-Cre-CTP fusion protein, Cre protein is the denotation used throughout the text. Empirically derived stereotaxic coordinates were validated with red retrobead injections into the SVZ and SGZ of R26R-lacZ mice (Fig 27). To evaluate the long-term utility of Cre protein induced recombination *in vivo*, we delivered Cre protein via stereotaxic injections into the brains of adult R26R-lacZ or R26R-EYFP (denoted by *ROSA26* or *ROSA26*$^{Y/Y}$) (Fig. 28). Within the SVZ of R26R-lacZ mice injected with Cre protein, constitutive β-galactosidase (β-gal) expression was restricted to injection sites indicating that Cre protein injection induces recombination within targeted sites in a highly localized manner (Fig. 28). Injection sites were largely demarcated from surrounding areas, as only minor β-gal expression was observed in cells outside the injection site. Using image flow cytometry analysis, we confirmed the high efficiency of Cre-mediated recombination within the injected areas of *ROSA26*$^{Y/Y}$ mice (Fig. 29). Immediately following dissection of hippocampal tissue for flow cytometry, cells from Cre protein injected hemispheres displayed YFP expression in regions corresponding to injection sites (Fig. 29B-C). Cells from Cre injected hemispheres increased 519% in YFP^{+} populations compared to hemispheres injected with vehicle solution (20% glycerol in PBS) (Fig. 29D-G). The ability of injected Cre protein to induce recombination localized to injection sites presents a novel approach in which genes can be genetically manipulated *in vivo* in a spatially-restricted manner. Importantly, our method leads to applications involving conditional knockout of small populations of cells and also genes expressed across multiple cell types simultaneously, such as examining the long-term regional effect of chromatin modifiers within neurogenic niches.

Conditional loss of Ezh2 or Suv4-20h function in adult SVZ and SGZ/DG by recombinant Cre protein

To further explore the use of Cre protein-mediated knock-out of candidate HMT genes, we stereotaxically injected Cre protein into specific brain regions harboring NSPCs. The chromatin modification enzymes Ezh2 and Suv4-20h, as well as resulting histone modifications, H3K27me3 and H4K20me3, respectively, are ubiquitously present in a wide range of cell types in adult mice. Within the SVZ and the SGZ/DG, such cell types include NSCs expressing GFAP and/or Nestin, and DCX^+ neuroblasts (NBs) (Fig. 30-32). The SGZ/DG also contains differentiated cell types including βIII-$Tubulin^+$ immature neurons and $NeuN^+$ mature neurons (Fig. 31-32). To delineate which subpopulations are most impacted by the loss of Ezh2 or Suv4-20h, we utilized stereotaxic injection of Cre protein into targeted sites within the adult SVZ and SGZ/DG of conditional *Ezh2* or *Suv4-20h1* knockout mouse models. These mouse models harbor floxed alleles of genomic sequence encoding the enzymatic SET domain of *Ezh2* (*Ezh2*$^{flox/flox}$) (Su et al., 2003) or *Suv4-20h1* (*Suv4-20h1* $^{flox/flox}$;*Suv4-20h2* $^{-/-}$) (Fig. 33) (Schotta et al., 2008). Of note, although murine histone methyltransferases responsible for H4K20me3 are catalyzed by Suv4-20h1 and Suv4-20h2, Suv4-20h1 is ubiquitously present in adult tissues including brain. By contrast, Suv4-20h2 displays restricted abundance in some adult tissues though not in the brain, and Suv4-20h2 null mice (*Suv4-20h2*$^{-/-}$) have no apparent phenotype (Schotta et al., 2008). Nonetheless, to exclude compensation between Suv4-20h1 and Suv4-20h2, we chose to use *Suv4-20h1*$^{flox/flox}$;*Suv4-20h2*$^{-/-}$ mice for our studies. To monitor knock-out efficiency, we bred *Ezh2*$^{flox/flox}$ mice or *Suv4-20h1*$^{flox/flox}$;*Suv4-20h2*$^{-/-}$ mice to *ROSA26* or *ROSA26*$^{Y/Y}$ mice with loxP sites flanking a stop cassette upstream of β-galactosidase (β-gal) or yellow fluorescent protein (YFP) (Fig. 33B). The crosses resulted in

homozygous alleles denoted as *Ezh2*$^{flox/flox}$;*ROSA26*, *Ezh2*$^{flox/flox}$;*ROSA26*$^{Y/Y}$, *Suv4-20h*$^{flox/flox}$;*ROSA26*, and *Suv4-20h*$^{flox/flox}$;*ROSA26*$^{Y/Y}$ mouse colonies for experiments (Fig. 33C).

Following stereotaxic injection, the Cre protein was capable of crossing the plasma membrane of adjacent cells, importing into the nucleus, and initiating recombination at loxP flanked genomic sites. Such Cre mediated recombination resulted in excision of the DNA sequence which encodes the enzymatic SET domain of Ezh2 (or Suv4-20h) as well as the stop cassette upstream of the *ROSA26* reporter to achieve simultaneous ablation of Ezh2 (or Suv4-20h) catalytic activity and constitutive expression of β-gal (or YFP) (Fig. 28, 29, 33D). In parallel with phenotypic analysis, RT-qPCR confirmed a significant 2.63 (range from 1.7 to 4.4) fold knock-down of *Ezh2* mRNA in Cre injected hemispheres compared to controls (Fig. 34A-C, Tables 1-2) in *Ezh2*$^{flox/flox}$;*ROSA26*$^{Y/Y}$ mice, 19 days post Cre injection into SGZ/DG. Sustained knock-down of *Ezh2* mRNA was detectable with 3.66-fold reduction at 32 days post Cre injection (data not shown). In addition, we validated the expression levels of Ezh2/H3K27me3 putative targets identified from our previous study using RT-qPCR (Rhodes et al., 2016). We demonstrated that *Pax5* increased ($p<0.003$) following knock-down of *Ezh2* transcript while *Hmx1, Hoxa5, Hoxc6, Hoxd13, Mnx1, Osr2, and Sp9* decreased ($p< 0.05$) 19 days post Cre injection into SGZ/DG (Fig. 34A). Moreover, Cre mediated recombination was highly efficient as virtually all β-gal-positive cells lacked H3K27me3 within injection sites of the SVZ (Fig. 34D).

Ezh2/H3K27me3 influences differentiation paradigm and maintenance of NSPCs in the mouse SVZ and SGZ/DG

To explore how differential H3K27me3 enrichment due to diminished Ezh2 activity affected the cell fate of NSPCs in the SVZ, we assessed the change in NSPC subpopulations at 10

and 32 days post-Cre protein injection into the SVZ of *Ezh2*$^{flox/flox}$;*ROSA26* (experimental group) and *ROSA26* reporter mice (control group). Ten days corresponded to the times required for SVZ NSCs to be repopulated while 32 days corresponded to the time period for SVZ NSPC differentiation (Alvarez-Buylla and Lim, 2004; Bond et al., 2015). Ten days post-Cre protein injection within the SVZ resulted in a substantial decrease of H3K27me3^{+}/DCX^{+} migrating NBs within the rostral migratory stream (RMS) but augmentation of DCX^{+} cells within the dorsal SVZ compared to control mice (Fig. 35). This phenotype was observed in the SVZ of multiple animals 10 days after Cre injection (n=6). Further, 32 days after Cre protein injection, immunostaining was used to assess NSPC populations within the SVZ including GFAP, Nestin, and DCX. Thirty-two days after injection (n=10), Cre injected SVZ of *Ezh2*$^{flox/flox}$;*ROSA26* mice did not show a significant change in either GFAP^{+} or Nestin^{+} populations compared to controls (Cre injected into *ROSA26* mice), whereas there was a substantial increase in the DCX^{+} population (Fig. 36, 37). The increase in DCX^{+} NBs was observed in multiple animals (n=10), 32 days after Cre injection into *Ezh2*$^{flox/flox}$;*ROSA26* mice compared to controls. Immunohistochemistry (IHC) results from 10 day post-Cre protein injected SVZ showed a decrease in DCX^{+} NBs along the RMS, suggesting NBs migrate away from the SVZ earlier than 10 days. In this regard, a shorter time point of 5 days post-Cre protein injection was chosen to detect early NBs migration, using sagittal sections (Fig. 38). Compared to vehicle injected controls, Cre injected hemispheres showed a moderate decrease in DCX^{+} NBs at the dorsal SVZ and substantial increases in DCX^{+} NBs along the RMS and migrating tangentially into the olfactory bulb (OB) (n=4).

To further assess the migratory capacity of NBs along the RMS to the OB by meso-scale imaging, we utilized a modified iDISCO tissue clearing protocol and lightsheet fluorescence microscopy (LSFM) to examine DCX^{+} populations originating from the SVZ. Consistent with our

short- and long-term IHC data, iDISCO/LSFM showed DCX^+ populations substantially increased in the dorsal SVZ and along the RMS upon Cre-mediated loss of Ezh2/H3K27me3 after 5 days (n=10) (Fig. 39B-D, 40A-E) while a moderate increase in DCX^+ cells was still detected in animals injected with Cre compared to vehicle (Fig. 39E-G, 40F-G) after 32 days post-injection (n=6). In addition, βIII-$Tubulin^+$ and $NeuN^+$ populations increased in the OB 10 days after loss of Ezh2/H3K27me3 (Fig. 41), as did the interneuron marker Calbindin (Fig. 42). To assess changes to behavior impacted by an increase in OB neurons, an olfaction test was utilized. Using an olfaction-based behavior assay, no difference was observed in *Ezh2*$^{flox/flox}$;*ROSA26* mice injected with Cre or vehicle into the SVZ at 19 and 46 days post-injection. Assessing potential striatal defects from SVZ originating cells following loss of Ezh2 in the SVZ, no difference was observed in a pole test in *Ezh2*$^{flox/flox}$;*ROSA26* mice injected with Cre or vehicle at 19 and 46 days post-injection. However, seizures in *Ezh2*$^{flox/flox}$;*ROSA26* mice were observed 46 days post-injection of Cre into the SVZ compared to vehicle injected controls.

The ubiquitous abundance and distribution of H3K27me3 among NSPCs within the SGZ/DG (Fig. 31) suggested distinct regulation by H3K27me3 in this adult neurogenic niche and compelled further investigation. We assessed the effect of loss of Ezh2/H3K27me3 at 19, 32, or 46 days after stereotaxic injection of Cre into the SGZ/DG, which corresponded to the times required for NSPC proliferation, differentiation/migration, and integration into neuronal circuit, respectively (Bond et al., 2015; Kempermann et al., 2015). In the SGZ/DG, we observed a notable increase in $NeuN^+$ (Fig. 43A-B) and a moderate increase in $Nestin^+$ cells but no change in $GFAP^+$ cells at 19 days post-Cre injection compared to vehicle injected controls (Fig. 44). Although the populations of DCX and βIII-Tubulin populations were not substantially changed 19 days after Cre injection (Fig. 45), unusual colocalization of DCX^+/$NeuN^+$ cells was observed in the Cre

injected SGZ/DG that was not evident in vehicle injected SGZ/DG 19 days after injections (Fig. 43C-F). Consistent with the 19 days immunohistochemistry data, flow cytometry analysis of SGZ/DG 32 days after Cre injection demonstrated an increase in DCX^+ NBs and substantial increase in $NeuN^+$ neurons (Fig. 46). Intriguingly, 46 days after Cre injection into SGZ/DG, $Nestin^+$ populations were substantially increased, while a moderate decrease in $NeuN^+$ neurons was detected compared to vehicle injected SGZ/DG (Fig. 47). Findings from three timepoints analyses suggest that regional loss of Ezh2/H3K27me3 in the adult SGZ/DG induced early differentiation at 19- and 32-day while $Nestin^+$ cells replenished NSPCs in response to declined $NeuN^+$ population at extended 46-day. Collectively, our results showed distinguishable cellular phenotypes, in which the DCX^+ population in the SVZ and the $NeuN^+$ population in the SGZ/DG were the most affected upon regional loss of Ezh2/H3K27me3.

Suv4-20h/H4K20me3 affects cell cycle of the adult NSPCs

Quiescent adult NSPCs divide very slowly during neurogenesis. The phenomenon of adult neurogenesis raises a fundamental question regarding epigenetic repression underlying the cell cycle of adult NSPCs. Importantly, our genomewide analyses with baboon NSPCs implicated H3K27me3 and H4K20me3 co-regulating a subclass of genes associated with cell cycle including contact growth inhibition (i.e., *SLC19A1*, *TTC5*), cell cycle progression (i.e., *ZIC1*, *MAP9*) and checkpoint control (i.e., *WNT9A*). Yet, a number of genes are independently enriched by either H3K27me3 (i.e., *CYP26B1*) or H4K20me3 (i.e., *MAP2K3*, *NRG1*, *DOT1L*), suggesting their unique role in cell cycle regulation. To assess the *in vivo* effect of cell cycle upon loss of Ezh2/H3K27me3 or Suv4-20h/H4K20me3, we used conditional knockouts of the enzymatic

domain (SET) essential for Ezh2 and Suv4-20h activity because germline deletion of *Ezh2* and *Suv4-20h1/ Suv4-20h2* is embryonically lethal (Schotta et al., 2008; O'Carroll et al., 2001).

Instead of knockout of a single subpopulation of SVZ cells, region-specific Cre injection provided a broad insight as to whether the H3K27me3 and H4K20me3 repressive marks are critical for cell cycle regulation within this neurogenic niche. Post–Cre injection on day 5, EdU and phosphorylated-histone H3 labeling was used to trace cell cycle at S phase and M phase, respectively. Loss of Ezh2 activity within the SVZ resulted in a moderate decrease in short-term DNA replication (S phase) (Figs. 48). Conversely loss of Suv4-20h activity dramatically decreased short-term DNA replication (S phase) (Fig. 49). Neither loss of Ezh2 nor Suv4-20h activity had a substantial effect on M phase (data not shown). These results suggest that both Ezh2/H3K27me3 and Suv4-20h/H4K20me3 are not dispensable in chromosome duplication during cell cycle of adult neurogenesis.

The marked change in EdU positive nuclei following Suv4-20h prompted us to examine cell cycle further. As Suv4-20h/H4K20me3 is canonically associated with cell cycle, we focused our investigation of cell cycle using *Suv4-20h*$^{flox/flox}$;*ROSA26* mice over long time periods. Also, empirical validation of thymidine analogs within the hippocampus led us to focus primarily on 12 hour EdU incorporation (Fig. 50), as opposed to the 2 hour EdU labeling used in the SVZ. Using the Cre protein approach, we assessed changes in NSPC populations and proliferation in *Suv4-20h*$^{flox/flox}$;*ROSA26* mice following Cre protein (experimental) or vehicle (control) injection into the SGZ/DG at the time-points described above. Forty six days post-Cre injection resulted in marginally increased numbers of total 5-ethynyl-2'-deoxyuridine (EdU) labeled cells following 12 hour post EdU injection (n=8) (Fig. 51A-5H). No significant changes were seen for M-phase cell cycle markers phospho-H3 Serine 10 (pH3-S10) or Rb protein with phosphorylated Serine 780 (p-

S780-Rb) at 46 days post Cre injection (Fig. 52). Additionally, 2 hour EdU labeling was not significantly different after 19 or 32 days post Cre injection (Fig. 53, 54).

In contrast to loss of Ezh2 activity, no significant change in cell type markers (i.e. $GFAP^+$, DCX^+, or $NeuN^+$ cells) was observed in subpopulations of NSPCs within the SGZ/DG 19 or 46 days after loss of Suv4-20h activity (Fig. 51I-L, 54, 55). Taken together, proliferation was consistently affected upon loss of Suv4-20h/H4K20me3 in the SGZ/DG and substantiate our previous findings that loss of Suv4-20h/H4K20me3 alters the S-phase of the cell cycle in the SVZ (Rhodes et al., 2016). Our results suggest an essential role for Suv4-20h/H4K20me3 in cell cycle regulation during adult neurogenesis. Further, the Cre protein based approach allowed us to monitor potential long-term phenotypes following reduction of Suv4-20h. Intriguingly, long-term knock-out of *Suv4-20h1* in the adult SVZ or *Ezh2* in the SGZ/DG resulted in instances of seizures over the one year post-treatment period (Data not shown).

CHAPTER FOUR: FIGURES AND TABLES

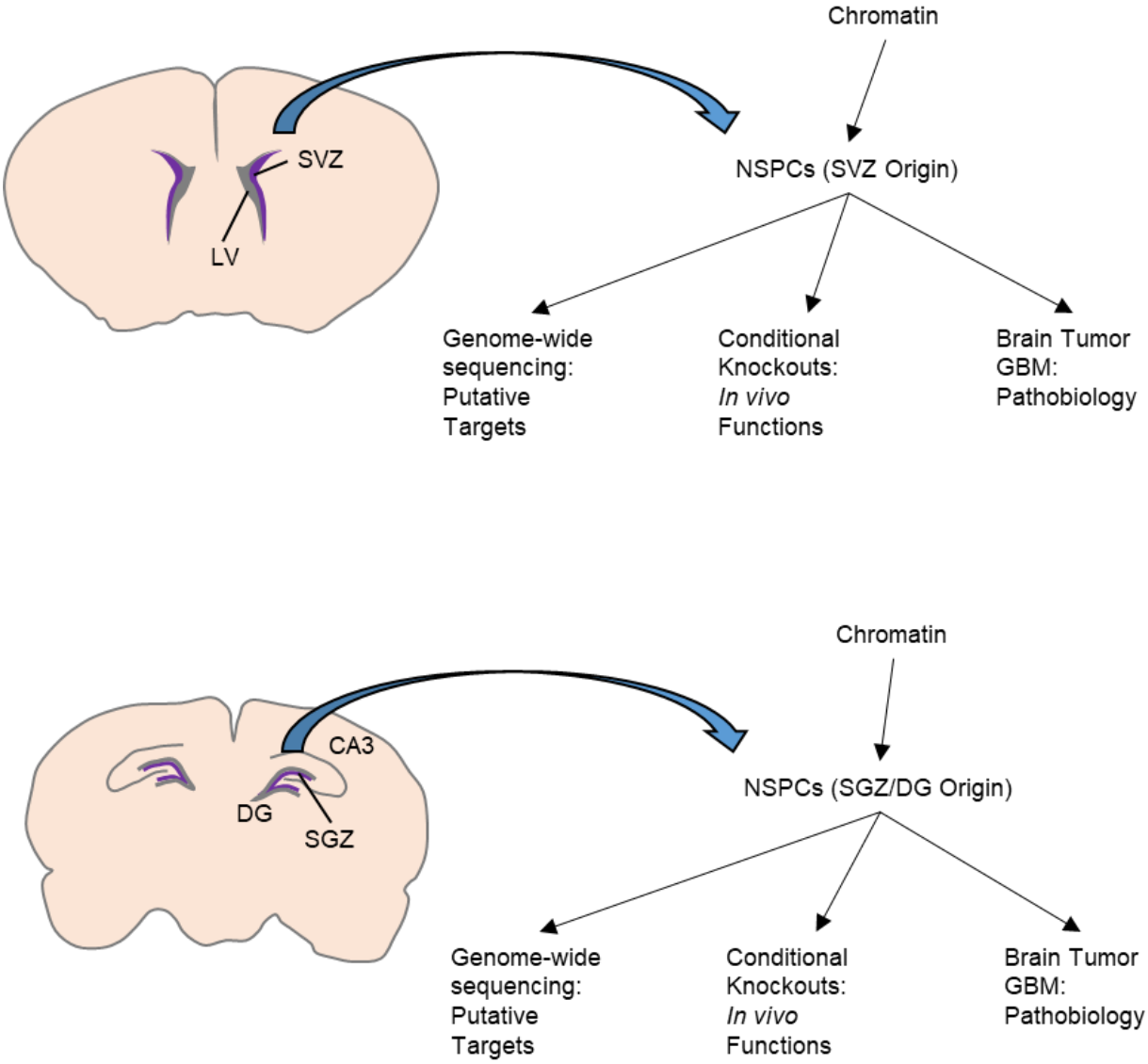

Figure 1. Project overview.
The chromatin state of neural stem progenitor cells within subventricular zone or subgranular zone of adult mouse, baboon, and human brains will be examined (only mouse brain displayed). Undifferentiated cells within baboon neurogenic niches are used for whole genome sequencing experiments. Conditional knockout mouse models will be used to manipulate genes encoding chromatin modification enzymes. Post-mortem specimens from unaffected humans and central nervous system tumor biopsies will be used to determine changes to epigenetic landscape in pathological states.

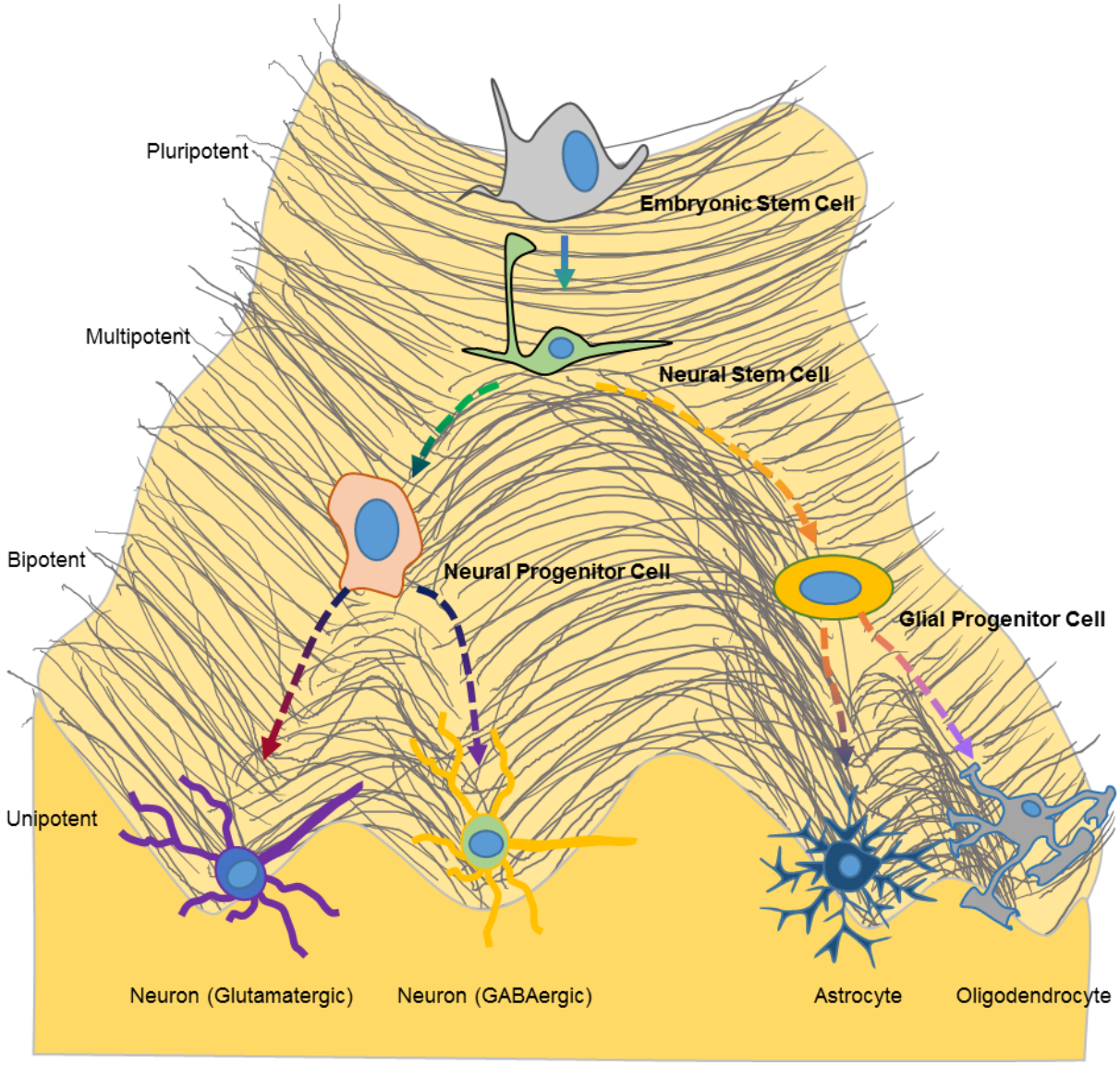

Figure 2. Cell fate determination in Waddington's landscape.

Waddington's landscape is a representation the process of a cell moving from a state of high cell fate capacity to a lineage restricted cell type with little or no cell fate capacity. The original concept of Waddington's landscape was a ball placed atop a hill and gravity only pulls the ball downward to the base of the hill. The ball represents a cell with many fate options. When the ball roll's down Waddington's landscape, it will progress down a specific valley. At this point, the ball is limited in the possible future paths it can take until reaching the base of a single valley. Cell fate can be represented on Waddington's landscape. Cells with high potency including multipotent embryonic stem cells and multipotent adult stem cells are the cell types nearest the top of Waddington's hill. When a cell comes to a point with more than one possible path (i.e. valley), the cell must make a cell fate decision. This results in progress down one path and a more differentiated cell that is slightly more lineage restricted and has less cell fate potential prior to the cell fate decision. Ultimately, cells reach an identity that is fundamentally limited to producing more to the same cell type, termed unipotent. Figure is from (Waddington, 1966).

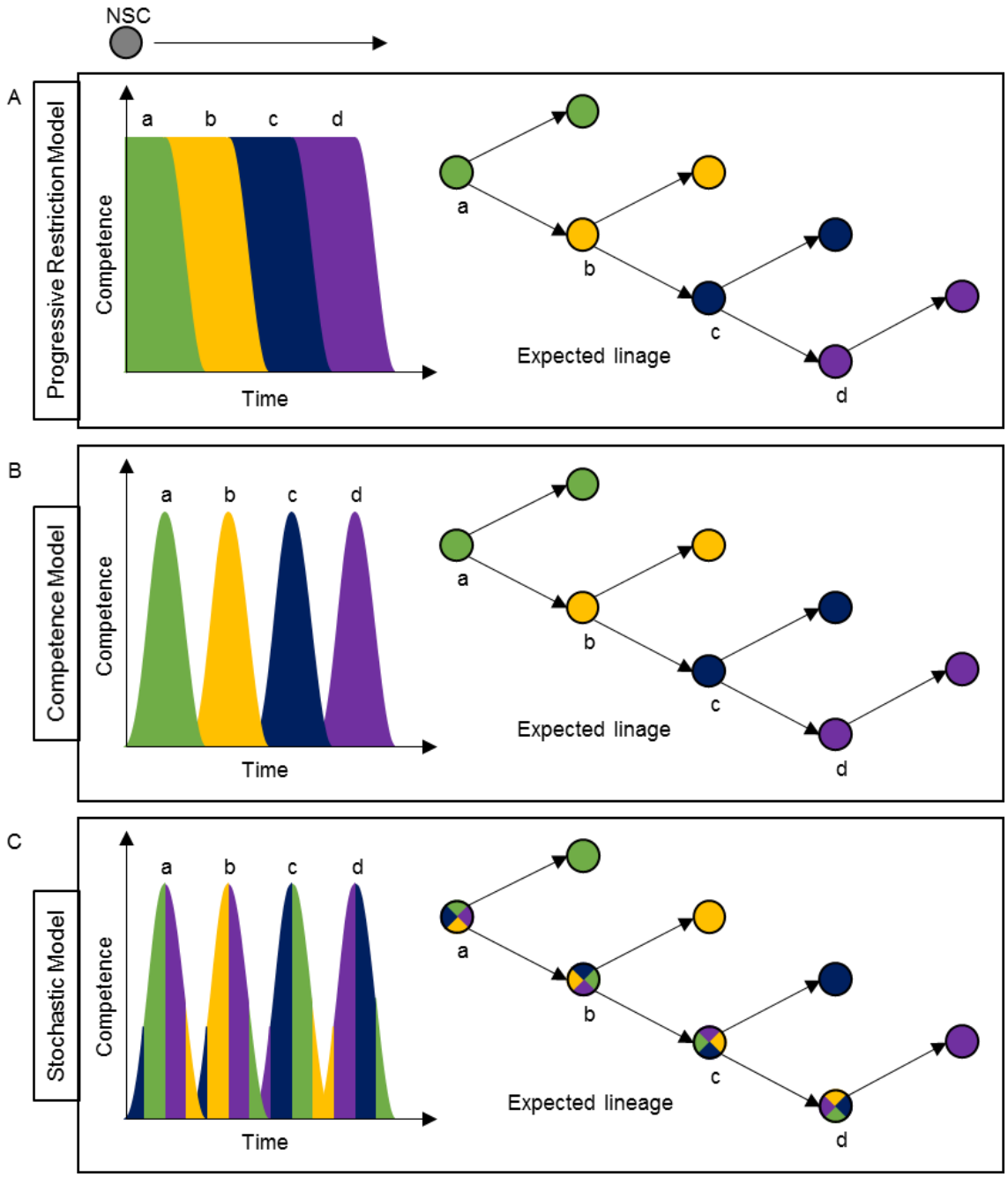

Figure 3. Models of cell fate determination.
Schema of the 3 major models proposed for cell fate in the central nervous system (CNS). (A) In the Progressive Restriction Model, the graph indicates the ability of a neural stem progenitor cells (NSPC) to generate a particular cell type (i.e. "Competence") with respect to developmental time (i.e. "Time"). NSPCs begin neurogenesis with the ability to generate all lineages. At each cell fate event, the progeny lose the ability to make earlier cell types. (B) In the Competence Model, any NSPC can produce myriad progeny lineages. However, a NSPC must first gain competence to produce a cell type, but also must lose any preexisting ability to produce other cell types. Such a model results in temporal regulation of cell lineages produced by NSPCs. (C) In the Stochastic Model, any NSPC can produce any progeny lineage at any given time. The exact lineage that progeny commit to is randomly chosen. Consequently, all lineages have a random probability of being generated at a cell fate event. In the left hand graph, this is denoted by many colors at each fate event, with each color representing a unique lineage to randomly choose from. Part (B) of figure is from (Livesey and Cepko, 2001).

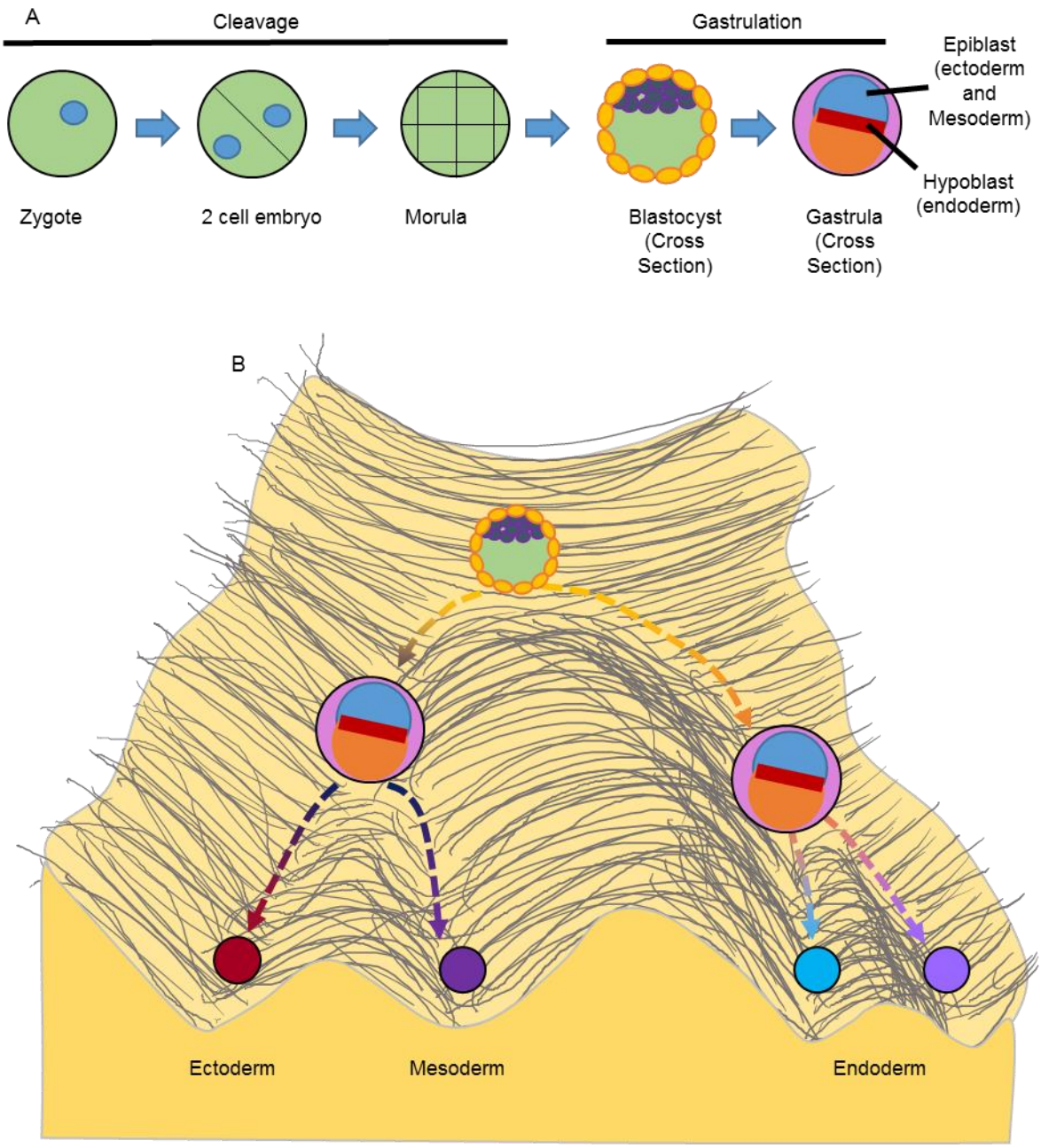

Figure 4. Cell fate during embryogenesis.
(A) Mammalian embryonic development. Oocyte fertilization results in a diploid zygote, which undergoes multiple cell divisions to generate a multicellular morula. During gastrulation, the blastocyst forms containing an inner cell mass (ICM) forms. Further development generates the gastrula which contains the three primordial germ layers that ultimately form all tissues and organs in the organism. (B) Cell fate during organismal development. In Waddington's landscape, the ICM contains pluripotent embryonic stem cells with high cell fate capacity. As cells proceed through cell fate events and form the primordial germ layers in the gastrula, cells become progressively lineage restricted with lower cell fate capacity. Ultimately, decreasing cell fate capacity locks a cell into a single lineage as a terminally differentiated cell type. Part (B) of figure from (Waddington, 1966).

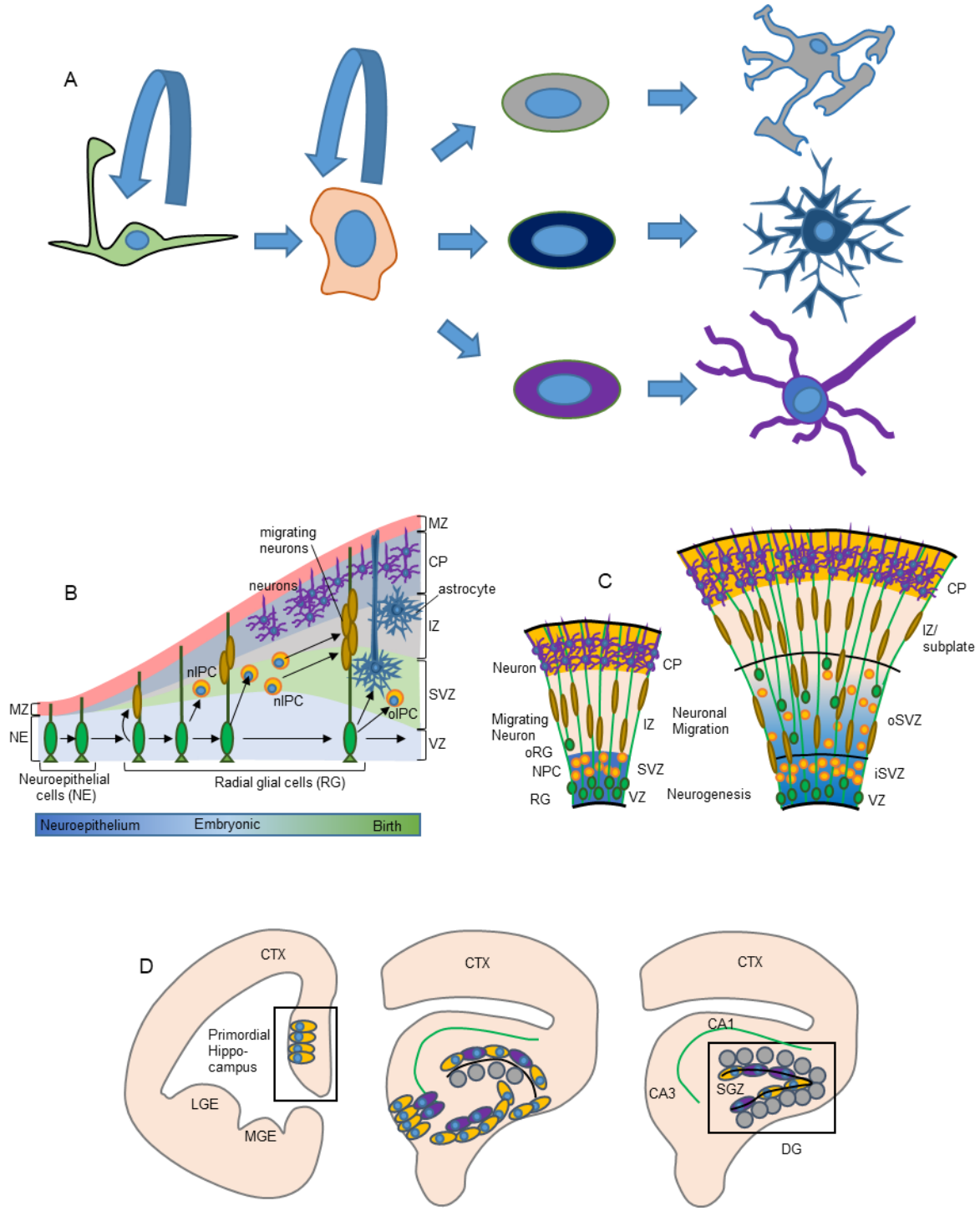

Figure 5. Neural stem cells and embryonic neurogenesis.
(A) Cell fate potential of adult neural stem cells. Neural stem cells are considered multipotent and can thus generate cell types in multiple lineages including neurons, oligodendrocytes, and astrocytes. In most depictions, a quiescent, multipotent stem cell becomes active, expands the population, generates lineage specific progenitor cells, and then terminally differentiated cell types. (B) Embryonic neurogenesis over time from a planar neuroepithelia to a more complex neurogenic niche. (C) Differences between rodent and human embryonic neurogenesis. (D) The subgranular zone of the dentate gyrus has a distinct developmental path compared to subventricular zone. Part (B) of figure from (Kriegstein and Alvarez-Buylla, 2009); part (C) of figure from (Bershteyn et al., 2017); part (D) of figure from (Yu et al., 2014).

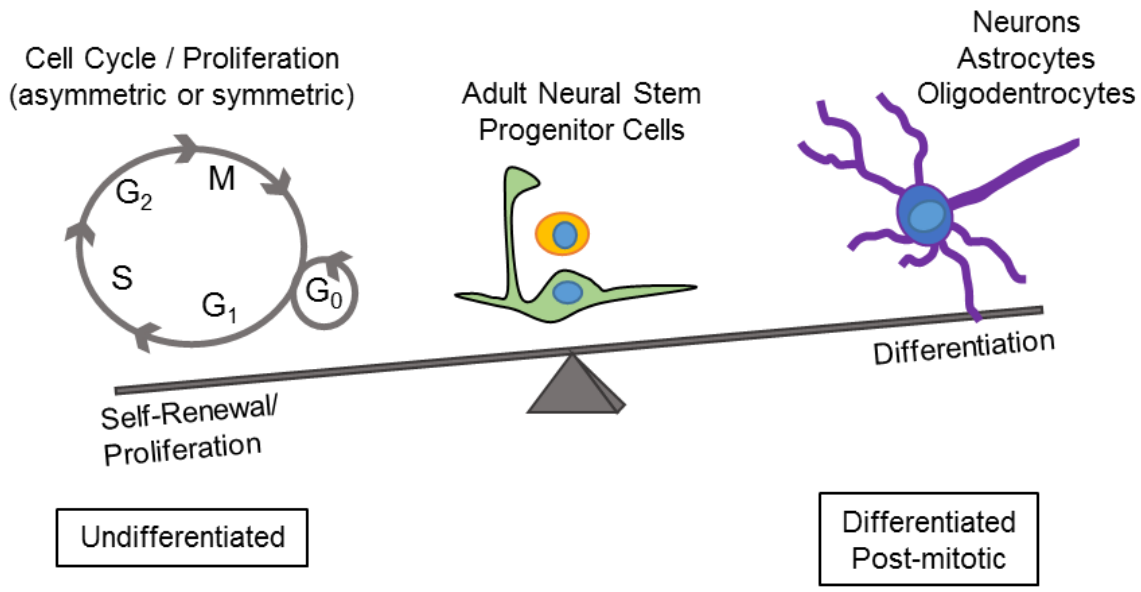

Figure 6. Neurogenic homeostasis.
Neurogenesis can broadly be represented as neural stem cells maintaining a delicate balance between an undifferentiated, proliferative stem cell state and a differentiated, non-proliferative neuronal state.

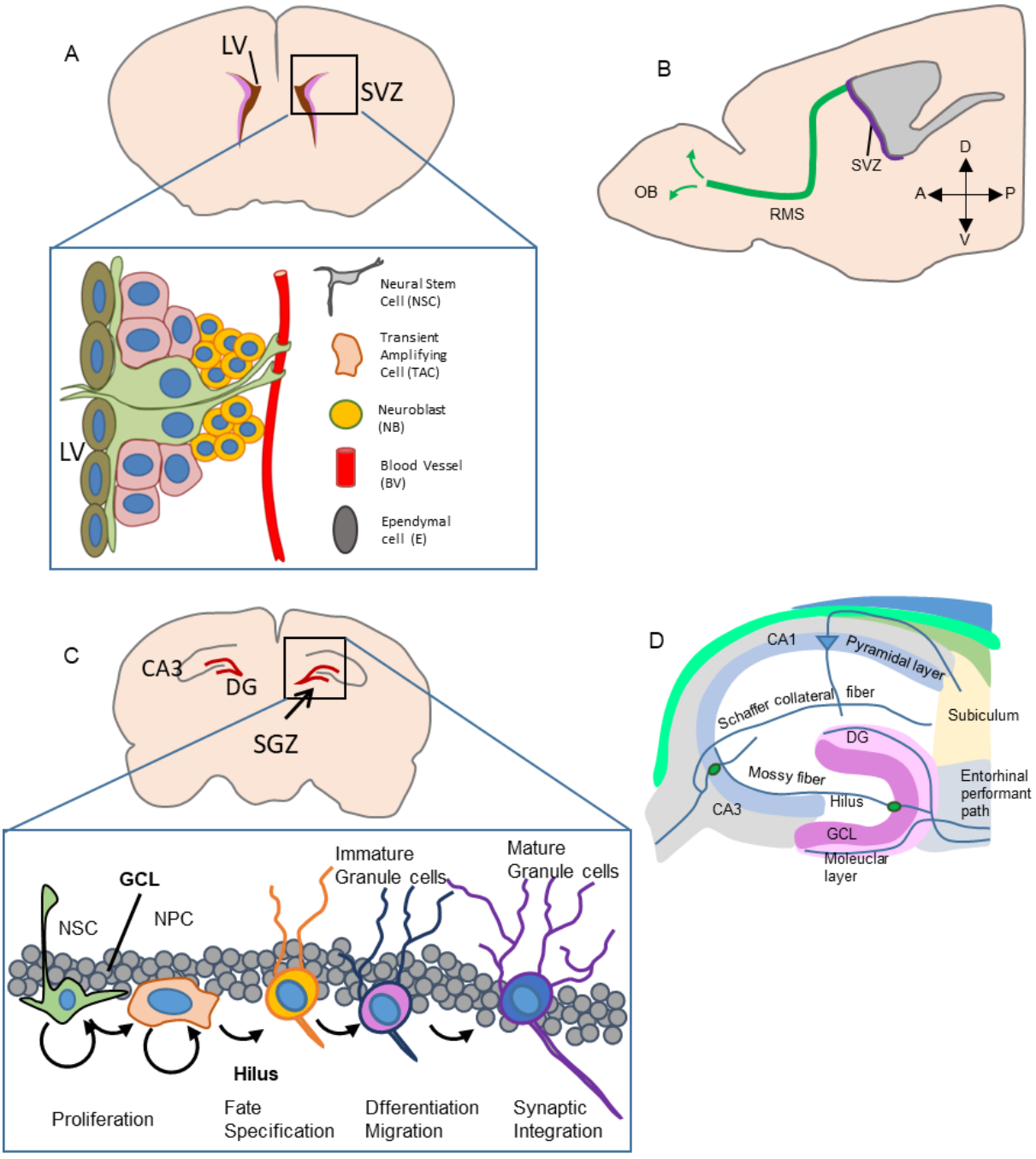

Figure 7. Adult neurogenic niches.

The two largest neurogenic niches within the adult mammalian brain are the subventricular zone (SVZ) adjacent to the lateral ventricle and the subgranular zone of the dentate gyrus (SGZ) Both niches are large, exhibit complex micro- and macroarchitecure, and contain a heterogeneous population of NSPCs and niche support cells. (A-B) The SVZ contains quiescent and active NSCs, neural progenitor cell called a neuroblast (NB), vasculature and a choroid plexus (not shown) (A). Mice also contain a transient amplyfiing population, which may exist in primates but reliable markers have yet to be established. NBs migrate out of the SVZ along the rostral migratory stream before integrating into the olfactory bulb in mice and humans. In humans, NBs of SVZ origin also migrate into the striatum. (C-D) The SGZ contains quiescent and active NSCs, neural progenitor cells, immature neurons and mature, integrated neurons in a thin layer between the hilus and granular cellular layer (GCL) (C). Mature neurons originating in the SGZ migrate into the GCL before integrating into the trisynaptic circuit of the hippocampus. (D). Parts (A, B, D) of figure is from (Ming and Song, 2011).

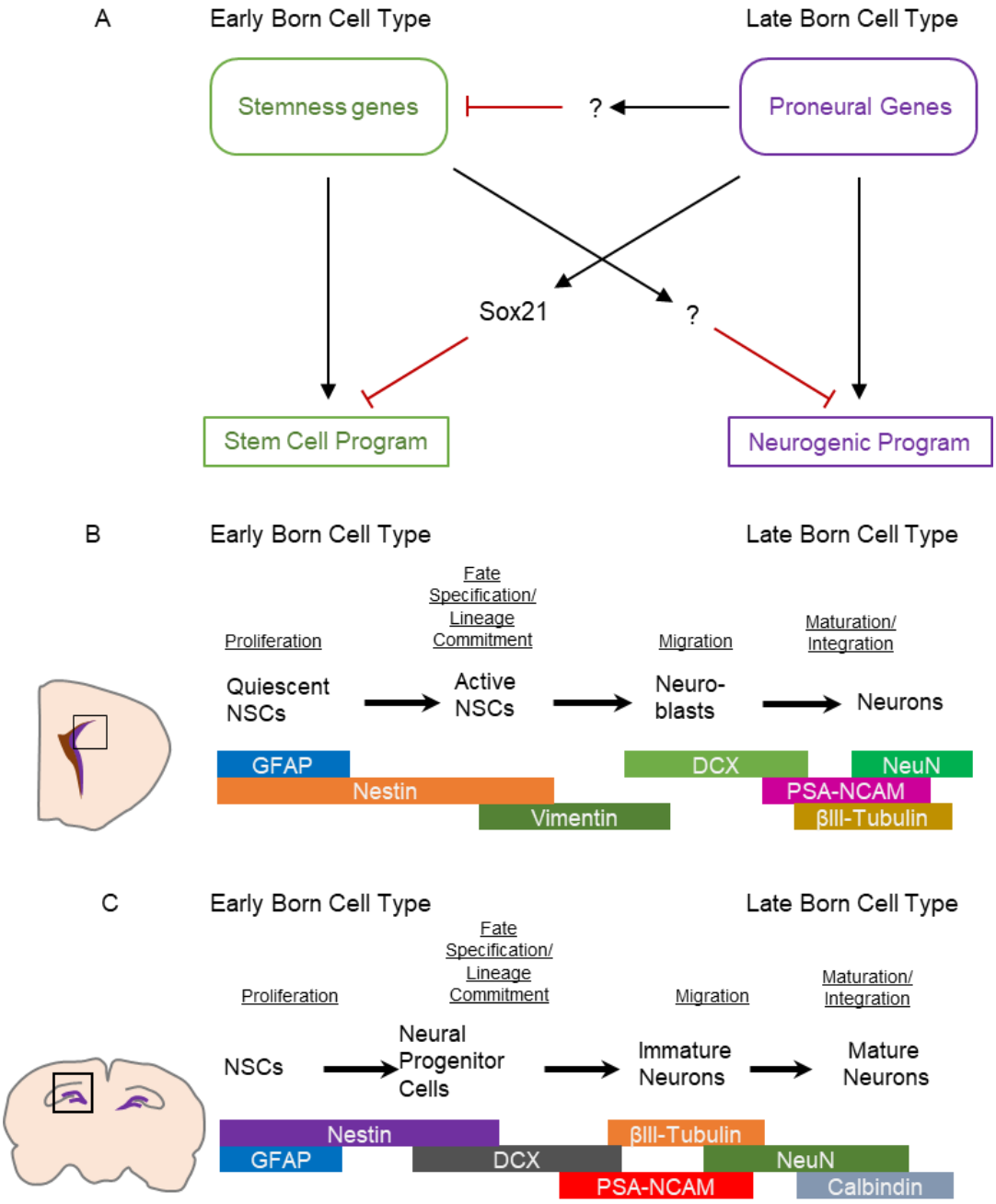

Figure 8. Stepwise differentiation.
(A) Prior to cell fate specification, NSCs express stemness genes which keep the cells retrained in an undifferentiated stem cell state. Expression of the stemness genes may inhibit genes involved in lineage commitment and differentiation. When a NSC receives an appropriate signal, stemness genes are inhibited while genes promoting commitment into the neuronal lineage are expressed. The genes responsible for cells differentiating into neurons have a feedback inhibition effect, thereby preventing cells from regressing back to a stem cell state. (B-C) While the balance between a stem cell state and a neuronal state are often simplified to either a stem cell program or a neurogeneic program as in (A), differentiation typically involves sequential progression through several distinct cell states. Each cell state is correlated with a unique combination of cell type specific markers and gene expression patterns. Stepwise progression through each cell state ultimately resulting in integrated neurons. Several important cell type specific markers are found in both the SVZ (B) and SGZ (C). Part (A) of figure from (Guillemot, 2007); part (B) of figure from (Ming and Song, 2011); part (C) of figure partially adapted from (Kempermann et al., 2004; Ming and Song, 2011; Schouten et al., 2012).

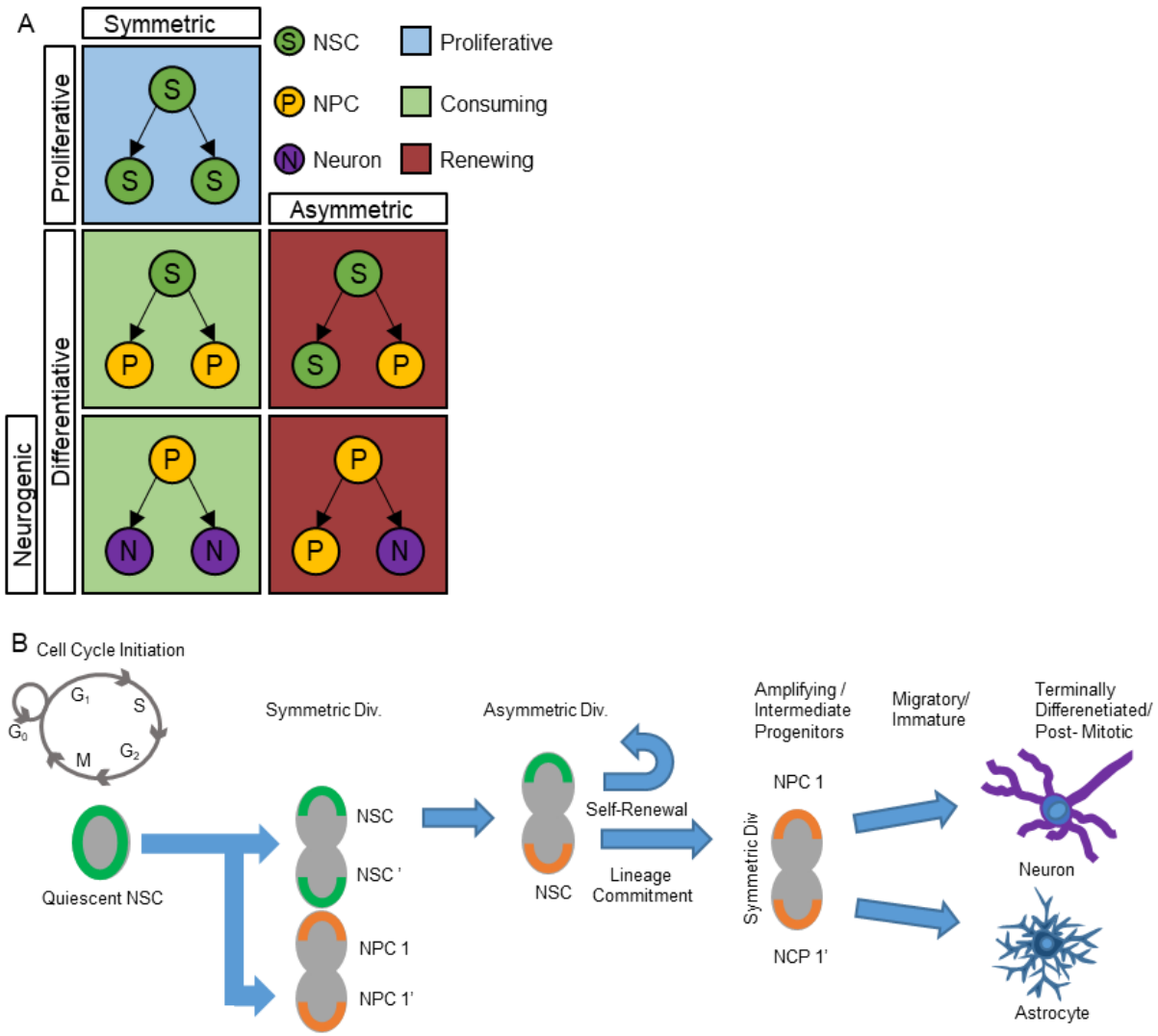

Figure 9. Self-renewal, proliferation and differentiation by cell division.
(A) Neurogenesis involves 3 common cell division strategies. NSPCs can divide to generate two daughter cells identical in cell state and epigenetic profiles to the mother cell or two daughter cells dissimilar from the mother cell state. Additionally, NSCs can perform asymmetric division in which one daughter cell retains the cell state and epigenetic landscape of the mother, and the second daughter cell is immediately distinct from the mother cell. (B) Neurogenesis typically involves all three forms of cell division. The quiescent NSCs (very slowly dividing) become mitotically active and undergo either proliferative or asymmetric cell divisions. As stepwise differentiation proceeds, cells will either undergo differentiative cell division, or directly differentiate into a terminal cell type without cell divisions (not shown). Part (A) of figure from (Florio and Huttner, 2014).

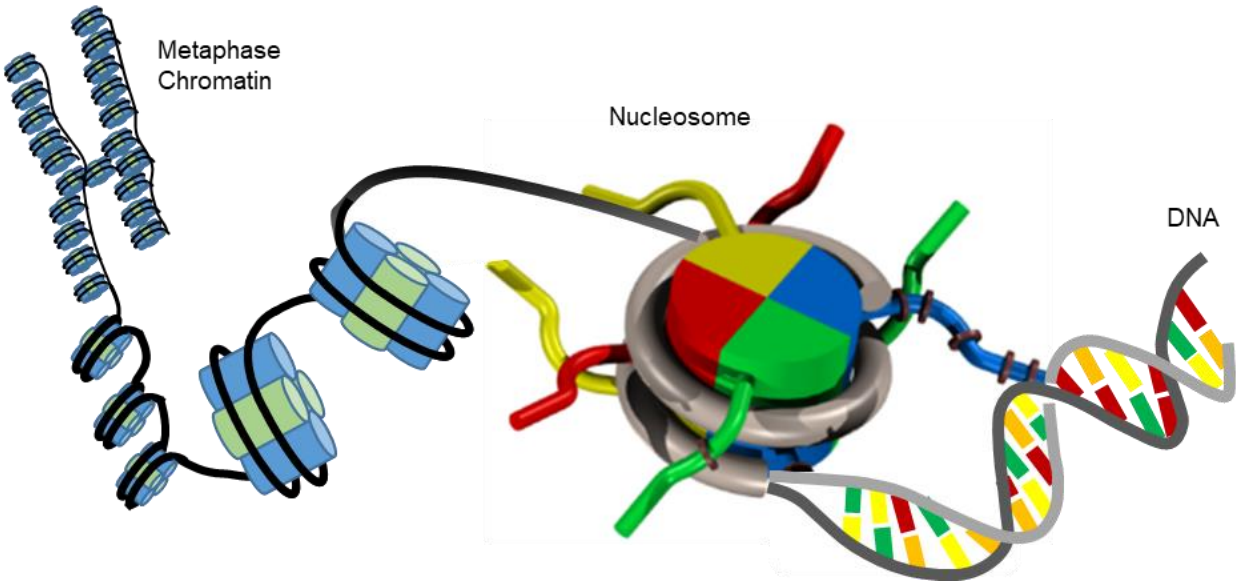

Figure 10. Chromatin and epigenetic modifiers.
Chromatin is genomic DNA and associated proteins, including histone core proteins that form the nucleosome and scaffold proteins which establish higher-order chromatin structure, including metaphase chromosomes and topological domains (not shown).

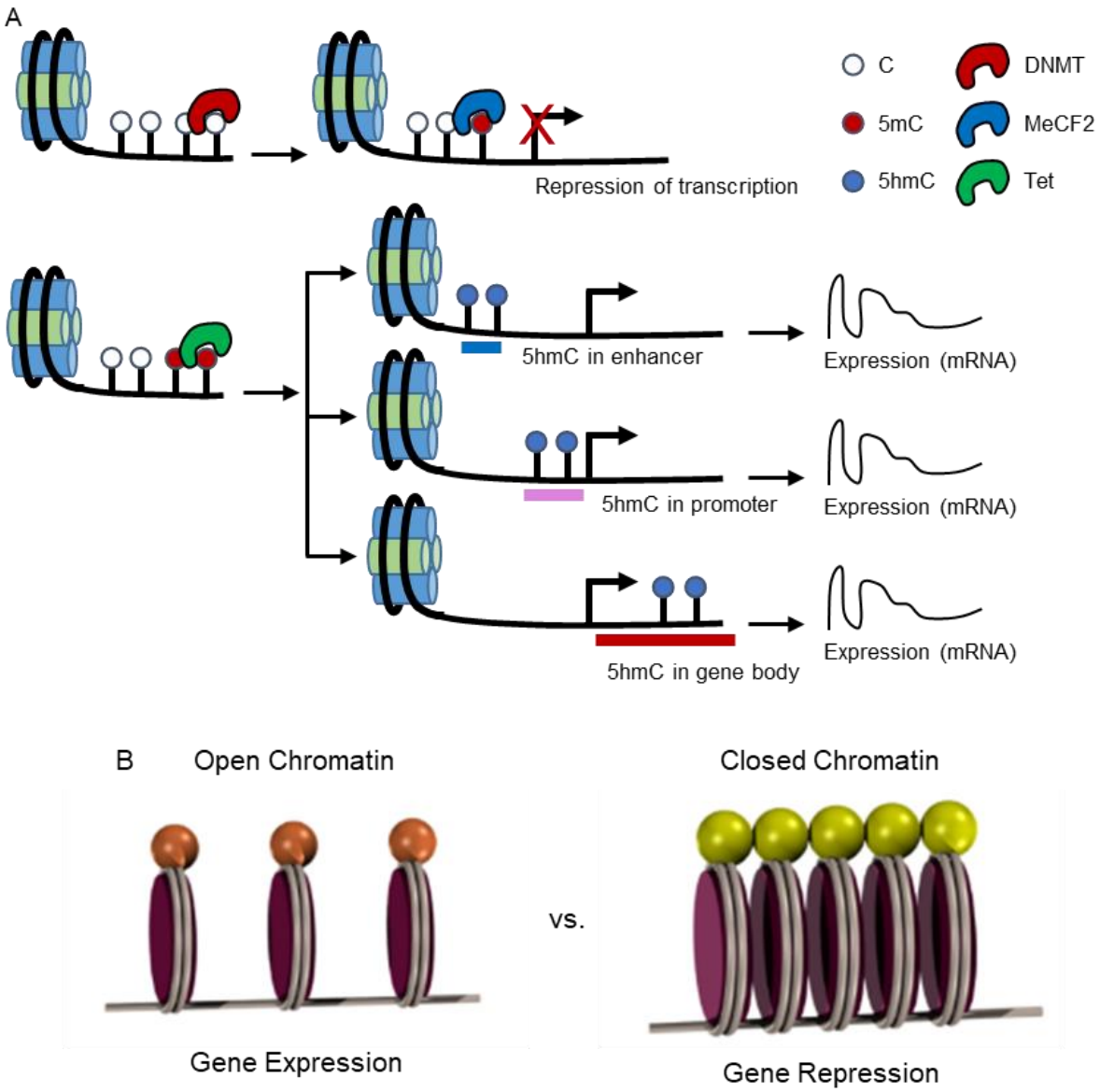

Figure 11. Epigenetic mechanisms.
Two of the primary epigenetic mechanisms involve altering chromatin structure. (A) DNA methylation (DNAme) involves adding a methyl group to DNA. This modification can be repressive (i.e. inhibit gene transcription) or activating (i.e. promote gene expression) depending on the local of the modification with respect to gene regulatory sequences and the gene body. (B) Histone modifications involve addition or removal of various chemical groups (orange or yellow spheres) to specific positions on the amino acid tails of histone core proteins (histone cores: purple disks). The effect of the histone modification is dependent on the type of chemical group transferred, which histone protein was modified, and amino acid position on the histone tail that was altered. If the net electrochemical charge of nucleosomes is repulsive, nucleosome density will decrease leading to a structure termed open chromatin. Open chromatin is canonically associated with gene expression. Conversely, attractive forces between nucleosomes can increase nucleosome packing and result in closed chromatin. Closed chromatin is canonically inhibits gene expression by preventing transcriptional proteins accessing promoters and other regulatory elements. Part (A) of figure from (Sun et al., 2014).

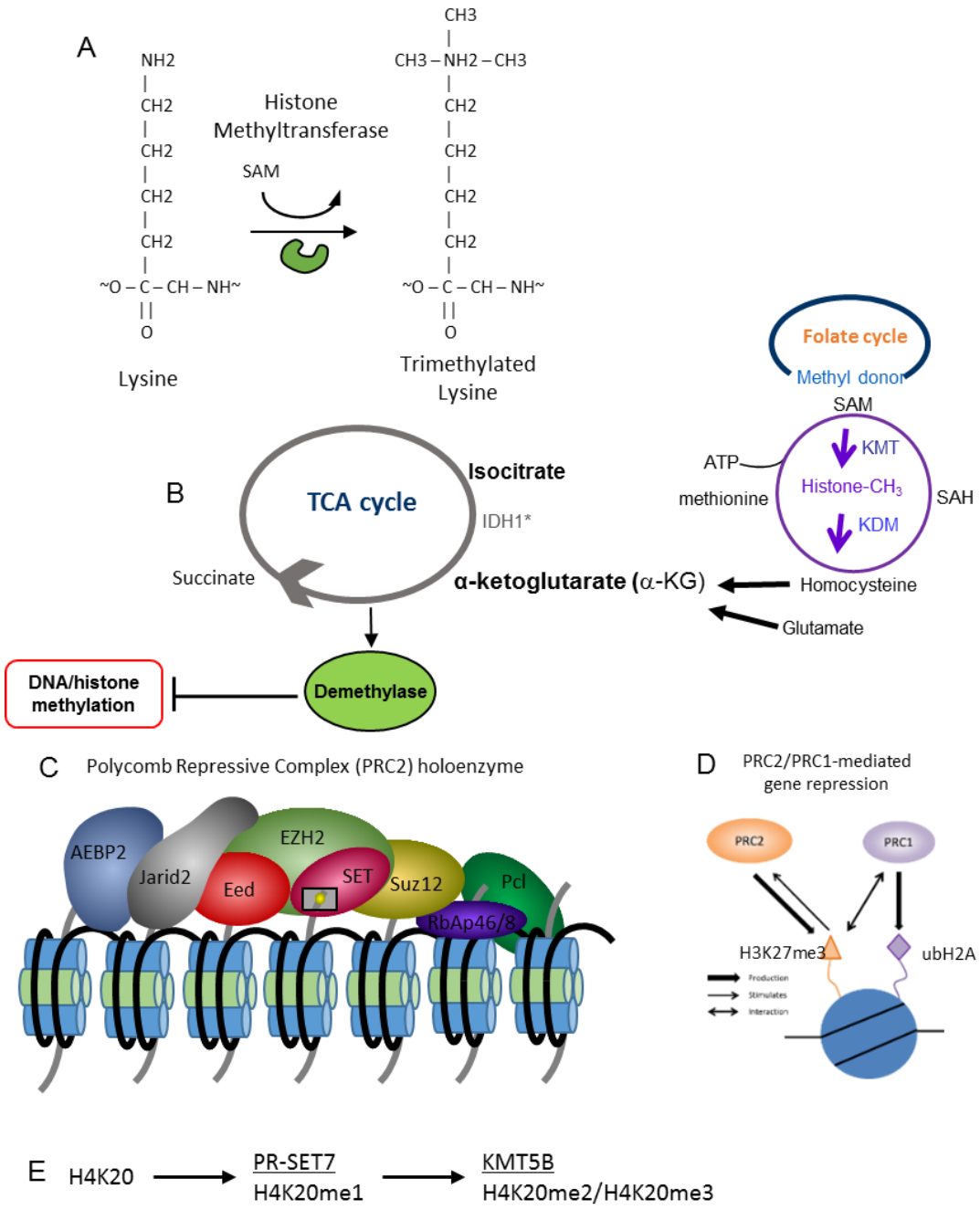

Figure 12. Influence of metabolic pathways on histone modifications.
(A) Mechanism for methylation of a lysine amino acid side chain during histone modification. During the reaction histone methyltransferase will catalyze the transfer of a methyl group from S-adenosyl methionine (methyl donor) to a lysine (methyl acceptor). (B) Schematic of several biochemical pathways relevant to epigenetic regulation. Transfer of methyl groups commonly involves the folate cycle and the TCA cycle. (C) EZH2 enzyme (mouse: Ezh2) is part of a larger complex called the polycomb repressive complex 2 (PRC2). EZH2 like all histone methyl transferases contains a SET domain as a catalytic center which catalyzes transfer of a third methyl group to histone 3 lysine 27 (H3K27me3). (D) Epigenetic regulation, including EZH2-PRC2 mediated repression, typically involve serval coordinated steps by different chromatin modification enzymes before achieving a final epigenetic state. (E) KMT5B (mouse: Suv4-20h1) mediates addition of a third methyl group to histone 4 lysine 27 (H4K20me3) within the mammalian brain. As with H3K27me3 repression, H4K20me3 chromatin repression requires multiple modifications performed sequentially by different histone modification enzymes. Part (C) of figure from (Margueron and Reinberg, 2011).

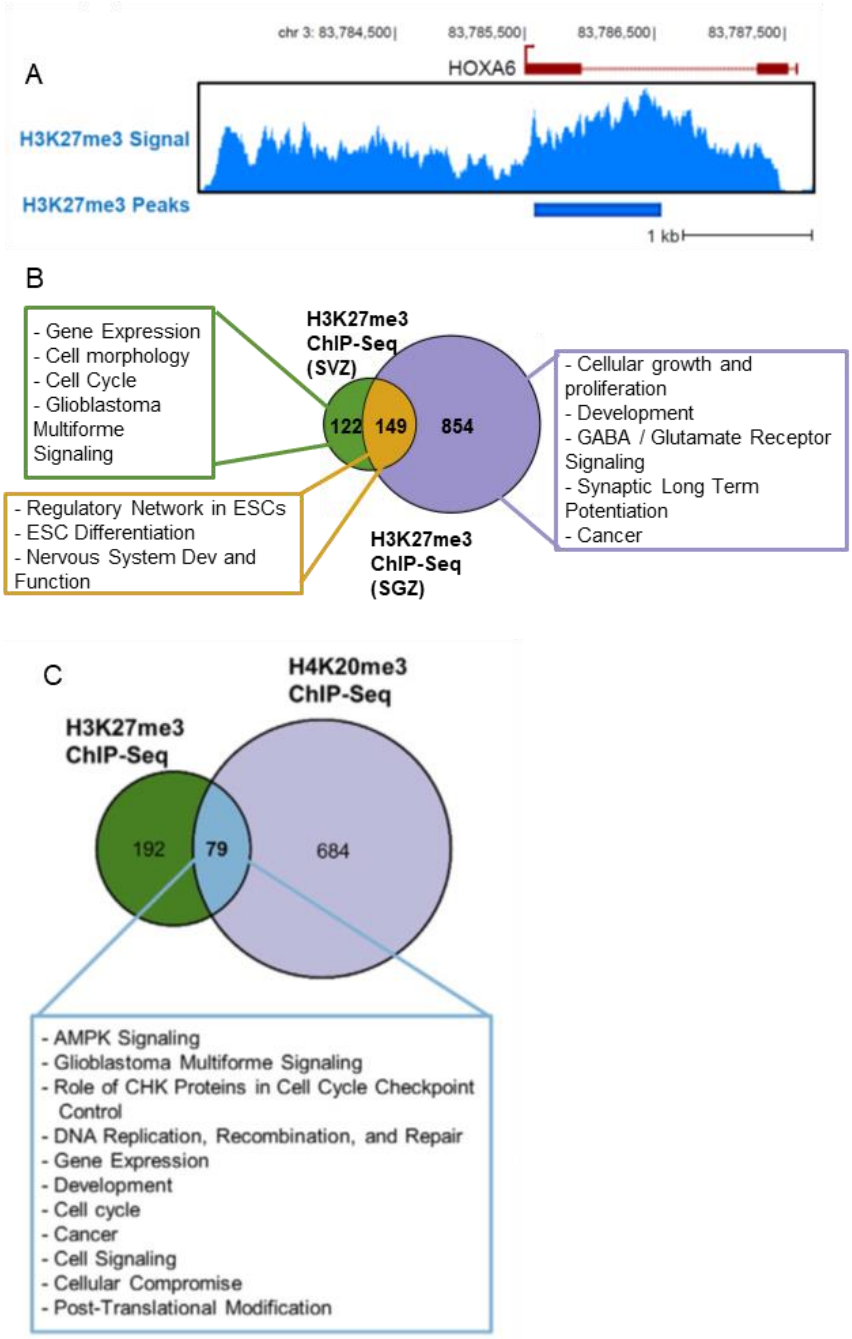

Figure 13. The role of H3K27me3 in adult neurogenesis.
(A) H3K27me3 is established as being abundant in gene bodies where it is correlated with repressing gene expression via competitive exclusion of transcriptional enzymes. (B) The function of genes enriched by H3K27me3 in both the SVZ and SGZ include stem cell differentiation and nervous system development. As H3K27me3 is repressive, such biological processes are expected to be repressed by H3K27me3 enrichment within NSPCs. (C) Different histone modifications can co-regulate biological functions. For instance, H3K27me3 and H4K20me3 target a common set of genes within the SVZ with functions that include cell cycle.

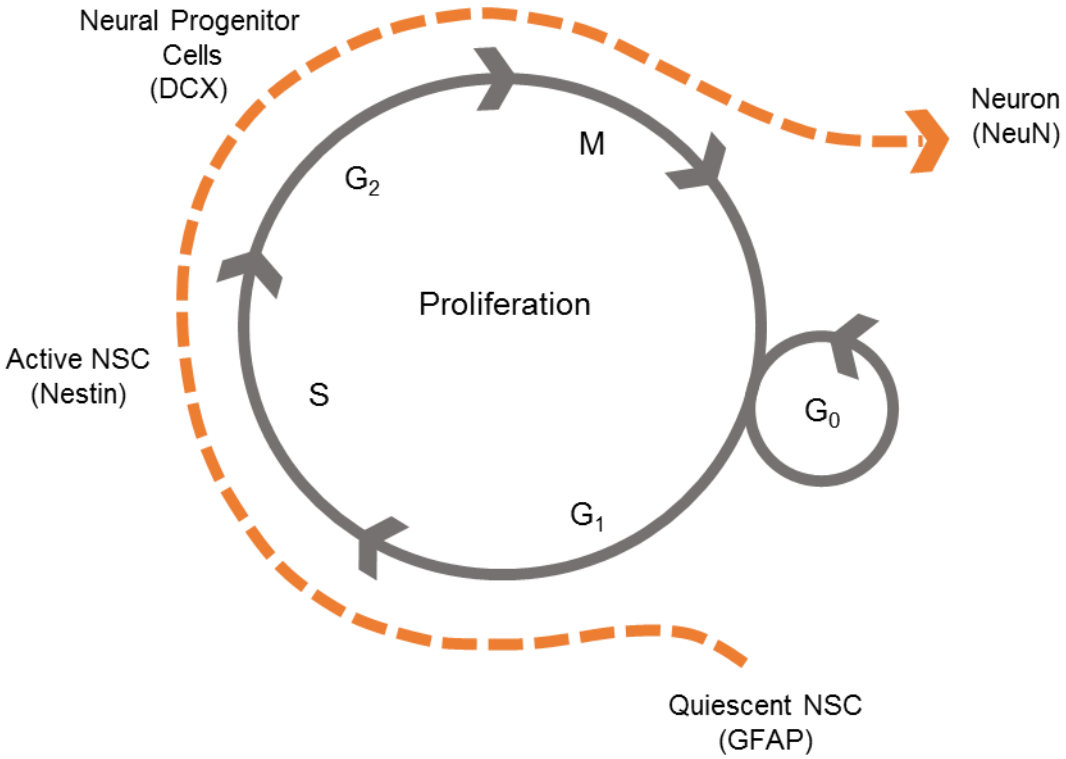

Figure 14. Neurogenesis as a function of cell cycle.
Neurogenesis is often represented by as a balance between proliferative NSCs and differentiating neurons. However, neurogenesis can also be represented as an extension of cell divisions. In such a scenario, NSPCs can be placed within the cell cycle diagram based on how proliferative the population tends to be. GFAP NSCs seldom divide and can be viewed as a "pre-mitotic" population. Active NSCs and NPCs are proliferative and undergo many cell divisions and can be placed within the cell cycle. Neurons do not normally initiate cell cycle and can be thought of as exited the cell cycle (post-mitotic).

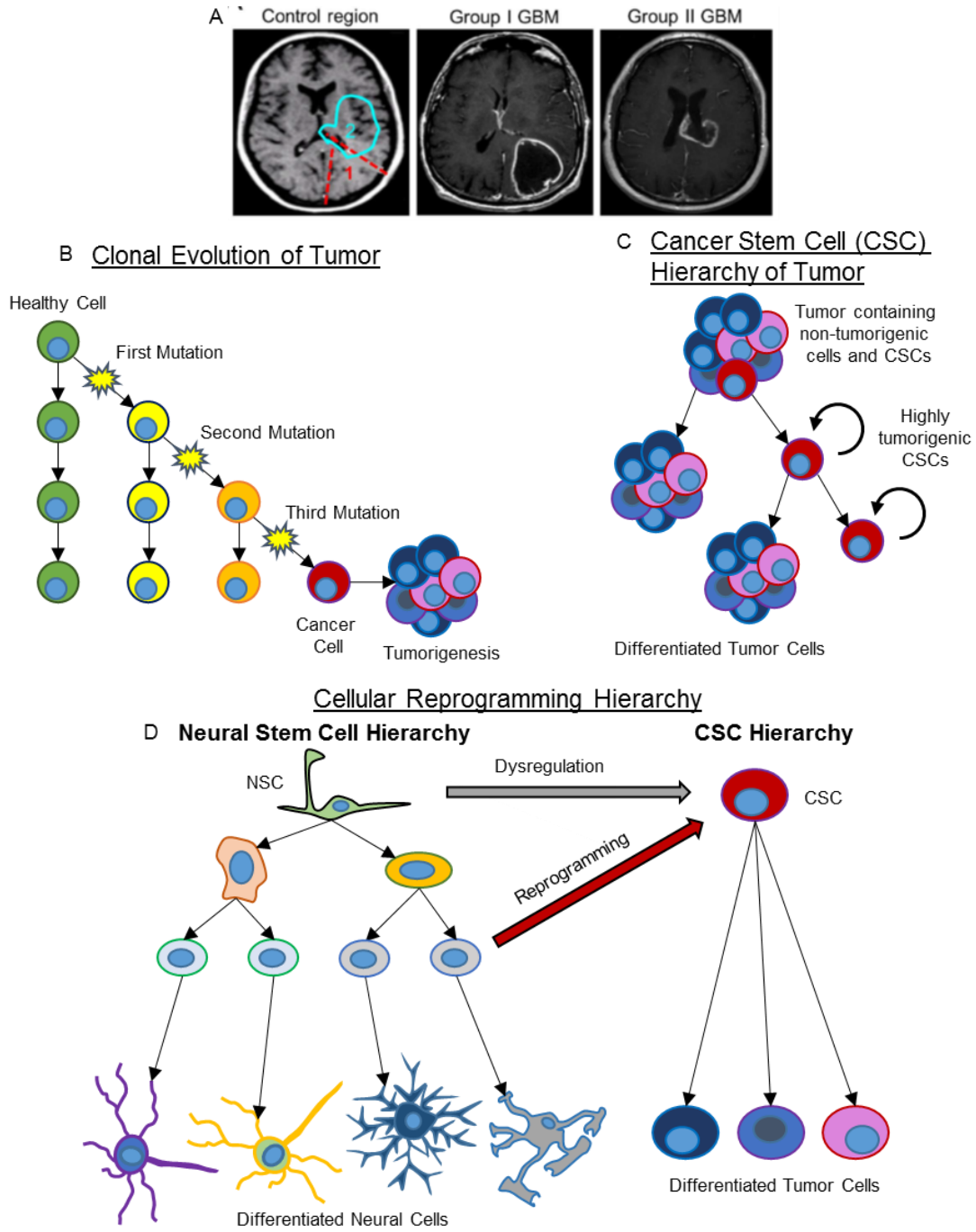

Figure 15. Models of central nervous system tumorigenesis.
(A) Representative MRI images of patients with healthy brain or containing GBM tumor. (B) Clonal evolution of central nervous system (CNS) tumors posits multiple genomic insults which ultimately generate an immortalized tumorigenic cancer cell. (C) The Cancer Stem Cell (CSC) model of CNS tumorigenesis involves dysregulation of endogenous NSCs to create CSCs. As NSCs can self-renew, any resulting CSCs are immortalized and can give rise to multiple lineages that constitute the bulk of a tumor. Such CSCs are suspected to be slowly dividing, and therefore a difficult target of current chemotherapeutics, resulting in high recurrence. (D) The cellular reprogramming model posits that a reprogramming event occurs within neural progenitors or neurons. The process is thought to be similar to reprogramming cells into induced pluripotent stem cells using Yamanaka factors. Once a cell is reprogrammed into a CSC, it can proceed down the CSC hierarchy proposed in the cancer stem cell theory of tumors. Parts (B, C) of figure from (Bradshaw et al., 2016); part (D) of figure from (Mack et al., 2016).

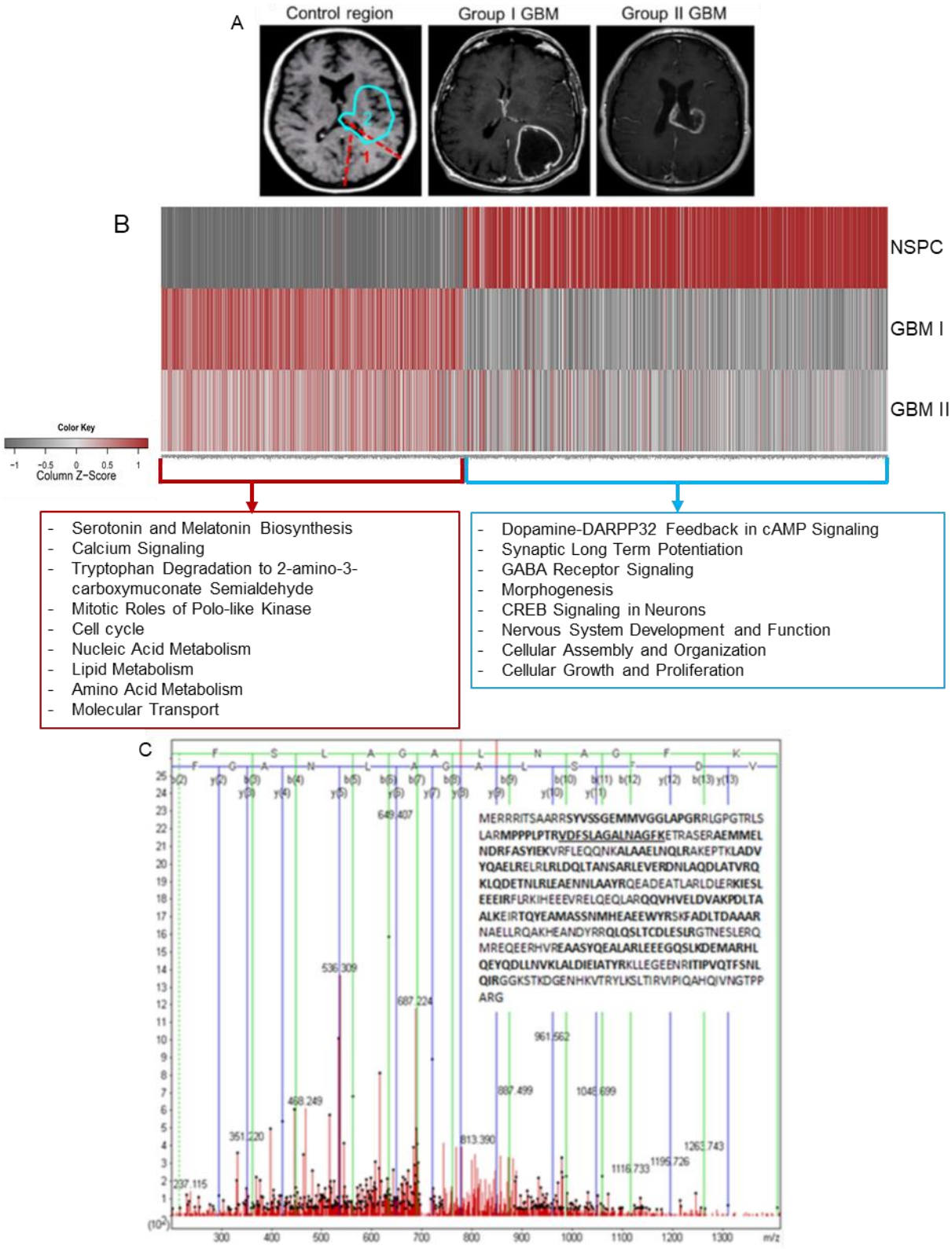

Figure 16. Neural stem cell – glioblastoma connections
(A) Representative MRI images of patients with healthy brain or containing GBM tumor. (B) Transcriptional profiles of differentially expressed genes in endogenous NSPCs and SVZ-associated GBM specimens. (C) Proteomic profiling of GBM specimens reveals the abundance of NSPC cell type markers.

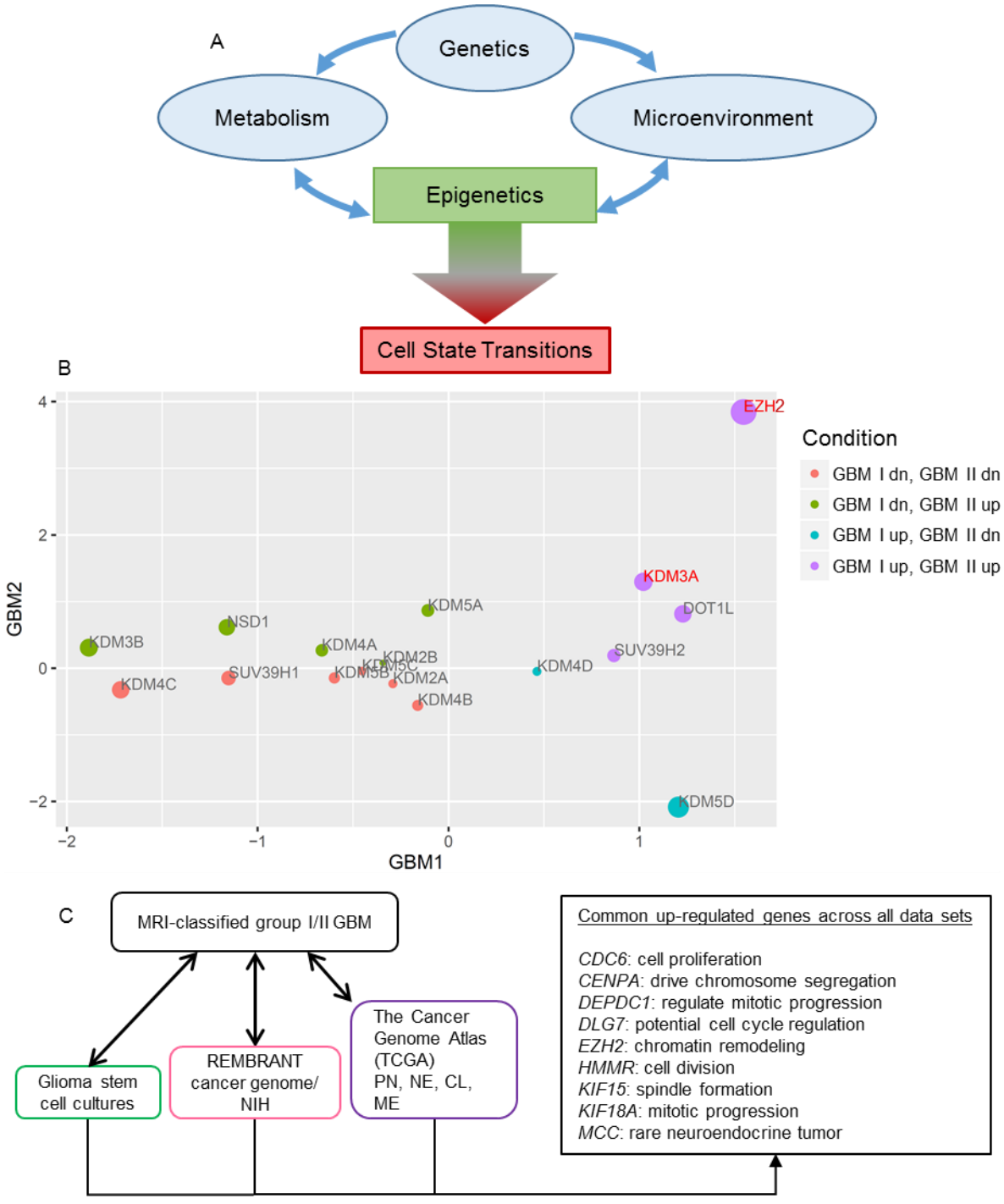

Figure 17. The epigenetic gateway to brain cancer.
Many intrinsic and extrinsic factors coalesce at the epigenome, including genetic components, local and organism-wide metabolic state, microenvironment cues and external factors from an organisms environment. (B) Differential expression of chromatin modification enzymes detected in multiple SVZ-associated GBM specimens. Genes that are differentially regulated (2 fold increase or decrease) across multiple specimens are labeled with red text. Diameter indicates relative variance of a given gene across samples. (C) Comparison of specimens analyzed in Lin lab with all samples reported in REMBRANT and The Cancer Genome Atlas datasets revealed 9 genes are universally amplified in all reported cases of GBM. Part (A) of figure from (Mack et al., 2016).

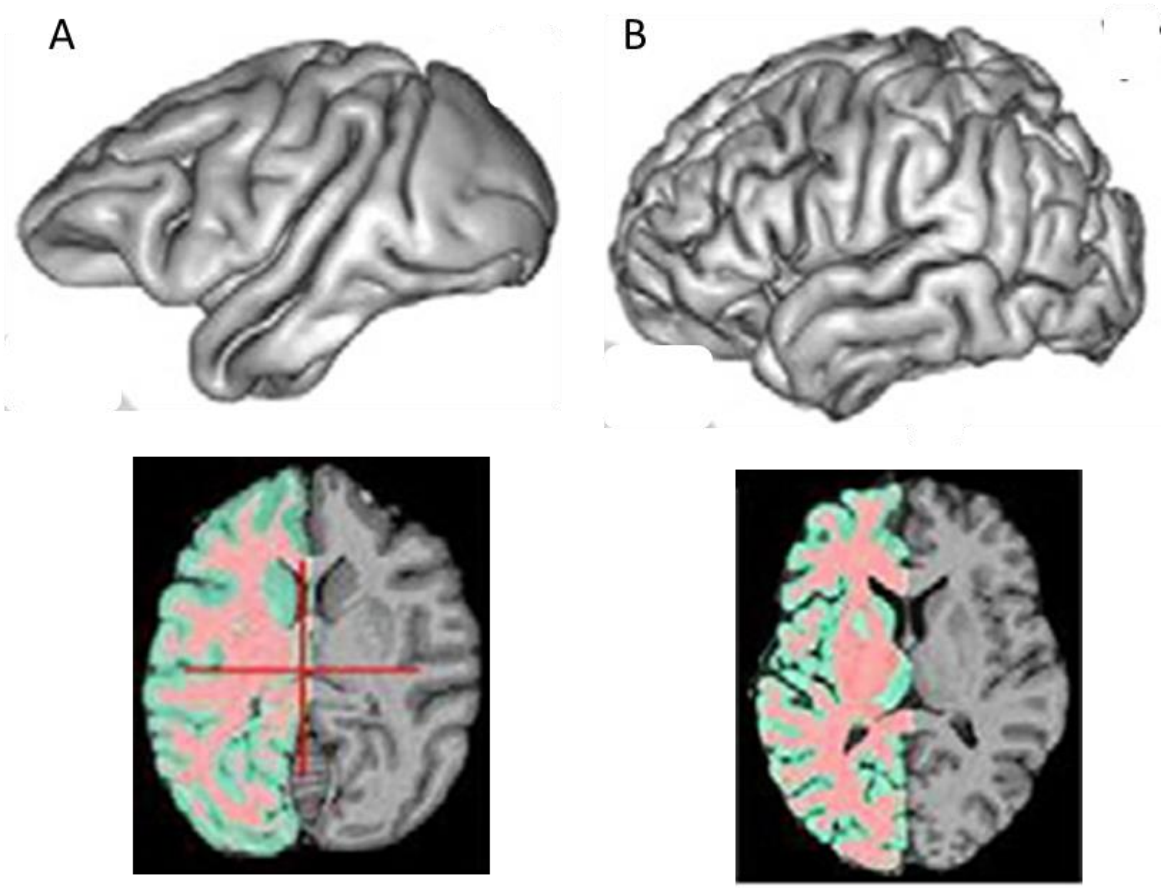

Figure 18. Species considerations for neurogenic studies.
The nature of a neuroscience experiment should be guided, at least in part, by the features of interest. Significant cortical folding is normally present in non-primate (baboon) brains (A) and human (B). Horizontal plane magnetic resonance imaging of respective species is shown below 3D volumetric renderings. Additionally, brain volume, microarchitecture and genomic sequence are more conserved between humans and non-human primates than rodent brains (not shown).

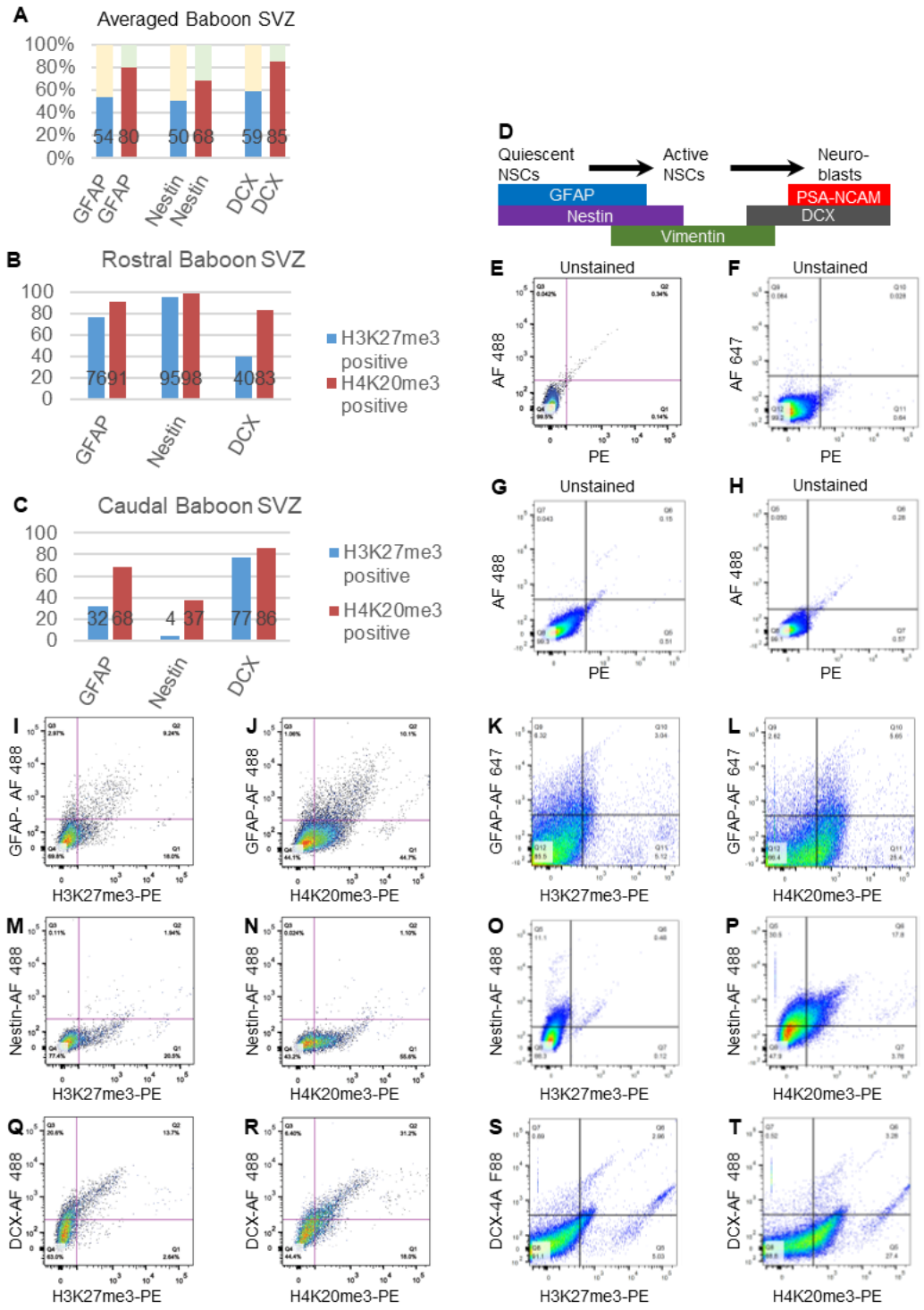

Figure 19. Quantification of H3K27me3 or H4K20me3 colocalization with cell type markers in baboon SVZ by flow cytometry.

(A-C) Bar graphs display H3K27me3 or H4K20me3 in SVZ subpopulations across entire niche (A), within rostral SVZ (B) and caudal SVZ (C). (D) Scheme dictates cell type–specific markers expressed in NSPCs in the SVZ. (E-H) Scatterplots of whole unstained cells isolated from rostral baboon SVZ (E, F) or caudal SVZ (G, H). (I-L) GFAP and H3K27me3 or H4K20me3 labeled cells of the rostral (I, J) or caudal baboon SVZ (K, L). (M-P) Nestin and H3K27me3 or H4K20me3 labeled cells of the rostral (M, N) or caudal baboon SVZ (O, P). (Q-T) DCX and H3K27me3 or H4K20me3 labeled cells of the rostral (Q, R) or caudal baboon SVZ (S, T).

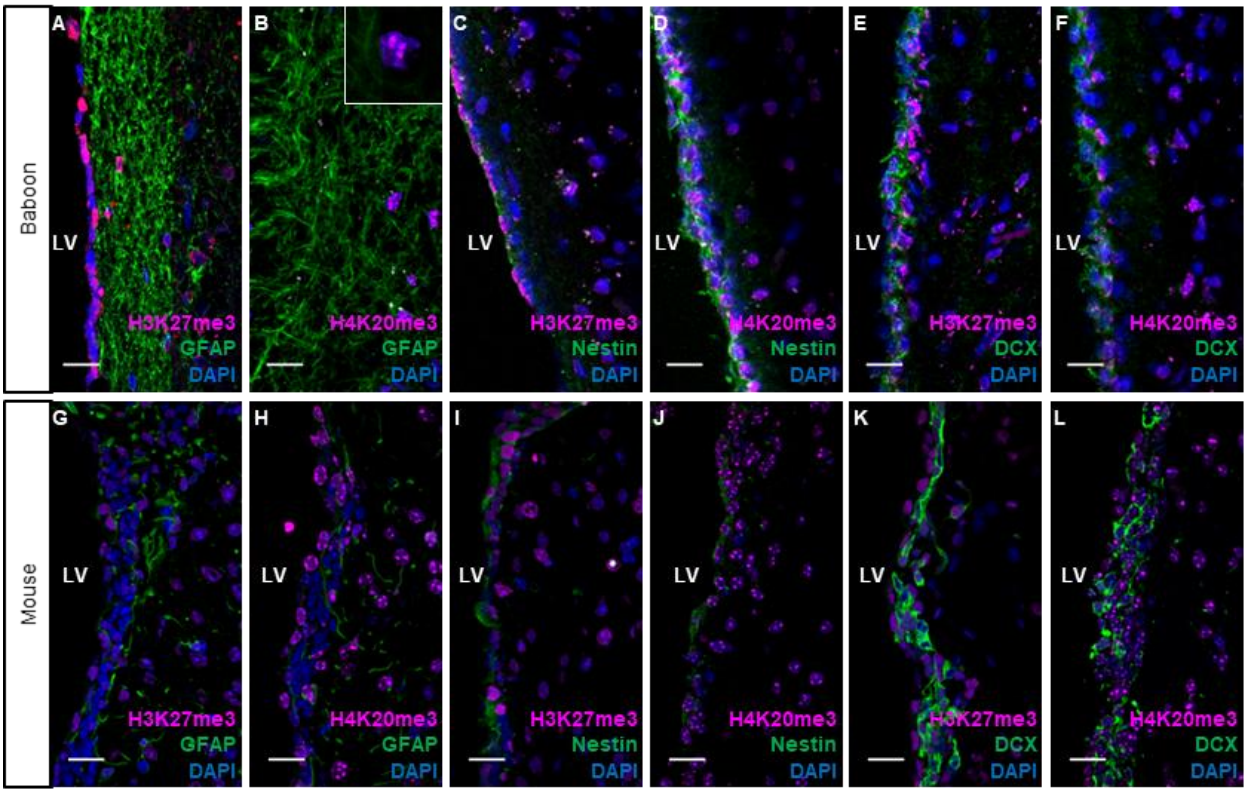

Figure 20. H3K27me3 and H4K20me3 distributions across SVZ subpopulations.
Co-immunostaining of H3K27me3 or H4K20me3 with cell type–specific markers GFAP, nestin, and DCX. Left panel presents coronal section of baboon brain, and right panel presents coronal section of mouse brain. 40X magnification; scale bar=20 μm. Inset shows 100X of H4K20me3 staining pattern.

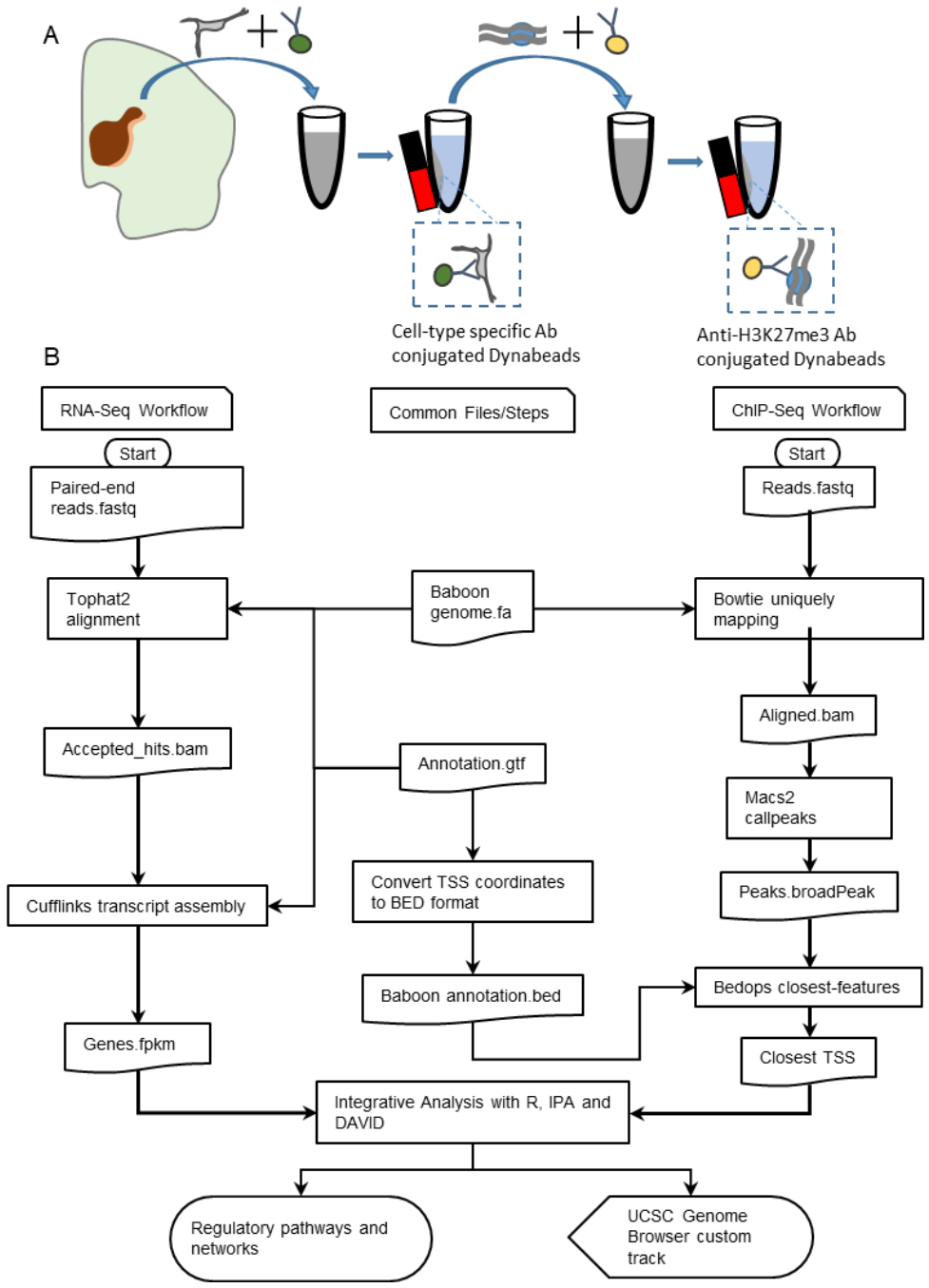

Figure 21. Workflow for ChIP-Seq and RNA-Seq analyses.
(A) Cell extraction and ChIP protocol. Tissue from a region of interest are extracted in a short post-mortem time period. Antibodies targeting cell type specific or chromatin specific antigens used for Dynabead isolation. (B) Commonly used bioinformatics tools were applied at all steps using default software parameters or well-accepted command options. Baboon (PapAnu2.0) reference genome and annotation files were obtained from Ensembl project. Basic workflow for RNA-Seq: align pass filtered RNA-Seq paired-end reads to PapAnu2.0 using Tophat2, then use Cufflinks transcript assembly tool to determine average read density within annotated gene regions. Basic workflow for ChIP-Seq: Align ChIP-Seq short reads with bowtie to PaPAnu2.0 genome lacking mitochondrial sequence. Using uniquely aligned reads, detect peaks with MACS2 to determine regions of significant enrichment compared to unmodified histone. Correlate peaks to nearest transcription start site with BEDOPS closest-features tool. By overlap analysis of ChIP-Seq and RNA-Seq, H3K27me3 or H4K20me3 enriched chromatin could then be associated with either expressed genes or genes with no detectable transcript.

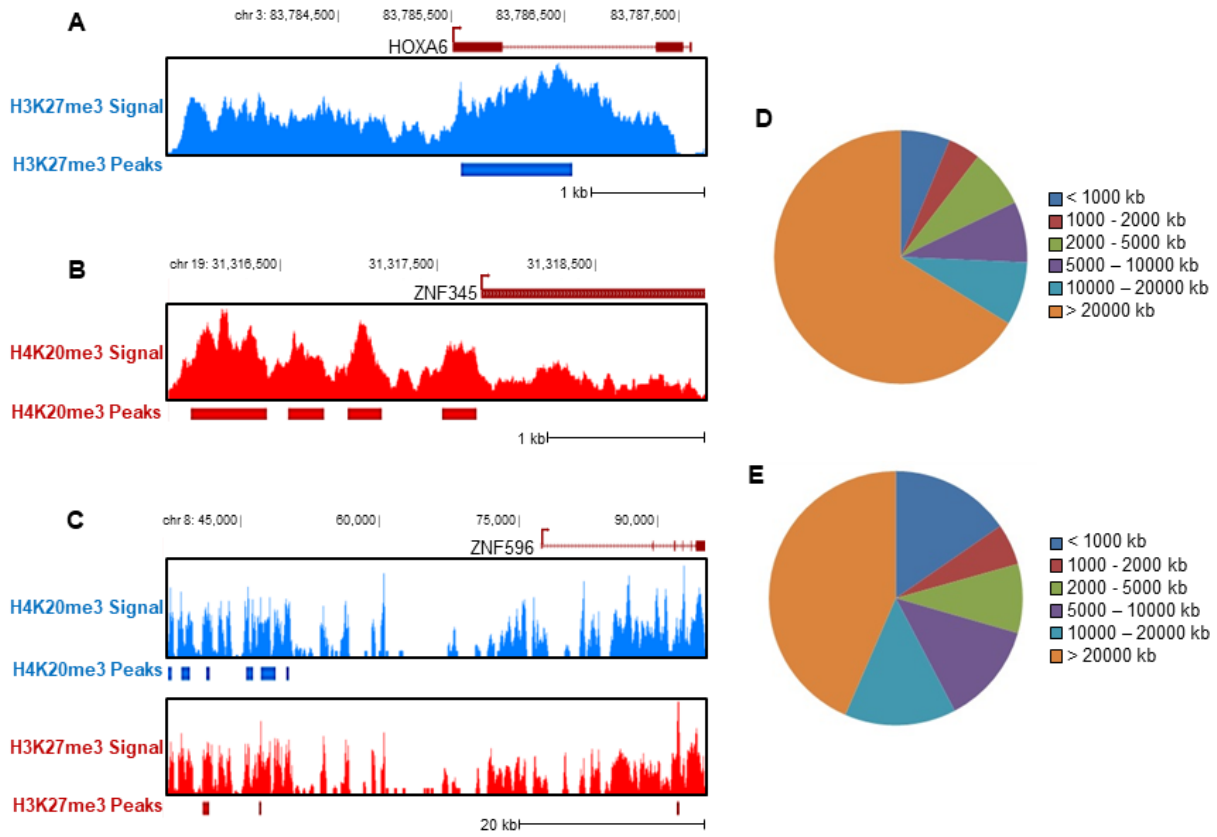

Figure 22. H3K27me3 and H4K20me3 genome-wide patterns in baboon SVZ.
(A-C) UCSC genome browser views of representative genes enriched with H3K27me3 (A), H4K20me3 (B) or H3K27me3 and H4K20me3 (C). Arrows within gene body indicates transcription direction. Arrows above genes denote transcription start site (TSS). "Signal" depicts "mapped read density" after normalization to unmodified H3 and/or H4. Peak tracks denote significantly enriched regions using FDR ≤ 0.05 and is derived from comparing H3K27me3 histone modifications to unmodified H3 enrichment or H4K20me3 histone modifications to unmodified H4 enrichment using binomial distribution model. (D) Of the 709 loci enriched with H3K27me3, the distance between a gene TSS and the nearest loci is: 40 are < 1 kb, 26 are 1 – 2 kb, 47 are 2 – 5 kb, 49 are 5 – 10 kb, 51 are 10 – 20 kb, and 418 are > 20 kb. (E) Among the 10,000 loci enriched with H4K20me3, the distance between a gene TSS and the nearest loci is: 196 are < 1 kb, 67 are 1 – 2 kb, 112 are 2 – 5 kb, 164 are 5 – 10 kb, 181 are 10 – 20 kb, and 554 are > 20 kb.

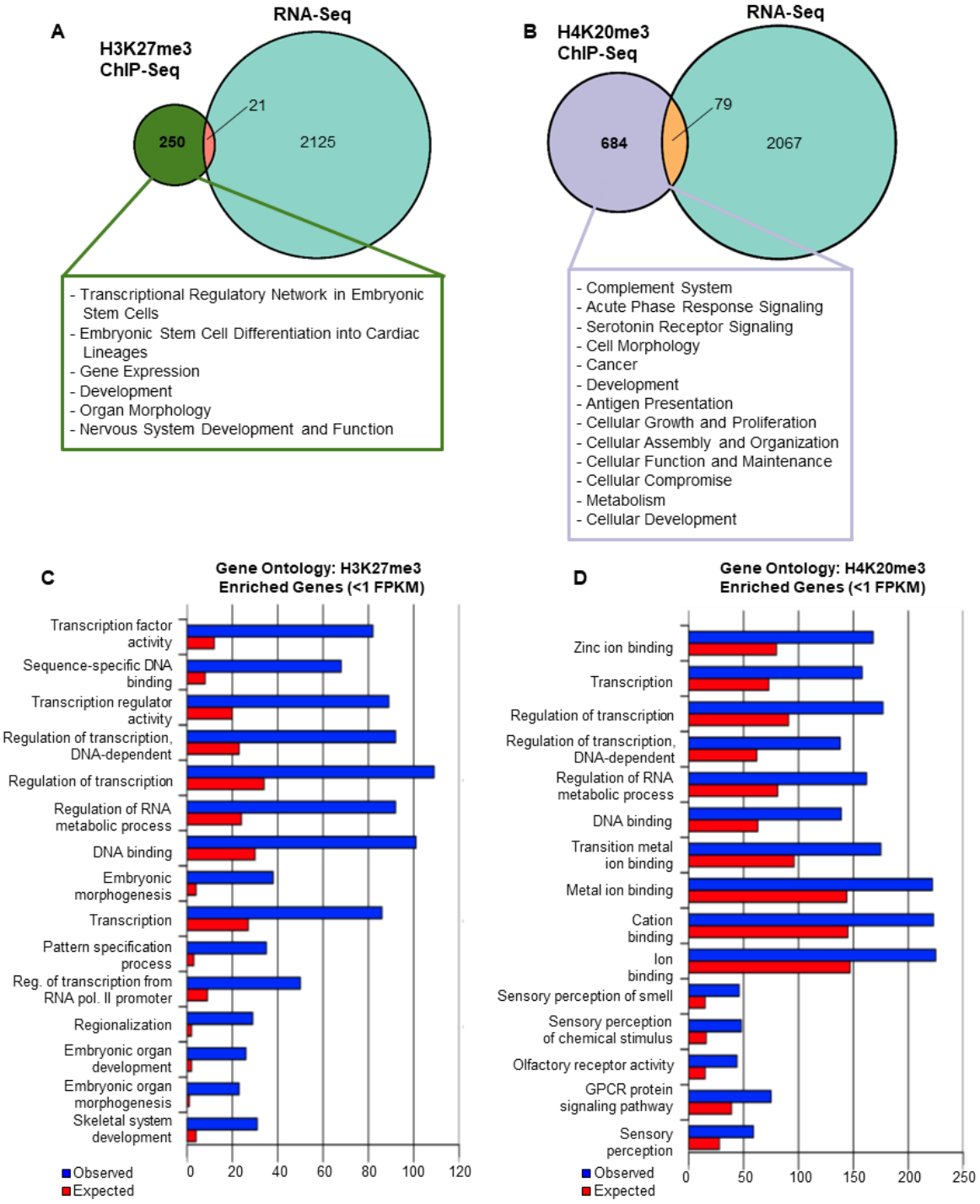

Figure 23. H3K27me3 and H4K20me3 genome-wide analysis in baboon SVZ.
(A) Proportional Venn diagrams represent genes with RNA-Seq detectable genes determined using expression threshold of FPKM > 1.0 and genes enriched with H3K27me3 (A) or H4K20me3 (B). Text boxes indicate IPA predicted functions correlated to genes enriched with H3K27me3 (or H4K20me3) but lacking transcripts (≤ 1 FPKM). (C, D) Gene Ontology analysis of genes lacking detectable transcripts (≤ 1 FPKM) and enriched with H3K27me3 (from green circle in A) (C) or H4K20me3 (from purple circle in B) (D) categorizes genes based on known biological processes or molecular functions. Top 15 most significant categories had Bonferroni-corrected P values ranging from 1.89 x 10−43 to 2.22 x 10−14 for H3K27me3 genes and 1.57 x 10−27 and 3.09 x 10−4 for H4K20me3 enriched genes.

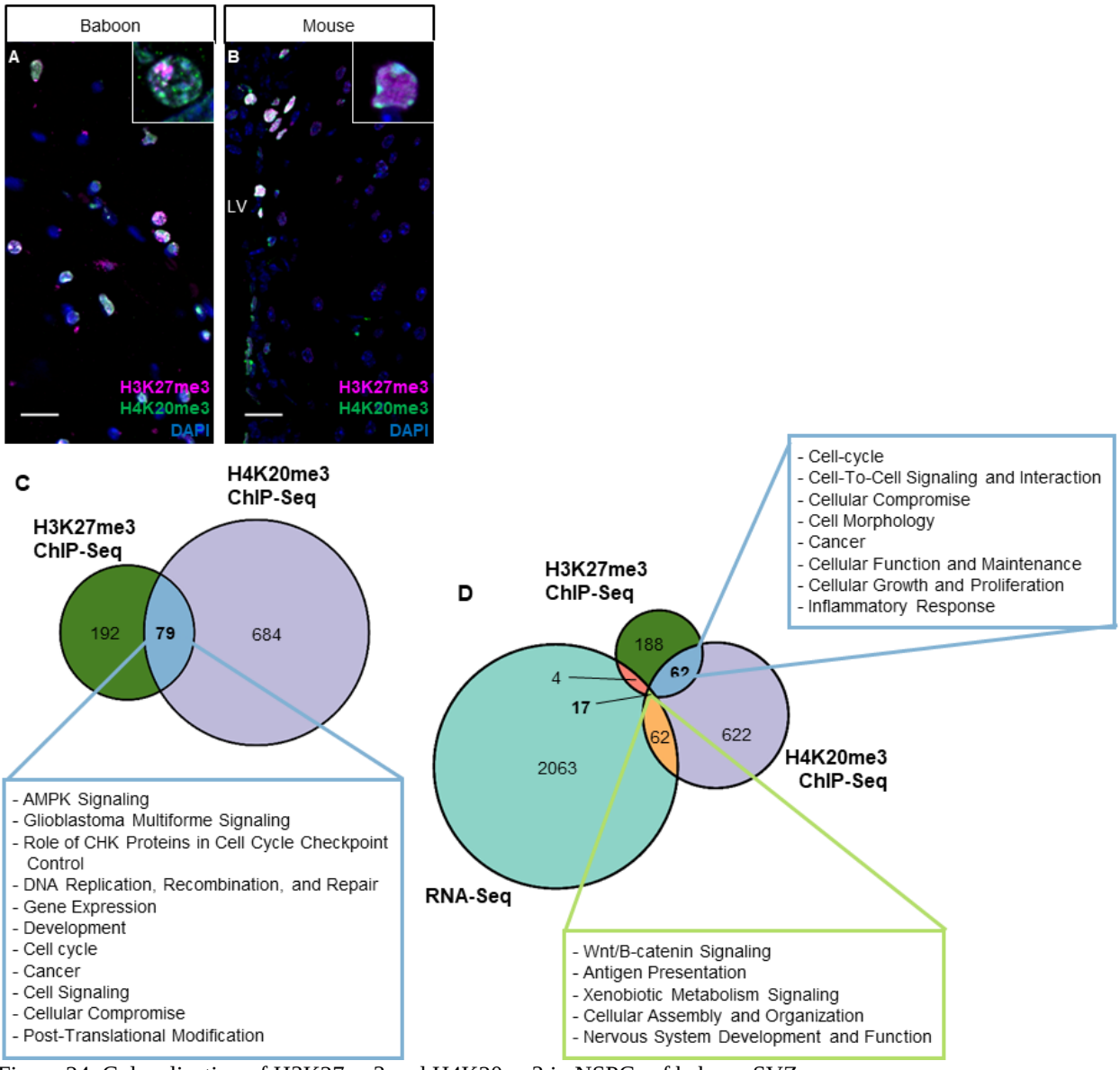

Figure 24. Colocalization of H3K27me3 and H4K20me3 in NSPCs of baboon SVZ.
(A) Co-immunostaining of H3K27me3 and H4K20me3 in baboon brain. Region imaged corresponds to coronal section of the astrocytic ribbon within baboon SVZ. 40X magnification; scale bar = 20 μm. Inset shows 100X of H3K27me3 and H4K20me3 staining patterns. (B) Co-immunostaining of H3K27me3 and H4K20me3 in mouse SVZ. 40X magnification; scale bar = 20 μm. Inset shows 100X of H3K27me3 and H4K20me3 staining patterns. (C) Proportional Venn diagram generated by comparing numbers of genes enriched by H3K27me3, H4K20me3, or both histone modifications. Green area represents H3K27me3 enriched genes (n = 192), purple represents H4K20me3-enriched genes (n = 684), and blue area represents genes enriched by H3K27me3 and H4K20me3 (n = 79). Text box describes functions of H3K27me3/H4K20me3 dual-enriched genes predicted by IPA software using known biochemical pathways and constructing de novo interaction networks. (D) Proportional Venn diagram generated by comparing numbers of genes enriched by H3K27me3, H4K20me3, and genes detectable by RNA-Seq. Dark blue portion indicates genes enriched with H3K27me3 and H4K20me3 with no detectable transcription (≤ 1 FPKM) (n = 62). Light green portion represents H3K27me3/H4K20me3 co-enriched genes with detectable RNA levels (> 1 FPKM) (n = 17).

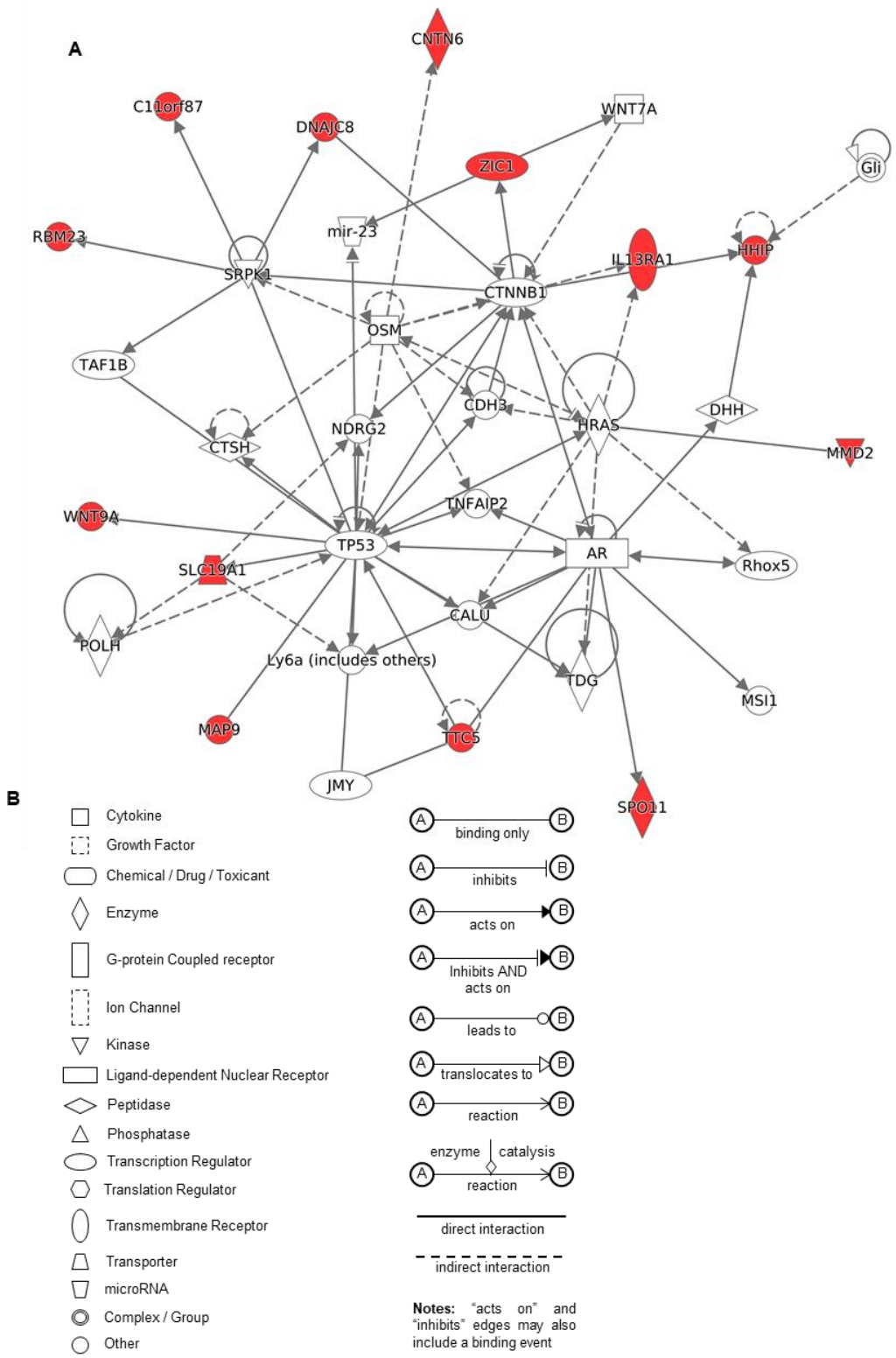

Figure 25. Network analyses by IPA for genes enriched by both H3K27me3 and H4K20me3 in undifferentiated cells of baboon SVZ and lacking detectable transcripts by RNA-Seq (FPKM ≤ 1).
Foci molecules (red) indicate genes significantly enriched by H3K27me3 and H4K20me3 within neural stem and progenitor cells in baboon SVZ. (A) Functional network in Cell Cycle, Cell-To-Cell Signaling and Interaction, Cellular Growth and Proliferation. (B) Symbol key for network and pathway analyses.

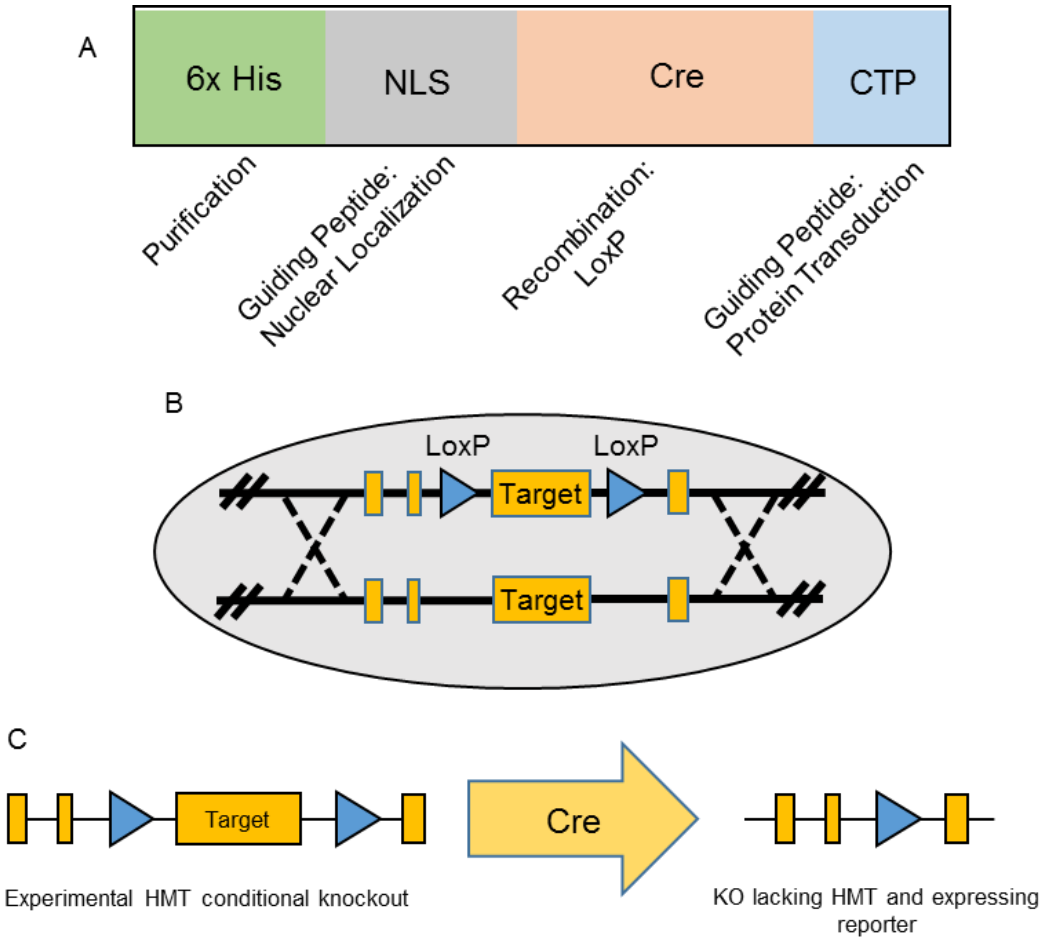

Figure 26. Cre protein design and recombination strategy.
(A) To generate region-specific conditional knockouts a translated, enzymatically active Cre is produced in *E. coli*. The Cre protein contains a 6x His sequence for affinity purification, a CTP peptide to promote movement across the plasma membrane into the cytosol, a nuclear localization sequence to shuttle the protein into the nucleus and Cre to mediate homologous recombination at loxP sequences. (B) Gene targeting strategy involves flanking the DNA sequence encoding the SET domain of histone methyltransferases (HMT) and targeting into a host genome. (C) Following Cre activity, sequences flanked by loxP sites are removed, resulting in loss of catalytic function in the HMT of interest.

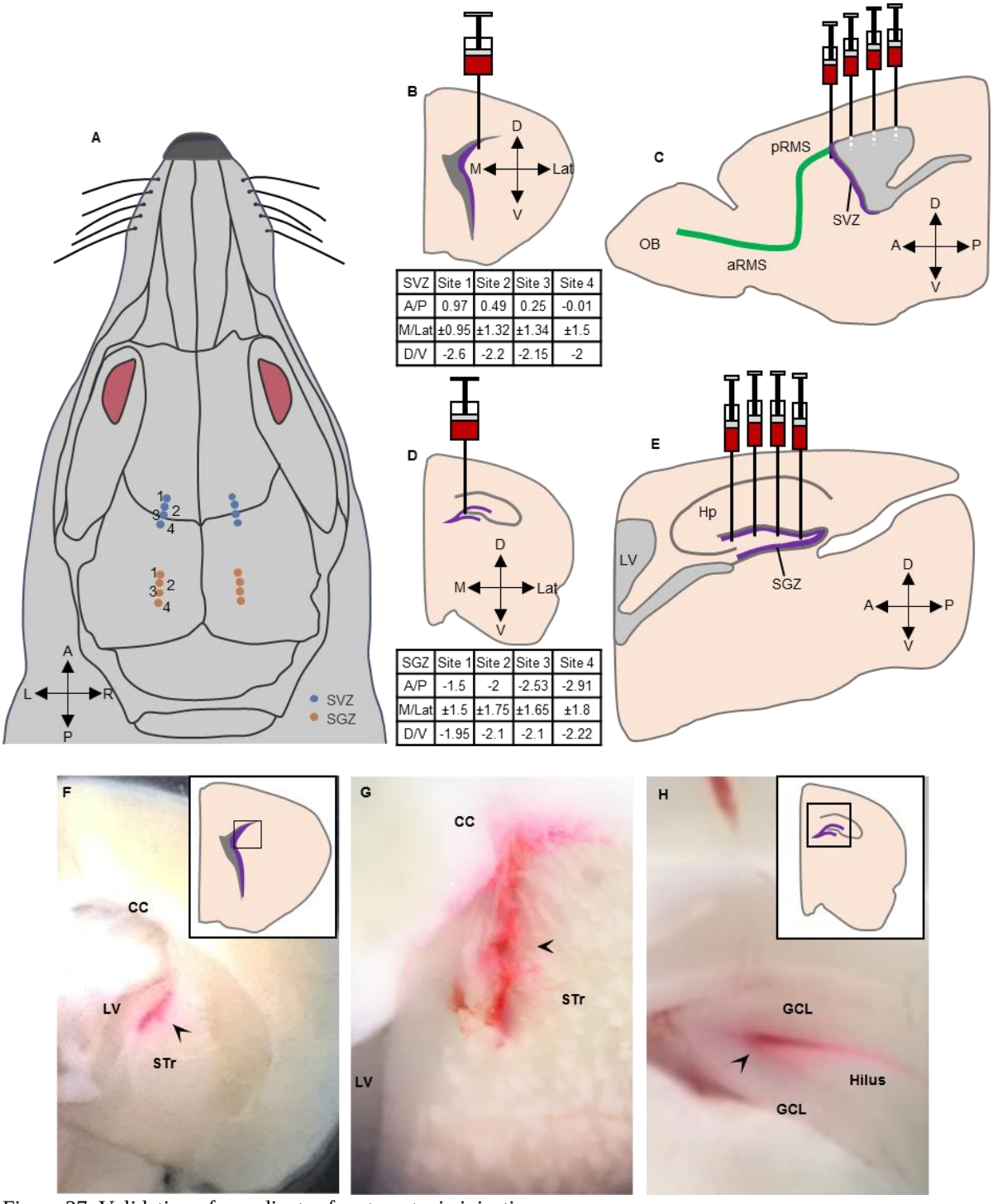

SVZ	Site 1	Site 2	Site 3	Site 4
A/P	0.97	0.49	0.25	-0.01
M/Lat	±0.95	±1.32	±1.34	±1.5
D/V	-2.6	-2.2	-2.15	-2

SGZ	Site 1	Site 2	Site 3	Site 4
A/P	-1.5	-2	-2.53	-2.91
M/Lat	±1.5	±1.75	±1.65	±1.8
D/V	-1.95	-2.1	-2.1	-2.22

Figure 27. Validation of coordinates for stereotaxic injections.
(A) Injection sites for SVZ and SGZ/DG at dorsal skull superimposed over diagram of head soft tissue. Closed blue circles indicate drill/ injection sites for SVZ. Closed orange circles indicate drill/injection sites for SGZ/DG. (B) Scheme of coronal view of mouse SVZ injection site. Table indicates drill coordinates. (C) Scheme of sagittal view of mouse SVZ region. Multiple syringes depict the 4 sites used for Cre injection into SVZ. White dashed lines at tips of needles indicates view of needle tip obstructed by LV/ependyma. (D) Scheme of coronal view of mouse SGZ/DG injection site. Table indicates drill coordinates. (E) Scheme of sagittal view of mouse SGZ/DG region. (F) Coronal section of mouse brain injected with 50 nL retrobeads (arrow); 2X. (G) SVZ injected with retrobeads (arrow); 5X. (H) SGZ/DG injected with retrobeads (arrow); 5X.

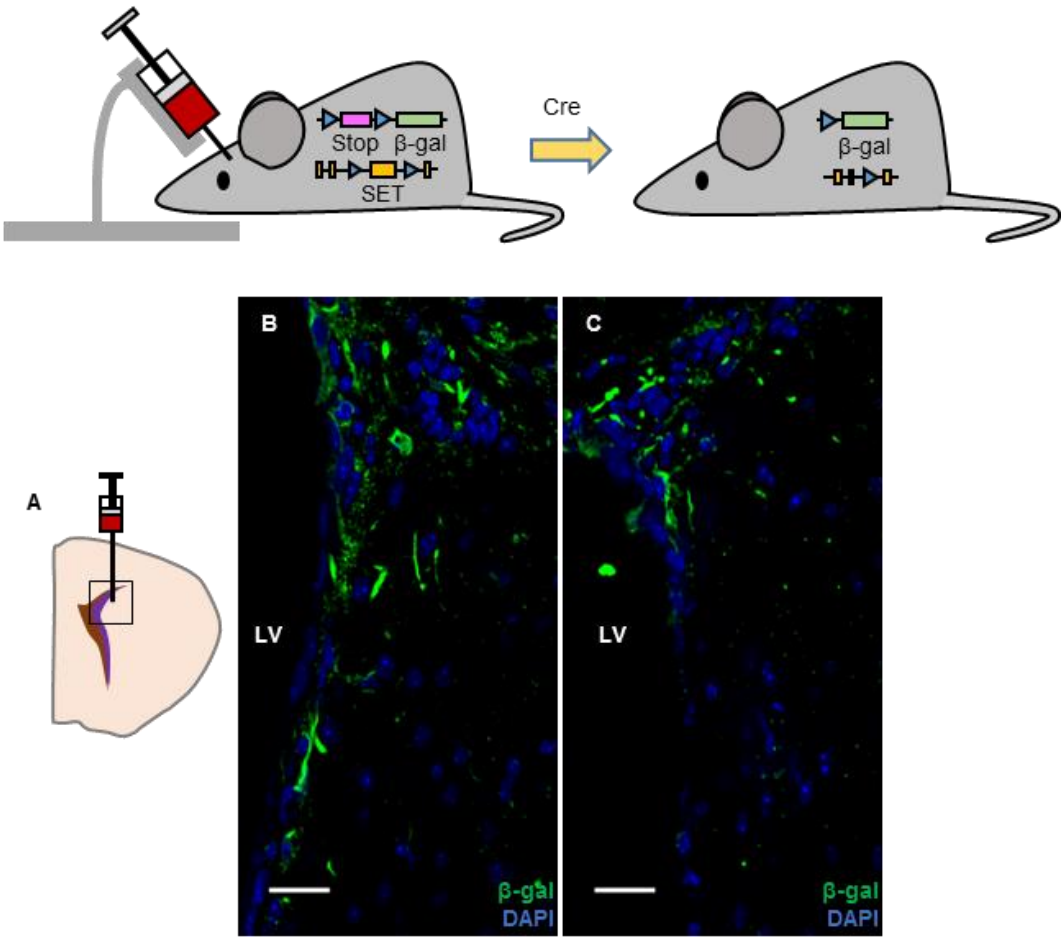

Figure 28. Injectable Cre protein induces recombination in the SVZ.
(A) Schema of the SVZ in coronal section. Black box indicates region imaged. (B-C) Dorsal SVZ of *ROSA26* mouse, 10 days (B) and 32 days post-injection of Cre (C) were stained with anti β-gal antibodies. Scale bars = 20 um.

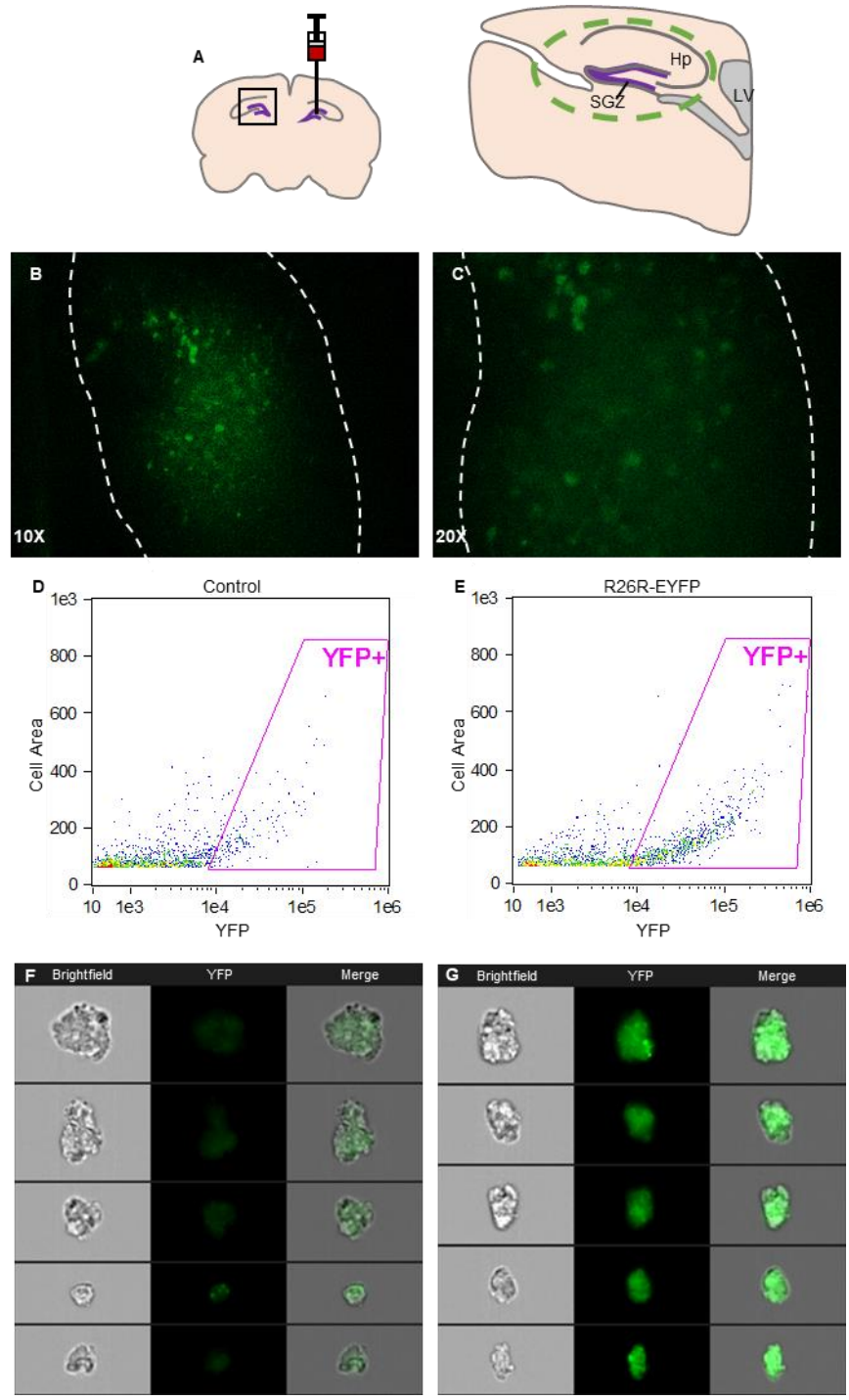

Figure 29. YFP expression is abundant following Cre injection into the SGZ/DG of *ROSA26*$^{Y/Y}$ reporter mice. (A) Schema of Cre protein injection into the SGZ/DG. Green dashed line represents region of SGZ/DG imaged in (B, C) and used for image flow cytometry. (B) Immediately following microdissection, hippocampus was isolated and the SGZ/DG imaged using fluorescent microscope to detect regions expressing YFP. White dashed line approximates Cre injection bolus containing predominantly YFP$^+$ cells, 10X. (C) YFP expression as in (B), 20X. (d) Imaging flow cytometry gating of YFP$^+$ cells from *ROSA26*$^{Y/Y}$ mouse, 10 days post-injection of vehicle. (E) Imaging flow cytometry gating of YFP$^+$ cells from *ROSA26*$^{Y/Y}$ mouse, 10 days post-injection of Cre. (F) Representative images of single cells from vehicle injected SGZ/DG of *ROSA26*$^{Y/Y}$ within YFP$^+$ gate (from D) obtained using image flow cytometry, 40X. (G) Representative images of single cells from Cre injected SGZ/DG of *ROSA26*$^{Y/Y}$ within YFP$^+$ gate (from E) obtained using image flow cytometry, 40X.

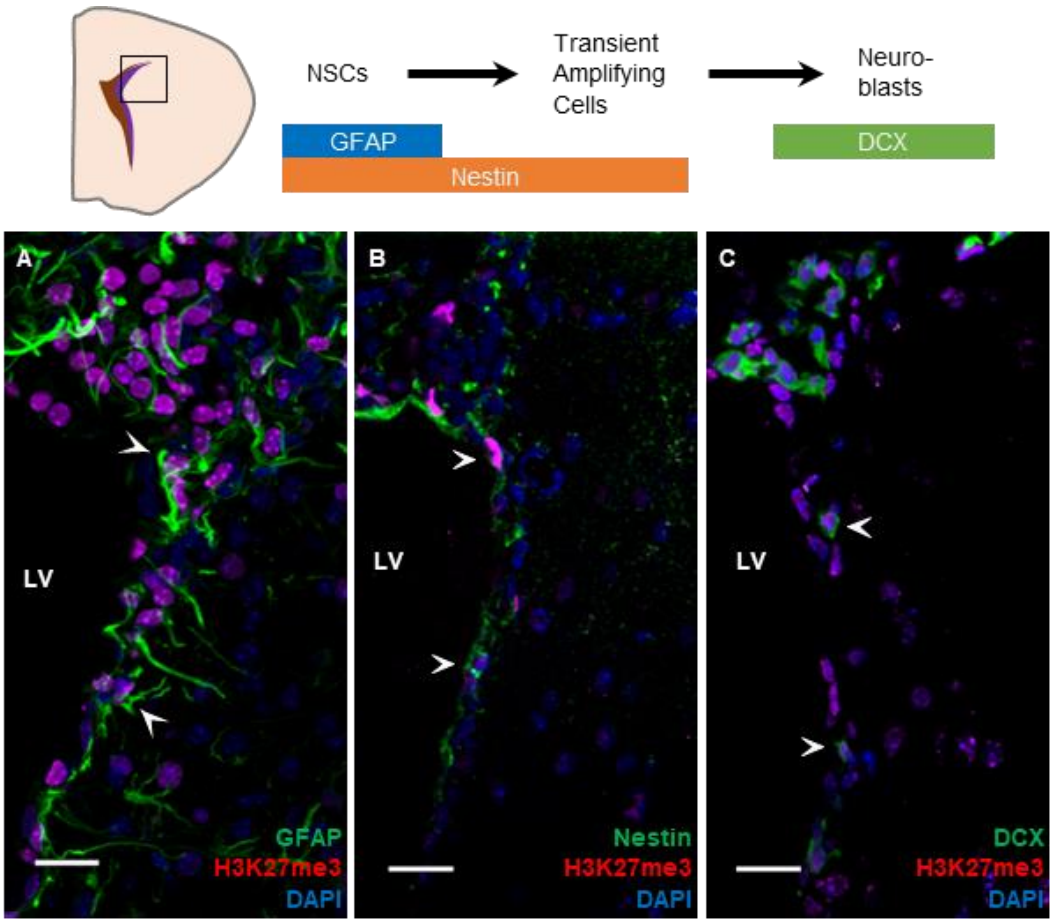

Figure 30. H3K27me3 is ubiquitous in NSPCs within adult SVZ of non-injected *Ezh2*$^{flox/flox}$;*ROSA26* mice. (A) H3K27me3 is abundant in GFAP^{+} NSCs, 40X. (B) H3K27me3 is abundant in pan-NSC marker Nestin^{+} cells, 40X. (C) H3K27me3 is abundant in DCX^{+} migrating neuroblasts, 40X. Scale bars = 20 µm

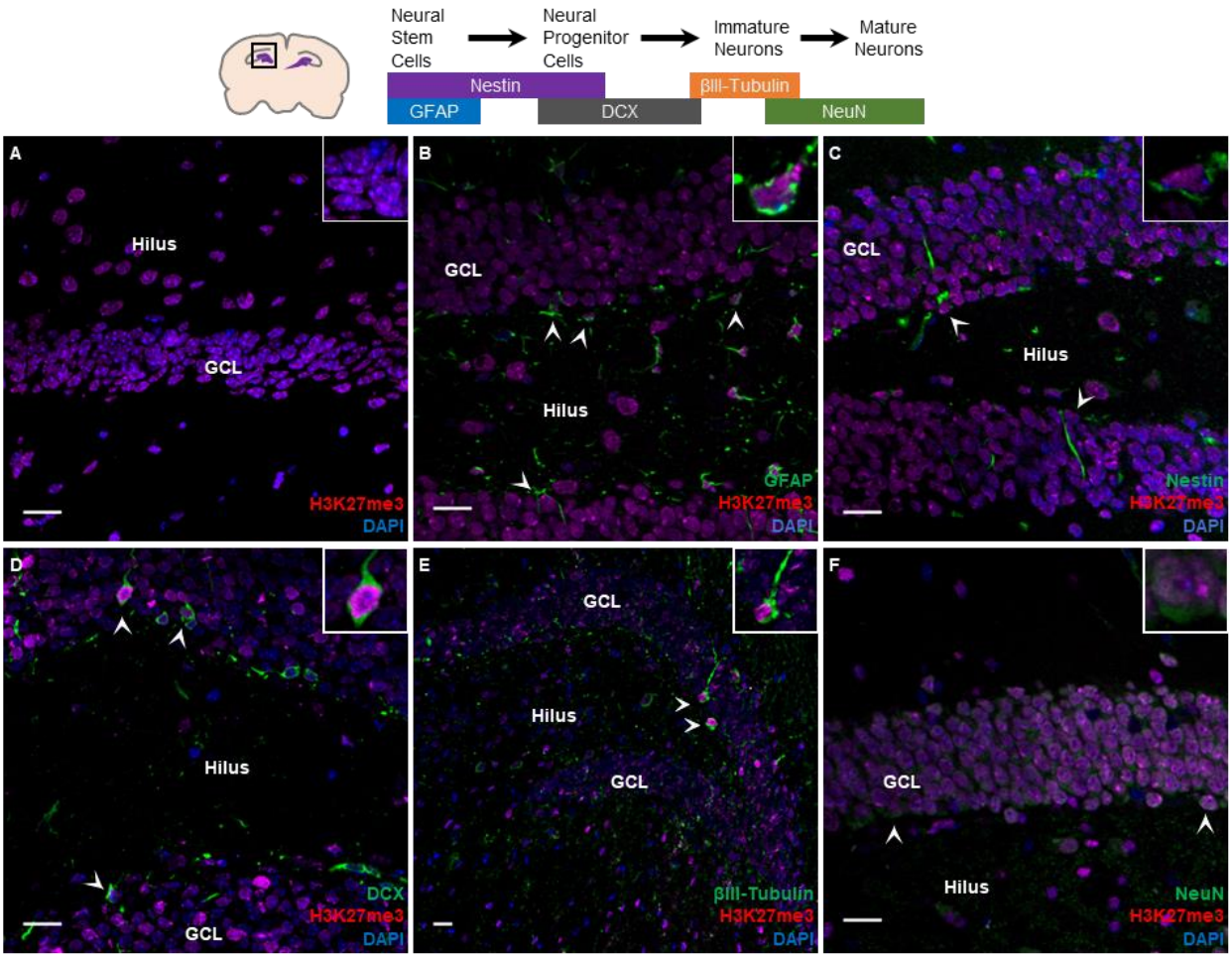

Figure 31. H3K27me3 is ubiquitous in NSPCs within adult SGZ/DG of non-injected *Ezh2*$^{flox/flox}$;*ROSA26* mice. (A) H3K27me3 is abundant at the SGZ/DG, 40X. (B) H3K27me3 is abundant in GFAP^{+} cells, 40X. (C) H3K27me3 is abundant in pan-NSC marker Nestin^{+} cells, 40X. (D) H3K27me3 is abundant in DCX^{+} cells, 40X. (E) H3K27me3 is abundant in βIII-Tubulin^{+} immature neurons, 20X. (F) H3K27me3 is abundant in NeuN^{+} mature neurons, 40X. Scale bars = 20 μm. Insets = 63X.

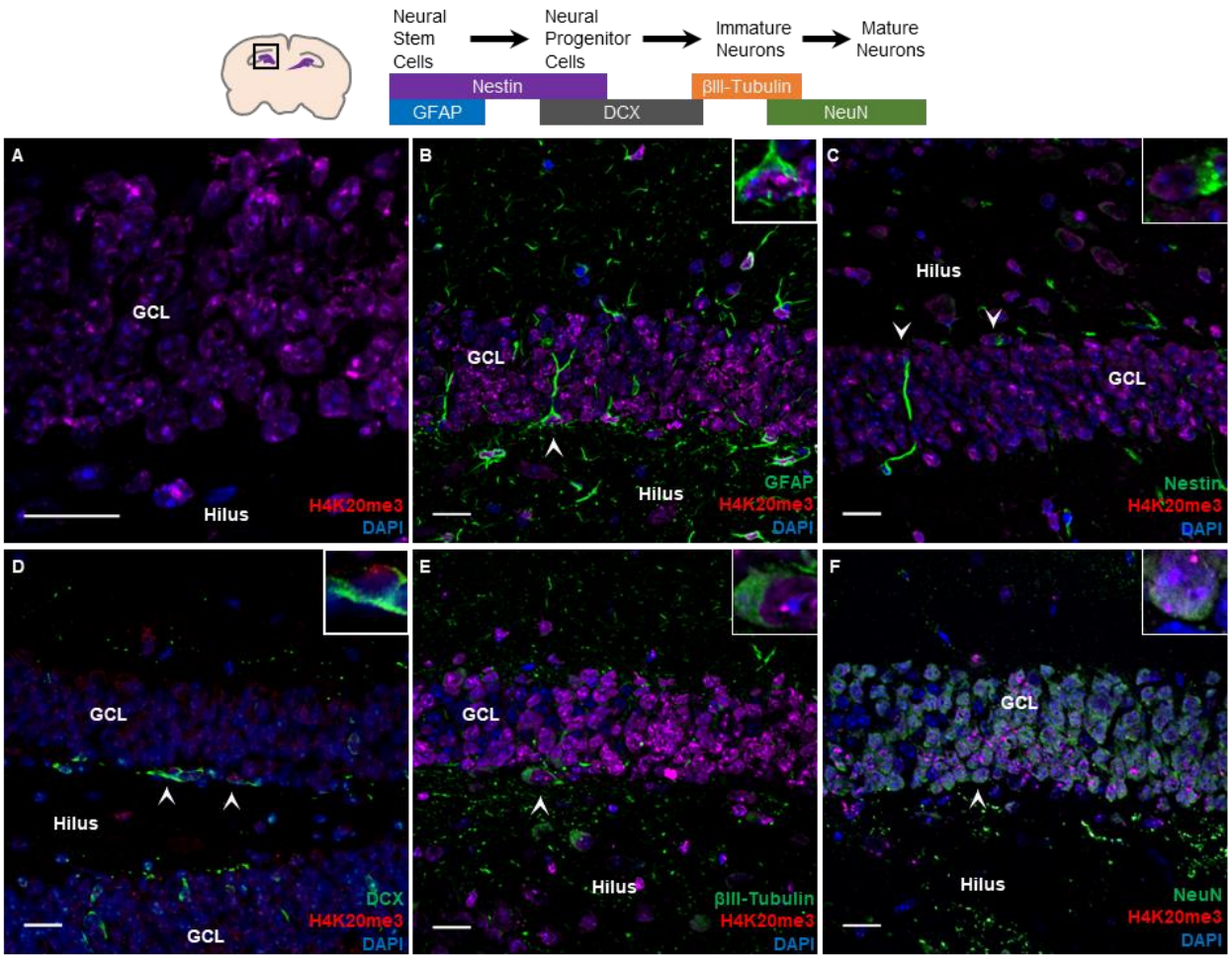

Figure 32. H4K20me3 is ubiquitous in NSPCs within adult SGZ/DG of non-injected *Suv4-20h*$^{flox/flox}$;*ROSA26* mice. (A) H4K20me3 is present in the SGZ/DG, 63X (B) H4K20me3 is abundant in GFAP^{+} cells, 40X. (C) H4K20me3 is present in pan-NSC marker Nestin^{+} cells, 40X. (D) H4K20me3 is present in DCX^{+} cells, 40X. (E) H4K20me3 is present in βIII-Tubulin^{+} immature neurons, 40X. (F) H4K20me3 is present in NeuN^{+} mature neurons, 40X. Scale bars = 20 μm. Insets = 63X.

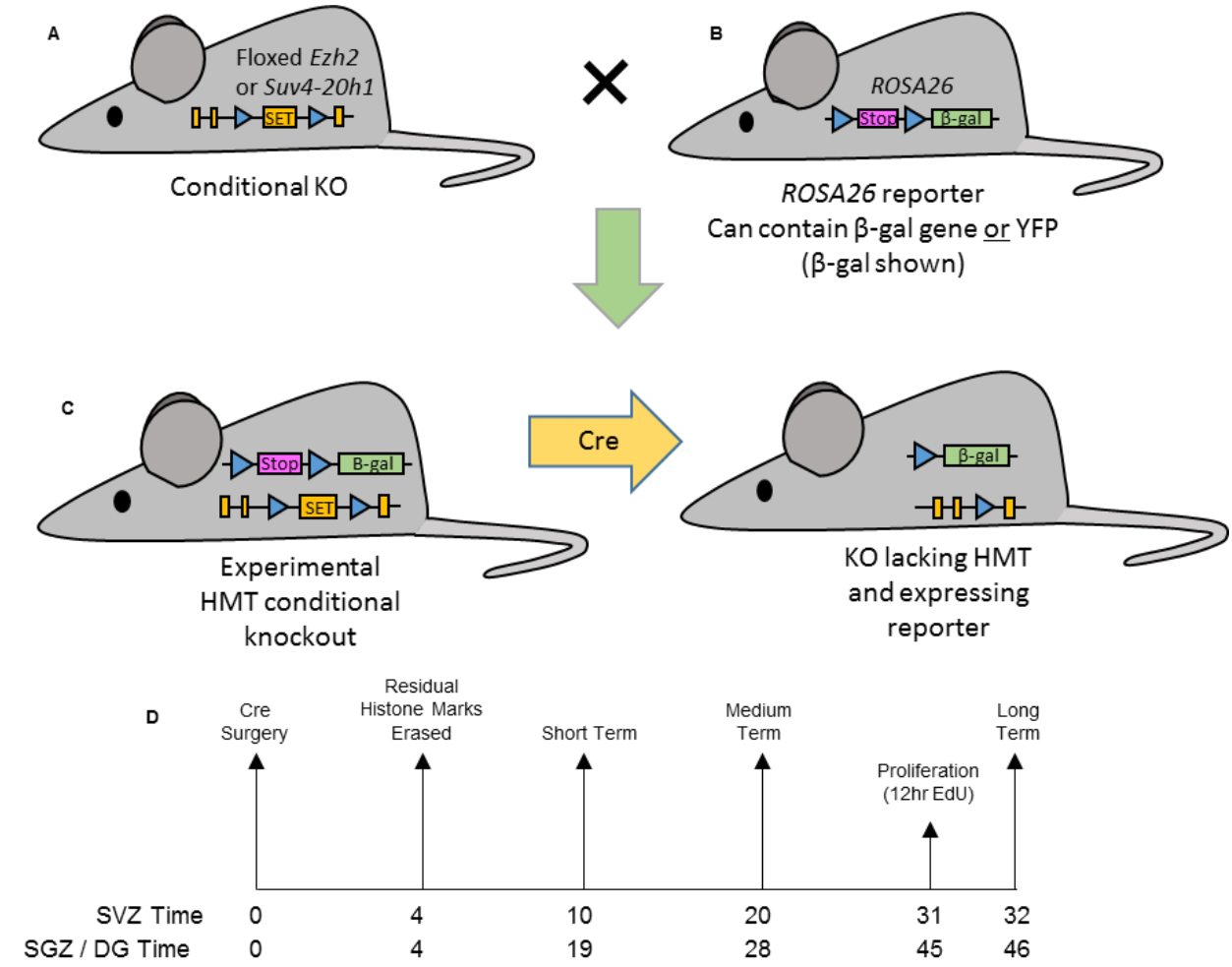

Figure 33. Conditional *Ezh2* or *Suv4-20h1* knockout (KO) approach.
(A) A floxed SET sequence within *Ezh2* or *Suv4-20h1* gene is inserted into the genome of a B6:129 embryo which grows to adult. (Blue arrow: loxP site). Adult mice are conditional Ezh2 or *Suv4-20h1* knockouts (SET: yellow rectangle). (B) To monitor Cre efficiency following stereotaxic Cre injection, a *ROSA26* or *ROSA26*$^{Y/Y}$ reporter is crossed with *Ezh2* or *Suv4-20h1* conditional KO mouse. ROSA loci contain a floxed stop cassette (purple rectangle) upstream of either a *LacZ* or YFP gene (green rectangle) (C) Cre protein delivered by stereotaxy deletes floxed sites and results in simultaneous loss of Ezh2 function and constitutive expression of B-galactosidase or YFP within a cell. (D) Timepoints used during conditional loss of function experiments in SVZ and SGZ/DG in adult mice.

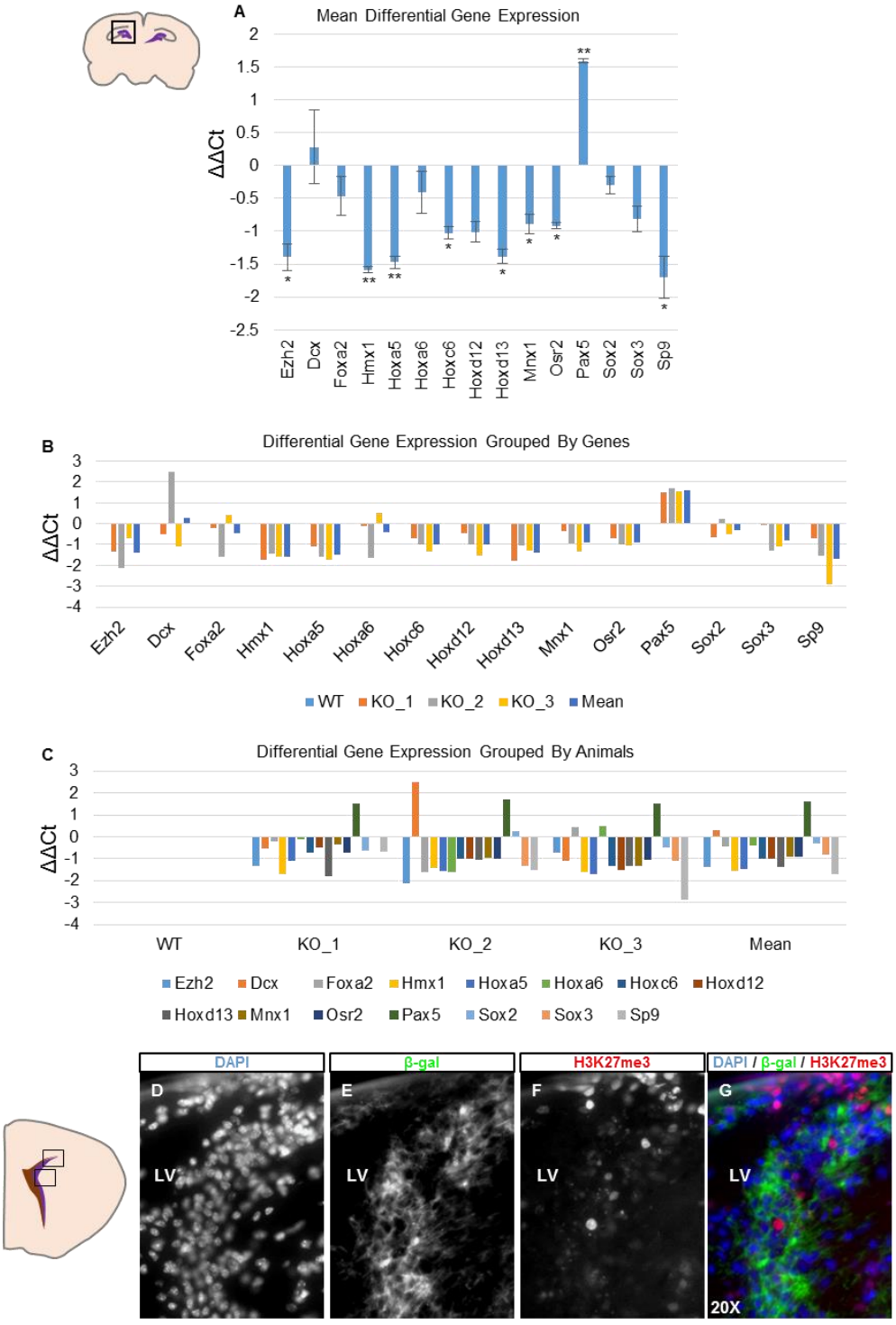

Figure 34. RT-qPCR examined the expression levels of *Ezh2* and selected Ezh2/H3K27me3 putative target genes. Three independent experimental samples from Cre injected hemisphere and one control were subjected to RT-qPCR validation. Each bar represents the average ΔΔCt on a log2 scale of 3 independent Cre-mediated *Ezh2* knock-outs after normalization to internal control *S16* (ΔCt) and then control (ΔΔCt). (A) The average of differential gene expression levels of 3 independent Cre-mediated knock-out versus controls. Error bars show standard error of the mean. (B) The differential gene expression was grouped by genes. (C) The differential gene expression was grouped by animals. (D-G) Immunostaining for dapi (D), β-galactosidase (E), H3K27me3 (F), and merged (G) in coronal sections obtained from the SVZ of an *Ezh2*$^{flox/flox}$;*ROSA26* mouse, 10 days post-injection of Cre. 20X.

Table 1. Cre protein induced changes in mRNA quantities.

Gene	ΔΔCt ± SE	Fold Change ± SE	p-value
Ezh2	-1.4 ± 0.42	-2.63 ± 0.82	0.0308
Dcx	0.28 ± 1.11	1.22 ± 1.28	0.9326
Foxa2	-0.46 ± 0.6	-1.38 ± 0.6	0.6214
Hmx1	-1.58 ± 0.08	-3 ± 0.17	0.0037
Hoxa5	-1.47 ± 0.19	-2.77 ± 0.34	0.0075
Hoxa6	-0.41 ± 0.63	-1.33 ± 0.62	0.6987
Hoxc6	-1.02 ± 0.18	-2.03 ± 0.26	0.0308
Hoxd12	-1.01 ± 0.3	-2.01 ± 0.42	0.0550
Hoxd13	-1.39 ± 0.22	-2.61 ± 0.43	0.0115
Mnx1	-0.89 ± 0.28	-1.86 ± 0.36	0.0773
Osr2	-0.91 ± 0.1	-1.89 ± 0.13	0.0356
Pax5	1.59 ± 0.06	3.01 ± 0.13	0.0035
Sox2	-0.3 ± 0.27	-1.23 ± 0.11	0.6142
Sox3	-0.81 ± 0.39	-1.76 ± 0.44	0.1540
Sp9	-1.7 ± 0.64	-3.26 ± 1.76	0.0428

Table 2. Primers selections for conditional knockout mice.

Gene	Forward ID	Forward Sequence	Reverse ID	Reverse Sequence	*Ezh2*	*Suv4-20h1*
Ccar1	Ccar1_A_550F	ATTGCCCACAAGCCTTAGCC	Ccar1_A_550R	TGTAGCTTTGTAACCACTCCTGT	no	yes
Ccar1	Ccar1_B_900F	TGCCACAGACAACGTTTGGT	Ccar1_B_900R	GGTGTAATAGAGGCAGCTGAGATCT	no	yes
Chrnb3	Chrnb3_A_300F	CAGTGCCACTCTCTCAGGTTC	Chrnb3_A_300R	GGGCGGACACATTTCTGATAAC	no	yes
Chrnb3	Chrnb3_B_3950F	GGTTCTTTAGATCGCCTTGCA	Chrnb3_B_3950R	TGGATCTTGTGGGCACACTATT	no	yes
Chst2	Chst2_A_1050F	CCGCTCGGGATGAAGGTATTT	Chst2_A_1050R	CATCGTGAGCACCAGTAGC	yes	yes
Chst2	Chst2_B_3150F	CCAGTGTTACTTGTCTCTGTAGCTTCA	Chst2_B_3150R	CATGTGAGAAAACAACTCTCGGTTA	yes	yes
Dcx	Dcx_A_300F	CATTTTGACGAACGAGACAAAGC	Dcx_A_300R	TGGAAGTCCATTCATCCGTGA	no	no
Dcx	Dcx_B_700F	CCCAACTGGTCTGTCAACGTAAA	Dcx_b_700R	CACCCCGCTGCGAATG	no	no
Foxa2	Foxa2_A_800F	CATGTTCGAGAACGGCTGCTA	Foxa2_A_800R	GCCAGTTGCTTCTCACACTTGA	yes	no
Foxa2	Foxa2_B_1300F	AACAGGTCATGCACTACCCA	Foxa2_B_1300R	GCTCTCCCAAAGTCTCCACT	yes	no
Galr1	Galr1_A_150F	GCGGGAAGAAGAGGCTCAA	Galr1_A_150R	AGCTGCGTCCCCTTGCT	no	yes
Galr1	Galr1_B_700F	TGAAGGGAATGGGAGCGAC	Galr1_B_700R	CACTACCAGCGTAATGAAGTTCT	no	yes
Ggh	Ggh_A_200F	CTTTCAAGTCCCGGGATGTC	Ggh_A_200R	AACTTCGCCATTTTCCCAAA	yes	yes
Ggh	Ggh_B_1000F	GGTTAAGGAGACGGCATCCT	Ggh_B_1000R	AGGAATCAGAACCAGGCACA	yes	yes
Grm6	Grm6_A_1350F	ATGAACAGGAGGGGAAGGTG	Grm6_A_1350R	GCTACCATTGAAGCGGACTG	no	yes
Grm6	Grm6_B_2550F	TGTATTATCTGGCTGGCTTTCG	Grm6_B_2550R	TGTGGTCGTTTGGATGTAGATCTT	no	yes
Hmx1	Hmx1_A_350F	GCTACGGAGGTGGTCTAAGTC	Hmx1_A_350R	GCGCTTCAGATCGAAAGTGGA	yes	no
Hmx1	Hmx1_B_1300F	AGGAACCGTATGGCGACTGT	Hmx1_B_1300R	CTGATGTCTGGGTTCCTGCAA	yes	no
Hoxa5	Hoxa5_A_300F	CTCATTTTGCGGTCGCTATCC	Hoxa5_A_300R	ATCCATGCCATTGTAGCCGTA	yes	no
Hoxa5	Hoxa5_B_950F	CGCCGAAGAAGGATCGAAA	Hoxa5_B_950R	CCTCCTGTTTTGGAACCAGATT	yes	no
Hoxa6	Hoxa6_A_200F	TTACCAACAGTCCAACTCGGT	Hoxa6_A_200F	CGCCACTGAGGTCTTTATCAGA	yes	no
Hoxa6	Hoxa6_B_400F	AGGCACCGACCGGAAGTAC	Hoxa6_B_400R	CACCCGCACAGGAATTCATC	yes	no
Hoxc6	Hoxc6_A_200F	CAACGTCGCCCTCAATTCCA	Hoxc6_A_200R	AGTCGAGTAGATCCGGTTCTG	yes	no
Hoxc6	Hoxc6_B_550L	TTTCACTTCAACCGCTACCTAACTC	Hoxc6_B_550R	TCGGTCAGGCACAGAGCAT	yes	no
Hoxd12	Hoxd12_A_150F	CTGAATTTACAGTCACCGGACTC	Hoxd12_A_150R	TGCGAGGGTATGAGATGGGG	yes	no
Hoxd12	Hoxd12_B_700F	GGCCCGCAAGAAGAGGAA	Hoxd12_B_700R	TCATTGACCAGGAATTCGTTCTC	yes	no
Hoxd13	Hoxd13_A_400F	CAACGGTTACTACAGCTGCC	Hoxd13_A_400R	ACACCATGTCGATGTAGCCA	yes	no
Hoxd13	Hoxd13_B_450F	GCACGGCGTAGGCTTACAG	Hoxd13_B_450R	GTACTTCTCCACCGGGAAACC	yes	no
Kmt5b	Kmt5b_A_1100F	ACTAGCGCCTTTCCTTCGAG	Kmt5b_A_1100R	GCCGAAATCTCACAGGATTGTTG	no	no
Kmt5b	Kmt5b_B_3850F	GGCTTTTGGTTTATTTGCTAGATGT	Kmt5b_B_3850R	AGCCAATGGTCTGCTATGGTAAC	no	no
Mnx1	Mnx1_A_100F	TGGCAAAAAATCGCAGTAACAA	Mnx1_A_100R	GTGCGGGCTTACGGAGACT	yes	no
Mnx1	Mnx1_B_1000F	GAACACCAGTTCAAGCTCAACA	Mnx1_B_1000R	GCTGCGTTTCCATTTCATTCG	yes	no
Osr2	Osr2_A_200F	CGGACTGCCGAAGACCAAT	Osr2_A_200R	CGGGAACCGAGAACATGATC	yes	no
Osr2	Osr2_B_800F	TCCTTCCAGCCCTACACAAG	Osr2_B_800R	GGTAAAGTGTCTGCCGCAAA	yes	no
Pax5	Pax5_A_150F	TCCCAGATGTAGTCCGCCAAA	Pax5_A_150R	TCCTGTCTCATAATACCTGCCAA	yes	no
Pax5	Pax5_B_400F	TTGGCAGAGCGAGTCTGTGA	Pax5_B_400R	TTTGTCCGAATGATCCTGTTGA	yes	no
Rps16	Rps16_A_200F	GTGGCCCACTGCAAACG	Rps16_A_200R	TGCGCGGCTCGATCAT	no	no
Rps16	Rps16_B_250F	CATCAAGGTGAACGGACGTC	Rps16_B_250R	AATTTGGGCCACATGTCCAC	no	no
Sox2	Sox2_A_200F	TTCCAAAAACTAATCACAACAATCG	Sox2_A_200R	GAGACGGGCGAAGTGCAA	no	no
Sox2	Sox2_B_700F	GCGGAGTGGAAACTTTTGTCC	Sox2_B_700R	GGGAAGCGTGTACTTATCCTTCT	no	no
Sox3	Sox3_A_550F	CAACTCCGAGATCAGCAAGC	Sox3_A_550R	CTTCTTGAGCAGCGTCTTGG	yes	no
Sox3	Sox3_B_1450F	GGACGCCTTGCTGTTTAGCT	Sox3_B_1450R	CCGACAGTTACGGCCAAACT	yes	no
Sp9	Sp9_A_650F	GCTTCCACTCGACCCTAGC	Sp9_A_650R	GAGCTGAAGTCGGGGTTGTA	yes	no
Sp9	Sp9_B_1950F	GAGTCCCACAAACGCAAGAAC	Sp9_B_1950R	GGACATTTCTGTGTATTGCTCTTCTC	yes	no
Zfp94	Zfp94_A_300F	GGTGCAACAGCTGCCATCTT	Zfp94_A_300R	GGCCACGTCCCTGAAGGT	no	yes
Zfp94	Zfp94_b_500F	TCTCAGTGGGAGACAAGAATCC	Zfp94_B_500R	AACCTGCTGCCAGATTTGTGA	no	yes

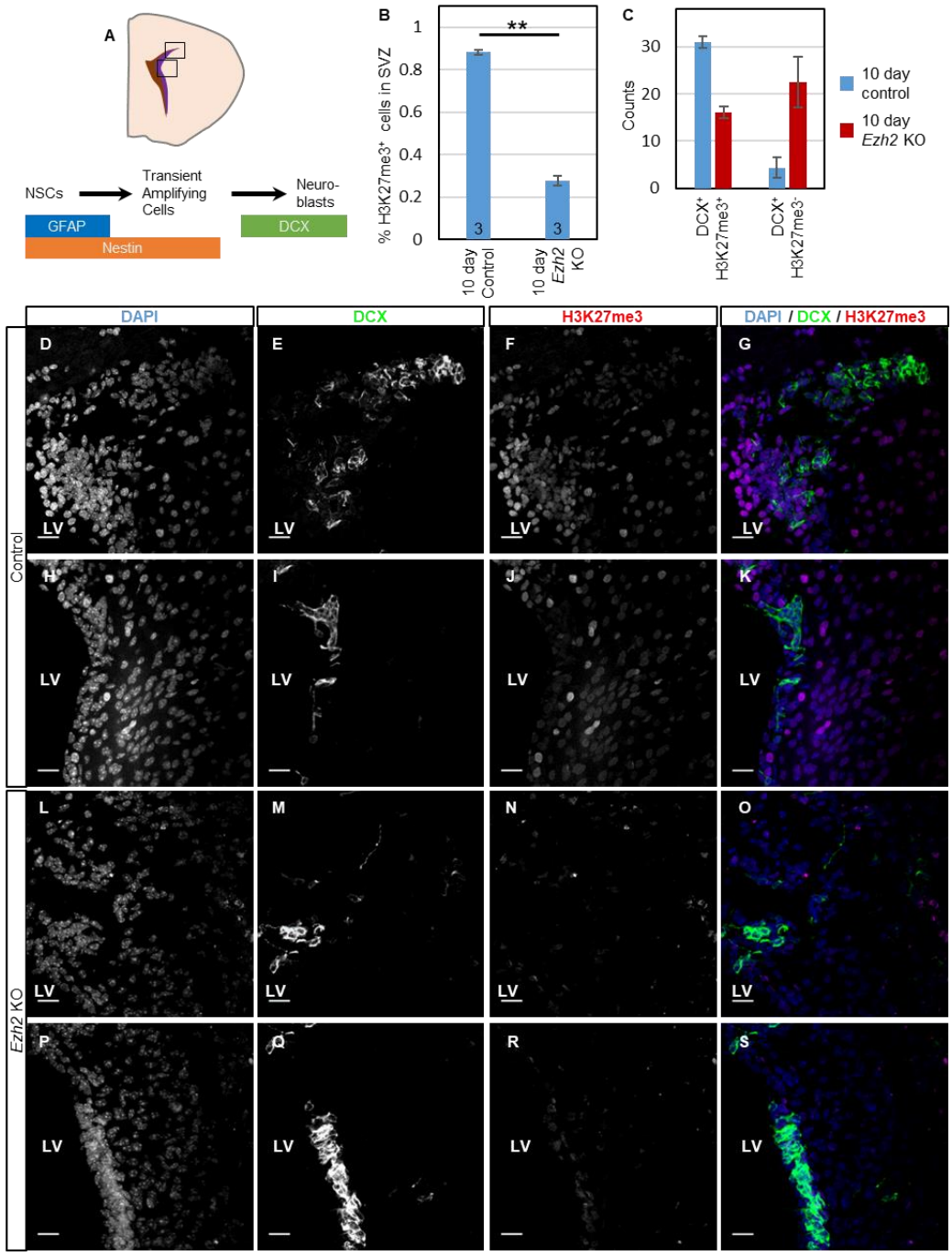

Figure 35. Loss of Ezh2 reorganizes neuroblast patterns in the SVZ.

(A) Schema of coronal sectioned mouse brain containing subventricular zone (SVZ). Black boxes indicate regions imaged. Horizontal bars depict stepwise cell fate transition of NSPC. (B) Bar graph of the percentage of H3K27me3-positive cells present in the dorsal SVZ of *ROSA26* or *Ezh2*$^{flox/flox}$;*ROSA26* mice, 10 days post-injection of Cre. n = 3 mice per experimental group, p-value = 0.012, determined using T-test. Control: mean = 0.916, standard error of mean = 0.006; *Ezh2* knockout: mean = 0.278, standard error of mean = 0.044 (C) Counts of DCX^{+};H3K27me3^{+} and DCX^{+};H3K27me3- cells within the dorsal SVZ of *ROSA26* or *Ezh2*$^{flox/flox}$;*ROSA26* mice, 10 days post-injection of Cre. n = 3 mice per experimental group, standard error of the mean displayed on bars. (D-K) Immunostaining for doublecortin (DCX) and H3K27me3 in coronal sections obtained from the SVZ of a *ROSA26* mouse, 10 days post-injection of Cre, 40X. (L-S) Immunostaining for doublecortin (DCX) and H3K27me3 in the SVZ of an *Ezh2*$^{flox/flox}$;*ROSA26* mouse, 10 days post-injection of Cre, 40X. Scale bars = 20 µm.

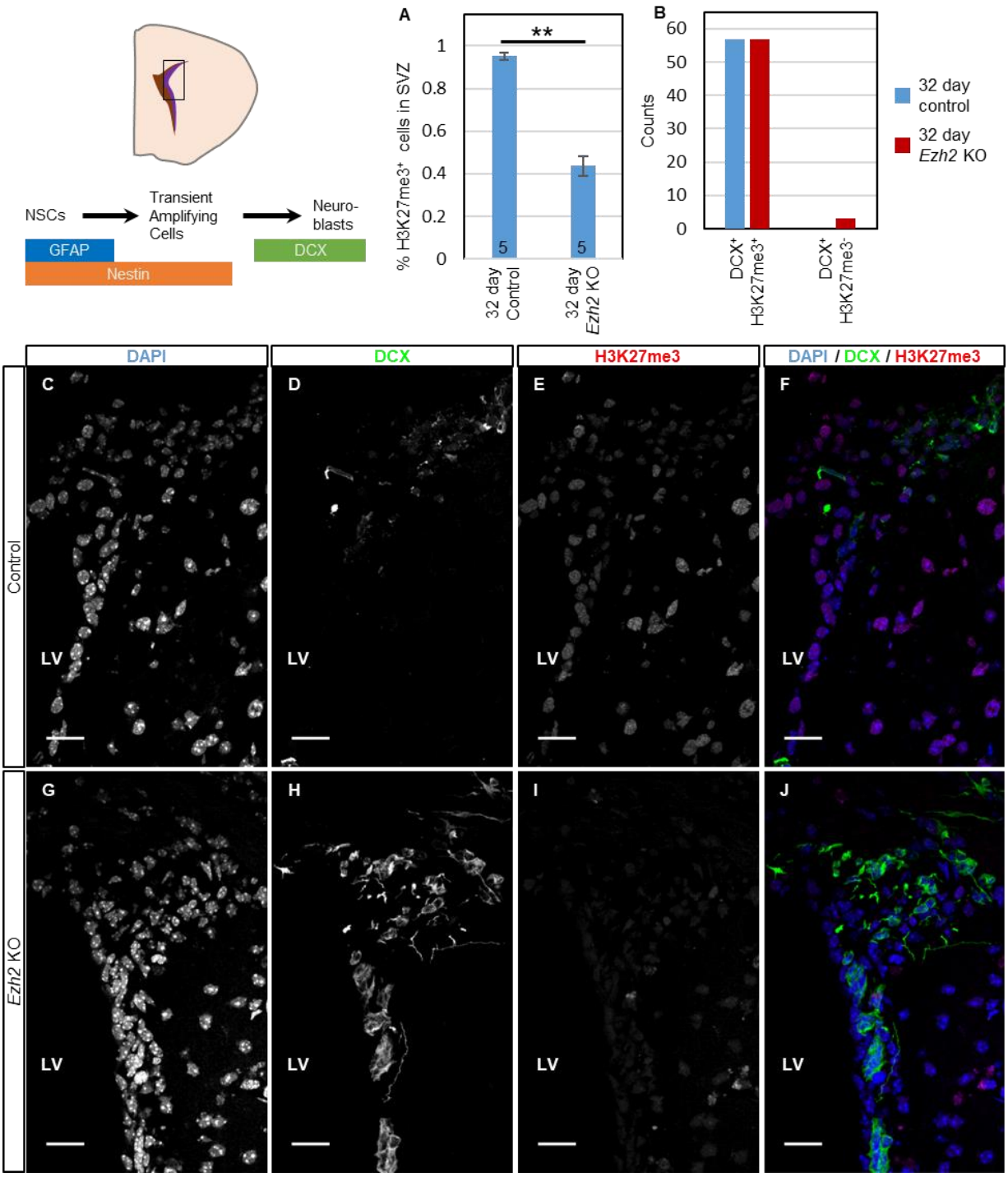

Figure 36. Loss of Ezh2 affects neuroblasts within the SVZ.

(A) Bar graph of the percentage of H3K27me3-positive cells present in the dorsal SVZ of *ROSA26* or *Ezh2*$^{flox/flox}$;*ROSA26* mice, 32 days post-injection of Cre. n = 5 mice per experimental group, p-value = 0.002, determined using T-test. Control: mean = 0.952, standard error of mean = 0.317; *Ezh2* knockout: mean = 0.436, standard error of mean = 0.052 (B) Counts of DCX^{+};H3K27me3^{+} and DCX^{+};H3K27me3- cells within the dorsal SVZ of *ROSA26* or *Ezh2*$^{flox/flox}$;*ROSA26* mice, 32 days post-injection of Cre. n = 5 mice per experimental group. (C-F) Immunostaining for doublecortin (DCX) and H3K27me3 in coronal sections obtained from the SVZ of a *ROSA26* mouse, 32 days post-injection of Cre, 40X. (G-J) Immunostaining for doublecortin (DCX) and H3K27me3 in the SVZ of an *Ezh2*$^{flox/flox}$;*ROSA26* mouse, 32 days post-injection of Cre, 40X. Scale bars = 20 µm.

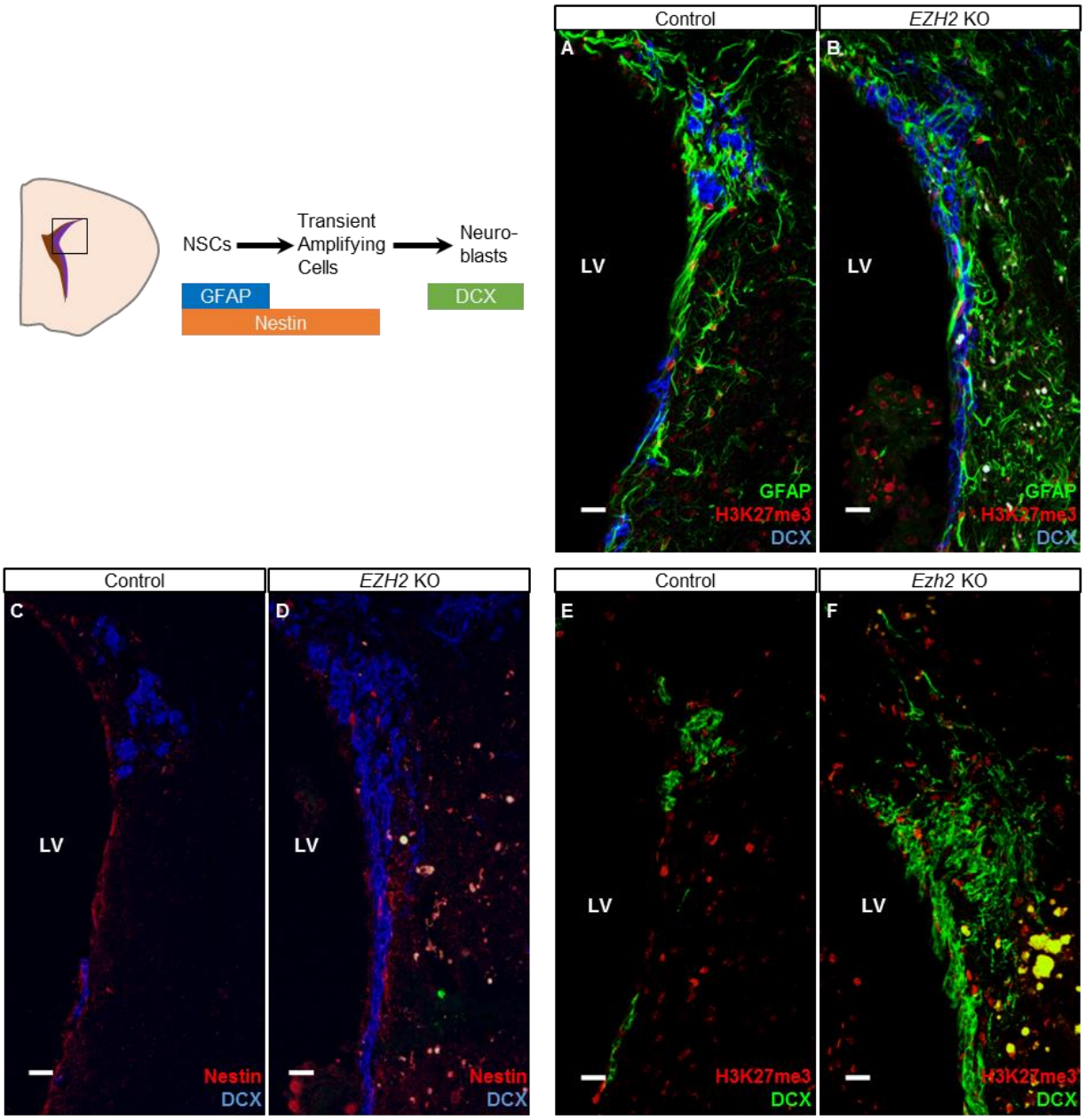

Figure 37. Sustained loss of Ezh2 alters H3K27me3-positive populations within adult SVZ.
(A-B) Triple immunostaining for GFAP, DCX and H3K27me3 for the SVZ of *Ezh2*$^{flox/flox}$;*ROSA26* control mouse (A) and 32 days post-injection of Cre protein (B). (C-D) Double immunostaining for Nestin and DCX for the SVZ from *Ezh2*$^{flox/flox}$;*ROSA26* control mouse (C) and 32 days post-injection of Cre protein (D). (E-F) Double immunostaining for H3K27me3 and DCX for the SVZ from *Ezh2*$^{flox/flox}$;*ROSA26* control mouse (E) and 32 days post-injection of Cre protein (F). Scale bars = 20 µm.

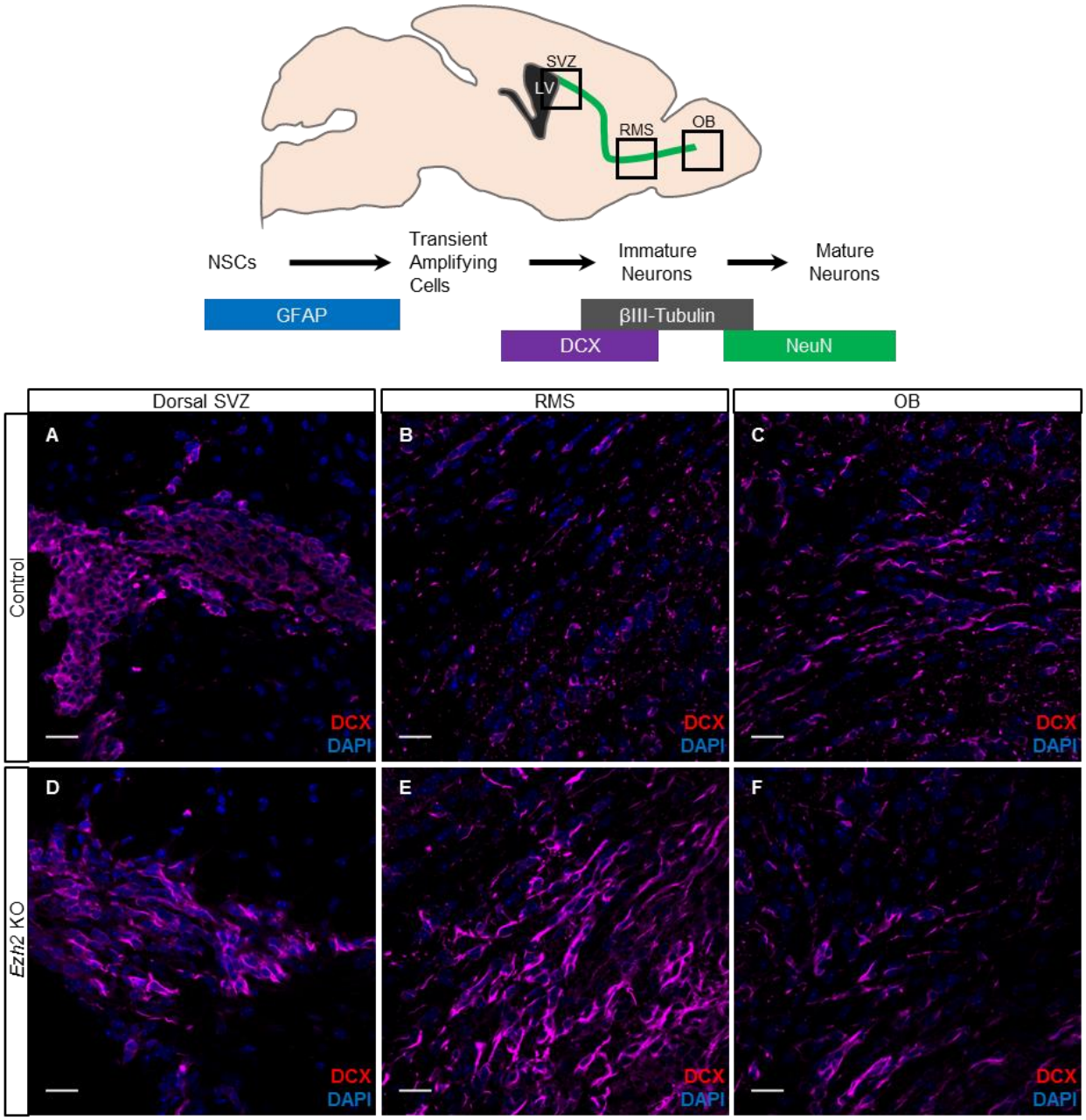

Figure 38. Loss of Ezh2 induces NB migration away from SVZ
(A-C) *Ezh2*$^{flox/flox}$;*ROSA26* mouse, 5 days post-injection of vehicle demonstrates typical DCX^{+} NBs within the dorsal SVZ (A), RMS (B), and olfactory bulb (C). (D-F) *Ezh2*$^{flox/flox}$;*ROSA26* mouse, 5 days post-injection of Cre protein demonstrates DCX^{+} NBs within the dorsal SVZ (D), RMS (E), and olfactory bulb (F).

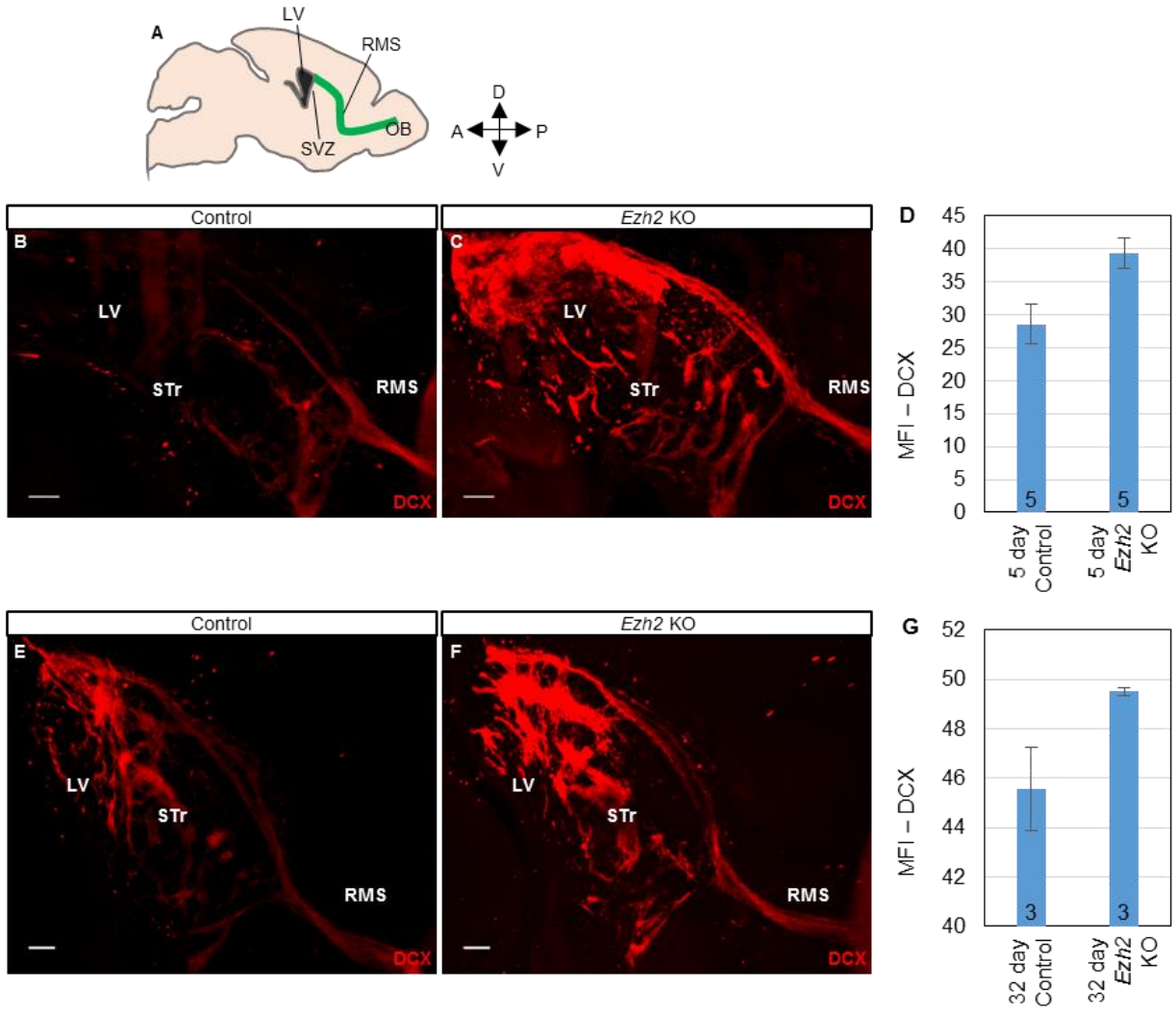

Figure 39. Loss of Ezh2 alters neuroblast migration.
(A) Scheme depicting sagittal sectioned adult mouse brain containing SVZ, RMS and OB. (B-G) Brain was sectioned along sagittal plane to a thickness of 2 mm prior to iDISCO based DCX detection (i.e. anti-DCX antibody incubation and tissue clearing). (B) Light sheet imaging of *Ezh2*$^{flox/flox}$;*ROSA26* forebrain, 5 days post-injection of vehicle. (C) Light sheet imaging of forebrain from *Ezh2*$^{flox/flox}$;*ROSA26* mouse 5 days post-injection (DPI) of Cre indicates increased DCX+ cells along dorsal SVZ, RMS, and nearby striatum. (D) The pixel mean fluorescence intensity (MFI) within the threshold regions was then recorded. n = 5 mice per experimental group, standard error of the mean displayed on bars. (E) Light sheet imaging of forebrain of *Ezh2*$^{flox/flox}$;*ROSA26* mouse, 32 days post-injection of vehicle. (F) Light sheet imaging of forebrain of *Ezh2*$^{flox/flox}$;*ROSA26*, 32 days post-injection of Cre, with pixel MFI in threshold regions shown in (G) n = 3 mice per experimental group, standard error of the mean displayed on bars. Scale bars = 200 µm.

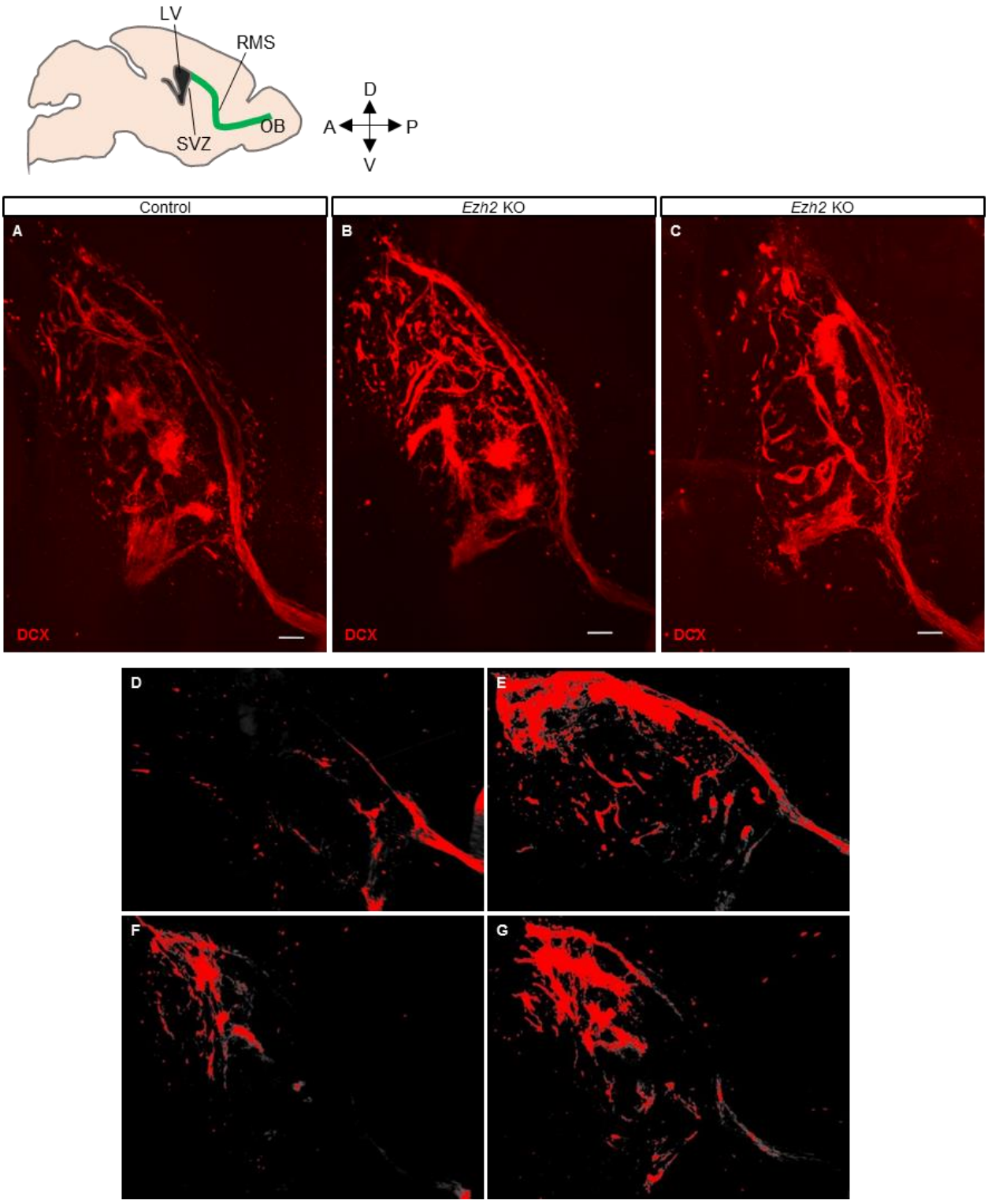

Figure 40. Light sheet microscopy images.
(A-C) Light sheet imaging of *Ezh2*$^{flox/flox}$;*ROSA26* SVZ, striatum and RMS in control (A), and 5 days post-injection (DPI) of Cre (B, C). (D-G) Representative quantification of light sheet microscopy images of SVZ in *Ezh2*$^{flox/flox}$;*ROSA26* mouse, 5 DPI of vehicle (D) 5 DPI of Cre protein (E), 32 DPI of vehicle (F), and 32 DPI of Cre protein (G). To quantify light sheet microscopy data, RGB images were converted into greyscale images prior to automatic pixel intensity thresholding by ImageJ (red region). Scale bars = 200 µm.

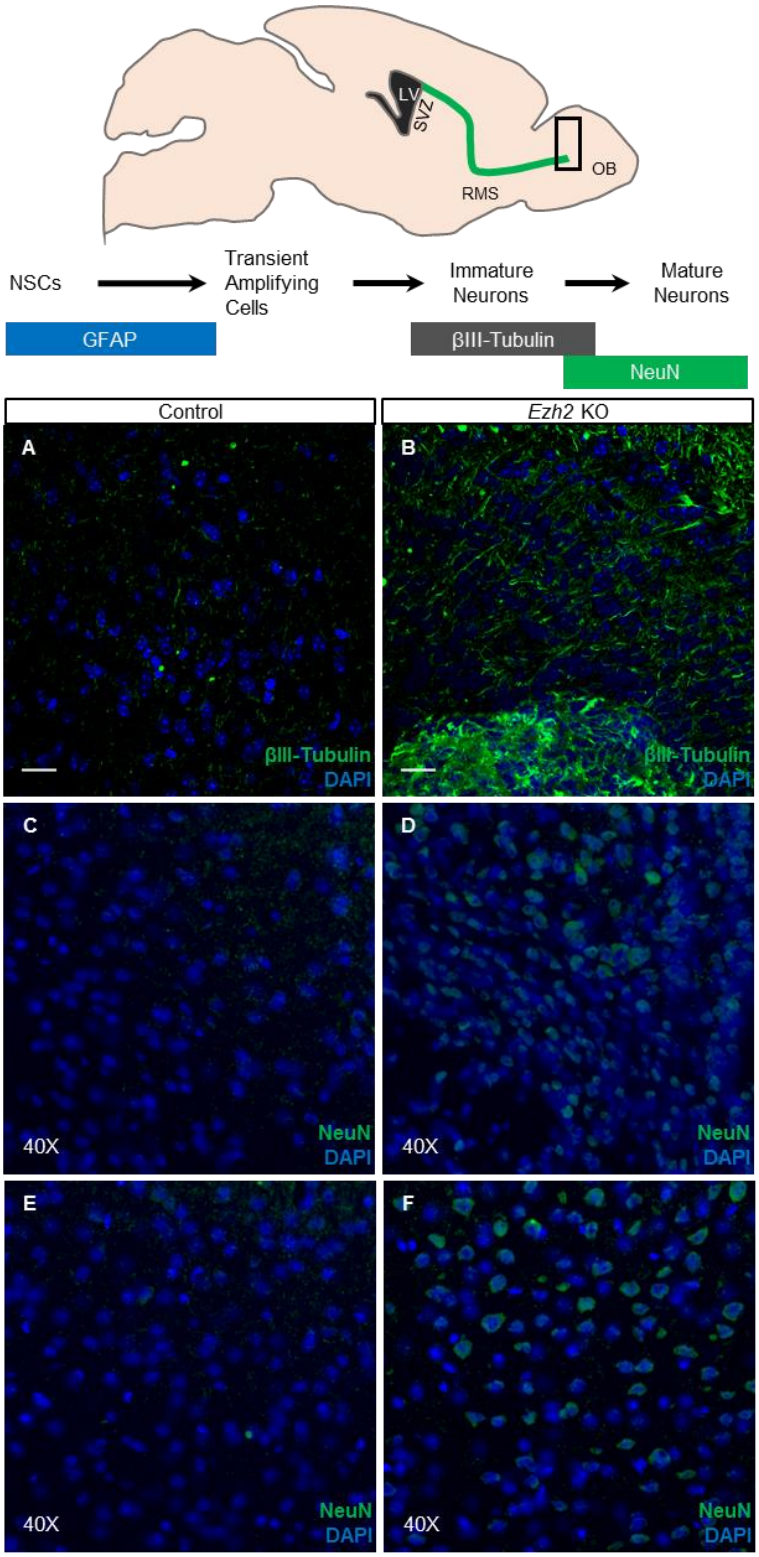

Figure 41. Loss of Ezh2 in the SVZ results in increased neuronal populations within olfactory bulb.
(A) *ROSA26* mouse olfactory bulb (OB), 10 days post-injection of Cre. OB was immunostained for βIII-Tubulin+ immature neurons. (B) OB from *Ezh2*$^{flox/flox}$;*ROSA26* mouse, 10 days post-injection of Cre. (C, E) OB from *ROSA26* mouse, 10 days post-injection of Cre. OB was immunostained for NeuN+ mature neurons, 40X. (D, F) OB from *Ezh2*$^{flox/flox}$;*ROSA26* mouse, 10 days post-injection of Cre, 40X. Scale bars = 20 µm.

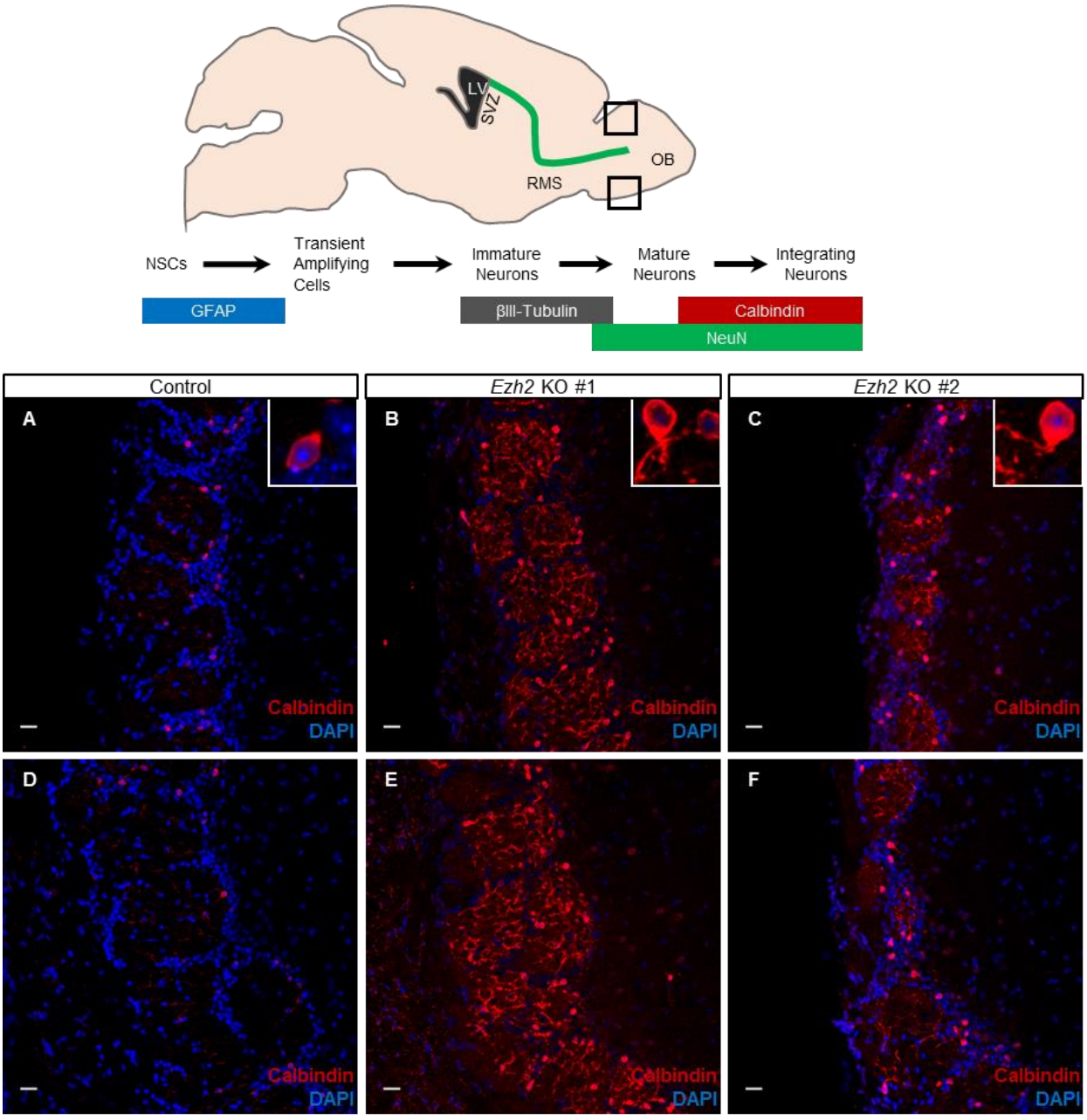

Figure 42. Loss of Ezh2 in the SVZ alters synaptic integration marker Calbinin in the olfactory bulb.
(A-C) Dorsal olfactory bulb (OB) 10 days post-injection of Cre into *ROSA26* mouse (A) or *Ezh2*$^{flox/flox}$;*ROSA26* mice (B,C). OB was immunostained for Calbindin, an interneuron marker. (D-F) Ventral olfactory bulb (OB) 10 days post-injection of Cre into *ROSA26* mouse (D) or *Ezh2*$^{flox/flox}$;*ROSA26* mice (E,F). 20X. Scale bars = 20 µm. Insets = 40X

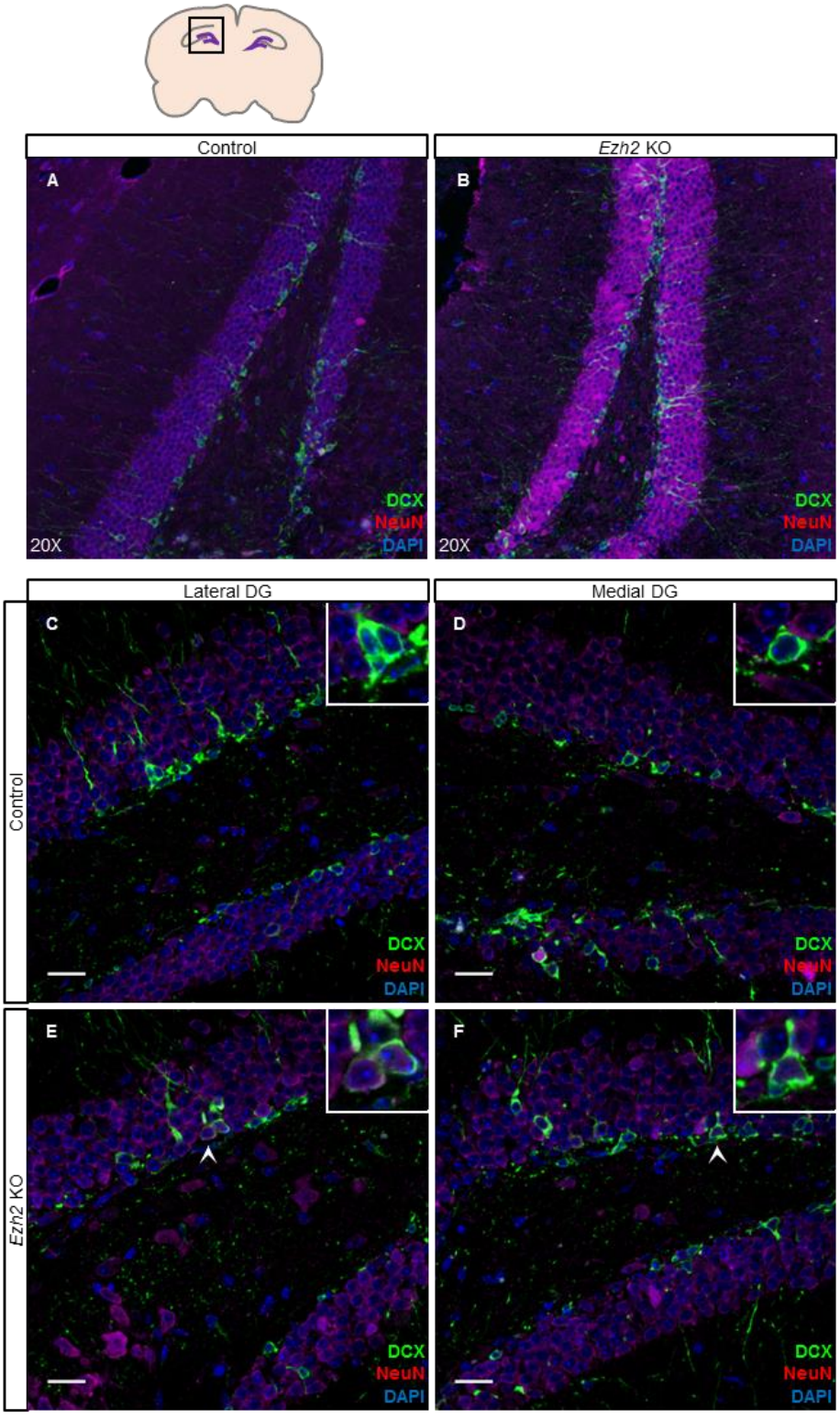

Figure 43. Loss of Ezh2 alters cell fate transition in the subgranular zone of the dentate gyrus. (A-B) The subgranular zone of the dentate gyrus (SGZ/DG) was immunostained to detect DCX^+ neuroblasts and $NeuN^+$ mature neurons of *Ezh2*$^{flox/flox}$;*ROSA26* mouse 19 days post-injection of vehicle (A) or 19 days post-injection of Cre (b), 20X. Representative images of the lateral DG (C and E) and medial DG (D and F) of *Ezh2*$^{flox/flox}$;*ROSA26* mouse, 19 days post-injection of vehicle (C and D) or 19 days post-injection of Cre (E and F). Arrows in (E,, F) indicate $DCX^+/NeuN^+$ cells. Scale bars = 20 µm. Insets = 40X.

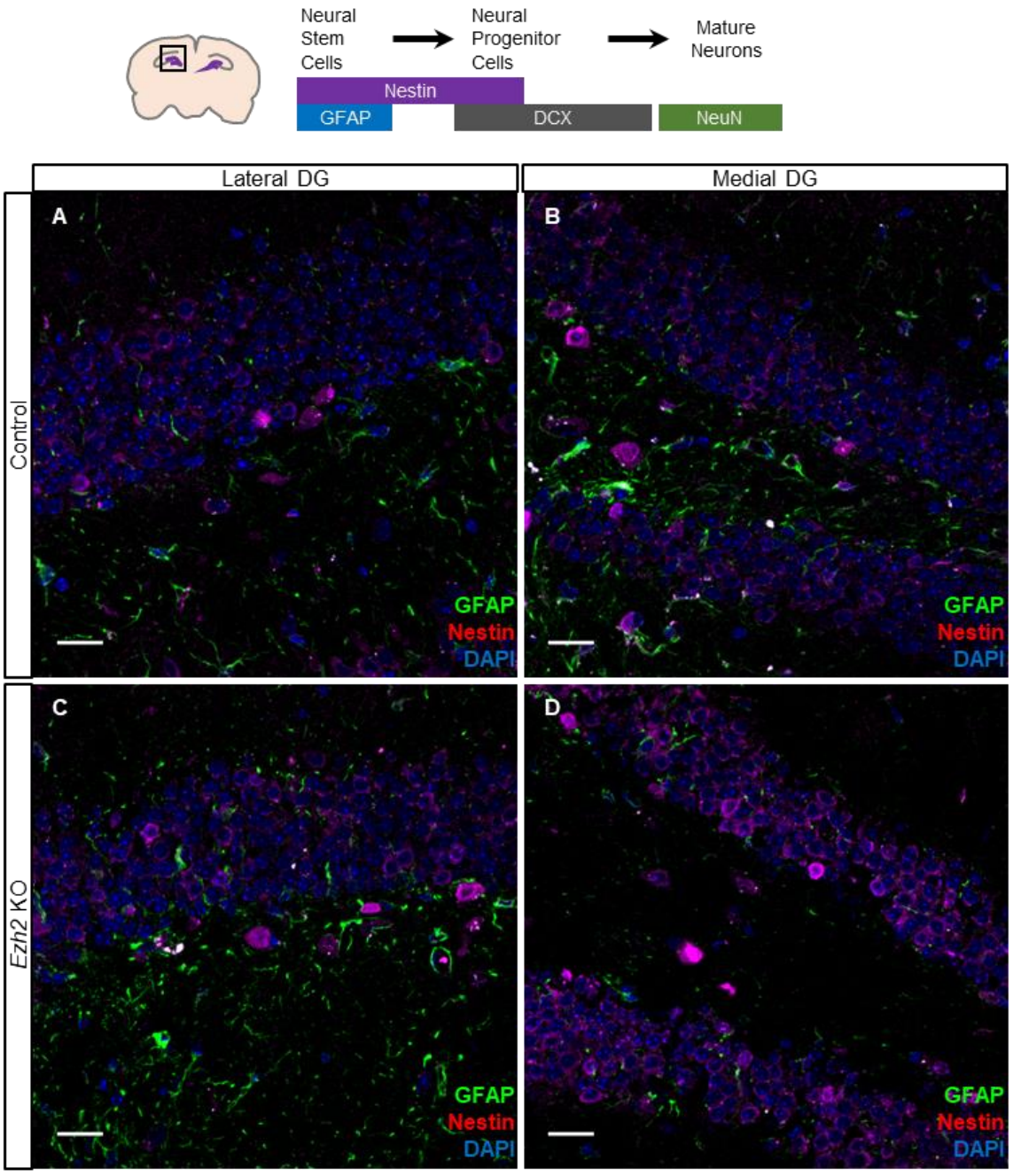

Figure 44. Loss of Ezh2 alters neural stem cell patterns in the SGZ/DG.
Lateral (A, C) and medial (B, D) regions of the SGZ/DG from *Ezh2*$^{flox/flox}$;*ROSA26* mouse, 19 days post-injection of vehicle (A and B) or Cre protein (C and D) were immunostained for GFAP and Nestin to compare distribution of NSCs, 40X. Scale bars = 20 µm.

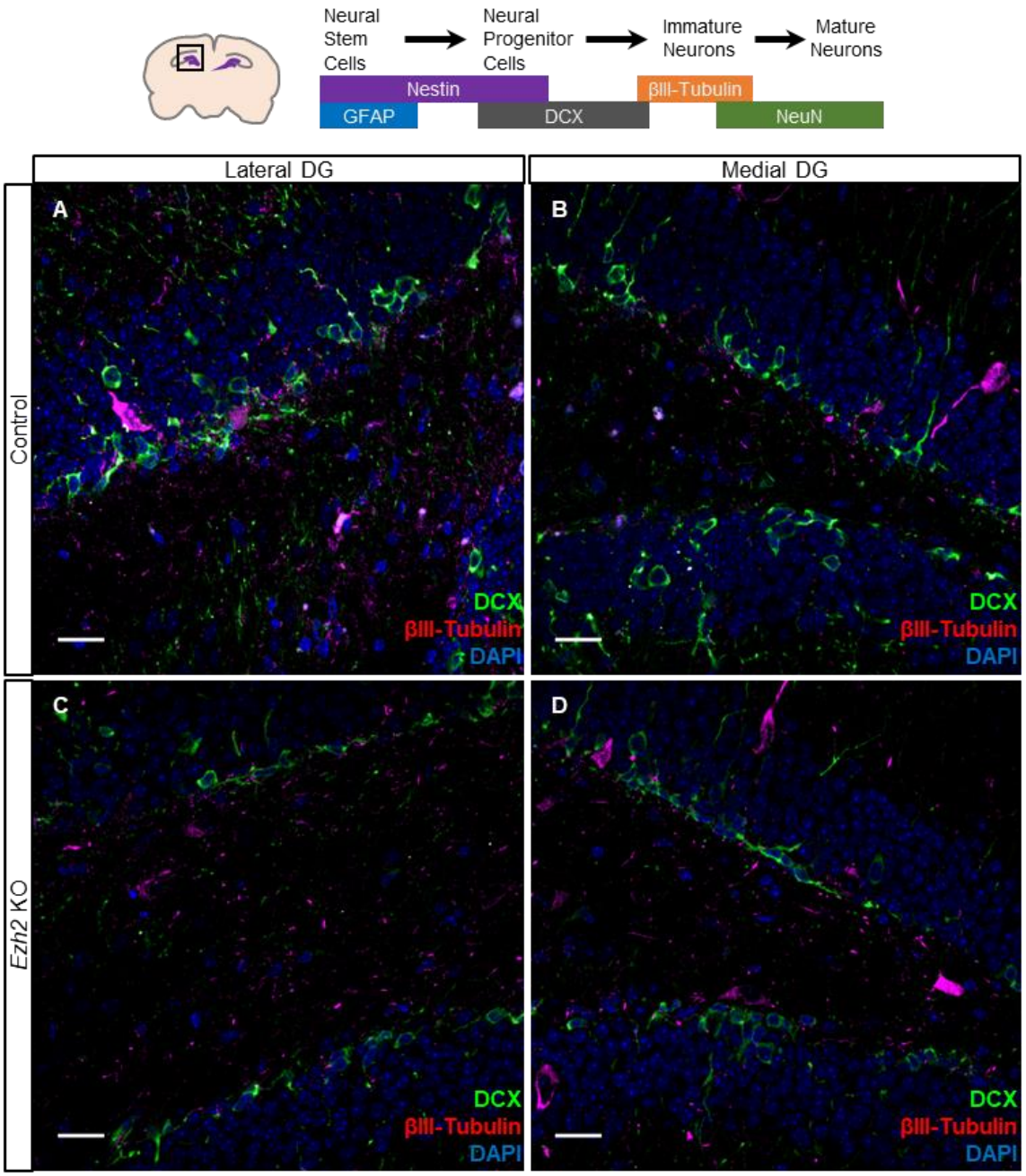

Figure 45. Loss of Ezh2 affects differentiation in SGZ/DG.
(A-B) SGZ/DG from an *Ezh2*$^{flox/flox}$;*ROSA26* mouse, 19 days post- injection of vehicle and immunostained for DCX and βIII-Tubulin. Lateral (A) and medial (B) SGZ/DG imaged. (C-D) SGZ/DG from an *Ezh2*$^{flox/flox}$;*ROSA26* mouse, 19 days post-injection of Cre protein and immunostained for DCX and βIII-Tubulin. Lateral (C) and medial (D) SGZ/DG imaged. 40X. Scale bars = 20 µm.

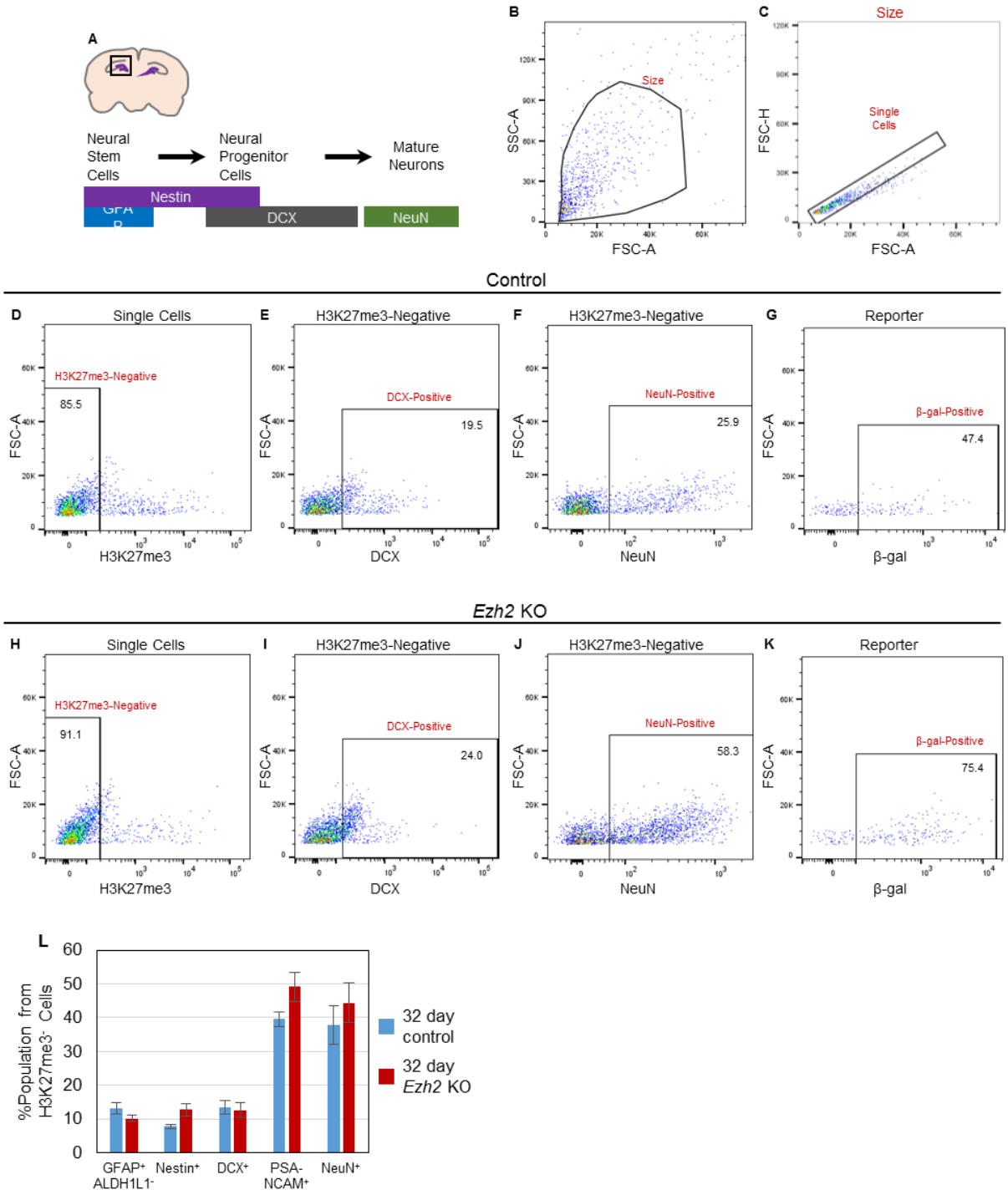

Figure 46. NSPC populations are altered post 32 day loss of Ezh2 in SGZ/DG.
(A) Schematic of NSPC markers in the SGZ/DG. Horizontal bars depict markers expressed during stepwise cell fate transition of NSPCs in the SGZ/DG. (B-K) Representative flow cytometry analysis of isolated cells from SGZ/DG shows gating strategy based on SSC-A/FSC-A (B), single cells (C), and H3K27me3-negative population in *Ezh2*$^{flox/flox}$;*ROSA26* mouse, 32 days post-injection of vehicle (control) (D-G) or Cre (*Ezh2* KO) (h-k). (E-G) Vehicle injected hemisphere. Lineage specific H3K27me3^{-}DCX^{+} (E), H3K27me3^{-}NeuN^{+} (F), and H3K27me3^{-}β-gal^{+} populations (G). (I-K) Cre injected hemisphere. Lineage specific H3K27me3^{-}DCX^{+} (I), H3K27me3^{-}NeuN^{+} (J), and H3K27me3^{-}β-gal^{+} populations (K). (L) Bar graph presents abundance of lineage specific populations. n = 4 mice per experimental group, standard error of the mean displayed on bars.

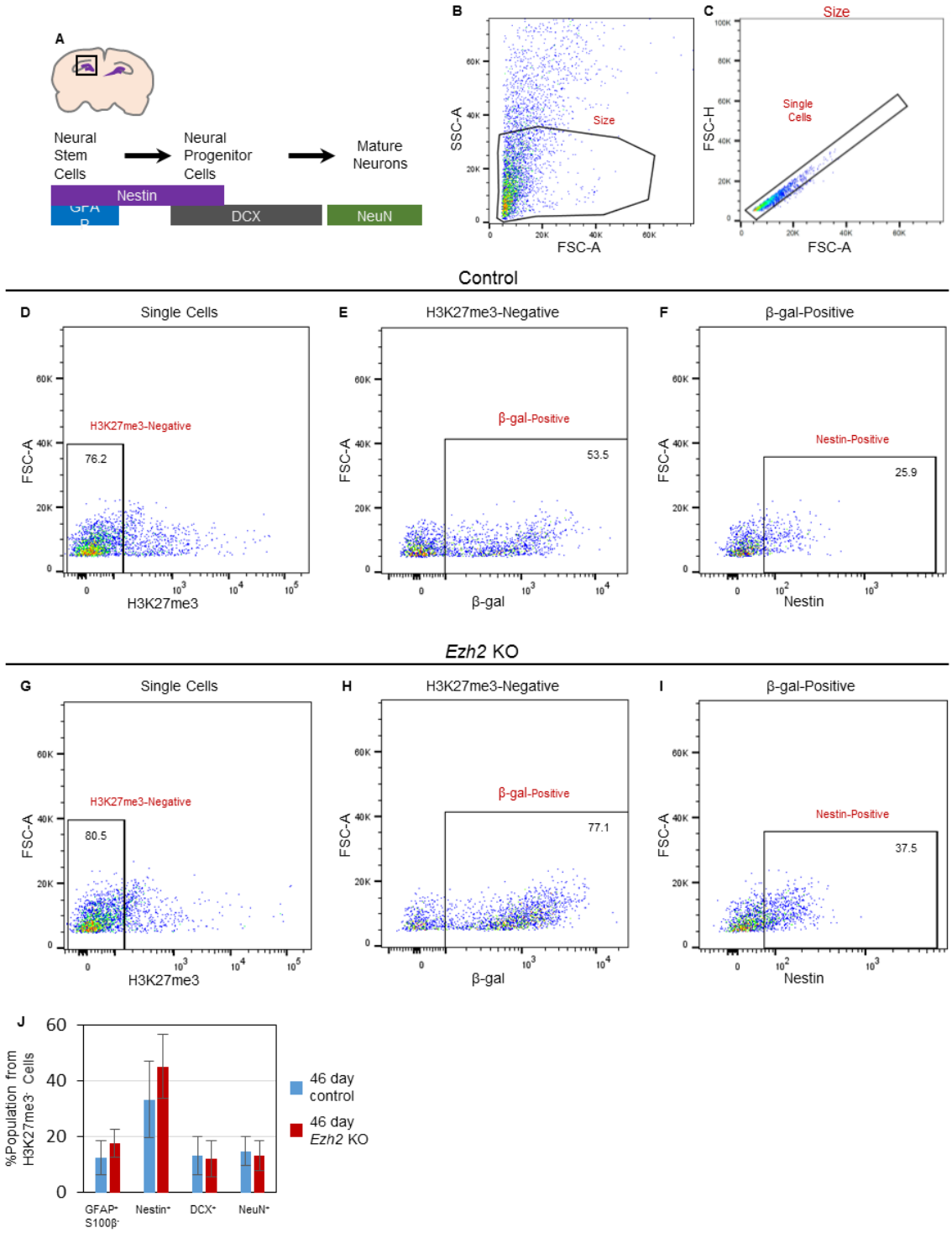

Figure 47. NSPC populations are altered post 46 day loss of Ezh2 in SGZ/DG.
(A) Schematic of NSPC markers in the SGZ/DG. Horizontal bars depict markers expressed during stepwise cell fate transition of NSPCs in the SGZ/DG. (B-I) Representative flow cytometry analysis of isolated cells from SGZ/DG shows gating strategy based on size (B), single cells (C), and H3K27me3-negative population in *Ezh2*$^{flox/flox}$;*ROSA26* mouse, 46 days post-injection of vehicle (control) (D) or Cre (*Ezh2* KO) (G). (E, F) Vehicle injected hemisphere. Lineage specific H3K27me3^{-}β-gal^{+} (E) and H3K27me3^{-}β-gal^{+}Nestin^{+} (F). (H, I) Cre injected hemisphere. Lineage specific H3K27me3^{-}β-gal^{+} (H) and H3K27me3^{-}β-gal^{+}Nestin^{+} (I). (J) Abundance of lineage specific populations are presented. n = 4 mice per experimental group, standard error of the mean displayed on bars.

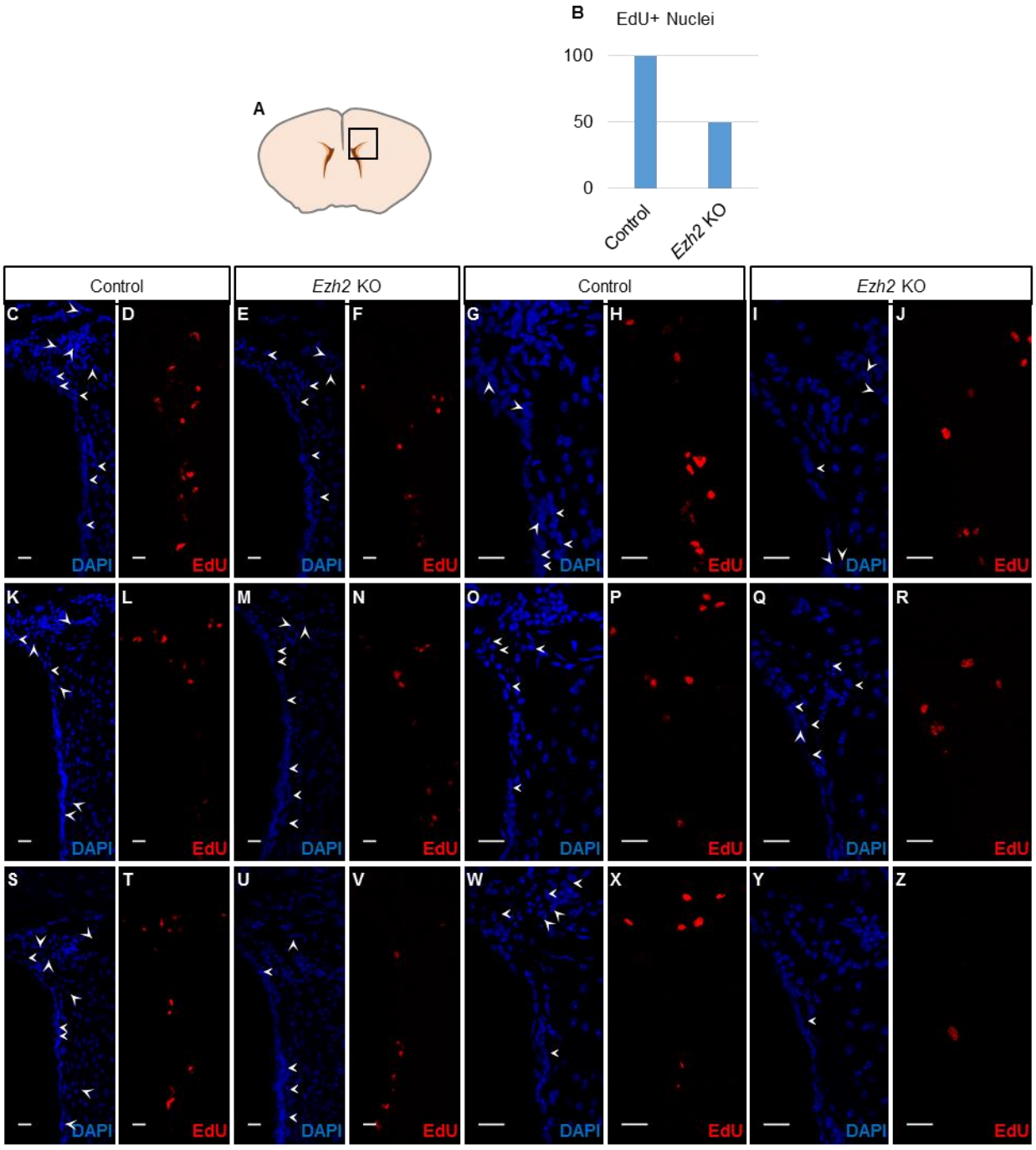

Figure 48. Ezh2/H3K27me3 influence cell cycle in the SVZ cells.
(A) Scheme of coronal sectioned mouse brain indicates region of immunostaining. Multiple images of dorsal SVZ and RMS were taken along rostrocaudal axis at 20X and 40X to obtain representative images of DAPI-positive and EdU positive nuclei. (B) Bar graph of EdU-positive nuclei within dorsal SVZ quantified using 40X magnification. y-axis indicates percentage of cells which are EdU-positive compared with control. n = 3 mice per experimental group, standard error of the mean displayed on bars. (C-Z) Cells in dorsal SVZ and rostral migratory stream 10 days after stereotaxic Cre injection into in *ROSA26* mouse (Columns labeled "Control") or *Ezh2*$^{flox/flox}$;*ROSA26* (Columns labeled "*Ezh2* KO"). DAPI counterstain detects nuclei, while EdU detects cells undergoing DNA synthesis in 2-hour labeling window. C, D, E, F, K, L, M, N, S, T, U, V = 20X; G, H, I, J, O, P, Q, R, W, X, Y, Z = 40X. Scale bars = 20 μm.

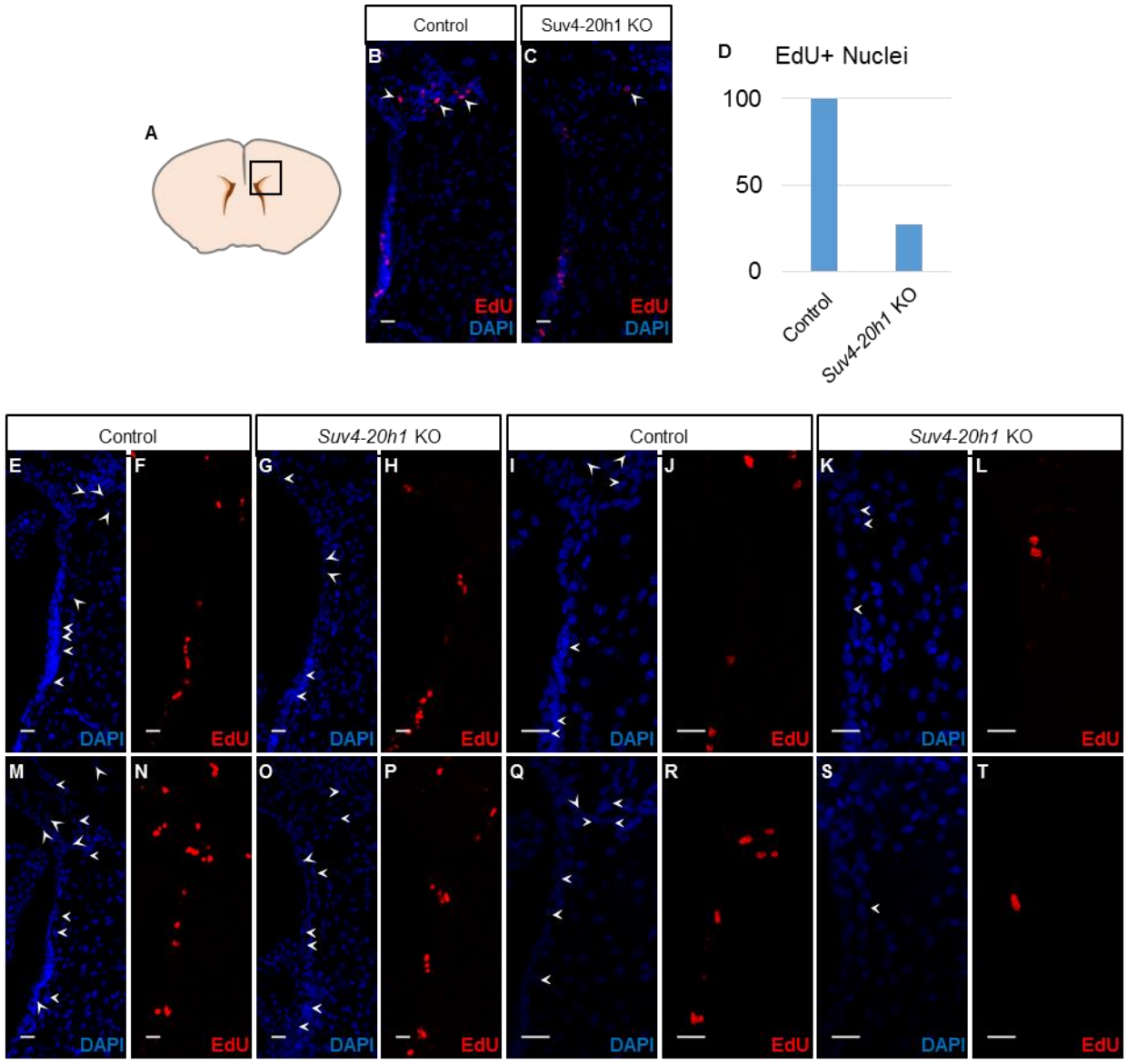

Figure 49. Suv4-20h/H4K20me3 influences cell cycle in the SVZ cells.
(A) Scheme of coronal sectioned mouse brain indicates region of immunostaining. (B, C) Colocalization of EdU and DAPI in *Suv4-20h*$^{flox/flox}$;*ROSA26*$^{Y/Y}$ mouse in noninjected SVZ (B) or Cre injected SVZ, 5 days post-injection (C). (D) Bar graph of EdU-positive nuclei within dorsal SVZ quantified using 40X magnification. y-axis indicates percentage of cells which are EdU-positive compared with control. n = 3 mice per experimental group, standard error of the mean displayed on bars. (E-S) Cells in dorsal SVZ and rostral migratory stream 10 days after surgery using *Suv4-20h*$^{flox/flox}$;*ROSA26*$^{Y/Y}$ mouse displaying uninjected SVZ (Columns labeled "Control") or Cre injected SVZ, 5 days post-injection (Columns labeled "*Suv4-20h1* KO"). DAPI counterstain detects nuclei, while EdU detects cells undergoing DNA synthesis in 2-hour labeling window. E, F, G, H, M, N, O, P = 20X; I, J, K, L, Q, R, S, T = 40X. Scale bars = 20 μm.

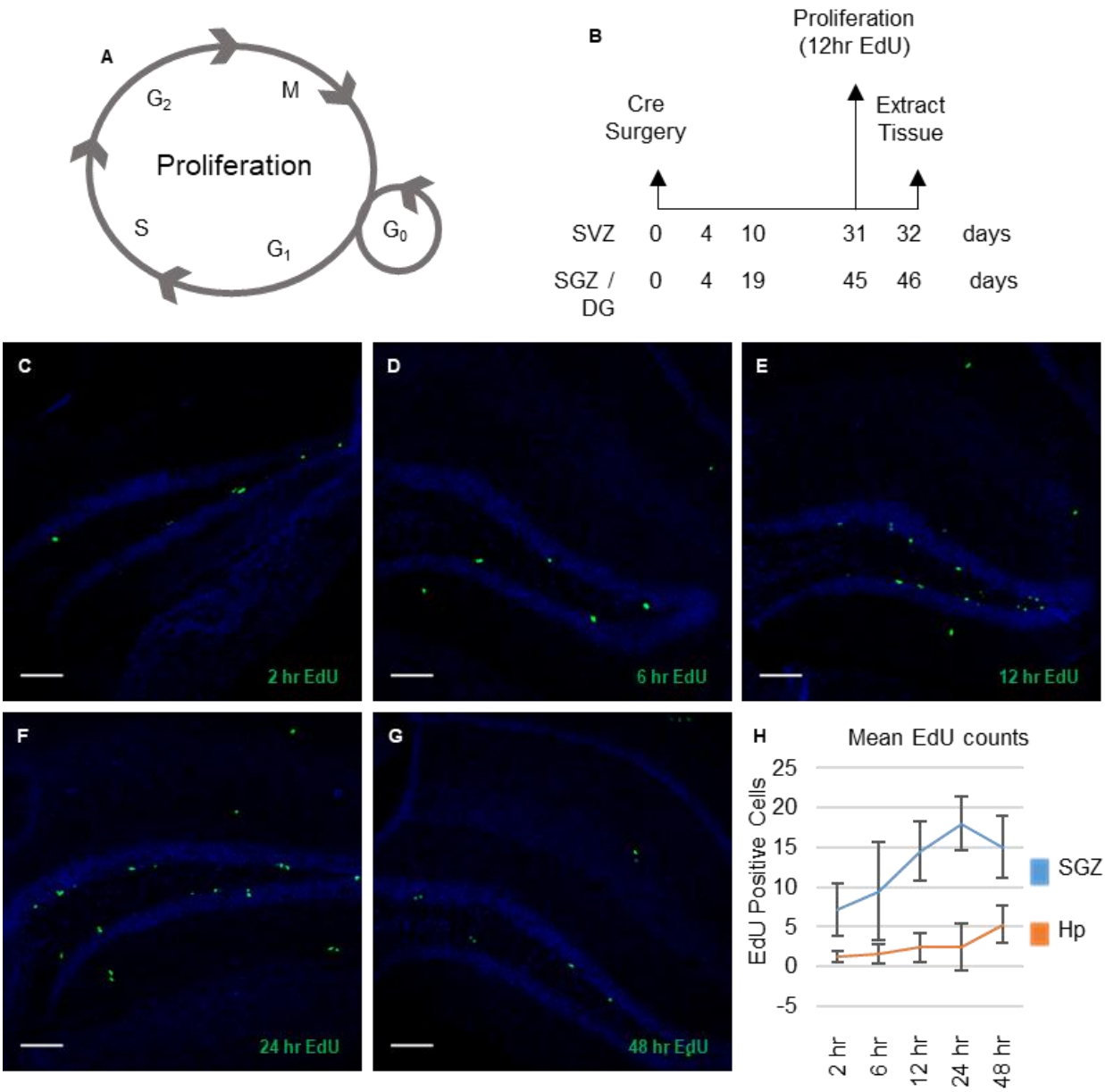

Figure 50. Edu labels NSPCs in S-phase within hippocampus of *Suv4-20h*$^{flox/flox}$;*ROSA26*$^{Y/Y}$ mice.
(A) Depiction of cell cycle stages. (B) Labeling scheme used for tracing proliferative NSPCs. Following a time course analysis, tissue collection 12 hours after intraperitoneal EdU injection. (C-G) IHC of coronal sectioned SGZ/DG following 2 hr, 6 hr, 12 hr, 24 hr, and 48 hr periods after EdU injection. (H) Graph depicting EdU-positive nuclei in the SGZ compared to the entire hippocampus.

A

Population	46 day control		46 day *Suv4-20h1* KO		p-value
	% Parent Gated - mean	% Parent Gated - SD	% Parent Gated - mean	% Parent Gated - SD	
All	100	0	100	0	NA
Focus	95.68666667	2.387055369	96.67	2.057304061	NA
Singlets	65.35666667	7.767170227	67.42333333	9.539393761	NA
Cells	56.2	4.655523601	58.68666667	3.765001107	NA
EdU	80.13333333	3.319824293	86.40666667	2.378578007	0.06247

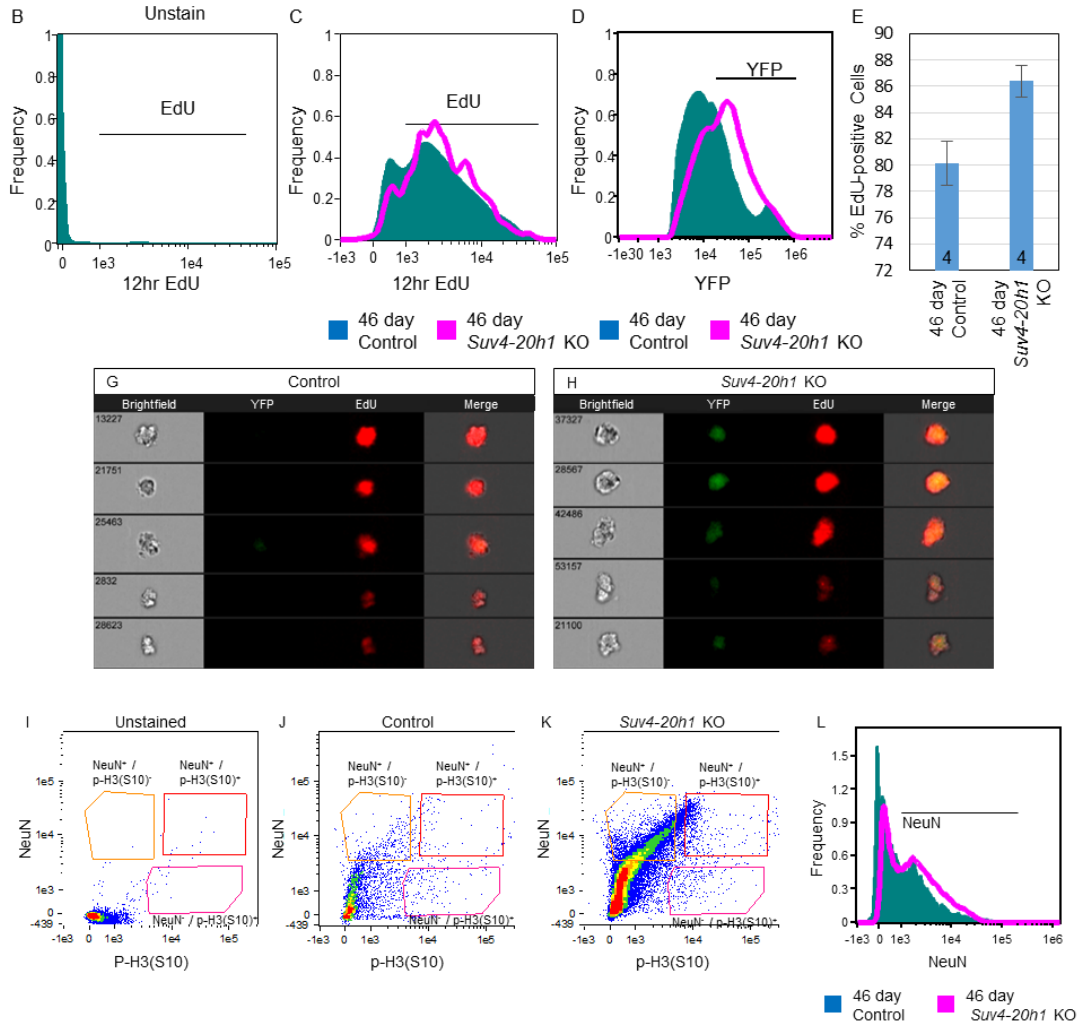

Figure 51. Suv4-20h mediates S-phase progression of NSPCs in SGZ/DG.
(A) Table indicating gating scheme used for population analyses, including test populations, mean % of parent population, standard deviation of each population and p-value, if applicable, for control and *Suv4-20h1* knockout experimental groups. (B-C) Histogram of EdU in SGZ/DG cells from unstained population (B), and vehicle or Cre (C) injected hemispheres of *Suv4-20h*$^{flox/flox}$;*ROSA26*$^{Y/Y}$ mouse, 46 days post-injection. (D) Histogram of YFP expression in SGZ/DG cells from vehicle or Cre injected hemispheres of *Suv4-20h*$^{flox/flox}$;*ROSA26*$^{Y/Y}$ mouse, 46 days post-injection. (E) Bar graph of the percentage of 12 hr. EdU-positive cells present in the dorsal SVZ of *ROSA26*$^{Y/Y}$ or *Suv4-20h*$^{flox/flox}$;*ROSA26*$^{Y/Y}$ mice, 46 days post-injection of Cre. n = 4 mice per experimental group, standard error of the mean displayed on bars. (G-H) Representative images of 12 hr. EdU labeled cells from vehicle injected (G) or Cre injected (H) hemispheres of *Suv4-20h*$^{flox/flox}$;*ROSA26*$^{Y/Y}$ mouse (from C), displaying brightfield, YFP, EdU and merged channels. (I-K) NeuN and phospho-H3(S10) in SGZ/DG cells from unstained population (I), vehicle injected (J), and Cre injected (K) hemispheres of *Suv4-20h*$^{flox/flox}$;*ROSA26*$^{Y/Y}$ mouse, 46 days post-injection (L) Histogram of NeuN^{+} neurons from vehicle and Cre injected hemispheres of *Suv4-20h*$^{flox/flox}$;*ROSA26*$^{Y/Y}$ mouse, 46 days post-injection

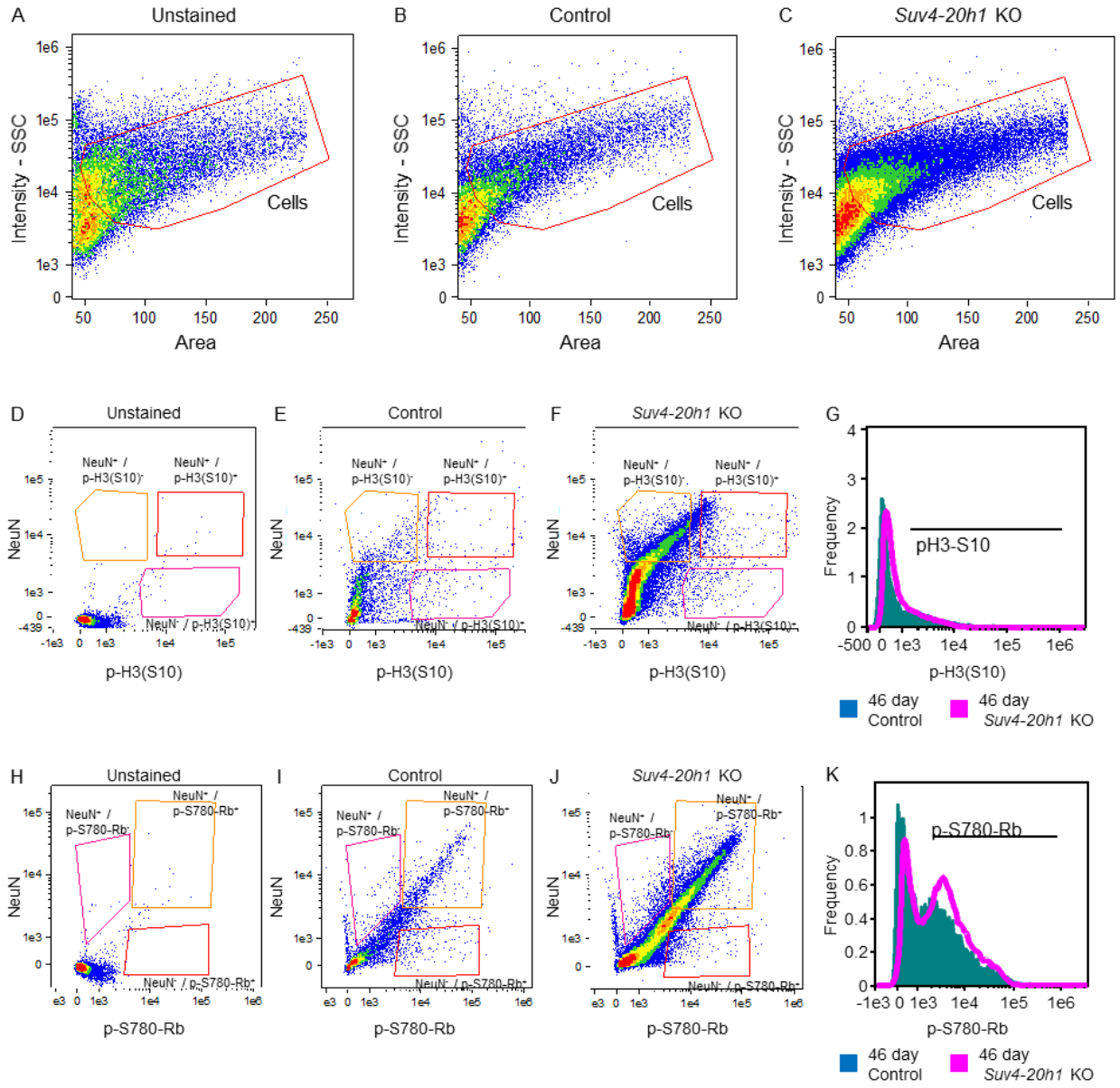

Figure 52. Loss of Suv4-20h has no effect on M-phase in the SGZ/DG.
(A-C) Representative flow cytometry analysis of isolated cells from SGZ/DG shows gating strategy based on Area/Intensity-SSC of unstained population (A), vehicle injected (control) (B), or Cre injected (*Suv4-20h1* KO) (C) in *Suv4-20h*$^{flox/flox}$;*ROSA26*$^{Y/Y}$ mouse, 46 days post-injection.
(D-F) Scatterplots of isolated cells from SGZ/DG of unstained (D), vehicle injected (control) (E) or Cre injected (F) populations in *Suv4-20h*$^{flox/flox}$;*ROSA26*$^{Y/Y}$ mouse, 46 days post-injection. Vehicle and Cre injected populations were labeled with NeuN and phospho-H3(S10). (G) Histogram of phospho-H3(S10) labeled cells from vehicle and Cre injected hemispheres of *Suv4-20h*$^{flox/flox}$;*ROSA26*$^{Y/Y}$ mouse, 46 days post-injection. (H-J) Scatterplots of isolated cells from SGZ/DG of unstained (H), vehicle injected (control) (I) or Cre injected (J) populations in *Suv4-20h*$^{flox/flox}$;*ROSA26*$^{Y/Y}$ mouse, 46 days post-injection. Vehicle and Cre injected populations were labeled with NeuN and phospho-S780-Rb. (K) Histogram of phospho-S780-Rb labeled cells from vehicle and Cre injected hemispheres of *Suv4-20h*$^{flox/flox}$;*ROSA26*$^{Y/Y}$ mouse, 46 days post-injection.

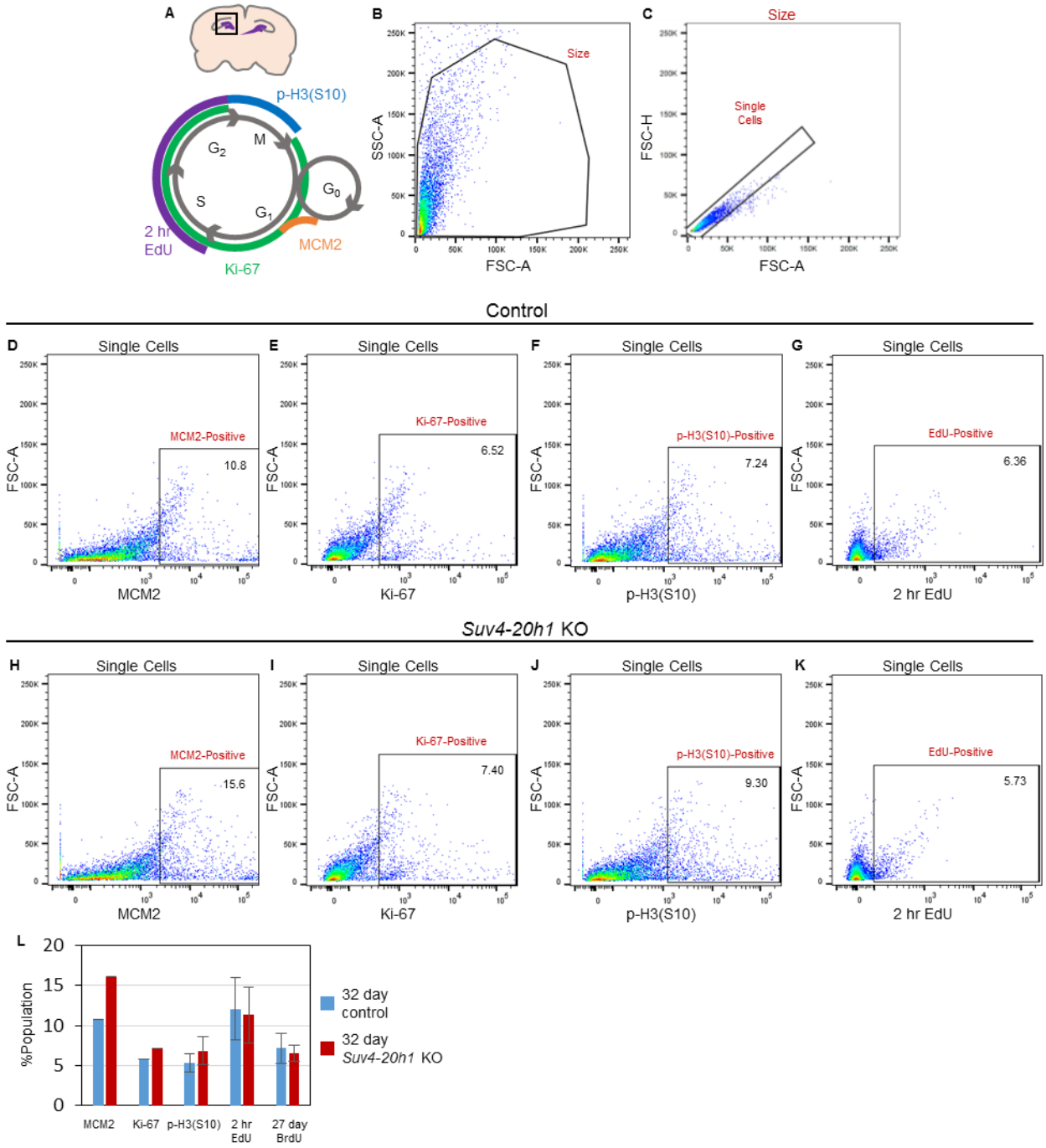

Figure 53. Loss of Suv4-20h marginally alters cell cycle progression in the SGZ/DG.
(A) Depiction of cell cycle specific markers used for flow cytometry analysis. (B-K) Representative flow cytometry analysis of isolated cells from SGZ/DG shows gating strategy based on SSC-A/FSC-A (B), single cells (C), and cell cycle specific markers (D-K) in *Suv4-20h*$^{flox/flox}$;*ROSA26* mouse, 32 days post-injection of vehicle (control) (D-G) or Cre (*Suv4-20h1* KO) (H-K). (D-G) Population analysis from vehicle injected hemisphere: Cell cycle markers MCM2+ (D), proliferating Ki-67+ (E), p-H3(S10)+ (F), and 2-hour EdU+ (G) . (H-K) Population analysis from Cre injected hemisphere: Cell cycle markers MCM2+ (H), proliferating Ki-67+ (I), p-H3(S10)+ (J), and 2-hour EdU+ (K). (L) Abundance of lineage specific populations are presented.

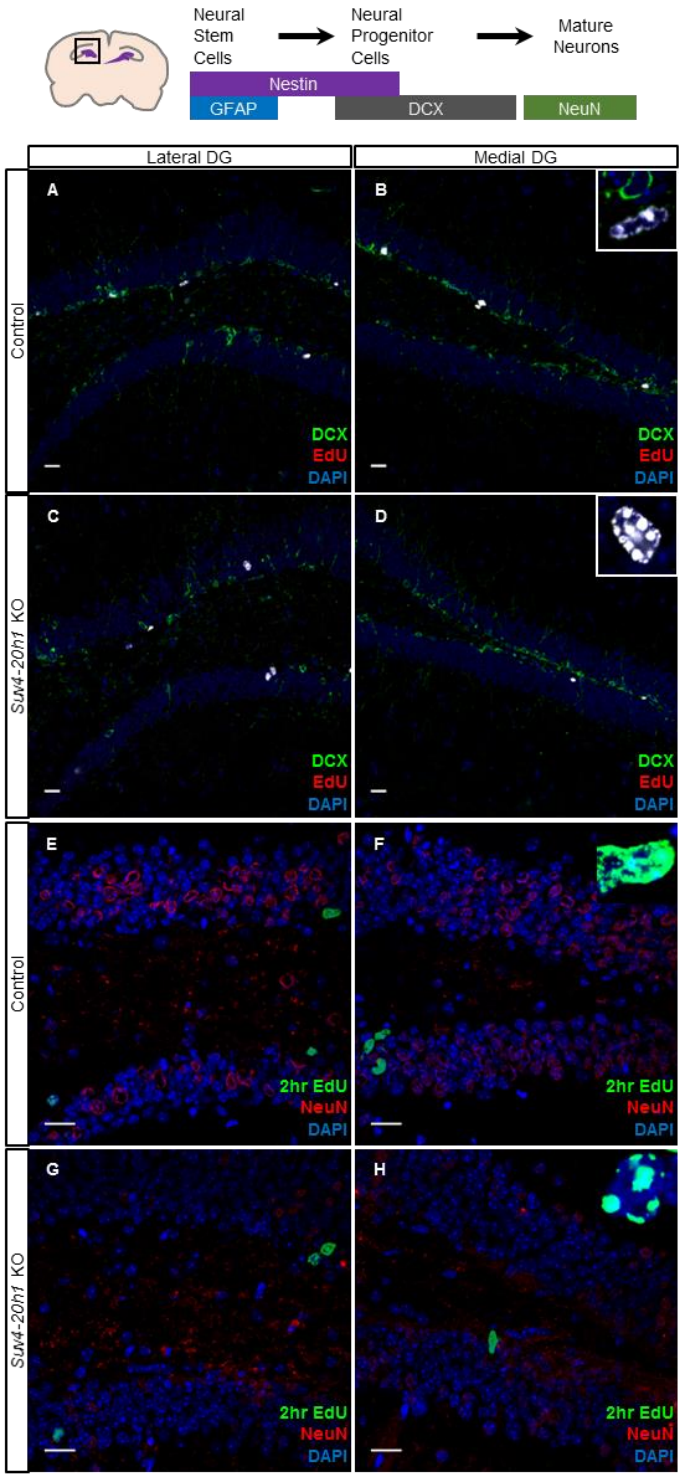

Figure 54. Loss of Suv4-20h has no significant effect on DCX^+, $NeuN^+$ and short-term tracing proliferative cells in the SGZ/DG.

(A-D) Representative images showed lateral SGZ/DG of *Suv4-20h*$^{flox/flox}$;*ROSA26* mouse with DCX immunostaining and 2 hr. EdU, 19 days post-injection of vehicle (A) or Cre (C). Medial SGZ/DG of *Suv4-20h*$^{flox/flox}$;*ROSA26* mouse was immunostained for DCX and 2 hr. EdU, 19 days post-injection of vehicle (B) or Cre (D). (E-H) Lateral SGZ/DG was immunostained for NeuN and 2 hr. EdU, 19 days post-injection of vehicle (E) or Cre (G). Medial SGZ/DG of *Suv4-20h*$^{flox/flox}$;*ROSA26* mouse was immunostained for NeuN and 2 hr. EdU, 19 days post-injection of vehicle (F) or Cre (H). Scale bars = 20 µm. Magnification: A-D = 20X, E-H = 40X. Insets for A-D = 40X, insets for F-H = 63X.

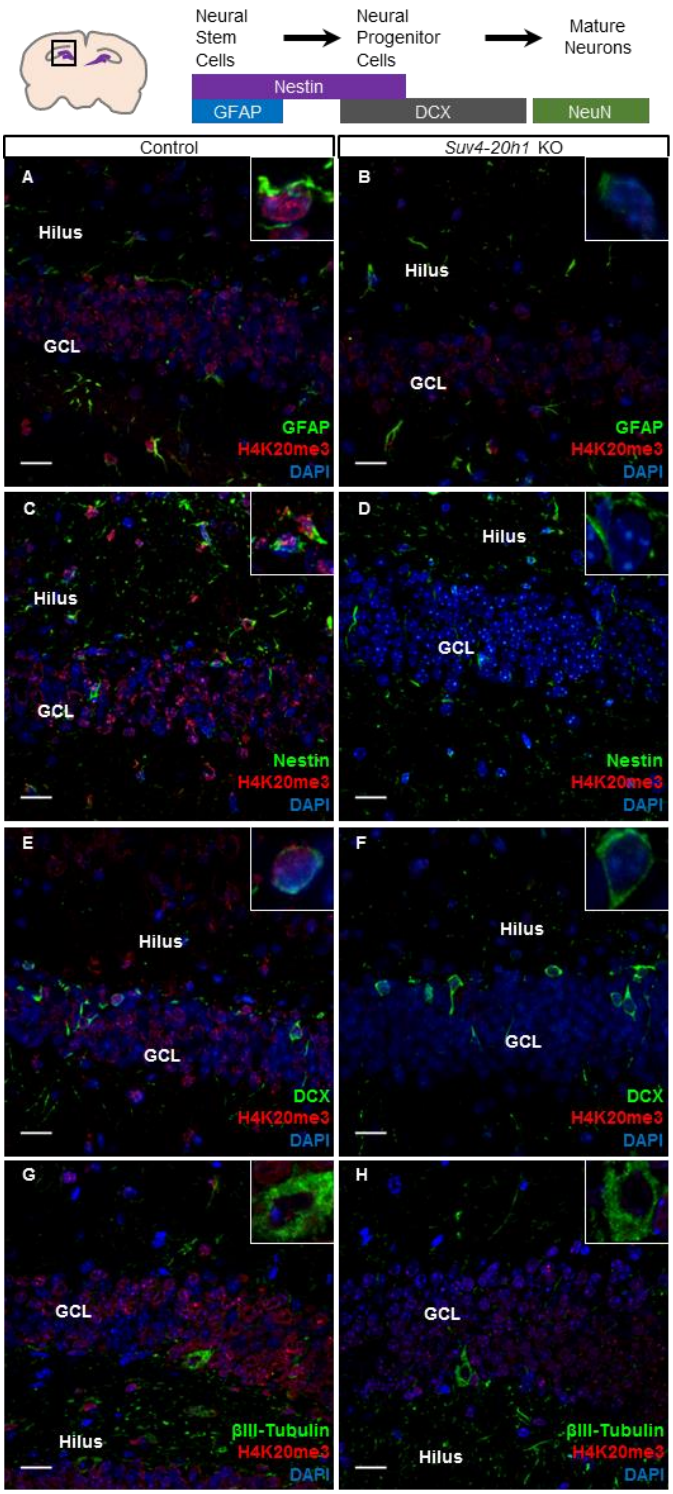

Figure 55. Loss of Suv4-20h marginally decreases NSPCs populations in the SGZ/DG.
(A-B) SGZ/DG from a *Suv4-20h*$^{flox/flox}$;*ROSA26* mouse, 19 days post-injection of vehicle (A) or Cre (B) was immunostained for GFAP and H4K20me3, 40X. (C-D) SGZ/DG of *Suv4-20h*$^{flox/flox}$;*ROSA26* mouse, 19 days post-injection of vehicle (C) or Cre (D) was immunostained for Nestin and H4K20me3, 40X. (E-F) SGZ/DG of *Suv4-20h*$^{flox/flox}$;*ROSA26* mouse, 19 days post-injection of vehicle (E) or Cre (F) was immunostained for DCX and H4K20me3, 40X. (G-H) SGZ/DG of *Suv4-20h*$^{flox/flox}$;*ROSA26* mouse, 19 days post-injection of vehicle (G) or Cre (H) was immunostained for βIII-Tubulin and H4K20me3, 40X. Scale bars = 20 µm. Insets for = 63X.

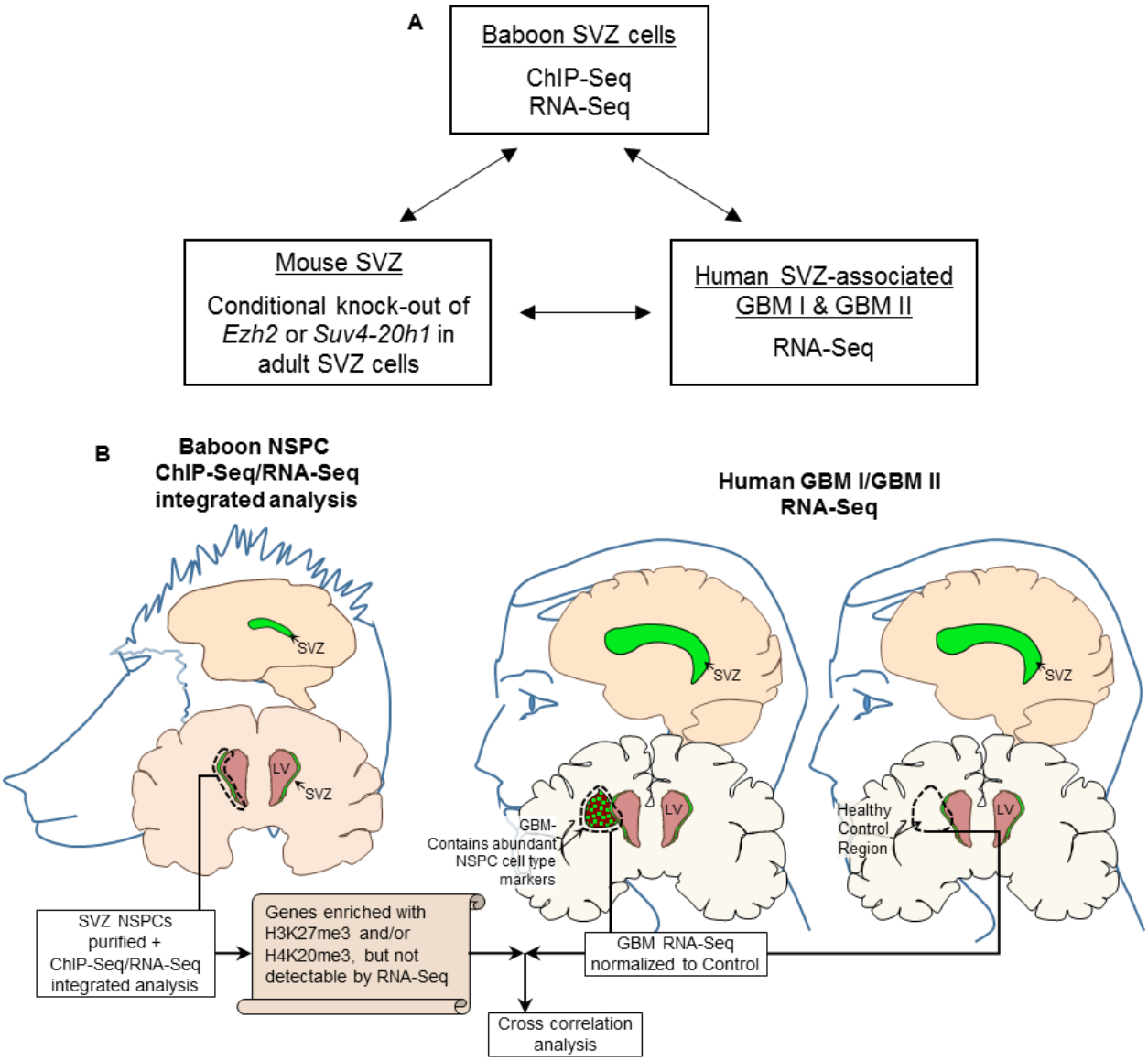

Figure 56. Experimental design for correlation between genes in normal NSPCs enriched with H3K27me3 or H4K20me3 without detectable transcripts and genes altered in MRI-classified group I and group II GBM.
Graphical diagram illustrates the experimental design and analyses. Left panel: ChIP-Seq identified H3K27me3- and H4K20me3-enriched genes in normal NSPCs isolated from baboon SVZ and RNA-Seq analysis of normal NSPCs isolated from baboon SVZ. Right panel: RNA-Seq and Cuffdiff determined differential gene expression of human GBM I and GBM II compared with normal human specimens within correlated brain regions.

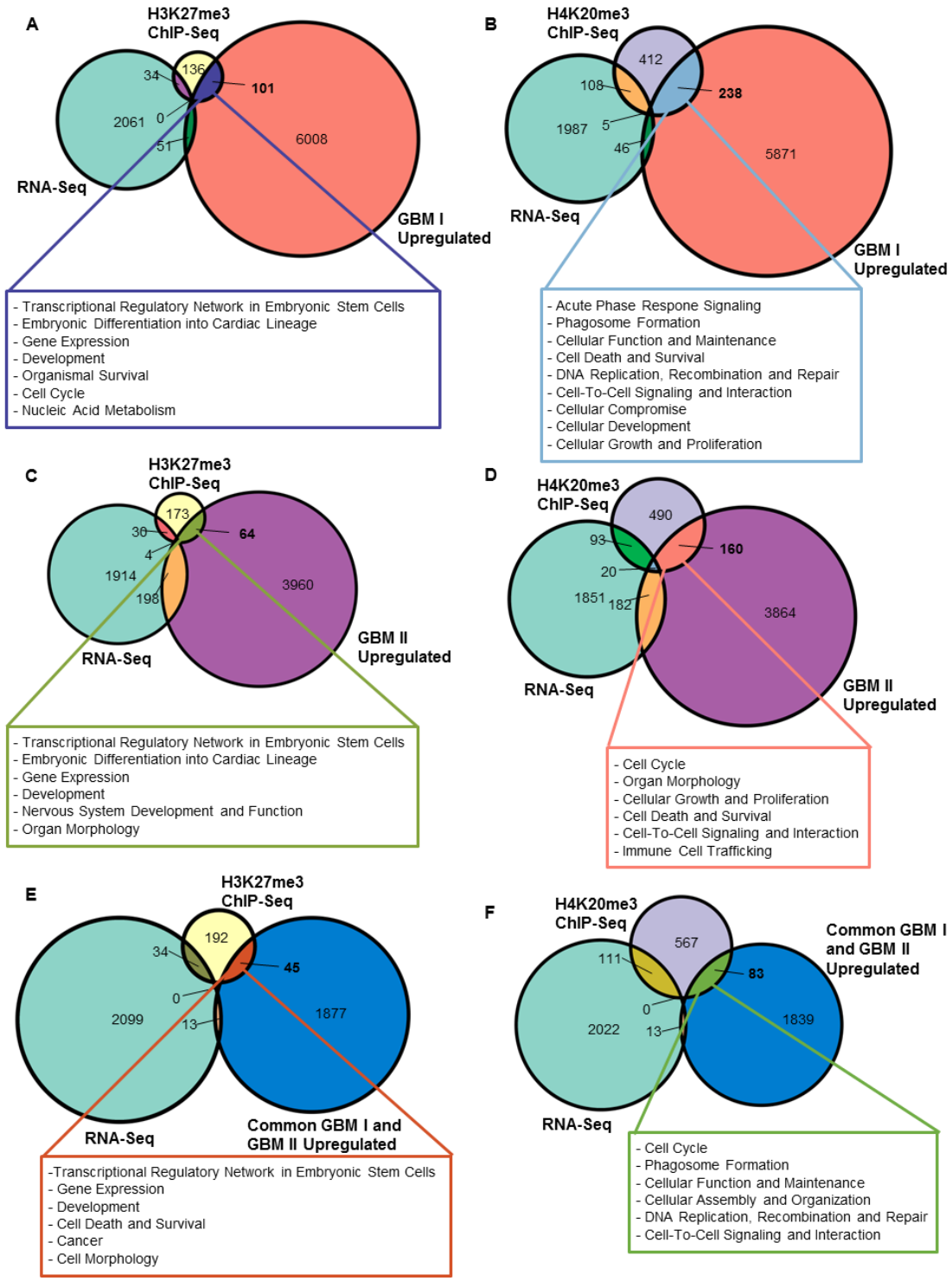

Figure 57. Comparison among genes in normal NSPCs enriched with H3K27me3 or H4K20me3, genes without detectable transcripts in normal NSPCs, and genes elevated in MRI-classified group I and group II GBM.
(A, B) Proportional Venn diagram of 3-way comparisons involving genes in NSPCs enriched with H3K27me3 (A) or H4K20me3 (B), undetectable genes in NSPCs by RNA-Seq (≤1 FPKM), and genes elevated in SVZ-associated human GBM I tumors. Text box indicates gene function as predicted by IPA. (C, D) Proportional Venn diagram of genes in NSPCs enriched with H3K27me3 (C) or H4K20me (D), undetectable genes in NSPCs by RNA-Seq (≤1 FPKM), and upregulated genes in GBM II. (E, F) Proportional Venn diagram of genes in NSPCs enriched with H3K27me3 (E) or H4K20me3 (F), undetectable genes in NSPCs by RNA-Seq (≤1 FPKM), upregulated genes in GBM I and GBM II.

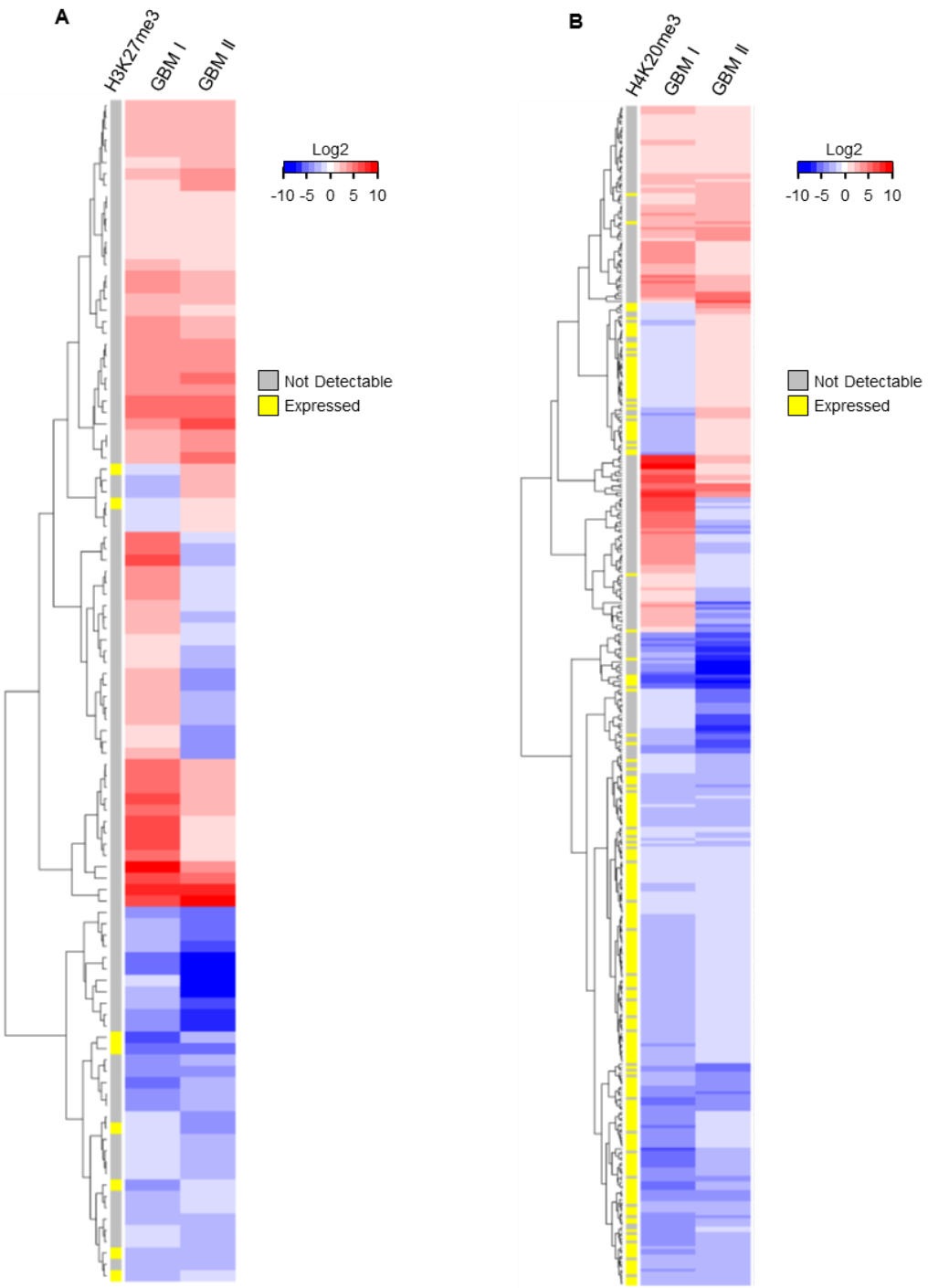

Figure 58. Differential expression analysis of genes of human GBM specimens.
(A, B) Heatmaps displaying differential expression of genes of human GBM specimens and corresponding enrichment in endogenous NSPCs with H3K27me3 (A) or H4K20me3 (B). Genes used for input are differentially expressed genes with greater than 2-fold change in human GBM corresponding to genes in normal NSPCs of baboon SVZ, which lack detectable transcript levels (≤1 FPKM) and are enriched by H3K27me3 (A) or H4K20me3 (B). Inset shows symmetric color scale indicating differences in expression level as the (base 2) log of the fold change of GBM sample divided by control. Red indicates increased expression of genes in GBM relative to control; blue color indicates decreased expression of genes in GBM compared with control. Colored bars in column to left of heatmap indicate whether corresponding gene in baboon NSPC is not detectable by RNA-Seq (≤1 FPKM) or is expressed (>1 FPKM). Dendrogram was determined by hierarchical clustering using Euclidian distance and complete linkage

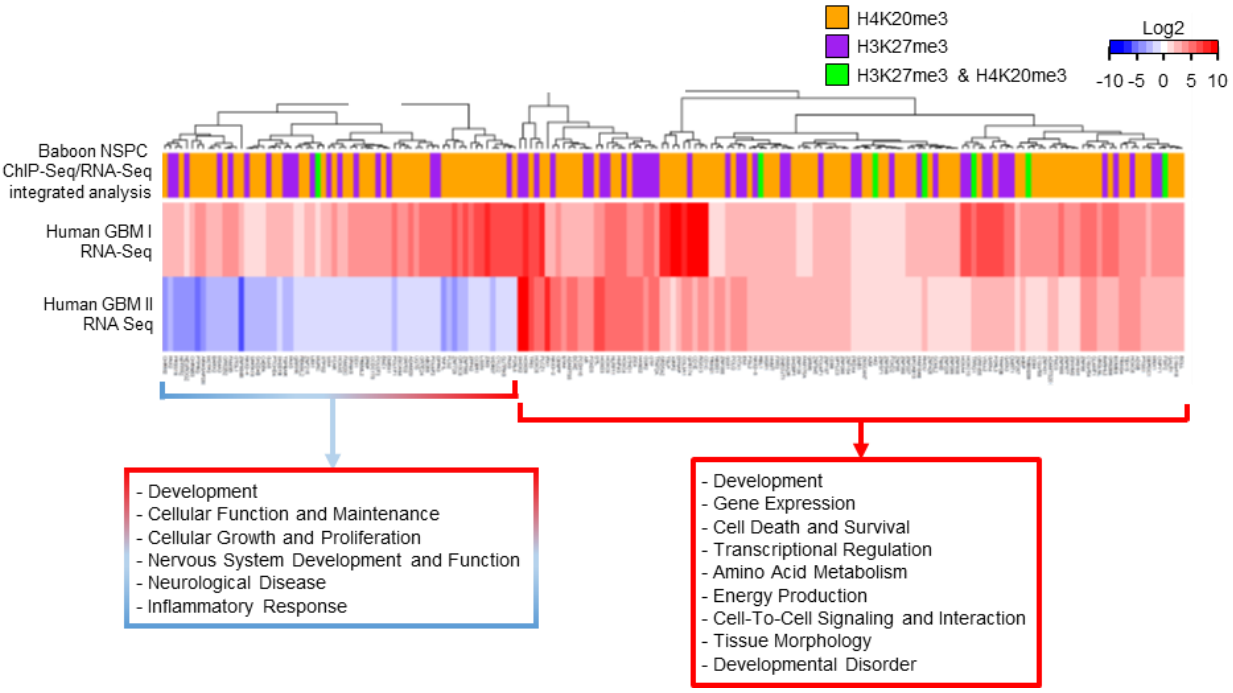

Figure 59. Correlation between genes in normal NSPCs enriched with H3K27me3 or H4K20me3 without detectable transcripts and genes altered in MRI-classified group I and group II GBM.
A heatmap for differential expression of genes of human GBM specimens. Genes used for input are 289 differentially expressed genes with greater than 2-fold change in human GBM corresponding to genes in normal NSPCs of baboon SVZ, which lack detectable transcript levels (≤1 FPKM) and are enriched by either H3K27me3 or H4K20me3, or co-enriched with H3K27me3/H4K20me3. Inset shows symmetric color scale indicating differences in expression level as the (base 2) log of the fold change of GBM sample divided by control. Red indicates increased expression of genes in GBM relative to control; blue color indicates decreased expression of genes in GBM compared with control. SVZ-associated GBM I and GBM II exhibit expression level changes in genes involved in multiple biological functions. Colored bars in column on top of heatmap indicate H3K27me3/H4K20me3 enrichment of corresponding genes in NSPCs of baboon SVZ. Dendrogram was determined by hierarchical clustering using Euclidian distance and complete linkage. Red text box indicates functions of clustered genes upregulated in both GBM I and GBM II, as predicted by IPA. Red and blue box indicates functions of clustered genes upregulated in GBM I and downregulated in GBM II, as predicted by IPA. Although there is no evident pattern of clustering of histone modifications with respect to particular GBM genes, there is a substantial increase in the number of upregulated GBM genes which correspond to H3K27me3 and H4K20me3 enrichment, yet lack detectable transcripts in the normal NSPCs of baboon SVZ.

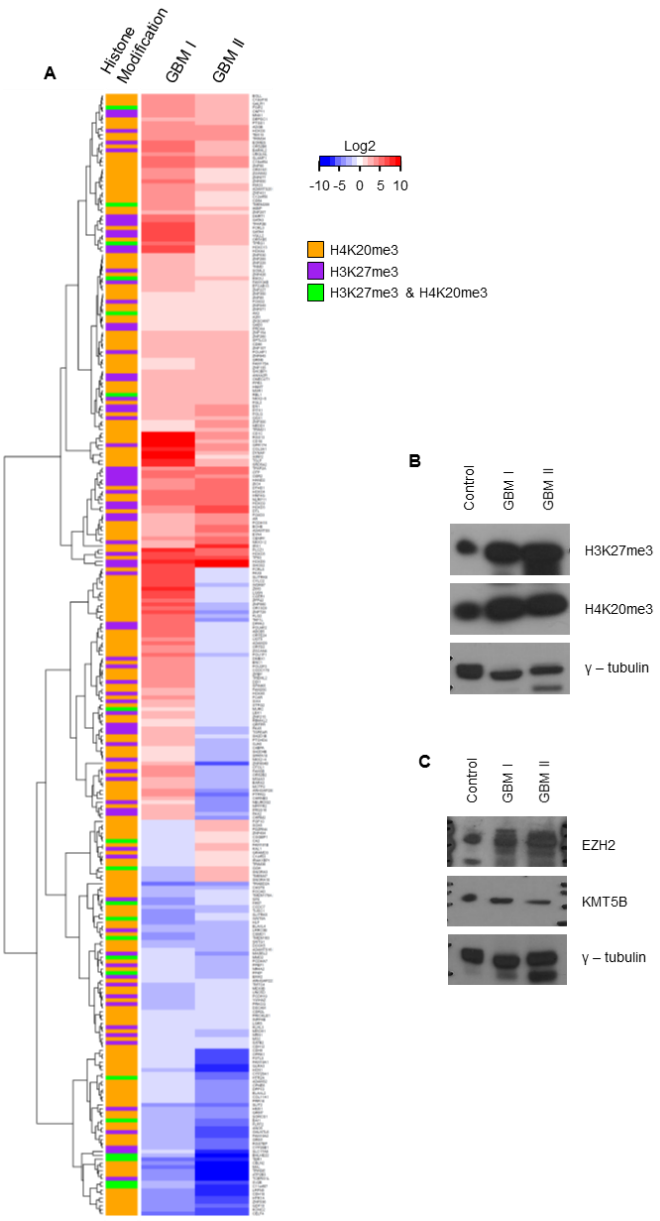

Figure 60. The correlation among H3K27me3, H4K20me3, NSPCs, and GBM.
Heatmap of all genes enriched with H3K27me3 or H4K20me3 in healthy neural stem and progenitor cells (NSPCs) of baboon SVZ and are either upregulated or downregulated in SVZ-associated GBM. The heatmap was generated using Euclidian distance and hierarchical clustering. To generate input gene lists for the heatmap, all genes in NSPCs purified from baboon SVZ that are significantly enriched with H3K27me3 and/or H4K20me3 with FPKM ≤ 1 (by RNA-Seq) were selected. The resulting gene list from healthy baboon SVZ NSPCs was then compared to corresponding gene expression levels in GBM I and GBM II of human origin. The heatmap illustrates transcript levels in GBM and the histone mark(s) of corresponding genes in baboon NSPCs. Prior to interspecies comparison, expression levels for GBM samples were normalized to a control region in the human brain, and then a 2-fold cut-off was used to detect differential gene expression in GBM specimens. Inset shows symmetric color scale indicating differences in expression level as the (base 2) log of the fold change of GBM sample divided by control. Colored column (i.e. "Histone Modification") indicates the type of histone modification present in baboon NSPC, as indicated by key. (B) Western Blot detected increased abundance of H3K27me3 and H4K20me3 in GBM I and GBM II compared to control specimen. γ-tubulin as loading control (C) Western Blot detected increased abundance of EZH2 and no substantial increase in KMT5B abundance in GBM I and GBM II compared to control specimen. γ-tubulin as loading control

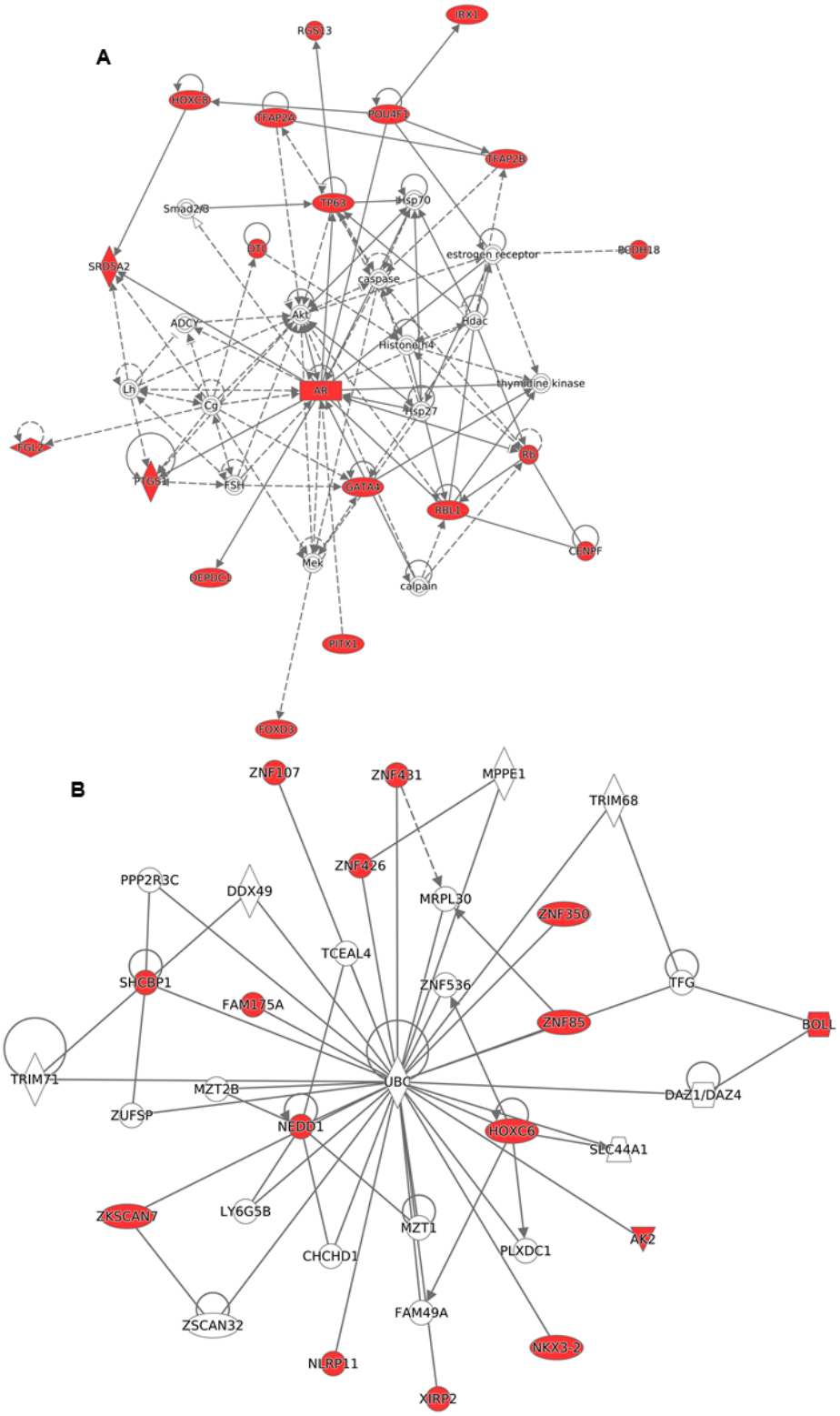

Figure 61. Genes that are substantially upregulated in SVZ-associated GBM participate in related cellular functions. Representative *de novo* interaction network predicted by IPA network analysis. Foci molecules (red) indicate genes in GBM used to build *de novo* interaction network. Network functions include: (A) Gene expression and cellular development; (B) cell death and survival. See Figure 25 for IPA symbol key.

CONCLUSION

The Role of Histone Methylation in Adult Neurogenesis

Genome-wide Targets of H3K27me3 and H4K20me3 in NSPCs

Multipotent NSPCs in adult SVZ must maintain a fine balance between self-renewal and differentiation (Doe, 2008). While epigenetic modifications are increasingly appreciated for playing an intrinsic role in the cell fate determination of NSPCs (Gao et al., 2011; Gotz and Huttner, 2005; Hwang et al., 2014; Lunyak and Rosenfeld, 2008; Ma et al., 2010; Molofsky et al., 2003; Montalban-Loro et al., 2015; Roman-Trufero et al., 2009; Yao and Jin, 2014; Zhang et al., 2014), the importance of proper control of proliferation and differentiation in NSPCs is underscored by H3K27me3 and H4K20me3 in healthy NSPCs of adult SVZ. To better understand the potential function of these 2 repressive marks in endogenous NSPCs, we performed genome-wide approaches employing ChIP-Seq and RNA-Seq on purified NSPCs from the SVZ of baboon brain to determine their molecular targets. We also demonstrate that EZH2 and Suv4-20h1 interact within undifferentiated cells of the primate SVZ. The putative interaction between EZH2 and Suv4-20h1 highlights previously unrecognized co-regulation through H3K27me3 and H4K20me3 important for adult neurogenesis, in that 62 overlapping genes co-enriched by H3K27me3 and H4K20me3 without detectable mRNA transcripts (<1 FPKM) are predominantly involved in cell-cycle, cellular maintenance, cellular compromise, cellular signaling, and cellular growth/proliferation.

Conditional Knock-out of Histone Methyltransferases within Adult Neurogenic Niches

A challenging and yet unresolved obstacle in genetic manipulations of mice is altering gene expression in tissue composed of heterogeneous cell types. Such heterogeneity is common in

virtually all adult stem cell niches, such as bone marrow, germ cell niches, and neurogenic niches. In such environments, there are circumstances where it would be beneficial to globally knockout a gene of interest across all cell types and examine any resulting phenotypes. For cell-type specific studies, a well-defined promoter can be applied to target a cell type of interest. For region-specific studies, our method of stereotaxic delivery of recombinant Cre protein presents a novel approach for a temporally and spatially-restricted knockout of a gene of interest. Injectable Cre proteins will not supplant other methods of tissue specific gene manipulation, including transgenic promoter-driven expression, viral expression systems, or tamoxifen/tetracycline inducible systems. However, our Cre protein approach is useful for gene manipulation within selected injection sites that results in Cre-induced recombination in targeted regions without exogenous Cre expression; the Cre gene was neither integrated into the host genome, nor maintained extra-chromosomally on a non-integrating vector. The high spatial precision of our technique for manipulating target cells offers enhanced modeling capabilities in murine models that would be useful for lineage tracing and cell fate studies at extended time-points.

Utilizing this novel region-specific gene manipulation in parallel with modified iDISCO whole brain imaging and quantitative image flow cytometry, we have demonstrated that Ezh2/H3K27me3 plays an important role in the maintenance of subpopulations within the SVZ and the SGZ/DG. Thus, our findings add to a compendium of previous studies on the role of Ezh2 in NSPCs using promoter-specific conditional knockout methods (Hwang et al., 2014; Pereira et al., 2010; Sher et al., 2012; Zhang et al., 2014). Moreover, our study is the first demonstration that the cell cycle within adult neurogenic niches is regulated, at least in part, by Suv4-20h/H4K20me3. Our studies using conditional knock-out of Ezh2 or Suv4-20h further reveal their *in vivo* functions important to cell cycle regulation during adult neurogenesis, suggesting Ezh2/H3K27me3 and

Suv4-20h/H4K20me3 may be a protective mechanism to minimize improper gene expression and modulate cellular proliferation, consequently preventing adult NSPCs from abnormal cell cycle re-entry or differentiation. Hence, Cre protein mediated knock-out of either Ezh2 or Suv4-20h underscores the importance of distinguishing roles of Ezh2/H3K27me3 from Suv4-20h/H4K20me3 in a region-specific manner. Perhaps more importantly, this region-specific protein-based approach for genetic manipulation enables future *in vivo* studies to understand the role of diverse epigenetic regulators distributed in a range of cell types within complex tissue architectures.

Cell autonomous versus Cell non-autonomous neurogenic processes

The combination of conditional HMT deletion and *ROSA26* reporter expression co-localized to a given injection site has utility in dissecting the role of various HMTs in complex processes such as cell fate transition. Within injection sites of the SVZ or SGZ/DG, two distinct populations of cells were observed following Cre recombination: cells with elevated levels of β-galactosidase and decreased histone modifications (i.e. cells having undergone Cre recombination), and cells with endogenous β-galactosidase levels, but high enrichment of histone methylation (i.e. cells which have not undertaken Cre recombination). The co-occupancy of both populations within an injected region acts as an internal control and becomes useful in probing the role of HMTs within these neurogenic niches.

The ability of injectable Cre protein to genetically manipulate many cell types simultaneously lends it to exploring cell non-autonomous processes in greater detail. Cell autonomous, or intrinsic, processes include the activation of transcriptional networks within a single cell. Conversely, a cell can participate in cell non-autonomous, or extrinsic, processes which

require extrinsic signals from other cells, including cell-cell signaling, paracrine signaling and endocrine signaling from distant cells. Cell non-autonomous processes critical to neural cell fate are understudied, largely due to challenges in generating region-specific changes and long-term cell tracking. Our Cre protein approach represents a novel method for examining cell non-autonomous processes following region-specific conditional knockouts in heterogeneous tissue. For example, loss of Ezh2 in (GFAP)-Cre mouse line results in deficit of postnatal neurogenesis in the mouse SVZ (Hwang et al., 2014). Alternatively, using a Nestin-CreERT2 and tamoxifen inducible system, *Ezh2* knockout within Nestin-positive NSCs in the SGZ /DG showed that Ezh2 is important for learning and memory capabilities in 6-week old mice (Zhang et al., 2014). However, neither previous study design well suited for long-term tracing of cells following loss of Ezh2 or examination of niche wide Ezh2 activity. Using our region-specific Cre protein approach, loss of Ezh2 induced NSPC differentiation and impacted maintenance of NSPCs in a cell autonomous manner. Further, post-Cre injection, the SVZ also displayed remarkable plasticity and ability to replenish niche neurogenic capacity in a manner consistent with a cell non-autonomous response. This niche-wide behavior is critical to establishment of homeostasis within healthy NSPC populations, yet niche wide genetic manipulation has not been well described. Our stereotaxic based, region-specific approach offers a novel alternative to study such niche wide responses to transient Cre protein activity. More broadly, our approach would potentially be useful for investigating any niche wide regulatory mechanisms via region-specific genetic manipulation. Examination of Suv4-20h mediated cell non-autonomous processes can also be performed in adult neurogenic niches. Using our Cre protein approach, loss of Suv4-20h within the adult SVZ impacted NSPC proliferation in S-phase. Upon Cre protein mediated loss of Suv4-20h in the adult SGZ/DG, two distinct phenotypes emerge. The proportion of EdU-positive/YFP-positive cells (i.e.

cells that have experienced Cre mediated recombination) increases, suggesting reduction in H4K20me3 may increase proliferation in a cell autonomous manner. Conversely, the total number of EdU positive cells within the dentate gyrus decreases. The loss of total EdU positive cells may be either a cell autonomous process (i.e. apoptosis) or a cell non-autonomous process (i.e. neuronal migration out of SGZ/DG). Further study is needed to clarify the exact mechanisms by which loss of Suv4-20h/H4K20me3 impacts NSPC proliferation in S-phase within the SGZ/DG and hippocampus.

Future applications of cell permeable proteins and protein based therapeutics

Future applications of region-specific gene knockouts might be followed by single cell transcriptomics, single cell proteomics, or microfluidic drug treatment to glean valuable insight into regulatory mechanisms at the molecular level within a heterogeneous population. Alternatively, microfluidic growth chambers could be utilized to track changes to metabolic load *in vitro* or in brain organoids following Cre mediated loss of HMTs *in vivo*.

In addition, while cancer treatment using EZH2 (mouse: Ezh2) inhibitors to target dysregulation of EZH2/H3K27me3 in glioblastoma subtypes is ongoing, our Cre protein-based manipulation uncovers long-term *in vivo* effects upon loss of Ezh2. The concept of non-cell type specific manipulation described in this work can be applied to modeling long-term *in vivo* effect of other epigenetic modifiers prior to the development and investment of drug inhibitors for therapeutics. In routine chemotherapy, a therapeutic agent is given systemically, via intravenous injection, ultimately impacting many cell types in the brain and throughout the body. Having experimental methods such as a region-specific knockout approaches will better model niche-wide responses to a drug. Furthermore, use of recombinant proteins for *in vivo* transduction of

therapeutic protein has already been performed to protect against cerebral infarction, ischemic brain injury, and neural apoptosis, via intraperitoneal injection in mice (Cao et al., 2002; Xi et al., 2012). Therefore, the cell permeable proteins, like CTP-tagged protein used in this study, could be potentially adapted for production of recombinant pharmaceutical proteins for therapeutic applications.

Our Cre mediated genetic manipulation approach is not limited to neurogenic niches, and can be successfully implemented in various models to address myriad tightly-controlled knockouts or knock-ons in many tissues or cells simultaneously. As a broader impact, our novel approach for gene manipulation is optimal for studying many other regulatory mechanisms in a site-specific fashion, and can be applied to additional brain regions and/or to targeted cell populations within complex, heterogeneous tissue architectures. In addition, this method would be particularly useful for investigating developmentally critical genes in localized regions of solid organs, where complete deletion *in utero* would result in embryonic or perinatal lethality.

A subset H3K27me3 and H4K20me3 enriched genes in NSPCs are altered in subtypes of glioblastoma

Improper control of the balance between proliferation and differentiation within NSPCs may shift otherwise normal neurogenesis towards oncogenesis or neurodegeneration. In line with this hypothesis, subtypes of SVZ-associated GBM represent similar signature of NSPCs (Haskins et al., 2013; Sandstrom et al., 2014) that further highlight the importance of cell fate regulation in health and disease conditions. While considerable evidence implicates EZH2 in GBM (de Vries et al., 2015; Kim et al., 2015; Suva et al., 2009), our current study demonstrates that several genes involved in cancer mechanisms are co-enriched with H3K27me3 and H4K20me3. As MRI-

classified group I and II GBM contain cells with a NSPC signature (i.e. abundant GFAP, Vimentin, and DCX in tumor) (Haskins et al., 2013), cells with poorly differentiated characteristics are apparent in subtypes of GBM. Given that i) epigenetic regulation by EZH2/H3K27me3 is known to suppress differentiation of stem cells; ii) EZH2 interacts with KMT5B (mouse: Suv4-20h); and iii) both EZH2/H3K27me3 and KMT5B/H4K20me3 have been implicated in cancer mechanisms, we were prompted to assess the relation of H3K27me3 and H4K20me3 in endogenous NSPCs and SVZ-associated subtypes of GBM (GBM I and GBM II). Although previous studies of the genome and transcriptome of glioblastoma have provided extensive data of molecular alterations that potentially drive glioblastoma pathogenesis and demonstrate that glioblastoma is a heterogeneous brain tumor across each particular subtype (2008; Beroukhim et al., 2007; Gunther et al., 2008; Parsons et al., 2008; Phillips et al., 2006; Verhaak et al., 2010), there is no report thus far deciphering the link between histone repressive marks and SVZ-associated GBM. Herein, we undertook a comparative genomics approach between healthy NSPCs and GBM specimens that include i) molecular targets of H3K27me3 and/or H4K20me3 in the NSPCs identified from ChIP-Seq; ii) mRNA expression data of *in vivo* NSPCs from baboon SVZ; and iii) differential gene expression of GBM I and GBM II compared to controls on a genome-wide scale (Fig. 56). As obtaining fresh controls from live humans for GBM ChIP-Seq is ethically unacceptable, we used the current baboon ChIP-Seq data as a baseline of the epigenetic landscape. While not an exact match to adult human SVZ specimens, the current baboon data will undoubtedly shed light on epigenetic interactions in NSPCs of adult primates (including humans) and subsequent changes to gene expression in neuropathology. Because both H3K27me3 and H4K20me3 are known to suppress gene expression, we focused on targets of H3K27me3 and/or H4K20me3 identified from ChIP-Seq that are not detectable (FPKM <1) by RNA-Seq for purified NSPCs from baboon SVZ.

Subsequently, differentially upregulated genes in GBM cases were compared to corresponding H3K27me3 and H4K20me3 enriched genes in NSPCs without detectable transcripts. Using this integrated analysis of genome-wide data across species, we identified candidate genes that are aberrantly upregulated in GBM related to the dysregulation of H3K27me3 and/or H4K20me3 (Fig. 57). Of H3K27me3 enriched genes in baboon NSPCs with no detectable transcript (<1 FPKM), 101 and 64 are upregulated in GBM I and GBM II, respectively (Fig. 57A, C; Supplementary Table 4i and ii online: http://dx.doi.org/10.1016/j.nepig.2016.04.001). These genes function in transcriptional regulation as well as nervous system and organismal development (Fig. 57A, C [Boxes]; Supplementary Table 4iii–vi online: http://dx.doi.org/10.1016/j.nepig.2016.04.001).

Additionally, 238 and 160 of H4K20me3 enriched genes in baboon NSPCs with undetectable transcript (<1 FPKM) are upregulated in GBM I and GBM II, respectively (Fig. 57B, D; Supplementary Table 5i and ii online: http://dx.doi.org/10.1016/j.nepig.2016.04.001). The 238 genes upregulated in GBM I are associated with cancer, cellular function and maintenance, cell death and survival, as well as DNA replication, recombination and repair (Fig. 57B [Box]; Supplementary Table 5iii and iv online: http://dx.doi.org/10.1016/j.nepig.2016.04.001). Similarly, the 160 genes upregulated in GBM II specimens have functions in cell cycle, cellular development, cellular growth and proliferation, cell death and survival, cell-to-cell signaling, and nervous system development (Fig. 57D [Box]; Supplementary Table 5v and vi online at http://dx.doi.org/10.1016/j.nepig.2016.04.001). Further, 45 of the H3K27me3 and 83 of the H4K20me3 enriched genes lacking expression in NSPCs have abnormally high expression levels in both GBM I and GBM II specimens (Fig. 57E, 57F; Supplementary Table 6i and ii online: http://dx.doi.org/10.1016/j.nepig.2016.04.001). Functional analysis predicted by IPA reveals that 45 of the genes function in transcriptional regulation, gene expression, development, cell death

and survival, cancer and cell morphology (Fig. 57E [Box]; Supplementary Table 6iii and iv online: http://dx.doi.org/10.1016/j.nepig.2016.04.001), while 83 genes function in cell cycle, cellular maintenance/assembly/organization, DNA replication/repair/recombination, as well as cell-to-cell signaling and interaction (Fig. 57F [Box]; Supplementary Table 6v and vi online at http://dx.doi.org/10.1016/j.nepig.2016.04.001). We generated a heatmap to better illustrate the correlation among i) the enrichment of H3K27me3 or H4K20me3, ii) expression signature of normal NSPCs, and iii) aberrant gene expression of GBM I and GBM II (Fig. 58A and 58B present H3K27me3 and H4K20me3 separately; Supplementary Table 7i online: http://dx.doi.org/10.1016/j.nepig.2016.04.001). A substantial proportion of upregulated genes in both GBM I and GBM II are enriched with H4K20me3 but lack detectable transcripts in NSPCs (Fig. 58B; Supplementary Table 7iii online at http://dx.doi.org/10.1016/j.nepig.2016.04.001). Visualizing the expression profiles of H3K27me3 and/or H4K20me3 enriched genes with a heatmap, the cluster containing only upregulated GBM I and GBM II genes (Fig. 59 [Red Box]; Fig. 60A; Supplementary Table 7iv in the online version at http://dx.doi.org/10.1016/j.nepig.2016.04.001) functions in development and cell death/survival predicted by IPA (Fig. 61; Supplementary Table 7v and vi in the online version at http://dx.doi.org/10.1016/j.nepig.2016.04.001). Genes upregulated in GBM I but downregulated in GBM II (Fig. 59 [Blue/Red Box]; Supplementary Table 7vii in the online version at http://dx.doi.org/10.1016/j.nepig.2016.04.001) also are involved in similar categories (i.e. development, cellular maintenance, growth and proliferation), yet consist of different gene sets (Supplementary Table 7viii online: http://dx.doi.org/10.1016/j.nepig.2016.04.001). As the heatmap dendrogram did not cluster genes into discernable groups of histone modifications (i.e. H3K27me3, H4K20me or both H3K27me3 and H4K20me3), we anticipate these two histone

marks heterogeneously enrich for genes aberrantly expressed in SVZ-associated GBM I and GBM II.

While DNA and RNA profiles of bulk tumors or single cells from GBM have enabled genetic and transcriptional classification (2008; Patel et al., 2014), the relationships between epigenetic alteration and heterogeneity of GBM remain obscure. Such epigenetic alteration can change global gene expression and manifest intratumoral heterogeneity of GBM, wherein different stages or expression signatures are associated with distinct outcomes or therapeutic responses. As conditional knock-down of Ezh2 and Suv4-20h in the NSPCs of rodent SVZ did not yield brain tumors over 46 weeks (unpublished data) and the levels of EZH2/H3K27me3 or KMT5B/H4K20me3 are not significantly changed in human specimens (Fig. 60B-C), we reason their effects could be in a gene-specific manner. Through integrated analyses of genome-wide data across species, we found that a significant set of genes enriched with H3K27me3 and H4K20me3 in the *in vivo* NSPCs are altered in GBM specimens harboring a NSPC signature. We identified that 37% (101/271) and 24% (64/271) of H3K27me3 potentially repressed genes are upregulated in GBM I and GBM II, respectively. Similarly, 31% (238/763) and 21% (160/763) of H4K20me3 potentially repressed genes are upregulated in GBM I and GBM II, respectively. Our results suggest that changes in subsets of gene expression due to failure to respond to repression by H3K27me3 or H4K20me3 may contribute to tumorigenesis in GBM subtypes. One would argue this is simply a correlation; yet considering the heterogeneous nature of GBM tumors (Inda et al., 2014; Sottoriva et al., 2013) in which a set of genes are putative targets of these 2 repressive marks and are upregulated in both GBM I and GBM II, influence by EZH2/H3K27me3 and KMT5B/H4K20me3 is highly likely. While extensive genomic characterization and transcriptome analysis have illustrated molecular landscape of glioblastoma (2008; Beroukhim et al., 2007;

Gunther et al., 2008; Parsons et al., 2008; Patel et al., 2014; Phillips et al., 2006; Verhaak et al., 2010), the work presented here provides a new insight into critical networks and pathways central to GBM pathobiology, which harbor molecular heterogeneity in conjunction with epigenetic alteration.

Implications of Histone Methylation in non-central nervous system cancers

Intriguingly, the roles of EZH2/H3K27me3 and KMT5B/H4K20me3 seem to have common roles in other tissues quite different from the brain. Esophageal adenocarcinoma (EAC) in humans, for instance, affects the epithelium of the trachea and is potentially formed from the primordial endoderm of developing embryos. This is not only a different tissue from the brain, but arises from a fundamentally different primordial germ layer. Endothelial cells arise from the endoderm, while the brain arises from the ectoderm. Yet in EAC, H3K27me3 appears to impact tissue in a similar fashion as H3K27me3 dysregulation in GBM (unpublished data). This universal influence of EZH2/H3K27me3 and other histone modifications is intriguing and requires more study to uncover potentially universal mechanisms of human neoplasia.

Cross-Species Pipeline

Our results provide an integrated view of epigenetic regulation by H3K27me3 and H4K20me3 to maintain neurogenic homeostasis in the adult mammalian brain. This includes regulating NSC differentiation into neurons as well as NSPC proliferation. Further, our cross-species approach may advance the understanding of potential roles of epigenetic mechanisms in SVZ-associated GBM tumorigenesis. Our use of multiple animal models has helped form an integrated perspective of highly related biological processes *in vivo* which are not easily attained

using a single model approach. Such insights include the roles of EZH2/H3K27me3 and KMT5B/H4K20me3 in endogenous NSPC (i.e., baboons) and manipulation of Ezh2 or Suv4-20h enzyme function in CNS stem cell niches (i.e., mouse). To gain a fuller understanding of histone methylations in the context of adult neurogenic niches and how such modifications influence NSPC cell fate, we further refined our cross-species *in vivo* approach to include human pathobiology, specifically to accommodate the heterogeneity reported in subtypes of GBM. By integrating cross-species *in vivo* analyses, the intersection of extrinsic factors, epigenetic gateway, intrinsic gene regulatory networks and cell state plasticity of adult NSPCs may be more fully understood.

Future Directions

Are EZH2 and KMT5B drivers or passengers of aggressive CNS tumors?

Histone modification enzymes (i.e. epigenetic writers), resulting histone marks, and the genomic targets clearly perform various distinct and separable roles in adult mammalian neurogenesis. Such roles include transcriptional activation of neuron specific transcriptional patterns (MLL1/H3K4me3), repression of non-neuronal differentiation programs (EZH2/H3K27me3) and influence in cell cycle of NSPCs (KMT5B; KMT5C/H4K20me3). Yet, chromatin modifications are commonly implicated in CNS tumorigenesis in pediatric and adult cases. For instance, mutations to the MLL family of histone modifiers is common in brain tumors and loss of H4K20me3 is a common hallmark of human cancer proliferative non-small cell lung cancer and several proliferative cancer cell lines (Fraga et al., 2005; Tryndyak et al., 2006; Van Den Broeck et al., 2008).

One epigenetic writer that is universally amplified across all recorded cases in large scale GBM studies is EZH2 (Lin et al., 2017). EZH2/H3K27me3 are implicated in repression of NSPC differentiation and pro-neuronal transcriptional networks during endogenous neurogenesis while EZH2 is essential for glioblastoma cancer stem cell maintenance (Rhodes et al., 2016; Suva et al., 2009). Additionally, the SVZ contains NSPCs in which EZH2 is abundant and the relationship between SVZ and glioblastoma is highly correlated with patient overall survival (Hwang et al., 2014; Jafri et al., 2013). Our functional genomics studies regarding EZH2 and our conditional *Ezh2* knockout experiments suggest that EZH2 amplification might make a transition from a stem cell program into a pro-neuronal differentiation program more difficult to initiate. This hypothesis implicates ectopic EZH2/H3K27me3 in directly driving tumorigenesis by forcing NSPCs to be maintained in an abnormal undifferentiated cell state. As these NSPCs are endogenously proliferative, the resulting population of undifferentiated, proliferative cells is very similar to putative cancer-initiating cells proposed in the cancer stem cell theory of CNS tumors.

An alternative explanation for trapping proliferative NSPCs in an undifferentiated state could be reduced activity of epigenetic erasers of H3K27me3. Two histone lysine demethylases are responsible for removing H3K27me3 during embryonic development as well as postnatal and adult neurogenesis: KDM6A (previously UTX) or KDM6B (previously JMJD3) (Kang et al., 2015; Khare et al., 2012; Park et al., 2014). In endogenous neurogenesis, EZH2 is present in all cell types of the neuronal lineage, from NSCs to differentiated neurons (Hwang et al., 2014; Zhang et al., 2014). Activation of neuron specific genes commonly requires JMJD3 mediated erasure of H3K27me3 marks (Iida et al., 2014; Park et al., 2014). Decreased H3K27me3 erasure by JMJD3/UTX is therefore potentially implicated in GBM tumorigenesis and other CNS tumors. Another alternative explanation for altered EZH2/H3K27me3 levels in GBM is be due to the local

microenvironment surrounding CNS tumors. The substrate for EZH2, SAM, is commonly utilized in many metabolic pathways. Dysregulation in a variety of reactions in the central metabolic pathway could result in direct or indirect alterations in SAM levels. In such a hypothesis, altered H3K27me3 patterns are a downstream effect from metabolic alterations in the local tumor microenvironment. Lastly, amplification of EZH2 transcription could be due to upstream alterations in transcriptional networks. This would ultimately result in NSPCs erroneously expressing EZH2 at inappropriate periods of neurogenesis as a result.

One simple experiment to directly address whether EZH2 amplification is a driver of GBM or a consequence of other processes would be to induce overexpression of *Ezh2* in the SVZ of adult mice. Examining the ongoing effects an *Ezh2* coding sequence in a *ROSA26* locus via gene-targeting in embryonic stem cells to generate conditional *Ezh2* knock-in will address this hypothesis (Hohenstein et al., 2008). Such an *Ezh2* knock-in could express up to 4 copies of *Ezh2* following Cre recombination, as opposed to 2 copies in a wildtype mouse. If needed, R26R-LacZ or R26R-YFP could be utilized as a Cre reporter, resulting in 3 copies of *Ezh2* expressed following Cre activity. Stereotaxic injection of Cre protein into such a mouse would result in region-specific *Ezh2* amplification. Alternatively, injection of a retroviral or lentiviral vector containing a copy of *Ezh2* would drive ectopic expression of *Ezh2* in mitotic and non-dividing NSPCs respectively. Using these methods as well as cell type specific markers and cell tracing, a clearer picture of the mechanisms driving GBM could be gleaned.

Additionally, reduction of KMT5B and/or loss of H4K20me3 are considered hallmarks of various highly proliferative tumors outside of the CNS, yet little is known about the role of KMT5B/H4K20me3 in the adult brain besides regulating endogenous NSPC proliferation (Fraga et al., 2005; Rhodes et al., 2016; Yokoyama et al., 2014). While EZH2 amplification is associated

with GBM, dysregulation of multiple histone modifiers could be detrimental to brain health and/or neurodevelopment. Such dysregulation of multiple histone modifiers would likely result from an abnormal niche microenvironment and may be sufficient to initiate CNS neoplasia. In such a scenario, EZH2 amplification might retain cells in an undifferentiated state, while cells with abnormal KMT5B (mouse: Suv4-20h1) activity would impact proliferation, both characteristics are hallmarks of aggressive CNS tumors. Such a hypothesis could be tested by injecting Cre protein into an adult mouse containing both a conditional *Ezh2* overexpression construct (knock-in) and a conditional *Suv4-20h1* knockout construct.

Role of histone modifications in NSPC cell cycle and neurons

Stem cell fate specification and adult neurogenesis in particular are often described in the context of maintaining a balance between an undifferentiated state and a terminally differentiated state. Such a balance is often described as a single step (i.e. a linear process). As such, once an arbitrary cell fate decision has been made, a NSPC will quickly be transformed from an undifferentiated to a differentiated state. Yet our results from *in vivo* neurogenesis studies portray a dynamic process with multiple feedback loops occurring at different points in stepwise differentiation. The very nature of neural stem cell biology is a cyclic process, involving self-renewal as well as symmetric and asymmetric cell divisions. Our results show that Suv4-20h has a large influence on cell cycle within neurogenic niches. Yet whether changes in cell cycle alter the ability of a niche to establish homeostasis is largely unknown. For example, if NSCs are forced into repeated cell cycle events, does this have any effect on self-renewal ability? Does it force differentiation? Would the cell initiate cell death? As such, continued experiments involving knockouts of *Suv4-20h1* followed by single cell sequencing, microfluidic arrays or long-term

tracing of cell type specific markers and cell cycle/cell death markers would be of considerable interest for understanding neural stem cell fate *in vivo*. Alternatively, Ezh2 is primarily described in retaining cells in an undifferentiated state, thus maintaining a sustainable neurogenic rate. The primary purpose of Ezh2 is to prevent neuronal genes from being expressed prematurely and thereby maintaining NSPCs populations. Ezh2 is expressed in all cells of the neuronal lineage, and H3K27me3 is present within terminally differentiated neurons which have integrated into existing functional networks. Consequently, Ezh2/H3K27me3 ostensibly performs critical functions in differentiated neural cells. Yet, the role of Ezh2 has only been described in early lineage commitment steps. By injecting viral vectors encoding a CAG promoter upstream of *Ezh2* or Cre recombinase, it is possible to overexpress or conditionally knockout Ezh2 in new-born neuron populations. Alternatively, change of function experiments could utilize stereotaxic injection of neuron specific viruses such as Rabies virus into the brains of experimental mice. This would help elucidate the role of Ezh2/H3K27me3 in mature neuronal cells and more fully describe mechanisms of histone regulation with respect to brain health.

REFERENCES

(2008). Comprehensive genomic characterization defines human glioblastoma genes and core pathways. Nature *455*, 1061-1068.

Ahmed, A.U., Auffinger, B., and Lesniak, M.S. (2013). Understanding glioma stem cells: rationale, clinical relevance and therapeutic strategies. Expert Rev Neurother *13*, 545-555.

Alfonso, J., Le Magueresse, C., Zuccotti, A., Khodosevich, K., and Monyer, H. (2012). Diazepam binding inhibitor promotes progenitor proliferation in the postnatal SVZ by reducing GABA signaling. Cell stem cell *10*, 76-87.

Alvarez-Buylla, A., Kohwi, M., Nguyen, T.M., and Merkle, F.T. (2008). The heterogeneity of adult neural stem cells and the emerging complexity of their niche. Cold Spring Harbor symposia on quantitative biology *73*, 357-365.

Alvarez-Buylla, A., and Lim, D.A. (2004). For the long run: maintaining germinal niches in the adult brain. Neuron *41*, 683-686.

Artavanis-Tsakonas, S., Rand, M.D., and Lake, R.J. (1999). Notch signaling: cell fate control and signal integration in development. Science *284*, 770-776.

Baker, M. (2011). Making sense of chromatin states. Nat Methods *8*, 717-722.

Benetti, R., Garcia-Cao, M., and Blasco, M.A. (2007). Telomere length regulates the epigenetic status of mammalian telomeres and subtelomeres. Nature genetics *39*, 243-250.

Berezovsky, A.D., Poisson, L.M., Cherba, D., Webb, C.P., Transou, A.D., Lemke, N.W., Hong, X., Hasselbach, L.A., Irtenkauf, S.M., Mikkelsen, T., *et al.* (2014). Sox2 promotes malignancy in glioblastoma by regulating plasticity and astrocytic differentiation. Neoplasia *16*, 193-206, 206 e119-125.

Bernstein, B.E., Mikkelsen, T.S., Xie, X., Kamal, M., Huebert, D.J., Cuff, J., Fry, B., Meissner, A., Wernig, M., Plath, K., *et al.* (2006). A bivalent chromatin structure marks key developmental genes in embryonic stem cells. Cell *125*, 315-326.

Beroukhim, R., Getz, G., Nghiemphu, L., Barretina, J., Hsueh, T., Linhart, D., Vivanco, I., Lee, J.C., Huang, J.H., Alexander, S., *et al.* (2007). Assessing the significance of chromosomal aberrations in cancer: methodology and application to glioma. Proceedings of the National Academy of Sciences of the United States of America *104*, 20007-20012.

Bershteyn, M., Nowakowski, T.J., Pollen, A.A., Di Lullo, E., Nene, A., Wynshaw-Boris, A., and Kriegstein, A.R. (2017). Human iPSC-Derived Cerebral Organoids Model Cellular Features of Lissencephaly and Reveal Prolonged Mitosis of Outer Radial Glia. Cell stem cell *20*, 435-449 e434.

Bertrand, N., Castro, D.S., and Guillemot, F. (2002). Proneural genes and the specification of neural cell types. Nature reviews Neuroscience *3*, 517-530.

Biteau, B., Hochmuth, C.E., and Jasper, H. (2011). Maintaining tissue homeostasis: dynamic control of somatic stem cell activity. Cell stem cell *9*, 402-411.

Bjerke, L., Mackay, A., Nandhabalan, M., Burford, A., Jury, A., Popov, S., Bax, D.A., Carvalho, D., Taylor, K.R., Vinci, M., *et al.* (2013). Histone H3.3. mutations drive pediatric glioblastoma through upregulation of MYCN. Cancer Discov *3*, 512-519.

Black, J.C., Van Rechem, C., and Whetstine, J.R. (2012). Histone lysine methylation dynamics: establishment, regulation, and biological impact. Molecular cell *48*, 491-507.

Blom, H.J., and Smulders, Y. (2011). Overview of homocysteine and folate metabolism. With special references to cardiovascular disease and neural tube defects. J Inherit Metab Dis *34*, 75-81.

Bogdanovic, O., Smits, A.H., Mustienes, E.D., Tena, J.J., Ford, E., Williams, R., Senanayake, U., Schultz, M.D., Hontelez, S., van Kruijsbergen, I., *et al.* (2016). Active DNA demethylation at enhancers during the vertebrate phylotypic period. Nature genetics *48*, 417-+.

Bonaguidi, M.A., Song, J., Ming, G.L., and Song, H. (2012). A unifying hypothesis on mammalian neural stem cell properties in the adult hippocampus. Current opinion in neurobiology *22*, 754-761.

Bonaguidi, M.A., Wheeler, M.A., Shapiro, J.S., Stadel, R.P., Sun, G.J., Ming, G.L., and Song, H. (2011). In vivo clonal analysis reveals self-renewing and multipotent adult neural stem cell characteristics. Cell *145*, 1142-1155.

Bond, A.M., Ming, G.L., and Song, H. (2015). Adult Mammalian Neural Stem Cells and Neurogenesis: Five Decades Later. Cell stem cell *17*, 385-395.

Bonthagarala, B., Dileep, C., and Manasa, K. (2013). STEM CELL: PAST, PRESENT AND FUTURE- A REVIEW ARTICLE.

Bracken, A.P., Pasini, D., Capra, M., Prosperini, E., Colli, E., and Helin, K. (2003). EZH2 is downstream of the pRB-E2F pathway, essential for proliferation and amplified in cancer. The EMBO journal *22*, 5323-5335.

Bradshaw, A., Wickremsekera, A., Tan, S.T., Peng, L., Davis, P.F., and Itinteang, T. (2016). Cancer Stem Cell Hierarchy in Glioblastoma Multiforme. Front Surg *3*, 21.

Calzolari, F., Michel, J., Baumgart, E.V., Theis, F., Gotz, M., and Ninkovic, J. (2015). Fast clonal expansion and limited neural stem cell self-renewal in the adult subependymal zone. Nat Neurosci *18*, 490-492.

Cao, G., Pei, W., Ge, H., Liang, Q., Luo, Y., Sharp, F.R., Lu, A., Ran, R., Graham, S.H., and Chen, J. (2002). In Vivo Delivery of a Bcl-xL Fusion Protein Containing the TAT Protein Transduction Domain Protects against Ischemic Brain Injury and Neuronal Apoptosis. The Journal of neuroscience : the official journal of the Society for Neuroscience *22*, 5423-5431.

Carlsson, S.K., Brothers, S.P., and Wahlestedt, C. (2014). Emerging treatment strategies for glioblastoma multiforme. EMBO Mol Med *6*, 1359-1370.

Chien, W.M., Liu, Y., and Chin, M.T. (2014). Genomic DNA Recombination with Cell-Penetrating Peptide-Tagged Cre Protein in Mouse Skeletal and Cardiac Muscle. Genesis.

Codega, P., Silva-Vargas, V., Paul, A., Maldonado-Soto, A.R., DeLeo, A.M., Pastrana, E., and Doetsch, F. (2014). Prospective Identification and Purification of Quiescent Adult Neural Stem Cells from Their In Vivo Niche. Neuron *82*, 545-559.

Czvitkovich, S., Sauer, S., Peters, A.H., Deiner, E., Wolf, A., Laible, G., Opravil, S., Beug, H., and Jenuwein, T. (2001). Over-expression of the SUV39H1 histone methyltransferase induces altered proliferation and differentiation in transgenic mice. Mech Dev *107*, 141-153.

de Vries, N.A., Hulsman, D., Akhtar, W., de Jong, J., Miles, D.C., Blom, M., van Tellingen, O., Jonkers, J., and van Lohuizen, M. (2015). Prolonged Ezh2 Depletion in Glioblastoma Causes a Robust Switch in Cell Fate Resulting in Tumor Progression. Cell reports.

Deaton, A.M., and Bird, A. (2011). CpG islands and the regulation of transcription. Genes & development *25*, 1010-1022.

Dehay, C., and Kennedy, H. (2007). Cell-cycle control and cortical development. Nature reviews Neuroscience *8*, 438-450.

Desai, A.R., and McConnell, S.K. (2000). Progressive restriction in fate potential by neural progenitors during cerebral cortical development. Development *127*, 2863-2872.

Dillon, S.C., Zhang, X., Trievel, R.C., and Cheng, X. (2005). The SET-domain protein superfamily: protein lysine methyltransferases. Genome biology *6*, 227.

Dixon, J.R., Selvaraj, S., Yue, F., Kim, A., Li, Y., Shen, Y., Hu, M., Liu, J.S., and Ren, B. (2012). Topological domains in mammalian genomes identified by analysis of chromatin interactions. Nature *485*, 376-380.

Doe, C.Q. (2008). Neural stem cells: balancing self-renewal with differentiation. Development *135*, 1575-1587.

Dulken, B.W., Leeman, D.S., Boutet, S.C., Hebestreit, K., and Brunet, A. (2017). Single-Cell Transcriptomic Analysis Defines Heterogeneity and Transcriptional Dynamics in the Adult Neural Stem Cell Lineage. Cell reports *18*, 777-790.

Ekdahl, C.T., Claasen, J.H., Bonde, S., Kokaia, Z., and Lindvall, O. (2003). Inflammation is detrimental for neurogenesis in adult brain. Proceedings of the National Academy of Sciences of the United States of America *100*, 13632-13637.

Ernst, A., Alkass, K., Bernard, S., Salehpour, M., Perl, S., Tisdale, J., Possnert, G., Druid, H., and Frisen, J. (2014). Neurogenesis in the striatum of the adult human brain. Cell *156*, 1072-1083.

Ernst, A., and Frisen, J. (2015). Adult Neurogenesis in Humans-Common and Unique Traits in Mammals. PLoS biology *13*.

Evans, M.J., and Kaufman, M.H. (1981). Establishment in culture of pluripotential cells from mouse embryos. Nature *292*, 154-156.

Evertts, A.G., Manning, A.L., Wang, X., Dyson, N.J., Garcia, B.A., and Coller, H.A. (2013). H4K20 methylation regulates quiescence and chromatin compaction. Mol Biol Cell *24*, 3025-3037.

Ezhkova, E., Pasolli, H.A., Parker, J.S., Stokes, N., Su, I.H., Hannon, G., Tarakhovsky, A., and Fuchs, E. (2009). Ezh2 orchestrates gene expression for the stepwise differentiation of tissue-specific stem cells. Cell *136*, 1122-1135.

Finn, R.D., Attwood, T.K., Babbitt, P.C., Bateman, A., Bork, P., Bridge, A.J., Chang, H.Y., Dosztanyi, Z., El-Gebali, S., Fraser, M., *et al.* (2017). InterPro in 2017-beyond protein family and domain annotations. Nucleic Acids Res *45*, D190-D199.

Fischer, J., Beckervordersandforth, R., Tripathi, P., Steiner-Mezzadri, A., Ninkovic, J., and Gotz, M. (2011). Prospective isolation of adult neural stem cells from the mouse subependymal zone. Nature protocols *6*, 1981-1989.

Florio, M., Albert, M., Taverna, E., Namba, T., Brandl, H., Lewitus, E., Haffner, C., Sykes, A., Wong, F.K., Peters, J., *et al.* (2015). Human-specific gene ARHGAP11B promotes basal progenitor amplification and neocortex expansion. Science *347*, 1465-1470.

Florio, M., and Huttner, W.B. (2014). Neural progenitors, neurogenesis and the evolution of the neocortex. Development *141*, 2182-2194.

Foret, M.R., Sandstrom, R.S., Rhodes, C.T., Wang, Y., Berger, M.S., and Lin, C.H. (2014). Molecular targets of chromatin repressive mark H3K9me3 in primate progenitor cells within adult neurogenic niches. Front Genet *5*, 252.

Fraga, M.F., Ballestar, E., Villar-Garea, A., Boix-Chornet, M., Espada, J., Schotta, G., Bonaldi, T., Haydon, C., Ropero, S., Petrie, K., *et al.* (2005). Loss of acetylation at Lys16 and trimethylation at Lys20 of histone H4 is a common hallmark of human cancer. Nature genetics *37*, 391-400.

Friedmann-Morvinski, D., Bushong, E.A., Ke, E., Soda, Y., Marumoto, T., Singer, O., Ellisman, M.H., and Verma, I.M. (2012). Dedifferentiation of neurons and astrocytes by oncogenes can induce gliomas in mice. Science *338*, 1080-1084.

Fuentealba, L.C., Rompani, S.B., Parraguez, J.I., Obernier, K., Romero, R., Cepko, C.L., and Alvarez-Buylla, A. (2015). Embryonic Origin of Postnatal Neural Stem Cells. Cell *161*, 1644-1655.

Funato, K., Major, T., Lewis, P.W., Allis, C.D., and Tabar, V. (2014). Use of human embryonic stem cells to model pediatric gliomas with H3.3K27M histone mutation. Science *346*, 1529-1533.

Gage, F.H. (2000). Mammalian neural stem cells. Science *287*, 1433-1438.

Gao, Z., Ure, K., Ding, P., Nashaat, M., Yuan, L., Ma, J., Hammer, R.E., and Hsieh, J. (2011). The master negative regulator REST/NRSF controls adult neurogenesis by restraining the neurogenic program in quiescent stem cells. The Journal of neuroscience : the official journal of the Society for Neuroscience *31*, 9772-9786.

Garcia-Cao, M., O'Sullivan, R., Peters, A.H., Jenuwein, T., and Blasco, M.A. (2004). Epigenetic regulation of telomere length in mammalian cells by the Suv39h1 and Suv39h2 histone methyltransferases. Nature genetics *36*, 94-99.

Gilbert, P.E., Kesner, R.P., and Lee, I. (2001). Dissociating hippocampal subregions: double dissociation between dentate gyrus and CA1. Hippocampus *11*, 626-636.

Golebiewska, A., Atkinson, S.P., Lako, M., and Armstrong, L. (2009). Epigenetic landscaping during hESC differentiation to neural cells. Stem cells *27*, 1298-1308.

Gollapalli, K., Ghantasala, S., Kumar, S., Srivastava, R., Rapole, S., Moiyadi, A., Epari, S., and Srivastava, S. (2017). Subventricular zone involvement in Glioblastoma - A proteomic evaluation and clinicoradiological correlation. Scientific reports *7*, 1449.

Goncalves, J.T., Schafer, S.T., and Gage, F.H. (2016). Adult Neurogenesis in the Hippocampus: From Stem Cells to Behavior. Cell *167*, 897-914.

Gonzales-Roybal, G., and Lim, D.A. (2013). Chromatin-based epigenetics of adult subventricular zone neural stem cells. Front Genet *4*, 194.

Goodrich-Hunsaker, N.J., Hunsaker, M.R., and Kesner, R.P. (2008). The interactions and dissociations of the dorsal hippocampus subregions: how the dentate gyrus, CA3, and CA1 process spatial information. Behav Neurosci *122*, 16-26.

Gotz, M., and Huttner, W.B. (2005). The cell biology of neurogenesis. Nature reviews Molecular cell biology *6*, 777-788.

Grandel, H., and Brand, M. (2013). Comparative aspects of adult neural stem cell activity in vertebrates. Dev Genes Evol *223*, 131-147.

Guillemot, F. (2007). Cell fate specification in the mammalian telencephalon. Progress in neurobiology *83*, 37-52.

Gunther, H.S., Schmidt, N.O., Phillips, H.S., Kemming, D., Kharbanda, S., Soriano, R., Modrusan, Z., Meissner, H., Westphal, M., and Lamszus, K. (2008). Glioblastoma-derived stem cell-enriched cultures form distinct subgroups according to molecular and phenotypic criteria. Oncogene *27*, 2897-2909.

Hagg, T. (2005). Molecular regulation of adult CNS neurogenesis: an integrated view. Trends Neurosci *28*, 589-595.

Haskins, W.E., Zablotsky, B.L., Foret, M.R., Ihrie, R.A., Alvarez-Buylla, A., Eisenman, R.N., Berger, M.S., and Lin, C.H. (2013). Molecular Characteristics in MRI-Classified Group 1 Glioblastoma Multiforme. Frontiers in oncology *3*, 182.

Heinrich, C., Blum, R., Gascon, S., Masserdotti, G., Tripathi, P., Sanchez, R., Tiedt, S., Schroeder, T., Gotz, M., and Berninger, B. (2010). Directing astroglia from the cerebral cortex into subtype specific functional neurons. PLoS biology *8*, e1000373.

Herrup, K., and Yang, Y. (2007). Cell cycle regulation in the postmitotic neuron: oxymoron or new biology? Nature reviews Neuroscience *8*, 368-378.

Hirabayashi, Y., and Gotoh, Y. (2010). Epigenetic control of neural precursor cell fate during development. Nature reviews Neuroscience *11*, 377-388.

Hirabayashi, Y., Suzki, N., Tsuboi, M., Endo, T.A., Toyoda, T., Shinga, J., Koseki, H., Vidal, M., and Gotoh, Y. (2009). Polycomb limits the neurogenic competence of neural precursor cells to promote astrogenic fate transition. Neuron *63*, 600-613.

Hohenstein, P., Slight, J., Ozdemir, D.D., Burn, S.F., Berry, R., and Hastie, N.D. (2008). High-efficiency Rosa26 knock-in vector construction for Cre-regulated overexpression and RNAi. Pathogenetics *1*, 3.

Hughes, T.R., and Lambert, S.A. (2017). Transcription factors read epigenetics. Science *356*, 489-490.

Hwang, W.W., Salinas, R.D., Siu, J.J., Kelley, K.W., Delgado, R.N., Paredes, M.F., Alvarez-Buylla, A., Oldham, M.C., and Lim, D.A. (2014). Distinct and separable roles for EZH2 in neurogenic astroglia. Elife *3*, e02439.

Iida, A., Iwagawa, T., Kuribayashi, H., Satoh, S., Mochizuki, Y., Baba, Y., Nakauchi, H., Furukawa, T., Koseki, H., Murakami, A., *et al.* (2014). Histone demethylase Jmjd3 is required for the development of subsets of retinal bipolar cells. Proceedings of the National Academy of Sciences of the United States of America *111*, 3751-3756.

Imitola, J., Raddassi, K., Park, K.I., Mueller, F.J., Nieto, M., Teng, Y.D., Frenkel, D., Li, J., Sidman, R.L., Walsh, C.A., *et al.* (2004). Directed migration of neural stem cells to sites of CNS injury by the stromal cell-derived factor 1alpha/CXC chemokine receptor 4 pathway. Proceedings of the National Academy of Sciences of the United States of America *101*, 18117-18122.

Inda, M.M., Bonavia, R., and Seoane, J. (2014). Glioblastoma multiforme: a look inside its heterogeneous nature. Cancers *6*, 226-239.

Inta, D., Cameron, H.A., and Gass, P. (2015). New neurons in the adult striatum: from rodents to humans. Trends Neurosci *38*, 517-523.

Jafri, N.F., Clarke, J.L., Weinberg, V., Barani, I.J., and Cha, S. (2013). Relationship of glioblastoma multiforme to the subventricular zone is associated with survival. Neuro Oncol *15*, 91-96.

Johnson, M.B., Wang, P.P., Atabay, K.D., Murphy, E.A., Doan, R.N., Hecht, J.L., and Walsh, C.A. (2015). Single-cell analysis reveals transcriptional heterogeneity of neural progenitors in human cortex. Nat Neurosci *18*, 637-646.

Juan, A.H., Wang, S., Ko, K.D., Zare, H., Tsai, P.F., Feng, X., Vivanco, K.O., Ascoli, A.M., Gutierrez-Cruz, G., Krebs, J., *et al.* (2016). Roles of H3K27me2 and H3K27me3 Examined during Fate Specification of Embryonic Stem Cells. Cell reports *17*, 1369-1382.

Jungk, C., Mock, A., Exner, J., Geisenberger, C., Warta, R., Capper, D., Abdollahi, A., Friauf, S., Lahrmann, B., Grabe, N., *et al.* (2016). Spatial transcriptome analysis reveals Notch pathway-associated prognostic markers in IDH1 wild-type glioblastoma involving the subventricular zone. BMC Med *14*, 170.

Kandasamy, M., Rosskopf, M., Wagner, K., Klein, B., Couillard-Despres, S., Reitsamer, H.A., Stephan, M., Nguyen, H.P., Riess, O., Bogdahn, U., *et al.* (2015). Reduction in Subventricular Zone-Derived Olfactory Bulb Neurogenesis in a Rat Model of Huntington's Disease Is Accompanied by Striatal Invasion of Neuroblasts. PloS one *10*.

Kang, S.C., Kim, S.K., Chai, J.C., Kim, S.H., Won, K.J., Lee, Y.S., Jung, K.H., and Chai, Y.G. (2015). Transcriptomic Profiling and H3K27me3 Distribution Reveal Both Demethylase-Dependent and Independent Regulation of Developmental Gene Transcription in Cell Differentiation. PloS one *10*, e0135276.

Kempermann, G., and Gage, F.H. (1999). New nerve cells for the adult brain. Sci Am *280*, 48-53.

Kempermann, G., Jessberger, S., Steiner, B., and Kronenberg, G. (2004). Milestones of neuronal development in the adult hippocampus. Trends Neurosci *27*, 447-452.

Kempermann, G., Song, H., and Gage, F.H. (2015). Neurogenesis in the Adult Hippocampus. Cold Spring Harbor perspectives in biology *7*, a018812.

Khare, S.P., Habib, F., Sharma, R., Gadewal, N., Gupta, S., and Galande, S. (2012). HIstome--a relational knowledgebase of human histone proteins and histone modifying enzymes. Nucleic Acids Res *40*, D337-342.

Kim, S.H., Joshi, K., Ezhilarasan, R., Myers, T.R., Siu, J., Gu, C., Nakano-Okuno, M., Taylor, D., Minata, M., Sulman, E.P., *et al.* (2015). EZH2 protects glioma stem cells from radiation-induced cell death in a MELK/FOXM1-dependent manner. Stem cell reports *4*, 226-238.

Kleer, C.G., Cao, Q., Varambally, S., Shen, R., Ota, I., Tomlins, S.A., Ghosh, D., Sewalt, R.G., Otte, A.P., Hayes, D.F., *et al.* (2003). EZH2 is a marker of aggressive breast cancer and promotes neoplastic transformation of breast epithelial cells. Proceedings of the National Academy of Sciences of the United States of America *100*, 11606-11611.

Kohwi, M., and Doe, C.Q. (2013). Temporal fate specification and neural progenitor competence during development. Nature reviews Neuroscience *14*, 823-838.

Kouzarides, T. (2007). Chromatin modifications and their function. Cell *128*, 693-705.

Kriegstein, A., and Alvarez-Buylla, A. (2009). The glial nature of embryonic and adult neural stem cells. Annual review of neuroscience *32*, 149-184.

Kukekov, V.G., Laywell, E.D., Suslov, O., Davies, K., Scheffler, B., Thomas, L.B., O'Brien, T.F., Kusakabe, M., and Steindler, D.A. (1999). Multipotent stem/progenitor cells with similar properties arise from two neurogenic regions of adult human brain. Exp Neurol *156*, 333-344.

Kulkarni, S., Micci, M.A., Leser, J., Shin, C., Tang, S.C., Fu, Y.Y., Liu, L., Li, Q., Saha, M., Li, C., *et al.* (2017). Adult enteric nervous system in health is maintained by a dynamic balance between neuronal apoptosis and neurogenesis. Proceedings of the National Academy of Sciences of the United States of America *114*, E3709-E3718.

Lachner, M., O'Carroll, D., Rea, S., Mechtler, K., and Jenuwein, T. (2001). Methylation of histone H3 lysine 9 creates a binding site for HP1 proteins. Nature *410*, 116-120.

Li, M., and Belmonte, J.C. (2017). Ground rules of the pluripotency gene regulatory network. Nature reviews Genetics *18*, 180-191.

Lim, D.A., Cha, S., Mayo, M.C., Chen, M.H., Keles, E., VandenBerg, S., and Berger, M.S. (2007). Relationship of glioblastoma multiforme to neural stem cell regions predicts invasive and multifocal tumor phenotype. Neuro Oncol *9*, 424-429.

Lim, D.A., Huang, Y.C., Swigut, T., Mirick, A.L., Garcia-Verdugo, J.M., Wysocka, J., Ernst, P., and Alvarez-Buylla, A. (2009). Chromatin remodelling factor Mll1 is essential for neurogenesis from postnatal neural stem cells. Nature *458*, 529-533.

Lin, C.A., Rhodes, C.T., Lin, C., Phillips, J.J., and Berger, M.S. (2017). Comparative Analyses Identify Molecular Signature of MRI-Classified SVZ-associated Glioblastoma. Cell Cycle, 0.

Lin, C.Y., Loven, J., Rahl, P.B., Paranal, R.M., Burge, C.B., Bradner, J.E., Lee, T.I., and Young, R.A. (2012). Transcriptional amplification in tumor cells with elevated c-Myc. Cell *151*, 56-67.

Lin, Q., Jo, D., Gebre-Amlak, K.D., and Ruley, H.E. (2004). Enhanced cell-permeant Cre protein for site-specific recombination in cultured cells. BMC biotechnology *4*, 25.

Lister, R., Pelizzola, M., Dowen, R.H., Hawkins, R.D., Hon, G., Tonti-Filippini, J., Nery, J.R., Lee, L., Ye, Z., Ngo, Q.M., *et al.* (2009). Human DNA methylomes at base resolution show widespread epigenomic differences. Nature *462*, 315-322.

Livesey, F.J., and Cepko, C.L. (2001). Vertebrate neural cell-fate determination: lessons from the retina. Nature reviews Neuroscience *2*, 109-118.

Llorens-Bobadilla, E., Zhao, S., Baser, A., Saiz-Castro, G., Zwadlo, K., and Martin-Villalba, A. (2015). Single-Cell Transcriptomics Reveals a Population of Dormant Neural Stem Cells that Become Activated upon Brain Injury. Cell stem cell *17*, 329-340.

Locasale, J.W. (2013). Serine, glycine and one-carbon units: cancer metabolism in full circle. Nat Rev Cancer *13*, 572-583.

Lunnon, K., Hannon, E., Smith, R.G., Dempster, E., Wong, C., Burrage, J., Troakes, C., Al-Sarraj, S., Kepa, A., Schalkwyk, L., *et al.* (2016). Variation in 5-hydroxymethylcytosine across human cortex and cerebellum. Genome biology *17*, 27.

Lunyak, V.V., and Rosenfeld, M.G. (2008). Epigenetic regulation of stem cell fate. Human molecular genetics *17*, R28-36.

Luzzati, F., De Marchis, S., Parlato, R., Gribaudo, S., Schutz, G., Fasolo, A., and Peretto, P. (2011). New Striatal Neurons in a Mouse Model of Progressive Striatal Degeneration Are Generated in both the Subventricular Zone and the Striatal Parenchyma. PloS one *6*.

Ma, D.K., Bonaguidi, M.A., Ming, G.L., and Song, H. (2009). Adult neural stem cells in the mammalian central nervous system. Cell research *19*, 672-682.

Ma, D.K., Marchetto, M.C., Guo, J.U., Ming, G.L., Gage, F.H., and Song, H. (2010). Epigenetic choreographers of neurogenesis in the adult mammalian brain. Nature neuroscience *13*, 1338-1344.

Mack, S.C., Hubert, C.G., Miller, T.E., Taylor, M.D., and Rich, J.N. (2016). An epigenetic gateway to brain tumor cell identity. Nat Neurosci *19*, 10-19.

Mall, M., Kareta, M.S., Chanda, S., Ahlenius, H., Perotti, N., Zhou, B., Grieder, S.D., Ge, X., Drake, S., Euong Ang, C., *et al.* (2017). Myt1l safeguards neuronal identity by actively repressing many non-neuronal fates. Nature *544*, 245-249.

Margueron, R., and Reinberg, D. (2011). The Polycomb complex PRC2 and its mark in life. Nature *469*, 343-349.

Martynoga, B., Drechsel, D., and Guillemot, F. (2012). Molecular control of neurogenesis: a view from the mammalian cerebral cortex. Cold Spring Harbor perspectives in biology *4*.

Mathis, L., and Nicolas, J.F. (2003). Progressive restriction of cell fates in relation to neuroepithelial cell mingling in the mouse cerebellum. Dev Biol *258*, 20-31.

Meyer, M., Reimand, J., Lan, X., Head, R., Zhu, X., Kushida, M., Bayani, J., Pressey, J.C., Lionel, A.C., Clarke, I.D., *et al.* (2015). Single cell-derived clonal analysis of human glioblastoma links functional and genomic heterogeneity. Proceedings of the National Academy of Sciences of the United States of America *112*, 851-856.

Mikkelsen, T.S., Ku, M., Jaffe, D.B., Issac, B., Lieberman, E., Giannoukos, G., Alvarez, P., Brockman, W., Kim, T.K., Koche, R.P., *et al.* (2007). Genome-wide maps of chromatin state in pluripotent and lineage-committed cells. Nature *448*, 553-560.

Miller, J.W., Beresford, S.A., Neuhouser, M.L., Cheng, T.Y., Song, X., Brown, E.C., Zheng, Y., Rodriguez, B., Green, R., and Ulrich, C.M. (2013). Homocysteine, cysteine, and risk of incident colorectal cancer in the Women's Health Initiative observational cohort. Am J Clin Nutr *97*, 827-834.

Ming, G.L., and Song, H. (2011). Adult neurogenesis in the mammalian brain: significant answers and significant questions. Neuron *70*, 687-702.

Moazed, D. (2011). Mechanisms for the inheritance of chromatin states. Cell *146*, 510-518.

Molofsky, A.V., Pardal, R., Iwashita, T., Park, I.K., Clarke, M.F., and Morrison, S.J. (2003). Bmi-1 dependence distinguishes neural stem cell self-renewal from progenitor proliferation. Nature *425*, 962-967.

Montalban-Loro, R., Domingo-Muelas, A., Bizy, A., and Ferron, S.R. (2015). Epigenetic regulation of stemness maintenance in the neurogenic niches. World journal of stem cells *7*, 700-710.

Moris, N., Pina, C., and Arias, A.M. (2016). Transition states and cell fate decisions in epigenetic landscapes. Nature reviews Genetics *17*, 693-703.

Morrison, S.J., and Spradling, A.C. (2008). Stem cells and niches: mechanisms that promote stem cell maintenance throughout life. Cell *132*, 598-611.

Nie, Z., Hu, G., Wei, G., Cui, K., Yamane, A., Resch, W., Wang, R., Green, D.R., Tessarollo, L., Casellas, R., *et al.* (2012). c-Myc is a universal amplifier of expressed genes in lymphocytes and embryonic stem cells. Cell *151*, 68-79.

Nimmo, R.A., May, G.E., and Enver, T. (2015). Primed and ready: understanding lineage commitment through single cell analysis. Trends Cell Biol *25*, 459-467.

Noctor, S.C., Martinez-Cerdeno, V., and Kriegstein, A.R. (2008). Distinct behaviors of neural stem and progenitor cells underlie cortical neurogenesis. The Journal of comparative neurology *508*, 28-44.

Ohinata, Y., Ohta, H., Shigeta, M., Yamanaka, K., Wakayama, T., and Saitou, M. (2009). A signaling principle for the specification of the germ cell lineage in mice. Cell *137*, 571-584.

Ohlemacher, S.K., Sridhar, A., Xiao, Y., Hochstetler, A.E., Sarfarazi, M., Cummins, T.R., and Meyer, J.S. (2016). Stepwise Differentiation of Retinal Ganglion Cells from Human Pluripotent Stem Cells Enables Analysis of Glaucomatous Neurodegeneration. Stem cells *34*, 1553-1562.

Ou, H.D., Phan, S., Deerinck, T.J., Thor, A., Ellisman, M.H., and O'Shea, C.C. (2017). ChromEMT: Visualizing 3D chromatin structure and compaction in interphase and mitotic cells. Science *357*.

Palmer, T.D., Markakis, E.A., Willhoite, A.R., Safar, F., and Gage, F.H. (1999). Fibroblast growth factor-2 activates a latent neurogenic program in neural stem cells from diverse regions of the adult CNS. The Journal of neuroscience : the official journal of the Society for Neuroscience *19*, 8487-8497.

Palmer, T.D., Ray, J., and Gage, F.H. (1995). FGF-2-responsive neuronal progenitors reside in proliferative and quiescent regions of the adult rodent brain. Mol Cell Neurosci *6*, 474-486.

Palmer, T.D., Takahashi, J., and Gage, F.H. (1997). The adult rat hippocampus contains primordial neural stem cells. Mol Cell Neurosci *8*, 389-404.

Pang, Z.P., Yang, N., Vierbuchen, T., Ostermeier, A., Fuentes, D.R., Yang, T.Q., Citri, A., Sebastiano, V., Marro, S., Sudhof, T.C., *et al.* (2011). Induction of human neuronal cells by defined transcription factors. Nature *476*, 220-223.

Park, D.H., Hong, S.J., Salinas, R.D., Liu, S.J., Sun, S.W., Sgualdino, J., Testa, G., Matzuk, M.M., Iwamori, N., and Lim, D.A. (2014). Activation of neuronal gene expression by the JMJD3 demethylase is required for postnatal and adult brain neurogenesis. Cell reports *8*, 1290-1299.

Parsons, D.W., Jones, S., Zhang, X., Lin, J.C., Leary, R.J., Angenendt, P., Mankoo, P., Carter, H., Siu, I.M., Gallia, G.L., *et al.* (2008). An integrated genomic analysis of human glioblastoma multiforme. Science *321*, 1807-1812.

Patel, A.P., Tirosh, I., Trombetta, J.J., Shalek, A.K., Gillespie, S.M., Wakimoto, H., Cahill, D.P., Nahed, B.V., Curry, W.T., Martuza, R.L., *et al.* (2014). Single-cell RNA-seq highlights intratumoral heterogeneity in primary glioblastoma. Science *344*, 1396-1401.

Peng, J.C., and Karpen, G.H. (2009). Heterochromatic genome stability requires regulators of histone H3 K9 methylation. PLoS genetics *5*, e1000435.

Pereira, J.D., Sansom, S.N., Smith, J., Dobenecker, M.W., Tarakhovsky, A., and Livesey, F.J. (2010). Ezh2, the histone methyltransferase of PRC2, regulates the balance between self-renewal and differentiation in the cerebral cortex. Proceedings of the National Academy of Sciences of the United States of America *107*, 15957-15962.

Peters, A.H., Mermoud, J.E., O'Carroll, D., Pagani, M., Schweizer, D., Brockdorff, N., and Jenuwein, T. (2002). Histone H3 lysine 9 methylation is an epigenetic imprint of facultative heterochromatin. Nature genetics *30*, 77-80.

Peters, A.H., O'Carroll, D., Scherthan, H., Mechtler, K., Sauer, S., Schofer, C., Weipoltshammer, K., Pagani, M., Lachner, M., Kohlmaier, A., *et al.* (2001). Loss of the Suv39h histone methyltransferases impairs mammalian heterochromatin and genome stability. Cell *107*, 323-337.

Phillips, H.S., Kharbanda, S., Chen, R., Forrest, W.F., Soriano, R.H., Wu, T.D., Misra, A., Nigro, J.M., Colman, H., Soroceanu, L., *et al.* (2006). Molecular subclasses of high-grade glioma predict prognosis, delineate a pattern of disease progression, and resemble stages in neurogenesis. Cancer cell *9*, 157-173.

Piatti, V.C., Davies-Sala, M.G., Esposito, M.S., Mongiat, L.A., Trinchero, M.F., and Schinder, A.F. (2011). The Timing for Neuronal Maturation in the Adult Hippocampus Is Modulated by Local Network Activity. Journal of Neuroscience *31*, 7715-7728.

Podobinska, M., Szablowska-Gadomska, I., Augustyniak, J., Sandvig, I., Sandvig, A., and Buzanska, L. (2017). Epigenetic Modulation of Stem Cells in Neurodevelopment: The Role of Methylation and Acetylation. Front Cell Neurosci *11*, 23.

Pollen, A.A., Nowakowski, T.J., Chen, J., Retallack, H., Sandoval-Espinosa, C., Nicholas, C.R., Shuga, J., Liu, S.J., Oldham, M.C., Diaz, A., *et al.* (2015). Molecular identity of human outer radial glia during cortical development. Cell *163*, 55-67.

Pollen, A.A., Nowakowski, T.J., Shuga, J., Wang, X., Leyrat, A.A., Lui, J.H., Li, N., Szpankowski, L., Fowler, B., Chen, P., *et al.* (2014). Low-coverage single-cell mRNA sequencing reveals cellular heterogeneity and activated signaling pathways in developing cerebral cortex. Nature biotechnology *32*, 1053-1058.

Qin, E.Y., Cooper, D.D., Abbott, K.L., Lennon, J., Nagaraja, S., Mackay, A., Jones, C., Vogel, H., Jackson, P.K., and Monje, M. (2017). Neural Precursor-Derived Pleiotrophin Mediates Subventricular Zone Invasion by Glioma. Cell *170*, 845-859 e819.

Redzic, Z.B., Preston, J.E., Duncan, J.A., Chodobski, A., and Szmydynger-Chodobska, J. (2005). The choroid plexus-cerebrospinal fluid system: from development to aging. Curr Top Dev Biol *71*, 1-52.

Rex, M., Orme, A., Uwanogho, D., Tointon, K., Wigmore, P.M., Sharpe, P.T., and Scotting, P.J. (1997). Dynamic expression of chicken Sox2 and Sox3 genes in ectoderm induced to form neural tissue. Dev Dyn *209*, 323-332.

Reynolds, B.A., and Weiss, S. (1992). Generation of neurons and astrocytes from isolated cells of the adult mammalian central nervous system. Science *255*, 1707-1710.

Rhodes, C.T., Sandstrom, R.S., Huang, S.A., Wang, Y., Schotta, G., Berger, M.S., and Lin, C.A. (2016). Cross-species Analyses Unravel the Complexity of H3K27me3 and H4K20me3 in the Context of Neural Stem Progenitor Cells. Neuroepigenetics *6*, 10-25.

Richards, L.J., Kilpatrick, T.J., and Bartlett, P.F. (1992). De novo generation of neuronal cells from the adult mouse brain. Proceedings of the National Academy of Sciences of the United States of America *89*, 8591-8595.

Rolls, E.T., and Kesner, R.P. (2006). A computational theory of hippocampal function, and empirical tests of the theory. Progress in neurobiology *79*, 1-48.

Roman-Trufero, M., Mendez-Gomez, H.R., Perez, C., Hijikata, A., Fujimura, Y., Endo, T., Koseki, H., Vicario-Abejon, C., and Vidal, M. (2009). Maintenance of undifferentiated state and self-renewal of embryonic neural stem cells by Polycomb protein Ring1B. Stem Cells *27*, 1559-1570.

Roopra, A., Qazi, R., Schoenike, B., Daley, T.J., and Morrison, J.F. (2004). Localized domains of G9a-mediated histone methylation are required for silencing of neuronal genes. Molecular cell *14*, 727-738.

Roy, N.S., Wang, S., Jiang, L., Kang, J., Benraiss, A., Harrison-Restelli, C., Fraser, R.A., Couldwell, W.T., Kawaguchi, A., Okano, H., *et al.* (2000). In vitro neurogenesis by progenitor cells isolated from the adult human hippocampus. Nature medicine *6*, 271-277.

Ruthenburg, A.J., Allis, C.D., and Wysocka, J. (2007). Methylation of lysine 4 on histone H3: intricacy of writing and reading a single epigenetic mark. Molecular cell *25*, 15-30.

Sandstrom, R.S., Foret, M.R., Grow, D.A., Haugen, E., Rhodes, C.T., Cardona, A.E., Phelix, C.F., Wang, Y., Berger, M.S., and Lin, C.H. (2014). Epigenetic regulation by chromatin activation mark H3K4me3 in primate progenitor cells within adult neurogenic niche. Scientific reports *4*, 5371.

Saxonov, S., Berg, P., and Brutlag, D.L. (2006). A genome-wide analysis of CpG dinucleotides in the human genome distinguishes two distinct classes of promoters. Proceedings of the National Academy of Sciences of the United States of America *103*, 1412-1417.

Schaefer, A., Sampath, S.C., Intrator, A., Min, A., Gertler, T.S., Surmeier, D.J., Tarakhovsky, A., and Greengard, P. (2009). Control of cognition and adaptive behavior by the GLP/G9a epigenetic suppressor complex. Neuron *64*, 678-691.

Schofield, R. (1978). The Relationship Between the Spleen Colony-forming Cell and the Haematopoietic Stem Cell, Vol 4.

Schotta, G., Sengupta, R., Kubicek, S., Malin, S., Kauer, M., Callen, E., Celeste, A., Pagani, M., Opravil, S., De La Rosa-Velazquez, I.A., *et al.* (2008). A chromatin-wide transition to H4K20 monomethylation impairs genome integrity and programmed DNA rearrangements in the mouse. Genes Dev *22*, 2048-2061.

Schouten, M., Buijink, M.R., Lucassen, P.J., and Fitzsimons, C.P. (2012). New Neurons in Aging Brains: Molecular Control by Small Non-Coding RNAs. Front Neurosci *6*, 25.

Schuurmans, C., and Guillemot, F. (2002). Molecular mechanisms underlying cell fate specification in the developing telencephalon. Current opinion in neurobiology *12*, 26-34.

Schweisguth, F. (2015). Asymmetric cell division in the Drosophila bristle lineage: from the polarization of sensory organ precursor cells to Notch-mediated binary fate decision. Wiley Interdiscip Rev Dev Biol *4*, 299-309.

Sha, K., and Boyer, L.A. (2008). The chromatin signature of pluripotent cells. In StemBook (Cambridge (MA)).

Shen, H., and Laird, P.W. (2013). Interplay between the cancer genome and epigenome. Cell *153*, 38-55.

Sher, F., Boddeke, E., and Copray, S. (2011). Ezh2 expression in astrocytes induces their dedifferentiation toward neural stem cells. Cell Reprogram *13*, 1-6.

Sher, F., Boddeke, E., Olah, M., and Copray, S. (2012). Dynamic changes in Ezh2 gene occupancy underlie its involvement in neural stem cell self-renewal and differentiation towards oligodendrocytes. PloS one *7*, e40399.

Sierra, A., Encinas, J.M., Deudero, J.J., Chancey, J.H., Enikolopov, G., Overstreet-Wadiche, L.S., Tsirka, S.E., and Maletic-Savatic, M. (2010). Microglia shape adult hippocampal neurogenesis through apoptosis-coupled phagocytosis. Cell stem cell *7*, 483-495.

Signolet, J., and Hendrich, B. (2015). The function of chromatin modifiers in lineage commitment and cell fate specification. FEBS J *282*, 1692-1702.

Singh, S.R. (2012). Stem cell niche in tissue homeostasis, aging and cancer. Curr Med Chem *19*, 5965-5974.

Soeda, A., Hara, A., Kunisada, T., Yoshimura, S., Iwama, T., and Park, D.M. (2015). The evidence of glioblastoma heterogeneity. Scientific reports *5*, 7979.

Song, C.X., Yi, C., and He, C. (2012). Mapping recently identified nucleotide variants in the genome and transcriptome. Nature biotechnology *30*, 1107-1116.

Sottoriva, A., Spiteri, I., Piccirillo, S.G., Touloumis, A., Collins, V.P., Marioni, J.C., Curtis, C., Watts, C., and Tavare, S. (2013). Intratumor heterogeneity in human glioblastoma reflects cancer evolutionary dynamics. Proceedings of the National Academy of Sciences of the United States of America *110*, 4009-4014.

Spyros Darmanis, S.A.S., Derek Croote, Marco Mignardi, Sophia Chernikova, Peyman Samghababi, Ye Zhang, Norma Neff, Mark Kowarsky, Christine Caneda, Gordon Li, Steven Chang, Ian David Connolly, Yingmei Li, Ben Barres, Melanie Hayden Gephart, Stephen R. Quake (July 19, 2017). Single-Cell RNAseq analysis of infiltrating neoplastic cells at the migrating front of human glioblastoma. biorxiv.

Steed, T.C., Treiber, J.M., Patel, K., Ramakrishnan, V., Merk, A., Smith, A.R., Carter, B.S., Dale, A.M., Chow, L.M., and Chen, C.C. (2016). Differential localization of glioblastoma subtype: implications on glioblastoma pathogenesis. Oncotarget *7*, 24899-24907.

Stricker, S.H., Feber, A., Engstrom, P.G., Caren, H., Kurian, K.M., Takashima, Y., Watts, C., Way, M., Dirks, P., Bertone, P., *et al.* (2013). Widespread resetting of DNA methylation in glioblastoma-initiating cells suppresses malignant cellular behavior in a lineage-dependent manner. Genes & development *27*, 654-669.

Su, I.H., Basavaraj, A., Krutchinsky, A.N., Hobert, O., Ullrich, A., Chait, B.T., and Tarakhovsky, A. (2003). Ezh2 controls B cell development through histone H3 methylation and Igh rearrangement. Nature immunology *4*, 124-131.

Sun, W.J., Zang, L.Q., Shu, Q., and Li, X.K. (2014). From development to diseases: The role of 5hmC in brain. Genomics *104*, 347-351.

Surani, M.A. (2015). Human Germline: A New Research Frontier. Stem Cell Reports *4*, 955-960.

Suva, M.L., Rheinbay, E., Gillespie, S.M., Patel, A.P., Wakimoto, H., Rabkin, S.D., Riggi, N., Chi, A.S., Cahill, D.P., Nahed, B.V., *et al.* (2014). Reconstructing and reprogramming the tumor-propagating potential of glioblastoma stem-like cells. Cell *157*, 580-594.

Suva, M.L., Riggi, N., and Bernstein, B.E. (2013). Epigenetic reprogramming in cancer. Science *339*, 1567-1570.

Suva, M.L., Riggi, N., Janiszewska, M., Radovanovic, I., Provero, P., Stehle, J.C., Baumer, K., Le Bitoux, M.A., Marino, D., Cironi, L., *et al.* (2009). EZH2 is essential for glioblastoma cancer stem cell maintenance. Cancer Res *69*, 9211-9218.

Tam, P.P., and Behringer, R.R. (1997). Mouse gastrulation: the formation of a mammalian body plan. Mech Dev *68*, 3-25.

Tam, P.P., and Loebel, D.A. (2007). Gene function in mouse embryogenesis: get set for gastrulation. Nature reviews Genetics *8*, 368-381.

Tavazoie, M., Van der Veken, L., Silva-Vargas, V., Louissaint, M., Colonna, L., Zaidi, B., Garcia-Verdugo, J.M., and Doetsch, F. (2008). A specialized vascular niche for adult neural stem cells. Cell stem cell *3*, 279-288.

Tchantchou, F., and Shea, T.B. (2008). Folate deprivation, the methionine cycle, and Alzheimer's disease. Vitam Horm *79*, 83-97.

Ting, A.H., McGarvey, K.M., and Baylin, S.B. (2006). The cancer epigenome--components and functional correlates. Genes & development *20*, 3215-3231.

Treves, A., Tashiro, A., Witter, M.P., and Moser, E.I. (2008). What is the mammalian dentate gyrus good for? Neuroscience *154*, 1155-1172.

Tryndyak, V.P., Kovalchuk, O., and Pogribny, I.P. (2006). Loss of DNA methylation and histone H4 lysine 20 trimethylation in human breast cancer cells is associated with aberrant expression of DNA methyltransferase 1, Suv4-20h2 histone methyltransferase and methyl-binding proteins. Cancer Biology & Therapy *5*, 65-70.

Urban, N., and Guillemot, F. (2014). Neurogenesis in the embryonic and adult brain: same regulators, different roles. Front Cell Neurosci *8*, 396.

Urban, N., and Guillemot, F. (2015). Neurogenesis in the embryonic and adult brain: same regulators, different roles (vol 8, 396, 2014). Frontiers in Cellular Neuroscience *9*.

Van Den Broeck, A., Brambilla, E., Moro-Sibilot, D., Lantuejoul, S., Brambilla, C., Eymin, B., Khochbin, S., and Gazzeri, S. (2008). Loss of histone H4K20 trimethylation occurs in preneoplasia and influences prognosis of non-small cell lung cancer. Clin Cancer Res *14*, 7237-7245.

Varambally, S., Dhanasekaran, S.M., Zhou, M., Barrette, T.R., Kumar-Sinha, C., Sanda, M.G., Ghosh, D., Pienta, K.J., Sewalt, R.G., Otte, A.P., *et al.* (2002). The polycomb group protein EZH2 is involved in progression of prostate cancer. Nature *419*, 624-629.

Verhaak, R.G., Hoadley, K.A., Purdom, E., Wang, V., Qi, Y., Wilkerson, M.D., Miller, C.R., Ding, L., Golub, T., Mesirov, J.P., *et al.* (2010). Integrated genomic analysis identifies clinically relevant

subtypes of glioblastoma characterized by abnormalities in PDGFRA, IDH1, EGFR, and NF1. Cancer cell *17*, 98-110.

Voigt, P., Tee, W.W., and Reinberg, D. (2013). A double take on bivalent promoters. Genes & development *27*, 1318-1338.

Waddington, C.H. (1966). Principles of development and differentiation (New York,: Macmillan).

Wagers, A.J., Christensen, J.L., and Weissman, I.L. (2002). Cell fate determination from stem cells. Gene Ther *9*, 606-612.

Wagers, A.J., and Weissman, I.L. (2004). Plasticity of adult stem cells. Cell *116*, 639-648.

Wang, X., Tsai, J.W., LaMonica, B., and Kriegstein, A.R. (2011). A new subtype of progenitor cell in the mouse embryonic neocortex. Nat Neurosci *14*, 555-561.

Wei, W., Shin, Y.S., Xue, M., Matsutani, T., Masui, K., Yang, H., Ikegami, S., Gu, Y., Herrmann, K., Johnson, D., *et al.* (2016). Single-Cell Phosphoproteomics Resolves Adaptive Signaling Dynamics and Informs Targeted Combination Therapy in Glioblastoma. Cancer Cell *29*, 563-573.

Wen, S., Li, H., and Liu, J. (2009). Epigenetic background of neuronal fate determination. Progress in neurobiology *87*, 98-117.

Wennekamp, S., Mesecke, S., Nedelec, F., and Hiiragi, T. (2013). A self-organization framework for symmetry breaking in the mammalian embryo. Nature reviews Molecular cell biology *14*, 452-459.

Will, E., Klump, H., Heffner, N., Schwieger, M., Schiedlmeier, B., Ostertag, W., Baum, C., and Stocking, C. (2002). Unmodified Cre recombinase crosses the membrane. Nucleic acids research *30*, e59.

Workman, A.D., Charvet, C.J., Clancy, B., Darlington, R.B., and Finlay, B.L. (2013). Modeling transformations of neurodevelopmental sequences across mammalian species. The Journal of neuroscience : the official journal of the Society for Neuroscience *33*, 7368-7383.

Wu, H., Coskun, V., Tao, J., Xie, W., Ge, W., Yoshikawa, K., Li, E., Zhang, Y., and Sun, Y.E. (2010). Dnmt3a-dependent nonpromoter DNA methylation facilitates transcription of neurogenic genes. Science *329*, 444-448.

Wu, J., and Izpisua Belmonte, J.C. (2016). Stem Cells: A Renaissance in Human Biology Research. Cell *165*, 1572-1585.

Wysocka, J., Swigut, T., Milne, T.A., Dou, Y., Zhang, X., Burlingame, A.L., Roeder, R.G., Brivanlou, A.H., and Allis, C.D. (2005). WDR5 associates with histone H3 methylated at K4 and is essential for H3 K4 methylation and vertebrate development. Cell *121*, 859-872.

Xi, J., Liu, Y., Liu, H., Chen, H., Emborg, M.E., and Zhang, S.C. (2012). Specification of midbrain dopamine neurons from primate pluripotent stem cells. Stem Cells *30*, 1655-1663.

Xie, J., Wooten, M., Tran, V., Chen, B.C., Pozmanter, C., Simbolon, C., Betzig, E., and Chen, X. (2015). Histone H3 Threonine Phosphorylation Regulates Asymmetric Histone Inheritance in the Drosophila Male Germline. Cell *163*, 920-933.

Xie, J., Wooten, M., Tran, V., and Chen, X. (2017). Breaking Symmetry - Asymmetric Histone Inheritance in Stem Cells. Trends Cell Biol *27*, 527-540.

Xie, W., Schultz, M.D., Lister, R., Hou, Z., Rajagopal, N., Ray, P., Whitaker, J.W., Tian, S., Hawkins, R.D., Leung, D., *et al.* (2013). Epigenomic analysis of multilineage differentiation of human embryonic stem cells. Cell *153*, 1134-1148.

Xu, Y., Pang, W., Lu, J., Shan, A., and Zhang, Y. (2016). Polypeptide N-Acetylgalactosaminyltransferase 13 Contributes to Neurogenesis via Stabilizing the Mucin-type O-Glycoprotein Podoplanin. The Journal of biological chemistry *291*, 23477-23488.

Xu, Y., Zhang, S., Lin, S., Guo, Y., Deng, W., Zhang, Y., and Xue, Y. (2017). WERAM: a database of writers, erasers and readers of histone acetylation and methylation in eukaryotes. Nucleic Acids Res *45*, D264-D270.

Yamanaka, S. (2012). Induced pluripotent stem cells: past, present, and future. Cell stem cell *10*, 678-684.

Yang, M., and Vousden, K.H. (2016). Serine and one-carbon metabolism in cancer. Nat Rev Cancer *16*, 650-662.

Yao, B., Christian, K.M., He, C., Jin, P., Ming, G.L., and Song, H. (2016). Epigenetic mechanisms in neurogenesis. Nature reviews Neuroscience *17*, 537-549.

Yao, B., and Jin, P. (2014). Unlocking epigenetic codes in neurogenesis. Genes & development *28*, 1253-1271.

Yokoyama, A., Somervaille, T.C., Smith, K.S., Rozenblatt-Rosen, O., Meyerson, M., and Cleary, M.L. (2005). The menin tumor suppressor protein is an essential oncogenic cofactor for MLL-associated leukemogenesis. Cell *123*, 207-218.

Yokoyama, Y., Matsumoto, A., Hieda, M., Shinchi, Y., Ogihara, E., Hamada, M., Nishioka, Y., Kimura, H., Yoshidome, K., Tsujimoto, M., *et al.* (2014). Loss of histone H4K20 trimethylation predicts poor prognosis in breast cancer and is associated with invasive activity. Breast Cancer Res *16*, R66.

Yu, D.X., Marchetto, M.C., and Gage, F.H. (2014). How to make a hippocampal dentate gyrus granule neuron. Development *141*, 2366-2375.

Zhang, J., Ji, F., Liu, Y., Lei, X., Li, H., Ji, G., Yuan, Z., and Jiao, J. (2014). Ezh2 regulates adult hippocampal neurogenesis and memory. The Journal of neuroscience : the official journal of the Society for Neuroscience *34*, 5184-5199.

Zhu, J., Adli, M., Zou, J.Y., Verstappen, G., Coyne, M., Zhang, X., Durham, T., Miri, M., Deshpande, V., De Jager, P.L., *et al.* (2013). Genome-wide chromatin state transitions associated with developmental and environmental cues. Cell *152*, 642-654.

VITA

For Christopher Thomas Rhodes, studying the fundamental processes of life has driven his desire to understand the world more completely and led to a greater appreciation of life and the environments in which life occurs. Beyond appreciating his surroundings, Christopher was attracted to biology because he saw it as an avenue to have a positive impact on the world. For example, he participated in clinical rotations in an undergraduate sports medicine program. During that time, he was fortunate enough to interact with physical therapists and orthopedic surgeons. As skilled as these professionals were, Christopher quickly realized they could only improve the quality of life for one individual at a time. As an alternative approach, through the careful examination of biological systems, Christopher hopes to expand our knowledge of life-changing conditions such as cancer, infectious diseases, and heritable chronic diseases, and consequently, effect paradigm shifts in medical treatment or diagnostic procedures. Furthermore, he does not limit this perspective to biomedical advances, and feels biologically informed decisions will positively influence veterinary medicine, wildlife conservation and agriculture. It is the potential to cause far-reaching improvements in a population, as opposed to affecting individuals separately, that has motivated Christopher to continue learning biology and applying his knowledge in novel ways. Christopher plans to become an independent researcher in the future.